Observational studies on chromospheric activities of pre-main-sequence stars

「前主系列星の彩層活動の観測的研究」

2023年度

山下 真依

兵庫県立大学大学院 理学研究科

Abstract

Young solar-type stars are considered to show strong chromospheric emission lines and have enormous starspots because of their strong surface magnetic field. We discuss the stellar activities of pre-main-sequence (PMS) stars and zero-age main-sequence (ZAMS) stars with respect to the strength of the chromospheric emission lines and with respect to their periodic light variation caused by a starspot.

What Drives the Chromospheric Activity of Pre-Main-Sequence Stars

We investigated light variation and chromospheric activities of 220 G, K, and M-type PMS stars in one molecular cloud and six moving groups. We analyzed high-resolution optical spectra of the 69 PMS stars obtained with VLT/UVES and VLT/X-Shooter, then examined the Hα ($\lambda 6563$ Å), Ca II IRT ($\lambda 8542$ Å), and infrared Mg I ($\lambda 8807$ Å) emission lines. To detect the weak chromospheric emission lines, we determined the atmospheric parameters ($T_{\rm eff}$ and $\log\ g$), projected rotational velocity, and the amount of veiling of the PMS star by comparing the observed spectrum with the photospheric model spectrum. After subtracting the photospheric model spectrum from the PMS spectrum, Hα, Ca II, and Mg I were detected as the emission lines.

The previous study for the activity of the main-sequence stars considered five parameters for the stellar dynamo activity, i.e., the rotation, the stellar mass, the spectral type ($=T_{\rm eff}$), the thickness of the convective zone, and the convective turnover time. They proposed the use of the Rossby number, which involves the rotation period and convective turnover time, as the indicator of the activity. They established the relationship between the Rossby numbers and the strength of the chromospheric Ca II emission lines for main-sequence stars.

On the other hand, PMS stars are active and show saturated Ca II emission lines. We found out that the faint Mg I emission line is a useful indicator of stellar activity even for such active stars. The strengths of the Mg I emission lines of the PMS stars with no veiling are comparable to those of ZAMS stars if both kinds of stars have similar Rossby numbers. The Mg I emission lines are considered to be formed by the dynamo activity similar to the ZAMS stars. The strengths of Mg I emission lines of the PMS stars with veiling are larger than those of the ZAMS stars. These objects are thought to have protoplanetary disks. The mass accretion from the protoplanetary disk makes a shock near the photosphere, and heats the chromosphere. We propose that the chromosphere of the PMS stars are activated not only by the dynamo process but also by mass accretion.

Mechanisms for Transporting Angular Momentum

We analyzed Transiting Exoplanet Survey Satellite (*TESS*) light curves for the 178 PMS stars. We categorize the PMS stars into three groups, i.e., the periodic variables, the quasi-periodic variables,

and the bursters. The rotational periods of the PMS stars range from 0.26 to 22 days. The amplitudes of the light curves range from $0.002 - 1.311$ mag. The 344 flares are also detected in the light curves of 37 solar-mass PMS stars. The total bolometric energy of the flare is estimated to be $10^{31} - 10^{36}$ erg.

The previous study proposed the star-disk interaction scenario for the stellar rotation of PMS stars. A classical T Tauri star (CTTS) has an optically thick disk. The magnetic field of the star connects to the inner edge of the disk. The magnetic fields are considered to put the brakes on the rotation. Because the radius of the inner disk is ~ 10 solar radius, its Keplarian rotation is several days. Once the disk disappears as it ages, the magnetic field also disappears. They claimed that, as a result, weak-line T Tauri stars (WTTSs) rotate faster than CTTSs.

We propose a different scenario for the stellar rotation. All the PMS stars with periodic variability show no near-infrared excess, and their spot coverage and strength of the Ca II emission line are comparable to those of the ZAMS stars. They are $> 10^7$ yr in age, and are considered to no longer have the optically thick disk and mass accretion, and their dynamo processes are like that of the ZAMS stars. A part of the burster PMS stars show near-infrared excess, larger light variation, and stronger Ca II emission lines than those of the ZAMS stars. It is suggested that these PMS stars have optically thick disks and the mass accretion from the disk induces the outburst and bright emission lines. We showed that the PMS stars obtained the angular momentum by the mass accretion while they still have the protoplanetary disks, and the angular momentum is enough to spin up the star.

We insist that I) mass accretion directly heats the chromosphere by shock and induces the emission lines, and that II) mass accretion transports angular momentum to the star and indirectly activates the chromosphere by accelerating the stellar rotation.

The PMS stars and the ZAMS stars have strong chromospheric emission lines, huge sunspots, and high-energy flares. This indicates that the PMS stars and the ZAMS stars have strong magnetic fields originating, at least partially, from the dynamo process.

Contents

1 Introduction

1.1 Structure of a Solar-type Star

A star is a sphere of ionized gas, plasma. In the core, the energy is produced by nuclear fusion. The center of the core is the hottest part, in which the temperature reaches 1.5×10^7 K in the case of the Sun. The energy is transported by radiation and convection to the photosphere. The atmosphere of solar-type stars is classified into the photosphere, chromosphere, transition region, and corona (figure 1).

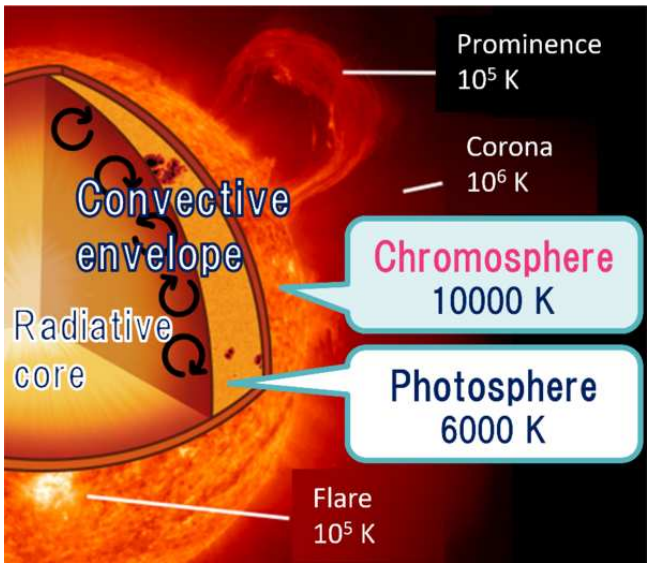

Fig. 1: Structure of a solar-type star. The atmosphere of a solar-type star is classified into the photosphere, chromosphere, transition region, and corona. Image reproduced from ISAS/JAXA.

Photosphere

Photosphere is the visible surface, and the innermost layer of the atmosphere of a star. The solar photosphere is only about $300-500$ km in thickness, while the solar radius is large as 7×10^5 km. The temperature of the photosphere is about 6000 K in the case of the Sun. It depends on the stellar mass. The stellar interior is optically thick, and has high optical depth, $\tau \equiv \int \kappa ds > 1$, where κ is absorption coefficient, and s is the length along the light path. For the Sun, the photosphere is defined as the depth at which the optical depth $\tau = 1$ at 5000 Å. The photosphere is a quiescent region. Most of the solar radiant energy is emitted from the photosphere as a continuum component. The photosphere is cooler than the center of the object and absorption lines are formed by atoms and molecules. The strengths of photospheric absorption lines depend on the temperature.

Chromosphere

The atmosphere above the photosphere is called as chromosphere. The temperature of the chromosphere gradually increases from 4×10^3 K to $\sim 10^4$ K with radial distance from the photosphere. The chromosphere has low optical depth. The optical depth gradually decreases from $\tau_{\lambda 5000\ \mathring{\mathrm{A}}} \approx 10^{-4}$ to $\approx 10^{-7}$ with radial distance from the photosphere (Frohlich & Lean 2004). In an active chromospheric region, atoms emit permitted lines such as Hα and Ca II. It is claimed that chromospheric activity is driven by the magnetic field, which is generated by the dynamo process. The heating mechanism of the chromosphere is unclear as same as coronal-heating problem described below. The details of the temperature structure of the chromosphere are described below.

Transition region

Outside a chromosphere, there is a transition region, where the chromosphere gradually goes over into the corona. The thickness of the transition region is a few thousand kilometers. The kinetic temperature increases rappidly from 10^4 K (in the inner parts) to 10^6 K (in the outer parts). Since the temperature of the transition layer depends on the temperature of the active chromosphere and active corona, it is difficult to establish a steady-state model for the transition region.

Corona

The corona is the atmosphere outside the transition region. The temperature of the solar corona is over 10^6 K. The corona emits X-rays, and emission lines excited to high energy states, such as Fe X (Fe^{9+} at 6374 Å) and Fe XIV (Fe^{13+} at 5303 Å). One of the most complicated questions in modern solar physics is the coronal heating problem. The coronal heating problem is the question of why the corona has such a high temperature. Several theories have been proposed to explain the coronal heating problem. Two promising theories are wave heating and magnetic reconnection (nano flares). It has believed that a combination of the two processes explains coronal heating, although the details are not yet understood.

1.2 Outline of Star Formation

Pre-main-sequence stars (PMS stars) are young stars. In the center of a PMS star, central hydrogen burning (nuclear fusion) is not stable or has not yet ignited. Surface radiative energy is generated by the gravitational contraction of a star. The evolution timescale from the formation of a PMS star to reaching the main-sequence depends on the stellar mass. We will describe below the observational facts or theories, mainly for a PMS star with approximately solar mass ($\sim 1\ \mathrm{M}_{\odot}$).

1.2.1 Evolutionary track

Hertzsprung-Russell diagram (HR diagram) plots the stellar luminosity as a function of the temperature. Because the stellar temperature and luminosity change are different in the different evolutional stages, the star moves to different regions on the HR diagram as it evolves. Figure 2 represents the evolutionaly tracks of PMS stars on HR diagram; birth line, Hayashi track, and Henyey track.

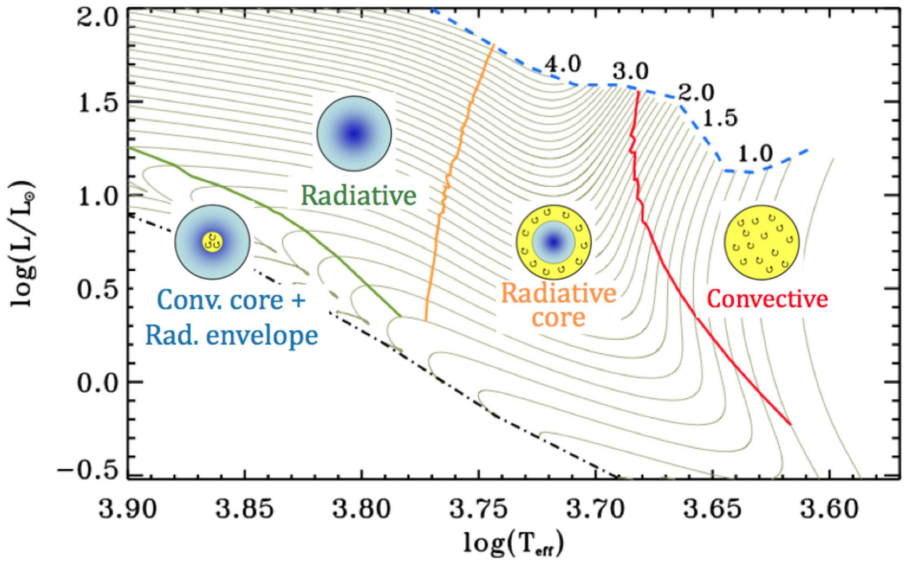

Fig. 2: HR diagram showing PMS evolutionary tracks for stellar masses of $1-4\ \mathrm{M}_{\odot}$. The dashed blue line and black dot-dashed line are the birthline of the stars and the Zero-age main-sequence (ZAMS). A star with a mass of $\leq 2.5\ \mathrm{M}_{\odot}$ has a fully convective interior near the birthline. Low-mass stars ($< 1.2\ \mathrm{M}_{\odot}$) in the PMS stage have either partially or fully convective interiors. Figure from Hussain&Alecian (2014).

Birth line

The curve connecting points on the HR diagram where stars first appear in the optical wavelength is called a birthline. At younger than a birth line, an object is not observable in the optical wavelength because optically thick dusts surround a PMS star. A star is not in equilibrium and collapses on the dynamic time scale.

Hayashi track

After the birth line, a solar-mass star settles on the Hayashi track. The star collapses and heats as gravitational potential energy is converted into thermal energy. In the HR diagram, the stars move almost vertically downwards as their luminosity and radius decrease. This trajectory is called as Hayashi track. A star evolves with the Kelvin-Helmholtz time scale;

$$t_{\rm KH} = \frac{G{M_*}^2}{R_* L}. \tag{1}$$

G, M_*, R_*, L are the gravitational constant, the stellar mass, the stellar radius, and the stellar luminosity. Until 3×10^6 yr, the energy is transported by convection throughout the interior (figure 3). As the temperature of the stellar center increases, the opacity diminishes and energy begins to be transported by radiation. The stars older than 3×10^6 yr have radiative core and convective envelope. This evolutionary track was clarified by theoretical calculations by Chushiro Hayashi in 1961.

Henyey track

After the Hayashi track, the Henyey track covers the final interval of a PMS stage for the stars of $\geq 0.4\ {\rm M}_\odot$. The temperature of the stellar surface increases and the star moves to the left in the HR diagram. The mass of the radiative region gradually increases. The central temperature continues to increase. When the inside temperature reaches 10^7 K, the nuclear fusion is expected to start. This corresponds to the age of 10^7 yr for a solar-mass star (figure 3). Not only the luminosity increases, but also the surface temperature increases. The boundary between the radiative core and the convective envelope inside the Sun is estimated to be $0.715\ {\rm R}_\odot$ with helioseismology.

Zero-age main-sequence (ZAMS)

The main-sequence is a line of stars extending from the upper left to the lower right in the HR diagram. The theoretical sequence obtained is called the zero-age main-sequence, ZAMS. In the case of the stellar mass exceeds $0.08\ {\rm M}_\odot$, the temperature of the core reaches 10^7 K and hydrogen fusion begins. Just after that, the stars are on the ZAMS. When the rate of nuclear fusion becomes enough high to balance the pressure and gravity, the fusion becomes self-sustaining.

The age of the PMS stars with $1\ {\rm M}_\odot$ is $\sim 10^6 - 10^8$ yr. According to Tout, Livio, & Bonnell (1999), it is very often unclear to define 0 yr for a forming star. Because a ZAMS can be defined uniquely, the ages of PMS stars are estimated by backward from the main-sequence. In other words, the more inaccurate in their age as they are younger, and it is difficult to measure the ages for $0 - 10^3$ yr.

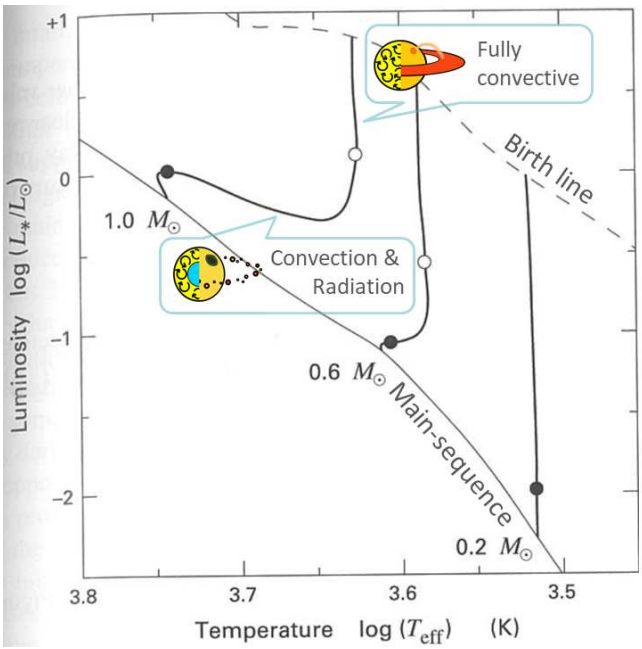

Fig. 3: Evolutionary tracks of PMS stars with $0.2, 0.6, 1.0$ $\mathrm{M}_\odot$. The open circles represent the onset when the energy begins to be transported by radiation in the core. The filled circles represent the onset of central hydrogen burning. The dashed line and thin solid line show the birthline and ZAMS, respectively. Figure reproduced from Stahler & Palla (2004).

1.2.2 Evolution of T Tauri stars

A PMS star below $2\ \mathrm{M}_{\odot}$ is called a T Tauri star (TTS). TTSs are after most of the circumstellar materials are accreted. In 1942, Joy noticed irregular variable stars, existing near or embedded in the Taurus-Auriga molecular cloud, and showing emission lines of hydrogen, Ca II HK, and other metals. Later, the four observational evidence pointed out that these objects correspond to young stars; I) association with a star-forming region, II) being located on the upper of the HR diagram, III) emission lines, and IV) high Li abundance. In this study, we call a young object in the stage from CTTS to PTTS "PMS star".

Classical T Tauri star (CTTS), 10^6 yr

A CTTS is defined as a TTS indicating a strong $\mathrm{H}\alpha$ emission line whose equivalent width (EQW) is ≥ 10 Å. A CTTS corresponds to the object going on the Hayashi track. They are considered to have developed a convective envelope, as described above. A CTTS consists of the central star, an optically thick protoplanetary disk (figure 4 and 5), a boundary layer, and a jet emanating from the dipole of the star. The near-infrared excess from the inner disk, and far-infrared excess from the outer disk are observed. The accretion shock at the boundary layer due to material accreting from the disk to the photosphere results in the infrared and ultraviolet excess. The continuum emission from the protoplanetary disk and the boundary layer veils the photospheric spectrum, and makes apparent spectral features weaken. This phenomenon is called veiling. Their spectra contain bright permitted emission lines (e.g. $\mathrm{H}\alpha$, $\mathrm{H}\beta$, Ca II, Fe I, He I) formed in the stellar chromosphere or mass accretion. CTTSs also show forbidden lines (e.g. [O I]), which can only be formed at extremely low-density region such as a jet. The strong X-ray is also observed due to the active corona (mainly), and the accretion shock from the disk to the star (Brickhouse et al. 2010). Lithium abundance of the CTTSs is relatively high, indicating that they are newly formed stars in which the central temperature has not yet become high enough to destroy lithium. Near T Tauri stars, interstellar gases such as dark clouds and emission nebula have been discovered. The brightness variations of the CTTSs are irregular.

Weak-line T Tauri star (WTTS), 10^7 yr

A WTTS corresponds to the star going on the Henyey track. The energy inside the WTTS has already begun to be partially transported by radiation. A WTTS has an optically thin protoplanetary disk surrounding the star, and no longer has a strong mass accretion and jet. A WTTS is defined as a TTS indicating a weak $\mathrm{H}\alpha$ emission line with EQW< 10 Å. Their infrared and ultraviolet excesses are also small. The weak emission lines and small excess indicate that the mass accretion is less than that of CTTS, suggesting that the disk of WTTS is disappearing, or

the WTTSs only have outer disks. Phenomena associated with strong magnetic field activity in the chromosphere, corona, and sunspots, such as strong X-rays, are observed in the WTTS stage.

Post T Tauri star (PTTS), 3×10^7 yr

A PTTS is a star just before entering ZAMS. A PTTS only has a central star (and perhaps planets or minor objects) and does not have an optically thick disk, mass accretion, or a bipolar jet. They do not show any excess or emission lines in their spectra. Some PTTSs belong to a moving group, which is a group of stars whose proper motion reaches a single point if the time is reversed. They are suggested that PTTSs belonged to a molecular cloud just after their birth.

Zero-age main-sequence star (ZAMS star), 10^8 yr

The stars just after reaching the main-sequence. They are the youngest main-sequence stars. A solar-mass star reaches the ZAMS at the age of $\sim 10^8$ yr. The details of ZAMS have been described above.

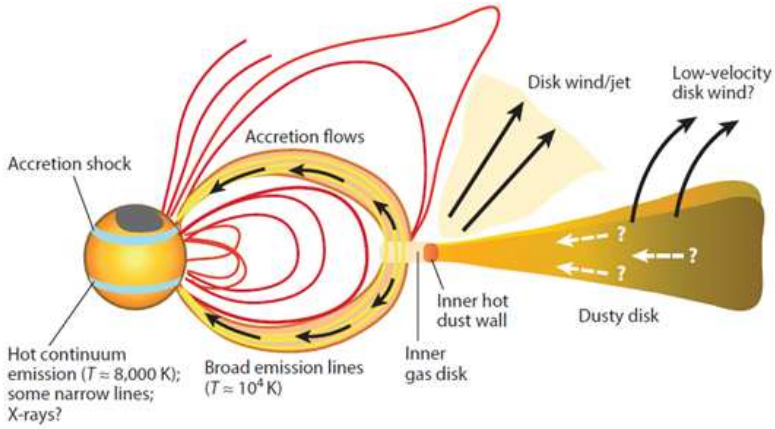

Fig. 4: Young star with mass accretion from a protoplanetary disk through the stellar magnetosphere. The red solid line represents the magnetic field lines. Material accretes from the inner part of the protoplanetary disk to the stellar surface along with the magnetic field line at near free-fall velocity making shocks at the stellar surface Figure from Hartmann, Herczeg & Calvet (2016).

Figure 4 shows a schematic view of a PMS star with a protoplanetary disk, and a mass accretion. A star is formed by gas in a molecular cloud. The gas does not accrete straight down because they have plenty of angular momentum. Then they form a disk at first. The accretion disk is heated by the central star, and part of the accretion flows are considered to be ionized. The ionized accretion flows fall along the magnetic field, to high latitudes of the star, at a free-fall velocity. This accretion is called magnetic accretion. The region where the stellar magnetic field dominates the motion of the accretion flows is called magnetosphere. If the star has strong magnetic fields, the accretion disk

is truncated by the stellar magnetosphere at a few stellar radii. Cranmer (2008) claimed that the magnetospheric accretion ends in CTTS whose age is $\sim 10^7$ yr.

The equilibrium temperature is calculated with this equation:

$$T_{\rm eq} = \sqrt{\frac{R_*}{2d}} T_*, \tag{2}$$

where d, R_*, and T_* represent the distance from the stellar photosphere, the stellar radius, and the temperature of the photosphere. The equilibrium temperature of the inner disk is estimated as $\sim 1000\,\mathrm{K}$. With Wien's displacement law, the inner disk with $1000\,\mathrm{K}$ has blackbody radiation with a peak in the near-infrared. The near-infrared excess from the heated inner disk is observed in J, H, K, $L-$bands ($1.25, 1.65, 2.2, 3.4\ \mu$m).

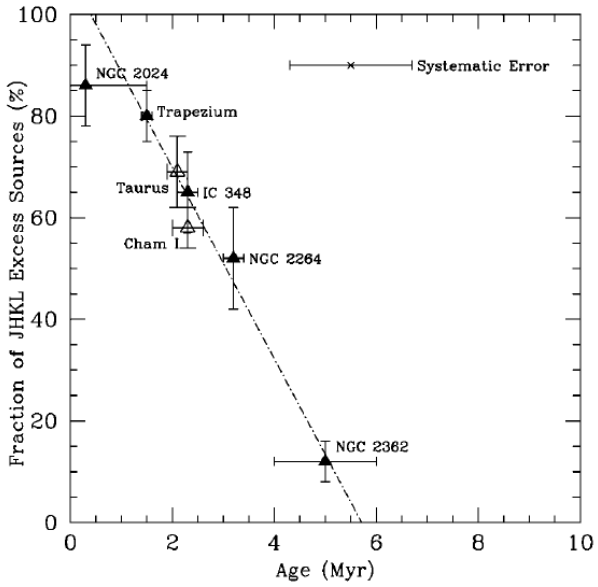

Fig. 5: J, H, K, L excess fraction of the protoplanetary disk as a function of mean cluster age. Figure from Haisch, Lada & Lada (2001).

Figure 5 shows excess fraction in J, H, K, $L-$bands of the protoplanetary disk as a function of mean cluster age. Haisch, Lada & Lada (2001) observed J, H, K, L colors and obtained the circumstellar disk fraction in each cluster. Their survey indicates that the cluster disk fraction is over $\sim 80\%$ in 10^6 yr and rapidly decreases with increasing cluster age. Almost half of the stars within the clusters lose their disks in 3×10^6 yr. The overall disk lifetime is suggested to be $\sim 6 \times 10^6$ yr in the surveyed cluster sample.

1.3 Temperature structure of chromosphere

1.3.1 The Sun

Vernazza et al. (1981) constructed the standard temperature models for the solar photosphere, chromosphere, and transition region (figure 6). The *Skylab* EUV observations in 1973 are used to determine brightness temperature and density. In the spectra of the Sun and solar-type stars, the main components of the chromospheric emission lines are Ca II K_2 and Mg II k_2, both of them are core of the Ca II and Mg II emission lines, respectively. The model shows that Ca II K_2 emission line is formed in the chromosphere at a temperature of $5000 - 6500$ K, which is $700 - 1500$ km above from the bottom of the photosphere.

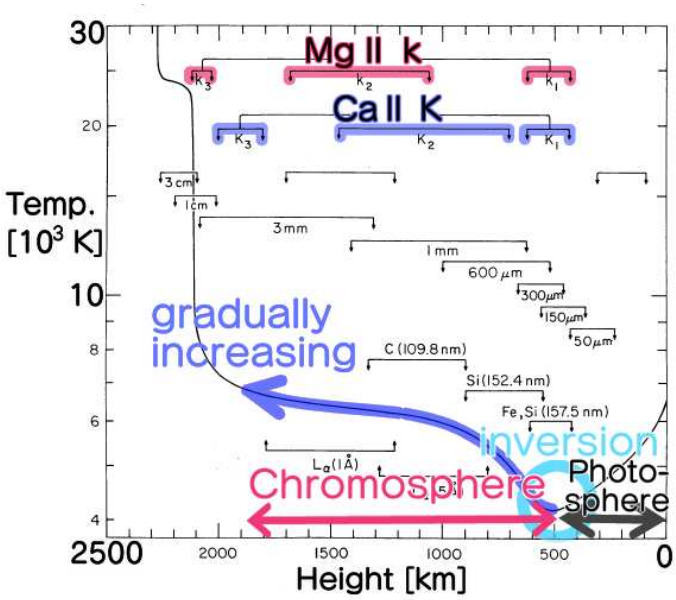

Fig. 6: The solid line shows the standard model of the solar chromosphere temperature distribution (VAL model). The zero point of the height is set to the location of $\tau = 1$. The bars with arrows on both sides indicate the approximate depths where the various continua and lines originate. Figure reproduced from Vernazza et al. (1981).

Carlsson, De Pontieu, & Hansteen (2019) compared the VAL models with observations in submillimeter and millimeter continua. They used the simulation snapshot from the quiet Sun simulation of the solar atmosphere and illustrated the basic properties of the solar chromosphere. Figure 7 indicates that the emission lines of Mg II h3 and Ca II H are formed in the upper chromosphere, and the emission lines of Na I and Mg I are formed in the lower chromosphere. They also showed that the plasma $\beta \equiv$ plasma pressure / magnetic pressure $= 1$ surface is located in the chromosphere. In the photosphere, the magnetic pressure is equal to the gas pressure if a magnetic field strength is about

1200 G. Their result indicates that plasma motions dominate the magnetic field in the photosphere and low chromosphere ($\beta > 1$), whereas the magnetic field dominates the dynamics in the upper chromosphere ($\beta < 1$).

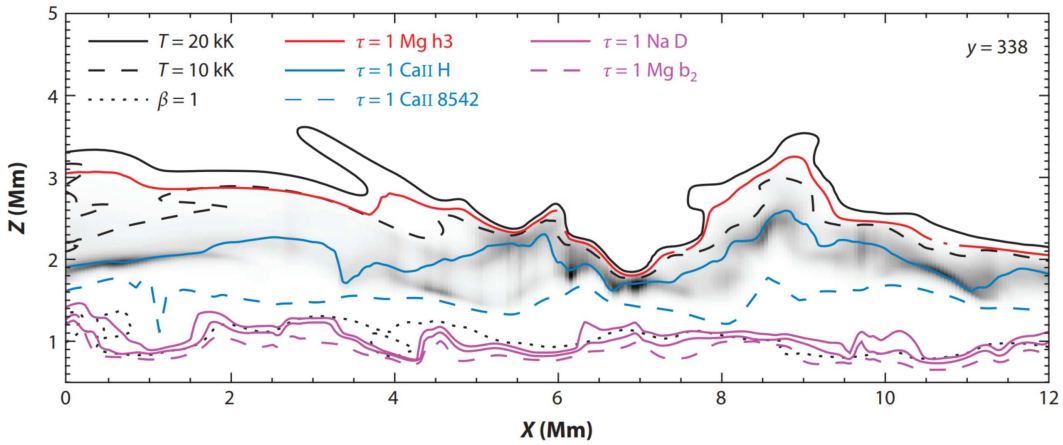

Fig. 7: Formation height of chromospheric emission lines. The X-axis and Z-axis are spatial direction and height. The zero point of Z is set to the location of the photosphere. The height of 25 Mm corresponds to the lower corona. The gray scale indicates the temperature. The plasma $\beta \equiv$ plasma pressure / magnetic pressure $= 1$ height is also given. Figure from Carlsson, De Pontieu, & Hansteen (2019).

1.3.2 Cool stars

The cool stars also have developed convective envelopes, chromosphere, and corona. Temperature models of the chromosphere have been constructed by (a) calculating multiple patterns of temperature gradients of the chromosphere, (b) obtaining model spectra generated by the temperature gradients in (a), and (c) changing the temperature gradients of the chromosphere so that the model and the observed spectra are well matched. Fuhrmeister, Schmitt, & Hauschildt (2010) constructed the temperature models of the chromosphere for the active M-type main-sequence star, CN Leo. They applied the above procedures (a)-(c) for the twelve chromospheric emission lines, including Hα emission line and infrared Ca II emission lines. Figure 8 shows the thermal structure models for the Sun and the M-type main-sequence star, GJ 832 (Fontenla et al. 2016). The photosphere and chromosphere of GJ 832 are about ~ 1000 K cooler than those of the Sun.

1.3.3 Pre-main-sequence stars

A TTS also has developed a convective envelope inside the photosphere, chromosphere, and corona. The chromospheric temperature models for TTS have been proposed only by Batalha & Basri (1993) (figure 9). They first assumed the chromospheric temperature distribution and solved the radiative transfer equations to calculate the intensities and profiles of the four emissions. The minimum temper-

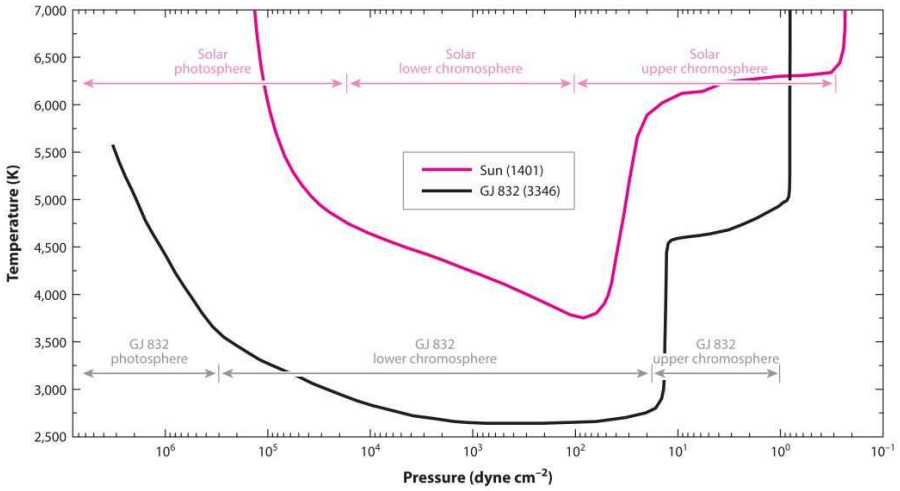

Fig. 8: Comparison of the thermal structures of quiet Sun model by Fontenla, Stancil, & Landi (2015) with model for the M1.5 V main-sequence star GJ 832 by Fontenla et al. (2016). The X-axis is pressure and its right side and left side correspond to inside (photosphere) and outside (upper chromosphere to transition region). Figure from Linsky (2017).

ature between the photosphere and chromosphere is estimated by comparing the wing of the observed Ca II HK emission line and the model spectrum. The core of the Ca II emission line at $\lambda 8542$ Å are considered to be formed on 6000 K. Then the mass column density at 6000 K is estimated by comparing the model spectrum with the core and wing of the observed Ca II emission line at $\lambda 8542$ Å. The mass column density and temperature of the transition region are assumed to be 10^{-5} g $\cdot$ cm^2 and 8000 K.

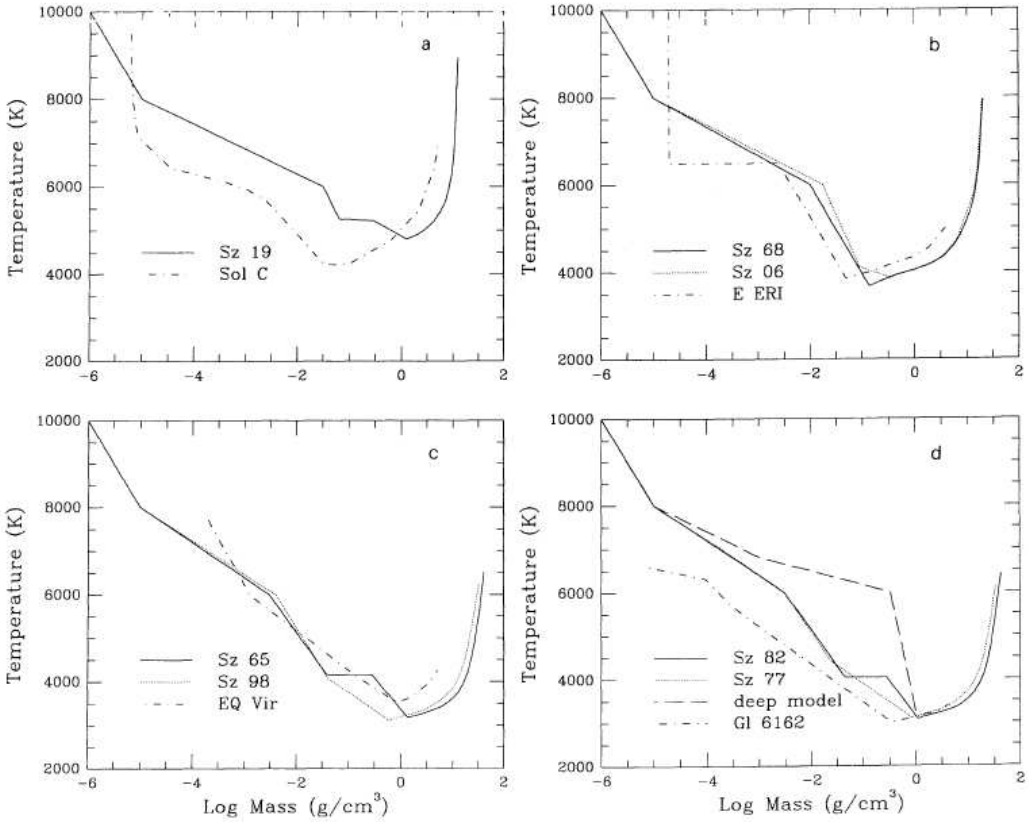

Fig. 9: Temperature models of chromosphere constructed for TTSs (Batalha & Basri 1993). The X-axis shows mass column density. The TTSs are represented by Sz numbers, and others are main-sequence stars. The solid line and dotted line in each panel show TTS; (a) G2 type TTS, Sz 19, (b) K2 type TTS, Sz 68 and Sz 06, (c) K7 type TTS, Sz 65 and Sz 98, and (d) M0 type TTS, Sz 82 and Sz77. The deep model in (d) is constructed for TTS based on Calvet, Basri & Kuhi (1984). The dash-dotted lines represent the models for main-sequence stars, especially that in (a) is solar VAL model (Vernazza et al. 1981). Figure from Batalha & Basri (1993).

1.4 Magnetic Activity

The most easily observable evidence of magnetic activity are spots, chromospheric emission lines, and the huge explosions known as flares. It is claimed that these activities are driven by the magnetic fields induced by the dynamo process. In the dynamo process, the Coriolis force (= rotational moment $\times$ convection velocity) balances the Lorentz force (= current $\times$ magnetic strength / density of plasma) (Baliunas et al. 1996). Stellar rotation and convection are considered to be the main processes that drive the evolution of magnetic activities.

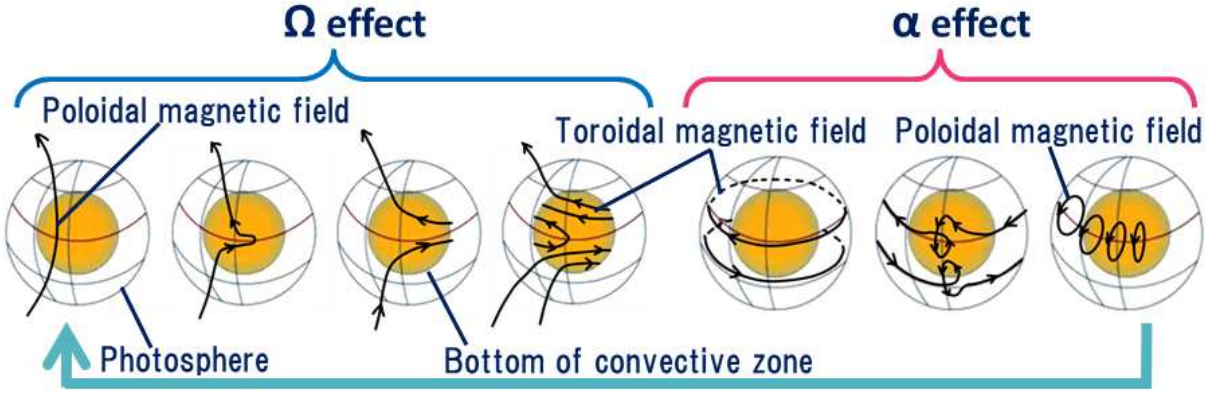

Fig. 10: Schematic view of the flux-transporting dynamo model (FTD model), which is the standard scenario for solar dynamo activity. The black solid lines represent magnetic field lines. These magnetic field lines are usually coherent and called magnetic flux tubes.

Stellar rotation

The Sun rotates every 25 days at the equator and 30 days at the poles. This is known as differential rotation. Differential rotation stretches the entire magnetic field, which makes the magnetic field stronger. This is called the Ω effect (figure 10). The star rotates faster, the differential rotation is getting stronger. The magnetic flux tube is stretched to float to the stellar surface (and generate spots). Therefore, it is necessary to stretch the magnetic flux tube by differential rotation.

Convection

The convection turnover time, $\tau_{\rm c}$, is the typical timescale for a gas eddy convect — rises and falls. Deinzer (1965) discussed the mixing length theory of sunspots, and obtained equation 3 for the convection velocity, v_c,

$$< v_c >^2 = \frac{1}{8}\frac{RT}{\mu}\left(\frac{l}{H_p}\right)^2(\nabla - \nabla'), \tag{3}$$

where μ is the molecular mass, l is the mixing length, H_p is the pressure scale height, ∇ is the

temperature gradient, and ∇' is the temperature gradient following changes in the turbulent state; α dynamo theory show that $\tau_{\rm c}$ is inversely proportional to the magnetic diffusion coefficient, η. $\tau_{\rm c}$ depends on the mixing length parameter $\alpha(=\frac{l}{H_p})$, the ratio of the mixing distance, l, to the pressure scale height, H_p. $\tau_{\rm c}$ cannot be observed directly, then $\tau_{\rm c}$ is obtained by theory or numerical calculation. $\tau_{\rm c}$ for a PMS star must be obtained from a stellar evolutionary track that includes the internal structure (figure 11).

Gilman (1980) models differential rotation in main-sequence stars with convective zones. The differential rotation of the stellar surface is forced by convection. They revealed that the convective model with larger α has longer $\tau_{\rm c}$ and thicker convective zone. The thicker convection zone is considered to sustain an equatorial acceleration, and amplify magnetic fields over a wider region.

Here, Several researchers have constructed the models of local $\tau_{\rm c}$ or global $\tau_{\rm c}$. The local $\tau_{\rm c}$ is determined from the convection velocity, v_c, at a height half the mixing length from the bottom of the convection zone (Gilliland 1986). In this study, we use the local component of the convective turnover time as τ_c.

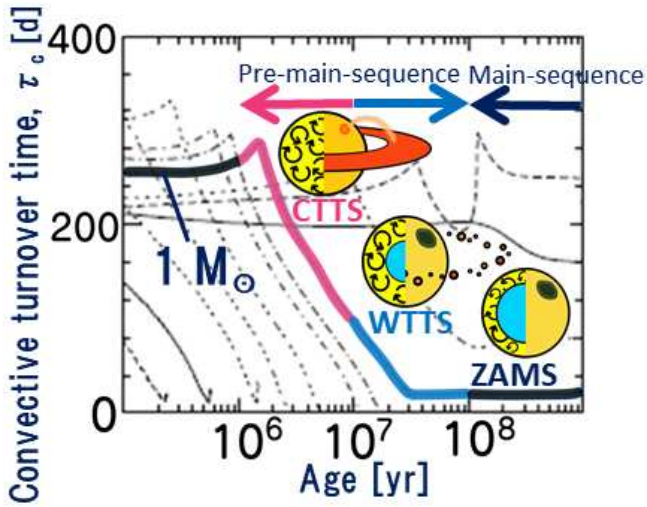

Fig. 11: The models of the convective turnover time, $\tau_{\rm c}$. Figure reproduced from Jung & Kim (2007).

Rossby number

Noyes et al. (1984) introduced the Rossby number, $N_{\rm R}$, as an indicator of magnetic activity. It is defined as $P/\tau_{\rm c}$, where P is the stellar rotational period and $\tau_{\rm c}$ is the convective turnover time. The Rossby number expresses how much rotation affects convection (Gilman 1980). With the smaller Rossby number, the fluid element moves and Coriolis forces have more time to act on it. In general, in the deeper convective zone, $\tau_{\rm c}$ is longer, and the rotational influence will be

stronger. N_{R} can be approximated as the inverse square of the dynamo number, N_D, the wave solution of the dynamo equation. Magnetic fields develop when $|N_D| > 1$. The Rossby number can be understood as the ratio of the effects of amplification and diffusion of the magnetic fields. The Rossby number itself was originally defined in meteorology and geophysical fluid dynamics, as a dimensionless quantity related to the ratio of inertial force and Coriolis forces given to a rotating fluid flow.

A gas in a photosphere is almost completely ionized, and the magnetic field is ”frozen” into the plasma. Magnetic flux is carried as the gas eddy moves (frozen-in of magnetic field). The magnetic flux tube is strengthened and reconnected due to differential rotation and amplifies the magnetic field. Once the magnetic flux tubes reach the photosphere and form sunspots and chromospheric emission lines are formed.

1.4.1 Spots in the photosphere

A spot is a region with a stronger magnetic field ($2000 - 4000$ G), while quiet regions have only a few gausses. Actually, the Zeeman effects are observed in the spectra of the sunspot regions (Hale, 1908). The tight magnetic flux tubes suppress convection within the spot and prevent surrounding plasma from entering the spot. Therefore, sunspots are observed to be dark and cool. For example, the temperature of a sunspot is ≈ 4000 K. The sunspots are also known to be geometrically lower than the surrounding area. The toroidal magnetic field is strengthened and amplified below the surface by the dynamo process and rises because of magnetic buoyancy. When the magnetic flux tube rises to the photosphere, the cross-section of the flux tube is observed as a spot.

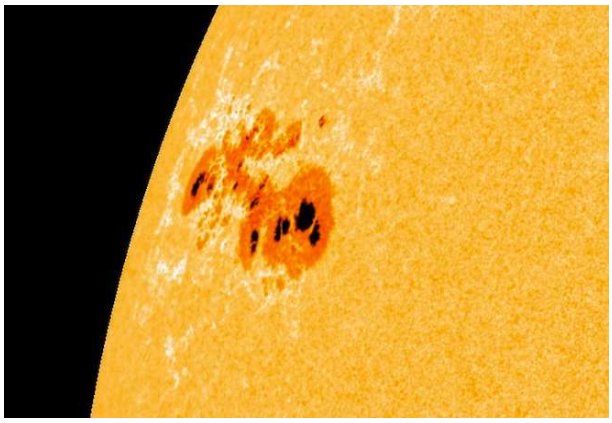

Fig. 12: The image of the solar active region. Solar spots are often surrounded by emission regions, namely faculae. In 1947, the largest solar spot decreased the brightness by $\sim 0.1\%$. Copyright by NASA/SDO.

Regarding the solar disk, it is known that spots are surrounded by emission regions, such as faculae in the photosphere and plages in the chromosphere (figure 12). Other observational evidence for the strong magnetic field of a star includes the periodic light variation caused by a starspot. The amplitude of the solar brightness variation caused by sunspots on the rotating solar surface is $0.01 - 0.1\%$ (Lanza et al. 2003).

In recent years, *Kepler* and Transiting Exoplanet Survey Satellite (*TESS*, Ricker et al. 2015) have been utilized to investigate stellar magnetic activities. The typical photometric precision of *Kepler* is 0.01% for a star of 12 mag (Koch et al. 2010). The time resolution of *Kepler* is approximately 30 minutes and 1 minutes. Rebull et al. (2016) presented *K2* light curves for F-, G-, K-, and M-type ZAMS stars in the Pleiades cluster. The rotational periods ranged from 0.082 d to 22.14 d. The amplitudes of the brightness ranged from 0.001 mag to 0.556 mag. Rebull et al. (2016) and Stauffer et al. (2016) investigated the relationship between the rotational periods and shapes of the light curves for ZAMS stars in the Pleiades cluster and found that approximately half of the F-, G-, and K-type ZAMS stars rotating rapidly have sinusoidal light curves.

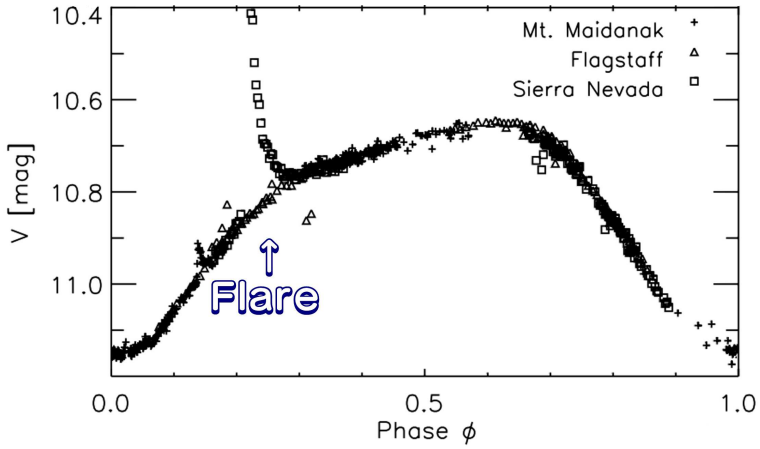

Fig. 13: The phase folded $V-$ band lightcurves of V410 Tau from 1984 to 1985. The light variation is considered to be caused by spot. Figure reproduced from Stelzer et al. (2003).

From the light curves of the PMS stars, enormous star spots are suggested to be on their surface. Bouvier et al. (1993) first detected sinusoidal light curves from TTS. In Stelzer et al. (2003), WTTS, V410 Tau shows large light variation of $\Delta V \sim 0.6$ mag (figure 13). It is considered to have an enormous spot/spot group with the surface coverage of $\sim 29\%$ and a strong magnetic field of 500 G.

1.4.2 Chromospheric emission lines

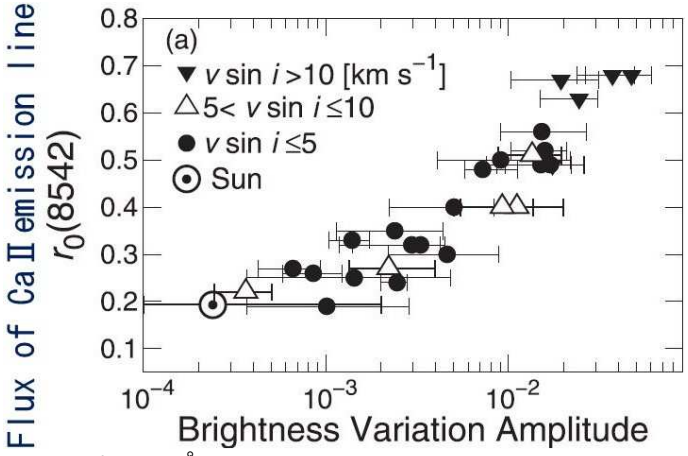

Fig. 14: The Ca II emission line ($\lambda 8542$ Å) and the amplitude of the light curve of the superflare stars. Solar-type main-sequence stars with the larger amplitude of the light curve (= larger spot) show the brighter Ca II emission line. Figure reproduced from Notsu et al. (2015).

Chromospheric emission lines are observational evidence of a strong magnetic field. Notsu et al. (2015) indicated that the Sun and superflare stars show a rough positive correlation between the amplitude of the light curve and the $r_0(8542)$ index, the residual core flux normalized by the continuum level at the line core of the Ca II IRT. They claimed that the magnetic field strengths of

superflare stars are higher than that of the Sun (figure 14).

The relationship between chromospheric line strength and the Rossby number has been examined for ZAMS stars. Marsden et al. (2009) detected Ca II infrared triplet (IRT; $\lambda 8498, 8542, 8662$ Å) emission lines from low-mass stars in the young open clusters IC 2391 and IC 2602. The cluster members are considered to be on ZAMS or in the last evolution phase before ZAMS. They calculated $\log_{10} R'_{\rm IRT}$ from the equivalent widths (EQWs)[1]. $R'_{\rm IRT}$ describes the ratio of the surface flux of the Ca II IRT emission lines to the stellar bolometric luminosity. They found that $R'_{\rm IRT}$ decreases with increasing $N_{\rm R}$ for stars with $N_{\rm R} \geq 10^{-1.1}$. This region is called the unsaturated regime. In contrast, $R'_{\rm IRT}$ is constant at levels of approximately $10^{-4.2}$ for stars with $N_{\rm R} \leq 10^{-1.1}$. This region is called the saturated regime. Marsden et al. (2009) suggested that the chromosphere is completely filled by the emitting regions for the stars in the saturated regime. Recently, Fritzewski et al. (2021) found that some of the FGKM-type stars in the young open cluster NGC 3532 (300 Myr) also show saturation at $R'_{\rm IRT} \sim 10^{-3.7}$.

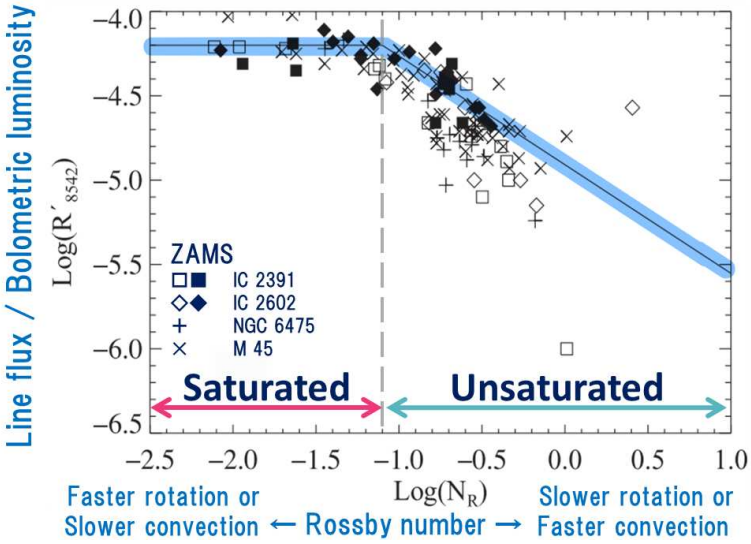

Fig. 15: The relationship between the Rossby number, $\log_{10} N_{\rm R}$, and the chromospheric emission ratio in the Ca II emission line at $\lambda 8542$ Å, $\log_{10} R'$, of the ZAMS stars in the young open cluster IC 2391 (squares), IC 2602 (diamonds), the Pleiades (crosses), and NGC 6475 (pluses). $N_{\rm R}$ of the filled symbols are calculated with the rotational period, and that of the open symbols are calculated with the projected rotational velocity, $v \sin i$. Figure reproduced from Marsden et al. (2009).

Yamashita et al. (2020) investigated the relationship between $N_{\rm R}$ and the Ca II IRT emission lines of 60 PMS stars. Only three PMS stars showed broad and strong emissions, indicative of large mass accretion. Most of the PMS stars presented narrow and weak emissions, suggesting that their emission lines are formed in the chromosphere. All their Ca II IRT emission lines have $R'_{\rm IRT} \sim 10^{-4.2}$,

[1] All of the logarithms in this paper have a base of 10.

which is as large as the maximum $R'_{\rm IRT}$ of ZAMS stars. The PMS stars show $N_{\rm R} < 10^{-0.8}$ and constant $R'_{\rm IRT}$ against $N_{\rm R}$, i.e., their Ca II IRT emission lines are saturated (See Appendix).

Yamashita et al. (2022a) investigated the infrared Mg I emission lines at 8807 Å of 47 ZAMS stars in IC 2391 and IC 2602 using the archive data of the Anglo-Australian Telescope at the University College London Echelle Spectrograph. They found that ZAMS stars with smaller Rossby numbers show stronger Mg I emission lines, even for stars located in the Ca II saturated region (See Appendix).

These previous studies show that not only rotation but also convection determines stellar activity. This supports the solar dynamo theory.

1.4.3 Magnetic field structure of photosphere and chromosphre

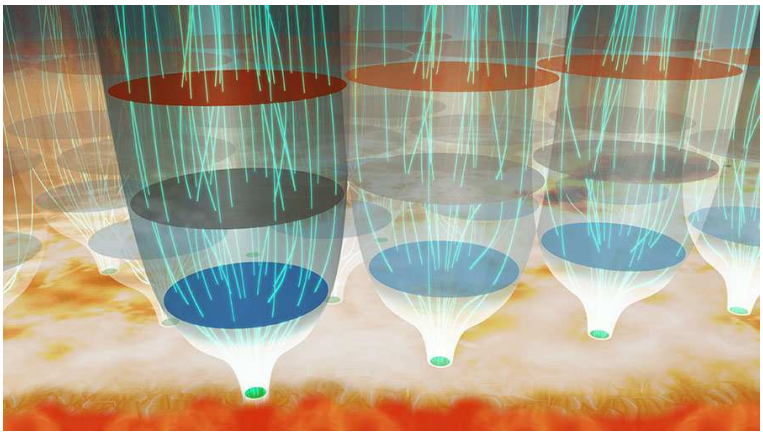

Fig. 16: Schematic view of the magnetic field of the photosphere and the chromosphere. Observations from the Hinode solar satellite and the Chromospheric LAyer Spectropolarimeter (CLASP2) revealed that the magnetic field lines are squeezed at the photosphere and spread out in the chromosphere (Ishikawa et al. 2021). The green solid lines represent the magnetic field lines. Copyright by NAOJ.

Ishikawa et al. (2021) studied the magnetic field structure of the photosphere, chromosphere, and transition region of the Sun based on observations of the Hinode solar satellite and the Chromospheric LAyer Spectropolarimeter (CLASP2). They confirmed that the magnetic field is narrow in the photosphere, and spreads horizontally in the upper chromosphere (figure 16). At the top of the chromosphere, the magnetic field strengths reach more than 300 G. This indicates the magnetic field strength in the chromosphere is weaker than in the photosphere. It was also found that even the chromosphere has a relatively strong magnetic field.

1.4.4 Flares

Flares are also observational evidence for a strong magnetic field. Flares are known as huge explosions that occur in active regions. Once magnetic reconnection occurs around the sunspots, gases in

the corona are suppressed, and then a part of the stored magnetic field energy is suddenly released, making a flare.

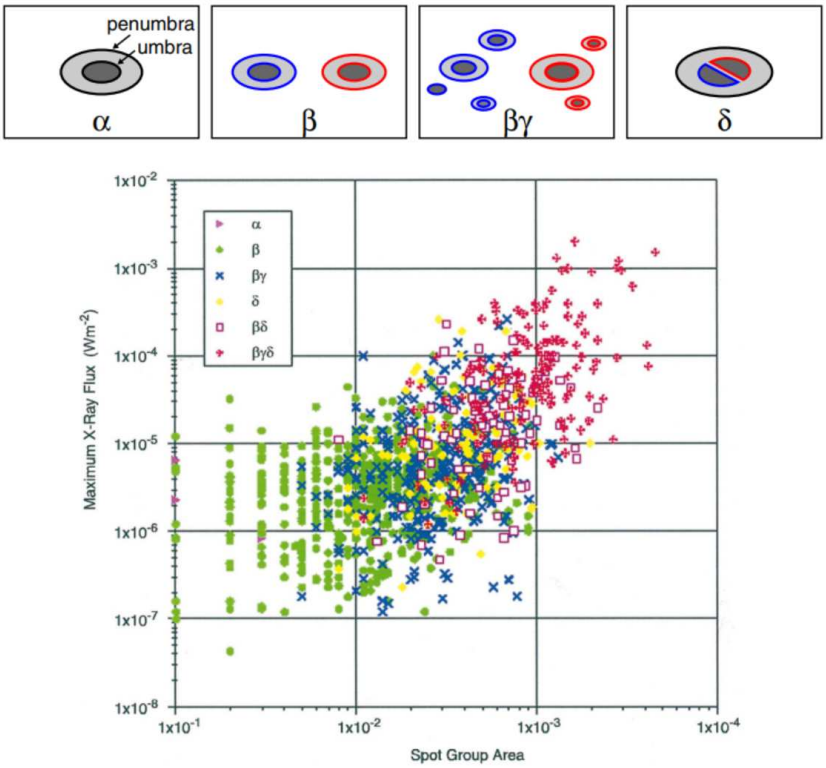

Fig. 17: Relationship between "the Mount Wilson classification" of sunspots, peak flare magnitudes as a function of maximum sunspot area (Hale 1919; Sammis et al. 2000). Figure from Toriumi & Wang (2019).

Sammis et al. (2000) revealed a clear positive correlation between the solar spot area and the maximum of X-ray ux. Furthermore, the shape of the sunspot becomes more complex, as the sunspot area and the maximum X-ray ux during their ares are larger. The largest sunspot is of $\beta\gamma\delta$ type, followed by type $\beta\delta$ (figure 17). The simpler α and β type spots have smaller sunspot areas and the maximum X-ray ux.

Maehara et al. (2012) detected 365 flares with *Kepler* data regarding 148 solar-type stars. The releasing energy of the flare is 100 times larger than those of solar flares. Such objects are called superflare stars. Notsu et al. (2015) found that the Sun and superflare stars show a positive correlation between the amplitude of the light curve and the $r_0(8542)$ index, the residual core flux of the Ca II IRT normalized by the continuum level at the line core. This correlation means that superflare stars have large starspots and high magnetic activity compared to the Sun. Ilin et al. (2019) detected 3844 flares from *K2* data from 2111 objects associated with open clusters. The cluster ages range from 0.1 Gyr to 3.6 Gyr. They found that flaring rates decline with age and decline faster for stars with higher mass.

1.4.5 Coronal emission

The solar corona has a high temperature of $\gtrsim 10^6$ K, which excites atoms to a high ionized state and emits X-rays. Wright & Drake (2016) showed that the saturation of X-ray emission $L_{\rm X}$ with increasing Rossby numbers is not due to the lack of a tachocline by finding fully convective M dwarfs in the non-saturated regime of the relationship between the Rossby numbers and $L_{\rm X}$.

1.4.6 Activity cycle

The solar activity has a pattern, called as "magnetic activity cycle". The average number of sunspots on the solar surface gradually rises and falls. At the solar maximum, the sunspots are most numerous, and the area of the chromospheric emitting region and frequency of flares increase. The length of time between maximums averages 11 yr. At the solar minimum, the days when no sunspots appear at all sometimes continue. The cool main-sequence stars show the year-scale or a decade-scale variation in the strength of Ca II HK emission lines (Boro Saikia et al. 2018). It is suggested that these stars also have an activity cycle.

1.5 Challenges

1.5.1 Issue 1: What drives the chromospheric activity of PMS stars

In this thesis, we investigate whether the chromospheric activity of a PMS star is determined by the dynamo process. For main-sequence stars, chromospheric activity is often discussed in the context of stellar rotation and convection. On the other hand, several researchers have pointed out that the chromosphere of PMS stars is activated by the mass accretion from their protoplanetary disks.

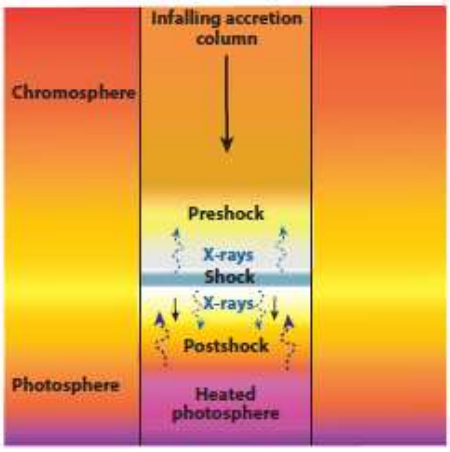

Fig. 18: Schematic diagram of an accretion shock structure of a PMS star. There are the precursor or preshock region, the postshock or cooling region, and the heated photosphere below the shock. Figure from Hartmann, Herczeg & Calvet (2016).

Many of the strongest optical lines of TTSs (e.g., the Balmer series) are formed in the extended magnetospheric infall region (figure 4), and some emission lines are produced in the shock region. Figure 18 shows the schematic view of an accretion shock structure (Calvet & Gullbring 1998), indicating that the shock occurs near the photosphere and generates continuum emission. Uchida & Shibata (1985) proposed an accretion model based on the magnetic interaction between the star and the circumstellar disk. Their model suggests that magnetic accretion forms hot spots on the star and produces emission lines.

Hamann & Persson (1992) carried out optical spectroscopy of PMSs and interpreted that narrow emission lines such as Ca II and Mg I (e.g. $\lambda 8807$ Å) are generated in the stellar chromosphere, and broad emission lines are generated by mass accretion. Several objects also have a broad line component of the Ca II IRT lines, which are well explained by the magnetospheric accretion model (e.g. Muzerolle et al. 1998). Mohanty, Jayawardhana, & Basri (2005) investigated the chromospheric activity of CTTSs, very low-mass young stars ($0.075 \leq M_* < 0.15$ $\mathrm{M}_\odot$), and young brown dwarfs ($M_* \leq 0.075$ $\mathrm{M}_\odot$). The surface flux of the Ca II emission line at $\lambda 8662$ Å, $F'_{\lambda 8662}$, exhibit correlation with the associated mass accretion rate, $\dot{M}$, for approximately 4 orders of magnitude. Hence, they

claimed that the Ca II emission line is an excellent quantitative measure for the accretion rate. Batalha et al. (1996) found correlations with veiling and near-infrared excesses and explained the Ca II and He I emission lines as the result of a "hot chromosphere" heated by the accretion shock. However, in Yamashita et al. (2020), $F'_{\lambda 8662}$ of the narrow lines did not show a positive correlation against $\dot{M}$ for the PMS stars. This is considered that $F'_{\lambda 8662}$ show saturation in such an active star like a PMS star. Yamashita et al. (2022a) showed that the Mg I emission lines are a good indicator of the activity of the fast-rotating and active ZAMS stars. In this study, we investigate the strength of the Mg I emission lines, and determine whether the chromosphere of the PMS stars is activated by the dynamo process or accretion.

1.5.2 Issue 2: Mechanisms for transporting angular momentum

While the Sun rotates every 27 days, the PMS stars have a short rotational period of a few days. Several researchers considered that the CTTSs have a magnetic field connecting the star to the inner edge of the disk, and it prevents the star from spinning up or reduces the spin up rate (Camenzind 1990; Koenigl 1991; Shu et al. 1994).

Because the radius of the inner disk is ~ 10 solar radius, its Keplarian rotation is several days. The typical rotational period of the CTTSs is 7 days. In Gallet & Bouvier (2013), the observed rotational evolution is in the best fit with the model with the disk lifetime of 5 Myr. Once the disk disappears as it ages, the magnetic field also disappears. They claimed that, as a result, WTTSs rotate faster than CTTSs. The typical rotational period of the PMS stars with 10^7 yr, corresponding to WTTSs, is about 3 days.

In this thesis, we investigate whether the mass accretion provides the angular momentum into the PMS stars. Mass accretion has been also considered to provide angular momentum to the star. Hamann & Persson (1992) carried out optical spectroscopy of PMSs and interpreted that narrow emission lines such as Ca II and Mg I (e.g. $\lambda 8807$ Å) are generated in the stellar chromosphere. Several objects also have a broad line component of the Ca II IRT lines, which are well explained by the magnetospheric accretion model (e.g. Muzerolle et al. 1998). We analyze the *TESS* light curves, and obtain the rotational period. We discuss the angular momentum of the photosphere gained by mass accretion.

2 Observations, Data Sets, and Data Reduction

2.1 Stellar parameters

Our targets are 220 G, K, and M-type PMS stars in one molecular cloud and six moving groups; the Taurus-Auriga molecular cloud, the Orionis OB 1c association, the TW Hydrae association, the η Chamaeleontis cluster, the "Cha-Near" region, the β Pictoris moving group, and the AB Doradus moving group. Hereafter, objects belonging to the molecular cloud and the moving groups are called "low-mass PMS stars". The metallicity of the molecular cloud and the moving groups have been determined to be close to the Sun. We did not observe binaries or triplets listed in Ghez et al. (1993), Kraus et al. (2009), Kraus et al. (2012), Neuhauser et al. (1995), Leinert et al. (1993), Wahhaj et al. (2010) and Zuckerman & Song (2004). All targets investigated in this study are listed in table 1 and 2.

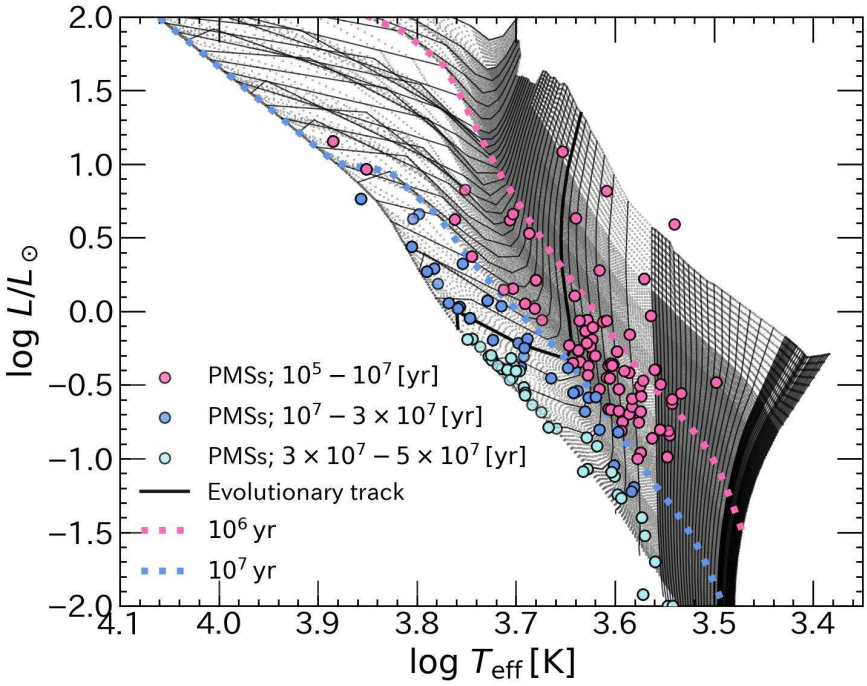

Fig. 19: HR diagram of the investigated PMS stars. The solid lines and dot lines denote the evolutionary tracks ($0.065 - 4.5$ $M_\odot$) and isochrones (2×10^5 yr to the main-sequence) of Jung & Kim (2007). We linearly interpolated that model to one-tenth of the original. The thick solid line denotes the evolutionary track for a 1 $M_\odot$ star. The circles represent the PMS stars. We categorized the PMS stars into three groups by their age, and their symbol colors represent the age; pink $0.1 - 10$ Myr, blue $10 - 30$ Myr, and cyan $30 - 50$ Myr.

Figure 19 presents the HR diagram of the investigated PMS stars. The luminosity, the effective temperature $T_{\rm eff}$, and the distance of the objects were taken from *Gaia* DR2 (Bailer-Jones et al. 2018).

We estimated the mass, age, and $\tau_{\rm c}$ values of the PMS stars by using the evolutionary models presented by Jung & Kim 2007. Then we categorized the PMS star into the following three groups: $0.1-10$ Myr (98 PMS stars), $10-30$ Myr (38 PMS stars), and $30-50$ Myr (40 PMS stars). According to Haisch, Lada & Lada (2001), the fraction of PMS stars showing $JHKL-$band excess due to a protoplanetary disk decreases from 100% to 0% during $0.1-10$ Myr. Takagi, Itoh & Oasa (2014) found that the fraction of the objects with the intrinsic near-infrared excess decreases with age, and concluded that the dissipation timescale of the circumstellar disk is $3-4\times10^6$ yr. The PMS stars with $10-30$ Myr are expected to rotate fastest in the PMS stage. Previous researches indicated that a solar-mass PMS star with 20 - 30 Myr is located at the turning point of their rotation; they end spinning up and start spinning down (e.g., Gallet & Bouvier 2013).

Table 1: Physical parameters of the 240 PMS stars.

Object Name	sp	TESS	X-ray	B	V	r	i	J	H	K
				[mag]	[mag]	[mag]	[mag]	[mag]	[mag]	[mag]
(1)	(2)	(3)	(4)	(5)	(6)	(7)	(8)	(9)	(10)	(11)
2MASS J03442257+3201536			o							
2MASS J04035084+2610531		o		15.58	14.14	13.59	12.39	10.37	9.75	9.53
2MASS J04182147+1658470		o		14.60	13.45	13.01	12.60	11.18	10.60	10.46
2MASS J16123916-1859284	o			15.61	14.05	13.32	12.43	10.28	9.47	9.11
51 Eri		o		5.56	5.25			4.74	4.77	4.54
AA Tau	o	o	o	16.10	14.31	13.56	12.73	9.43	8.55	8.05
AB Dor		o								
AD Leo		o		10.82	9.52	9.19	7.76	5.45	4.84	4.59
AU Mic	o	o	o	10.06	8.89	8.64	7.36	5.44	4.83	4.53
BD+21 584		o		10.04	9.58	9.61	11.41	8.42	8.26	8.16
BD-07 2388		o		10.20	9.61	9.04	8.72	7.56	7.10	6.92
BD-16351		o		11.07	10.24	10.03	9.64	8.61	8.10	7.96
BP Tau	o	o	o	13.13	12.12	11.57	10.98	9.10	8.22	7.74
CHX22	o		o	12.33	11.09	10.63	10.24	8.65	8.04	7.88
CO Ori	o			12.39	11.32	10.97	10.18	7.98	7.21	6.51
COUP 1287	o					17.69	16.58	14.89	14.31	13.90
COUP 1350			o	12.44	11.60	11.09	10.94	9.70	9.15	8.97
COUP 1423	o					13.97	13.91	11.78	10.97	10.50
CPD-43 7188		o	o	11.28	10.57	10.26	9.87	8.81	8.34	8.21
CQ Tau	o	o		10.46	9.91	10.08	9.57	7.93	7.06	6.17
CR Cha	o			12.15	10.99	10.51	10.07	8.46	7.82	7.31
CV Cha	o			11.90	10.83	10.36	10.00	8.29	7.46	6.85
CW Cha	o			15.75	14.45	14.60	13.64	10.91	9.85	9.13
CW Tau		o		14.12	12.72	12.02	11.36	9.56	8.24	7.13
CX Tau		o		15.23	13.69	13.03	11.92	9.87	9.05	8.81
CY Tau		o	o	14.85	13.51	12.86	11.83	9.83	8.97	8.60
CZ Tau		o		16.92	15.34	14.62	13.04	10.52	9.77	9.36
Cl* Melotte 111 AV 1693		o		11.10	10.28	10.12	9.88	8.91	8.54	8.45
Cl* Melotte 111 AV 1826		o		11.74	10.87	10.55	10.28	9.21	8.77	8.66
Cl* Melotte 111 AV 2177		o		11.39	10.61	10.39	10.14	9.03	8.60	8.58
Cl* Melotte 111 AV 523		o		12.44	11.41	11.08	10.75	9.58	9.11	8.99
Cl* Melotte 22 PELS 031		o	o	12.54	11.57	11.24	10.87	9.64	9.16	9.03
Cl* NGC 6530 SCB 7			o	11.59	10.63	10.36	9.92	8.72	8.31	8.14
Cl* NGC 6530 SCB 739			o	9.51	9.20	9.10	8.20	7.43	7.12	7.07
CoKu Tau 4		o		16.40	14.68	13.81	12.62	10.16	9.08	8.66
DD Tau		o		16.53	15.29	14.37	13.01	9.83	8.68	7.88
DE Tau	o	o		14.24	12.88	12.22	11.19	9.18	8.27	7.80
DF Tau	o	o		12.70	11.74	11.22	10.35	8.17	7.26	6.73
DG Tau	o	o	o	14.01	12.93	12.23	11.47	8.69	7.72	6.99
DH Tau		o	o					9.77	8.82	8.18
DI Tau		o						9.32	8.60	8.39
DK Tau	o	o	o	14.59	13.05	12.24	11.34	8.72	7.76	7.10
DL Tau		o		14.18	13.02	12.37	11.62	9.63	8.68	7.96
DM Tau	o	o		15.01	14.05	13.42	12.57	10.44	9.76	9.52
DN Tau	o	o	o	13.69	12.33	11.74	10.95	9.14	8.34	8.02
DO Tau		o		14.96	13.74	13.08	12.19	9.47	8.24	7.30
DQ Tau		o		15.00	13.43	12.65	11.79	9.51	8.54	7.98
DR Tau	o	o	o	12.62	11.76	11.33	10.83	8.85	7.80	6.87
DS Tau		o	o	13.16	12.30	11.84	11.32	9.47	8.60	8.04

Table 1: (Continued)

Object Name	sp	TESS	X-ray	B	V	r	i	J	H	K
				[mag]	[mag]	[mag]	[mag]	[mag]	[mag]	[mag]
(1)	(2)	(3)	(4)	(5)	(6)	(7)	(8)	(9)	(10)	(11)
DX Leo		o	o	8.05	7.16			5.58	5.24	5.12
EK Dra		o	o	8.37	7.67			6.32	6.01	5.91
EP Eri		o	o	7.16	6.15			4.83	4.23	4.17
EV Lac			o	11.85	10.26	9.79	8.35			
FN Tau		o	o	15.84	14.12	13.36	11.82	9.47	8.67	8.19
FO Tau		o		16.88	15.24	14.25	12.59	9.65	8.57	8.12
FP Tau	o	o		15.55	13.94	13.27	12.04	9.90	9.18	8.87
FQ Tau		o						10.49	9.70	9.31
FX Tau		o		15.18	13.61	12.88	11.65	9.39	8.40	7.92
GG Tau		o	o	13.48	12.12	11.44	10.71	8.67	7.82	7.36
GH Tau		o		14.82	13.34	12.61	11.45	9.11	8.23	7.79
GI Tau		o						9.34	8.42	7.89
GJ 729	o		o	12.19	10.43	9.83	8.38	6.22	5.66	5.37
GJ 799A		o		11.79	10.33	9.73	8.11	5.81	5.20	4.94
GK Tau		o	o					9.05	8.11	7.47
GM Aur	o	o	o	13.35	12.24	11.67	11.17	9.34	8.60	8.28
GO Tau		o	o	16.69	15.08	14.23	13.05	10.71	9.78	9.33
GQ Lup	o	o		12.76	11.66	11.12	10.58	8.61	7.70	7.10
GW Ori	o			10.70	9.80	9.55	9.02	7.70	7.10	6.59
HBC 167	o			11.45	10.76	10.56	10.38	9.43	9.00	8.65
HBC 347		o		13.06	12.17	11.88	11.57	10.32	9.86	9.70
HBC 374		o	o	14.35	12.69	11.96	10.99	8.56	7.64	7.29
HBC 376		o	o	13.32	12.22	11.78	11.39	10.03	9.42	9.27
HBC 392		o		13.83	12.63	12.16	11.72	10.28	9.71	9.50
HBC 407	o	o		13.77	12.73	12.33	11.93	10.58	10.08	9.90
HBC 427		o	o	13.07	11.72		10.70	8.96	8.32	8.13
HBC 741		o	o	11.31	10.25			8.31	7.75	7.48
HD 106506		o		9.19	9.29	9.12	8.00	7.25	6.96	6.85
HD 133938		o	o	11.17	10.50	10.25	9.95	8.95	8.52	8.45
HD 135127		o	o	9.90	9.65	9.45	8.94	8.24	8.04	7.99
HD 137059			o	10.13	9.50	9.22	8.36	7.41	7.10	6.99
HD 141943		o								
HD 143978			o	10.02	9.57	9.50	8.82	8.14	7.97	7.86
HD 147048		o	o	11.25	10.44	10.20	9.97	8.96	8.57	8.47
HD 171488		o								
HD 283572		o		9.90	9.39	9.40	8.62	7.41	7.01	6.87
HD 285751		o		12.29	11.34	10.99	10.68	9.41	8.93	8.81
HD 285778		o	o	10.78	10.12	9.87	9.70	8.78	8.39	8.30
HD 285898		o		11.74	10.95	10.69	10.42	9.32	9.00	8.92
HD 286179		o		10.93	10.29	10.11	9.97	8.91	8.58	8.46
HD 29615		o								
HD 35296		o								
HD 6569		o		10.33	9.70	9.60	8.91	7.91	7.43	7.34
HH Leo		o		9.00	8.84			6.30	5.90	5.80
HII 296		o		12.32	11.54	11.23	10.96	9.96	9.51	9.41
HIP 10272			o	9.01	8.75	8.69	7.78	6.20	5.83	5.73
HIP 12545		o		11.33	10.22	9.88	9.27	7.90	7.23	7.07
HIP 16853		o		9.20	8.88	8.77	7.78	6.49	6.26	6.14
HIP 17695	o	o	o	13.07	11.56	10.96	9.78	7.80	7.17	6.93
HK Tau		o		16.69	15.29	14.42	13.11	10.45	9.25	8.59

Table 1: (Continued)

Object Name	sp	TESS	X-ray	B	V	r	i	J	H	K
				[mag]	[mag]	[mag]	[mag]	[mag]	[mag]	[mag]
(1)	(2)	(3)	(4)	(5)	(6)	(7)	(8)	(9)	(10)	(11)
HL Tau		o		15.89	14.49	13.80	13.01	10.62	9.17	7.41
HN Tau		o		14.98	14.17	13.41	12.84	10.70	9.47	8.38
HP Tau	o					13.35	12.36	9.55	8.47	7.63
HR 0806		o		4.05	4.10			4.44	4.43	4.25
HV Tau		o		16.43	14.74	13.90	12.19	9.23	8.28	7.91
IP Tau		o		14.24	13.14	12.59	11.80	9.78	8.89	8.35
IQ Tau	o	o		15.38	14.03	13.34	12.35	9.42	8.42	7.78
IT Tau		o		16.76	14.63	13.67	12.47	9.87	8.59	7.86
L 1551-51		o		13.43	12.23	11.75	11.20	9.70	9.06	8.85
LO Peg		o	o	10.57	9.35			7.08	6.52	6.38
LQ Hya		o								
LkCa 01		o		15.32	13.81	13.21	11.75	9.64	8.87	8.63
LkCa 03		o		13.57	12.03	11.41	10.32	8.36	7.63	7.42
LkCa 04	o	o	o	14.33	12.84	12.24	11.34	9.25	8.52	8.32
LkCa 05		o		15.20	13.69	13.07	11.98	9.98	9.29	9.05
LkCa 07		o		13.78	12.38	11.84	10.99	9.13	8.38	8.26
LkCa 08		o		14.24	13.14	12.59	11.80	9.78	8.89	8.35
LkCa 14		o	o	12.97	11.76	11.28	10.78	9.34	8.71	8.58
LkCa 15	o	o	o	13.31	12.05	11.52	10.97	9.42	8.60	8.16
LkCa 19		o	o	11.68	10.73	10.41	10.04	8.87	8.32	8.15
LkHa 86			o	17.98	16.53	15.38	14.43	12.05	11.13	10.79
Mel25 151		o		10.86	9.96	9.70	9.27	8.13	7.63	7.52
Mel25 179		o	o	10.40	9.50	9.35	9.01	7.89	7.46	7.35
Mel25 43		o	o	10.59	9.47			7.72	7.28	7.15
Mel25 5		o		10.30	9.59	9.55	9.10	7.65	7.27	7.12
NGC 2264 108			o	12.55	12.01	11.86	11.71	10.74	10.23	9.67
NGC 2264 121			o					10.78	10.31	10.21
NGC 2264 84			o	12.53	12.00	11.83	11.70	10.76	10.28	9.84
NLTT26194	o							7.27	6.62	6.42
OV Ori	o			16.24	14.87	14.53	13.67	11.51	10.70	10.32
PAR 102		o		11.01	10.45	10.27	10.10	9.03	8.46	7.97
PAR 1391		o		11.05	10.57	10.47	10.39	9.65	9.40	9.37
PAR 1394			o	10.85	10.30	10.08	9.95	8.99	8.63	8.28
PAR 1455			o	11.54	10.88	10.66	10.52	9.59	9.32	9.19
PAR 1646		o		10.26	9.79	9.69	9.63	8.85	8.66	8.62
PAR 1736			o	12.24	11.00	10.51	9.96	8.17	7.54	7.19
PAR 2244			o	13.71	12.53	12.08	11.57	9.95	9.28	9.12
PW And		o		10.02	8.96			7.02	6.51	6.39
PX Vul		o	o	12.35	11.57	11.23	10.82	9.32	8.55	7.91
RECX 04	o		o	14.20	12.76	12.20	11.41	9.54	8.78	8.62
RECX 06	o	o	o	15.54	14.08	13.49	12.36	10.23	9.58	9.29
RECX 07	o		o	12.02	10.87	10.41	10.03	8.42	7.76	7.64
RECX 09	o	o	o	16.43	14.97	14.43	12.76	10.26	9.67	9.34
RECX 10	o	o	o	13.97	12.54	11.96	11.31	9.65	8.92	8.73
RECX 11	o	o	o	12.35	11.15	10.77	10.32	8.73	8.03	7.66
RECX 15	o		o	14.70	13.88	13.47	12.67	10.51	9.83	9.43
RW Aur		o		11.60	10.78	10.40	9.99	8.38	7.62	7.02
RX J1147.7-7842	o			15.10	13.55	12.96	11.56	9.52	8.86	8.59
RX J1204.6-7731	o	o	o	15.15	13.64	13.01	11.80	9.77	9.13	8.88
RY Lup		o	o	11.82	10.85	10.54	10.18	8.55	7.69	6.98

Table 1: (Continued)

Object Name	sp	TESS	X-ray	B	V	r	i	J	H	K
				[mag]	[mag]	[mag]	[mag]	[mag]	[mag]	[mag]
(1)	(2)	(3)	(4)	(5)	(6)	(7)	(8)	(9)	(10)	(11)
RY Tau	o		o	11.38	10.32	10.05	9.30	7.16	6.13	5.40
SU Aur		o	o	10.59	9.64	9.43	8.89	7.20	6.56	5.99
StKM 2-809		o		14.25	12.56	11.94	10.63	8.59	7.99	7.76
T Tau	o	o	o	11.22	10.12	9.70	9.10	7.24	6.24	5.33
TAP 10			o	12.40	11.52		11.02	10.45	10.01	9.86
TIC 150097417		o		14.20	12.69	12.05	11.17	9.24	8.48	8.28
EV Lac		o		11.85	10.26	9.79	8.35			
TIC 29900813		o		8.66	7.75			6.23	5.90	5.75
TIC 357019659		o		14.32	12.66	12.05	11.31	8.96	7.86	6.95
TWA 01	o	o	o	12.06	11.10	10.43	9.99	8.22	7.56	7.30
TWA 06	o	o		12.73	11.45	10.90	10.28	8.87	8.18	8.04
TWA 07	o	o		13.23	11.75	11.16	9.97	7.79	7.13	6.90
TWA 10		o		14.56	13.06	12.45	11.12	9.12	8.48	8.19
TWA 14	o	o		14.37	12.83	12.23	11.26	9.42	8.73	8.50
TWA 22	o	o	o	15.69	13.96	13.34	11.26	8.55	8.09	7.69
TWA 23		o		14.16	12.64	12.05	10.63	8.62	8.03	7.75
TWA 25	o	o		12.59	11.16	10.58	9.86	8.17	7.50	7.31
TWA 3A		o		13.53	12.05	11.44	9.83	7.65	7.04	6.77
TWA 5A		o	o	12.87	11.39	10.80	9.71	7.67	6.99	6.75
TWA 5B	o			12.87	11.39	10.80	9.71	7.67	6.99	6.75
TWA 8A	o	o		13.70	12.27	11.63	10.43	8.34	7.66	7.43
TWA 8B	o			17.24	15.65	14.80	13.08	9.84	9.28	9.01
TWA 9A	o	o		12.39	11.14	10.64	10.15	8.68	8.03	7.85
TWA 9B	o	o		15.43	14.00	13.50	12.01	9.98	9.38	9.15
TYC 0486-4943-1		o		12.15	11.15	10.74	10.45	9.30	8.78	8.66
TYC 1987-509-1		o		11.17	10.44	10.20	9.93	9.02	8.63	8.59
TYC 5164-567-1		o		10.94	10.10	9.82	9.56	8.48	8.03	7.92
UX Tau	o	o	o	11.76	10.78	10.40	9.98	8.62	7.96	7.55
UY Aur		o		12.84	11.83	11.29	10.74	9.13	7.99	7.24
V1001 Sco			o	12.77	11.62	11.15	10.65	8.98	8.32	8.09
V1002 Sco			o	12.11	10.90	10.42	9.94	8.31	7.66	7.49
V1152 Sco			o	12.84	11.71	11.27	10.83	9.32	8.71	8.52
V1023 Tau		o	o	14.35	12.69	11.96	10.99	8.56	7.64	7.29
V1044 Ori	o		o	12.19	11.39	11.14	10.91	9.70	9.15	8.69
V1067 Tau		o		13.83	12.83	12.45	12.07	10.84	10.32	10.16
V1110 Tau		o		11.26	10.36	10.04	9.69	8.42	7.93	7.80
V1149 Sco	o			10.98	10.16	9.88	9.66	8.36	7.69	7.05
V1204 Tau		o	o	11.79	10.80	10.46	10.12	8.90	8.36	8.24
V1297 Tau		o	o	12.11	11.31	11.05	10.79	9.78	9.35	9.21
V1298 Tau		o		11.32	10.37	10.07	10.35	8.69	8.19	8.09
V1299 Tau		o		10.07	9.48	9.72	9.92	8.13	7.83	7.76
V1304 Tau		o		14.75	13.34	12.81	11.83	9.96	9.25	9.05
V1320 Tau		o		14.05	12.66	12.10	11.39	9.71	9.04	8.79
V1321 Tau		o	o	15.31	13.74	13.07	12.03	10.00	9.23	9.02
V1346 Tau		o		13.24	12.11	11.69	11.33	9.97	9.41	9.25
V1348 Tau		o	o	13.21	12.11	11.72	11.30	9.88	9.31	9.15
V1354 Tau	o	o		11.94	11.09	10.81	10.47	9.28	8.82	8.69
V1368 Tau		o		9.93	9.37	9.46	8.83	7.82	7.51	7.40
V1458 Ori	o					13.34	13.28	10.85	9.97	9.62
V1840 Ori		o	o	12.71	11.68	11.33	11.06	9.66	9.09	8.95

Table 1: (Continued)

Object Name	sp	TESS	X-ray	B	V	r	i	J	H	K
				[mag]	[mag]	[mag]	[mag]	[mag]	[mag]	[mag]
(1)	(2)	(3)	(4)	(5)	(6)	(7)	(8)	(9)	(10)	(11)
V2062 Oph	o			13.88	12.61	11.94	11.21	9.23	8.25	7.61
V2129 Oph	o			12.88	11.57	11.06	10.48	8.44	7.67	7.21
V2247 Oph	o			14.87	13.27	12.61	11.53	9.42	8.63	8.41
V4046 SgrA		o		11.66	10.77			8.07	7.44	7.25
V4046 SgrB		o		11.66	10.77			8.07	7.44	7.25
V410 Tau		o	o	12.02	10.81	10.38	9.87	8.45	7.79	7.63
V439 And		o		7.95	7.48	7.35	6.33	4.73	4.63	4.31
V447 Lac			o	8.97	8.57			6.04	5.64	5.59
V577 Per		o		8.95	7.88	8.04	7.46	6.84	6.46	6.37
V773 Tau		o		12.12	10.71	10.16	9.49	7.49	6.64	6.21
V819 Tau		o	o	14.55	13.01	12.35	11.54	9.50	8.65	8.42
V826 Tau		o		13.18	11.87	11.32	10.69	9.07	8.43	8.25
V827 Tau		o		14.00	12.63	12.15	11.29	9.17	8.49	8.23
V830 Tau		o	o	13.69	12.38	11.81	11.11	9.33	8.61	8.42
V836 Tau		o	o	15.00	13.49	12.82	12.38	9.91	9.08	8.60
V898 Per		o		9.60	8.99		8.54	7.79	7.49	7.43
V927 Tau		o		16.30	14.73	14.03	12.23	9.73	9.06	8.77
V928 Tau		o		15.98	14.10	13.27	12.05	9.54	8.43	8.11
V999 Tau		o						9.79	8.66	8.23
XZ Tau		o		13.77	12.83	12.31	11.34	9.39	8.15	7.29
YY Ori			o	14.75	13.82	13.73	13.30	10.95	10.04	9.40
YZ CMi		o		12.38	11.02	10.49	8.93	6.58	6.01	5.70
ZZ Tau		o		15.95	14.36	13.72	11.94	9.50	8.70	8.44
YZ CMi		o		12.38	11.02	10.49	8.93	6.58	6.01	5.70
ZZ Tau		o		15.95	14.36	13.72	11.94	9.50	8.70	8.44

(2) Objects whose spectra are analyzed in this study. (3) Objects for which TESS data were analyzed in this study. (4) Objects whose X-ray data is analyzed. References for parameters: (5)(6) $B-$mag and $V-$mag: The AAVSO Photometric All-Sky Survey. (7)(8) $r-$mag and $i-$mag: UCAC4 Catalogue (Zacharias et al. 2013). (9)(10)(11) $J-$mag, $H-$mag and $K_{\rm s}-$mag: 2MASS survey (Cutri et al. 2003).

Table 2: Physical parameters of the 240 PMS stars.

Object Name	A_V [mag]	Excess	$T_{\rm eff}$ [K]	Lum. [$L_\odot$]	Dist. [pc]	Age [Myr]	Mass [$M_\odot$]	τ_c [day]	$v \sin i$ [$\rm km \cdot s^{-1}$]
(1)	(2)	(3)	(4)	(5)	(6)	(7)	(8)	(9)	(10)
2MASS J03442257+3201536			4278		249				
2MASS J04035084+2610531	-0.25	-0.34	3518	0.16	129	1.9	0.26	225	
2MASS J04182147+1658470	0.65	-0.48	4380	0.21	180	30.0	0.77	66	
2MASS J16123916-1859284	0.57	-0.26	3488	0.21	139	1.2	0.25	224	12.3
51 Eri			7190	5.83	30	13.0	1.51		84.0
AA Tau	0.40	0.00	4267	0.74	137	2.3	0.78	267	12.7
AB Dor	0.05	-0.28	5117	0.40	15	40.0	0.87	35	
AD Leo		-0.24	3630	0.02		66.0	0.32	188	6.2
AU Mic	-0.90	-0.10			10				8.0
BD+21 584	0.24		6064	1.96	121	21.1	1.18	12	25.0
BD-07 2388		-0.21	4905	0.61	54	18.0	1.01	56	
BD-16351	0.08	-0.36	4988	0.61	88	20.0	1.00	48	
BP Tau	0.45	-0.02	4320	0.46	129	7.6	0.93	131	11.4
CHX22	1.80	-0.46	4366	2.28	203	0.5	0.81	248	11.3
CO Ori	2.00		4468	3.58	400	0.4	0.92	251	56.6
COUP 1287	1.13				585				32.7
COUP 1350	1.00	-0.33	4854	3.52	386	1.3	1.54	191	21.3
COUP 1423	0.62	0.04	5096		413				40.7
CPD-43 7188	0.70	-0.33	5189	1.09	127	13.0	1.17	54	
CQ Tau	0.40		5050	1.44	162	6.8	1.38	70	107.5
CR Cha	0.56		4259	2.35	186	0.4	0.71	242	36.7
CV Cha	0.62	0.40	4411	2.39	192	0.5	0.86	251	30.3
CW Cha		0.35	3681	0.08	195	9.4	0.35	244	29.6
CW Tau	1.80	0.99	3956	0.15	132	12.0	0.57	196	31.7
CX Tau	0.25	-0.55	3417	0.28	127	0.6	0.23	222	19.1
CY Tau	0.35	-0.29	4068	0.20	128	10.0	0.65	176	10.5
CZ Tau	0.50	-0.01	4594						
Cl* Melotte 111 AV 1693	0.03	-0.33	5341	0.50	84	41.1	0.91	28	
Cl* Melotte 111 AV 1826	0.04	-0.37	5056	0.36	84	43.7	0.84	35	6.0
Cl* Melotte 111 AV 2177	0.03	-0.59	5099	0.50	90	30.0	0.90	39	
Cl* Melotte 111 AV 523	0.04	-0.39	4828	0.23	86	54.2	0.76	38	
Cl* Melotte 22 PELS 031	0.07	-0.35	5217	0.57		30.0	0.92	35	12.2
Cl* NGC 6530 SCB 7		-0.16	4866	5.35	285	0.7	1.62	239	
Cl* NGC 6530 SCB 739		-0.32	5854	5.29	130	6.8	1.69	22	
CoKu Tau 4	1.75	-0.50	4070	0.11	170	30.0	0.64	96	
DD Tau	0.75	0.42	3810	0.06	123	25.0	0.45	179	
DE Tau	0.35	-0.09	3853	0.38	127	1.7	0.44	236	10.0
DF Tau	0.10	0.02	3666	0.93	125	0.2	0.30	220	19.1
DG Tau	1.60	0.49	3731	0.34	121	1.2	0.35	229	21.7
DH Tau	0.65	0.30	3752	0.27	135	2.1	0.39	234	10.4
DI Tau	0.70	-0.52	4059	0.36	135	3.6	0.59	262	10.4
DK Tau	0.70	0.32	3855	0.20	128	5.4	0.49	257	11.4
DL Tau	1.80	0.48	3998	0.44	159	1.9	0.51	242	
DM Tau	0.10	-0.39	3769	0.18	145	4.0	0.39	238	10.0
DN Tau	0.55	-0.32	3964	0.53	128	1.3	0.48	236	9.4
DO Tau	0.45	0.66	3755	0.31	139	1.6	0.38	231	12.4
DQ Tau	1.40	0.05	4238	0.43	196	5.8	0.82	178	25.4
DR Tau	0.45	0.88	4328	0.87	195	2.3	0.86	267	10.0
DS Tau	0.25	0.19	4041	0.43	158	2.5	0.57	250	10.6

Table 2: (Continued)

Object Name	$A_{\rm V}$ [mag]	Excess	$T_{\rm eff}$ [K]	Lum. [$L_\odot$]	Dist. [pc]	Age [Myr]	Mass [$M_\odot$]	$\tau_{\rm c}$ [day]	$v \sin i$ [$\rm km \cdot s^{-1}$]
(1)	(2)	(3)	(4)	(5)	(6)	(7)	(8)	(9)	(10)
DX Leo	0.04	-0.18	5300	0.47	18	41.7	0.90	29	5.9
EK Dra	0.05	-0.19	5584	0.90	34	28.0	1.00	26	17.2
EP Eri		-0.72	5178	0.41		43.6	0.87	32	5.8
EV Lac									8.9
FN Tau	1.15	0.08	4250	0.14	131	34.0	0.69	78	
FO Tau	2.05	-0.42	4152	0.12	157	32.0	0.66	88	
FP Tau	0.60	-0.27	3486	0.24	128	0.9	0.25	224	23.5
FQ Tau	1.60	-0.14	4080	0.32		4.8	0.63	263	
FX Tau	0.80	-0.22	3745						10.0
GG Tau	1.05	-0.08	3753	0.11	2349	7.9	0.39	247	10.1
GH Tau	0.40	-0.13	3800						25.2
GI Tau	2.55	0.03	3486	0.25	130	0.9	0.25	223	14.6
GJ 729		-0.09			5552				
GJ 799A		-0.22	3744	0.04		40.0	0.40	163	
GK Tau	1.35	0.29	3898	0.39	129	1.7	0.45	236	14.6
GM Aur	0.30	-0.25	4339	0.55	159	5.4	0.93	158	13.0
GO Tau	1.50	-0.21	3985	0.08	144	36.0	0.55	112	19.2
GQ Lup	1.60	0.26	4093	0.85	151	1.0	0.58	241	
GW Ori	1.30		4473	26.56	398	0.0	1.34	278	41.7
HBC 167	0.40		5505	7.32	407	2.5	2.21	57	18.0
HBC 347	0.10	-0.27	4926	0.31	146	42.0	0.81	41	75.0
HBC 374	1.35	-0.46	4007	0.43	125	2.1	0.53	244	
HBC 376	0.25	-0.51	4389	0.28	121	19.0	0.85	82	68.0
HBC 392	0.40	-0.29	4346	0.29	140	17.0	0.85	92	17.0
HBC 407	0.80	-0.27	4649	0.16	126	70.5	0.70	39	10.0
HBC 427	0.20	-0.45	4250	0.87	148	1.8	0.77	265	10.0
HBC 741	0.24	-0.10	4865	3.39	188	1.4	1.54	184	
HD 106506	0.35	-0.13	5778	4.21	107	7.0	1.64	29	97.5
HD 133938	0.25	-0.45	5379	1.77	164	10.0	1.35	43	
HD 135127	0.25	-0.17	6392	2.75	126	17.6	1.31		
HD 137059		-0.16	5096		82				17.0
HD 137059		-0.16	5096		82				17.0
HD 141943			5673	2.11		12.0	1.35		
HD 143978	0.30		5984	1.71	97	21.0	1.16	16	
HD 147048	0.37	-0.31	5159	1.40	145	8.5	1.33	60	
HD 171488			5718	1.07		25.0	1.07	24	36.2
HD 197481	-0.90		3992	0.09		28.0	0.57	121	
HD 283572	0.50	-0.23	5083	4.16	130	1.8	1.87	121	92.5
HD 285751	0.22	-0.37	4811	0.34	104	30.0	0.85	49	
HD 285778	0.25	-0.32	5359	1.19	120	16.0	1.14	43	16.0
HD 285898	0.92	-0.26	5049	4.59	325	1.5	1.86	139	10.0
HD 286179	0.24	-0.20	4910	1.13	123	7.3	1.29	76	
HD 29615			5737	1.05		25.9	1.06	24	
HD 35296			6171	1.86		21.9	1.18	12	
HD 6569	0.11	-0.48	5087	0.34	45	49.7	0.81	31	
HH Leo	0.05	-0.32	5451	0.58	26	37.5	0.94	27	7.1
HII 296	0.26	-0.38	5069	0.48	133	33.3	0.90	36	15.4
HIP 10272		-0.29			32				6.0
HIP 12545		-0.55	4167	0.26	44	11.0	0.77	138	8.0
HIP 16853	0.13	0.00	6015	1.55	45	21.8	1.15	17	19.0

Table 2: (Continued)

Object Name	$A_{\rm V}$ [mag]	Excess	$T_{\rm eff}$ [K]	Lum. [$L_\odot$]	Dist. [pc]	Age [Myr]	Mass [$M_\odot$]	$\tau_{\rm c}$ [day]	$v \sin i$ [$\rm km \cdot s^{-1}$]
(1)	(2)	(3)	(4)	(5)	(6)	(7)	(8)	(9)	(10)
HIP 17695	0.06	-0.30	3714	0.03	17	54.0	0.38	154	
HIP10272		-0.29	5288	0.64	32	28.0	0.95	35	6.0
HK Tau	2.40	-0.03	3831	0.06	133	29.0	0.46	159	18.9
HL Tau	2.50		4060	6.60		0.1	0.55	231	
HN Tau	1.15	1.04	4250	0.09	136	87.0	0.60	53	52.8
HP Tau	3.15	0.62	3689	0.29	176	1.4	0.34	229	66.0
HV Tau	1.40	-0.40	3924	0.15	133	8.8	0.51	249	12.4
IP Tau	0.75	0.12	3826	0.26	130	2.7	0.42	238	11.0
IQ Tau	0.85	0.20	3654	0.14	131	3.4	0.31	230	12.0
IT Tau	3.10	0.04	3913	0.18	161	6.4	0.49	262	
L 1551-51	0.25	-0.41	4195	0.51	143	3.6	0.74	252	27.0
LO Peg	0.09	-0.44	4564	0.16	24	66.4	0.70	41	69.0
LQ Hya			4909	0.28		48.0	0.78	38	
LkCa 01	0.45	-0.50	3828	0.23	128	2.9	0.40	236	
LkCa 03	0.00	-0.56	4443	1.66		1.1	0.93	264	
LkCa 04	0.35	-0.53	3621	0.40	129	0.6	0.30	224	
LkCa 05	0.05	-0.40	3751	0.21	130	2.7	0.37	234	
LkCa 07	0.05	-0.77	4029	0.35	126	3.2	0.56	254	
LkCa 08	0.75	0.12	3826	0.26	130	2.7	0.42	238	
LkCa 14	0.00	-0.57	4218	0.58	128	2.9	0.74	267	
LkCa 15	0.30	-0.07	4201	0.64	158	2.3	0.71	264	
LkCa 19	0.50	-0.37	4784	1.63	159	3.2	1.37	128	
LkHa 86		-0.47	3657	0.14	322	3.2	0.31	229	
Mel25 151		-0.43	4922	0.49	65	25.0	0.93	47	
Mel25 179	0.17	-0.36	4960	0.42	49	29.0	0.88	46	4.0
Mel25 43	-0.10	-0.31	4974	0.39	46	31.8	0.87	43	
Mel25 5	0.16	-0.15	5016	0.40	46	36.5	0.87	39	
NGC 2264 108			5830	6.51	695	4.6	1.90	31	56.0
NGC 2264 121		-0.44	4972	5.56	706	1.0	1.86	173	99.9
NGC 2264 84			5975	6.55	685	5.4	1.84		36.0
NLTT26194		-0.42			989				
OV Ori	1.04	-0.17	3871	0.39	390	1.6	0.43	235	20.1
PAR 102	0.39		5640	6.67	342	3.6	2.01		
PAR 1391		-0.29	6281	4.59	308	11.0	1.49		
PAR 1394			5857	10.36	382	3.0	2.25	27	
PAR 1455		-0.04	5805	5.74	384	5.2	1.83		
PAR 1646		-0.17	6368	4.26	207	12.0	1.47		
PAR 1736	2.90	-0.01	4120						56.3
PAR 2244		-0.56	4321		1960				
PW And	0.09	-0.43	4908	0.27	28	55.8	0.79	33	22.4
PX Vul			4500	12.13	623	0.1	1.15	263	
RECX 04		-0.68	4023	0.21	99	7.9	0.59	225	
RECX 06		-0.18	3526	0.10	98	3.8	0.26	226	
RECX 07		-0.65	4325	0.71	98	3.2	0.88	223	30.0
RECX 09	0.00		3933		1547				
RECX 10		-0.59	4089	0.21	98	10.0	0.67	170	11.0
RECX 11	0.00	-0.07	4393	0.45	98	8.8	0.95	117	
RECX 15	0.00		3719	0.06	92	18.0	0.37	235	30.0
RW Aur	0.10		5096		157				20.4
RX J1147.7-7842		-0.25	3881	0.16	101	7.0	0.47	261	

Table 2: (Continued)

Object Name	$A_{\rm V}$	Excess	$T_{\rm eff}$	Lum.	Dist.	Age	Mass	$\tau_{\rm c}$	$v \sin i$
	[mag]		[K]	[$L_\odot$]	[pc]	[Myr]	[$M_\odot$]	[day]	[km · s^{-1}]
(1)	(2)	(3)	(4)	(5)	(6)	(7)	(8)	(9)	(10)
RX J1204.6-7731	0.00	-0.30	3585	0.16	100	2.4	0.29	227	9.5
RY Lup	0.31		4721	0.88	158	7.3	1.20	88	25.0
RY Tau	1.85	0.41	4418	10.26	444	0.1	0.96	254	50.8
SU Aur	0.65		4360	4.31	158	0.2	0.82	245	65.6
StKM 2-809	0.05	-0.26	3730	0.01	25	88.0	0.26	261	
T Tau	1.25	0.91	4320	3.04	144	0.3	0.78	244	21.0
TAP 10		-0.28	4859	1.02	273	7.6	1.25	79	42.5
TIC 150097417	0.40	-0.59	4060	0.87		0.8	0.54	237	
TIC 154101678			3521	0.01		88.0	0.23	242	
TIC 29900813	0.06	-0.10	5303	0.47	24	41.7	0.90	29	4.4
TIC 357019659	10.30	0.76	4290	0.08	109	74.7	0.59	59	
TWA 01	0.00	-0.29	4236	0.26	60	14.0	0.80	116	15.0
TWA 06	0.05	-0.65	4269	0.21	66	22.0	0.78	86	
TWA 07	-0.10	-0.39	4018	0.08	34	38.0	0.57	102	63.2
TWA 10		-0.19	3925	0.07	58	30.0	0.51	134	
TWA 14	0.10	-0.40	3853	0.20	92	4.2	0.44	244	
TWA 22					20				
TWA 23	0.05	-0.15	3508	0.14	56	2.1	0.26	225	
TWA 25	0.05	-0.46	4020	0.22	53	7.0	0.58	240	12.9
TWA 3A	0.05	-0.20	3960	0.06	37	54.0	0.52	94	15.0
TWA 5A	-0.20	-0.37	3947	0.21	49	6.0	0.53	260	
TWA 5B		-0.37			49				59.0
TWA 8A	0.05	-0.38	3778	0.10	46	9.7	0.40	254	5.0
TWA 8B	0.20	-0.13			46				5.0
TWA 9A	-0.05	-0.47	4240	0.37	76	7.9	0.84	147	
TWA 9B	0.00	-0.28	3928	0.05	76	54.0	0.51	97	
TYC 0486-4943-1	0.29	-0.45	4729	0.21	70	54.2	0.74	41	
TYC 1987-509-1	0.07	-0.45	5316	0.50	89	38.1	0.91	31	
TYC 5164-567-1	0.25	-0.38	5229	0.43	67	43.5	0.88	30	
UX Tau	0.65		4428	0.59	139	6.4	1.01	129	20.7
UY Aur	1.00	0.27	3849	0.70	155	0.6	0.41	229	17.6
V 1001 Sco	1.40	-0.39	4299	0.67	137	3.2	0.85	234	
V 1002 Sco	0.39	-0.52	4350	1.29	135	1.2	0.82	259	
V 1152 Sco	0.44	-0.43	4340	0.65	139	3.8	0.89	204	8.0
V1023 Tau	1.35	-0.46	4007	0.43	125	2.1	0.53	244	
V1044 Ori	2.00		5138	4.45	388	1.9	1.95	107	22.3
V1067 Tau		-0.34	5143		279				
V1077 Tau	0.80	-0.27	4649	0.16	126	70.5	0.70	39	
V1110 Tau	0.20	-0.37	4883	0.65	86	15.0	1.04	66	
V1149 Sco	0.45		5013	2.51	165	3.0	1.64	101	
V1204 Tau	0.20	-0.49	4801	1.05	139	6.4	1.26	90	
V1297 Tau	0.28	-0.27	5040	0.44	118	33.5	0.88	40	
V1298 Tau	0.10	-0.48	4962	0.92	108	10.0	1.20	65	
V1299 Tau		-0.28	5773						
V1304 Tau	0.40	-0.51	3747	0.26	137	1.9	0.37	232	
V1320 Tau	0.35	-0.35	4129	0.30	127	6.8	0.70	196	
V1321 Tau	0.70	-0.59	4042	0.22	146	8.2	0.62	209	
V1346 Tau	0.20	-0.40	4620	0.35	140	24.0	0.88	60	
V1348 Tau		-0.43	4442	0.41	156	12.0	0.94	98	
V1354 Tau	0.40	-0.32	4918	0.57	122	20.0	0.99	50	

Table 2: (Continued)

Object Name	$A_{\rm V}$	Excess	$T_{\rm eff}$	Lum.	Dist.	Age	Mass	$\tau_{\rm c}$	$v \sin i$
	[mag]		[K]	[$L_\odot$]	[pc]	[Myr]	[$M_\odot$]	[day]	[$\rm km \cdot s^{-1}$]
(1)	(2)	(3)	(4)	(5)	(6)	(7)	(8)	(9)	(10)
V1368 Tau	0.26	-0.19	5559	2.37	109	9.4	1.42	37	
V1458 Ori	0.59	-0.38	4077		1211				20.3
V1840 Ori	0.20	-0.45	4617	0.59	150	10.0	1.07	86	
V2062 Oph	3.80	0.21	3875	0.51	145	1.0	0.43	232	8.5
V2129 Oph	0.25	0.07	3926	0.90	130	0.5	0.47	232	15.8
V2247 Oph	7.10	-0.58	3829	0.24	112	3.0	0.42	238	43.1
V4046 SgrA	0.00	-0.45	4254	0.61	72	3.0	0.78	262	
V4046 SgrB	0.00	-0.45	4254	0.61	72	3.0	0.78	262	
V410 Tau	0.31	-0.55	4375	1.28	130	1.5	0.89	272	
V439 And			5552	0.65		39.4	0.97	21	
V447 Lac	0.07	-0.44			22				
V577 Per	0.15	-0.32	5612	0.65	36	39.4	0.97	21	
V773 Tau	0.95	-0.11	4132	1.91	128	0.3	0.61	237	
V819 Tau	1.00	-0.67	3948	0.30	131	3.2	0.50	247	15.0
V826 Tau	0.40	-0.46	4191	0.78	144	1.7	0.69	255	
V827 Tau	0.05	-0.30	4169	0.50	163	3.2	0.70	268	
V830 Tau	0.45	-0.55	4020	0.44	130	2.2	0.55	247	
V836 Tau	0.60	0.03	3632	0.40	169	0.6	0.30	224	
V898 Per	0.20	-0.28	5865	1.14	70	26.8	1.08	19	
V927 Tau	-0.20	-0.22	3145	0.33		0.2	0.17	219	
V928 Tau	1.95	-0.77	3862						
V999 Tau	2.60	-0.51	4639		123				
XZ Tau	1.50	0.42	3971	3.90		0.1	0.48	226	
YY Ori		0.34	4000	1.12	392	0.5	0.51	233	16.0
YZ CMi		-0.04	3482	0.01		88.0	0.23	242	5.7
ZZ Tau	0.55	-0.51	4131	0.16	134	20.0	0.70	108	

(2) Interstellar extinction of $V-$band: Herczeg et al. (2014), Wahhaj et al. (2010), Gontcharov et al. (2018), Yu et al. (2023), Furlan et al. (2009), Yang et al. (2012), Da Rio et al. (2012), Michel et al. (2021). (4)(5) Effective temperature and luminosity: *Gaia* DR2 (Gaia Collaboration 2018). (6) Distance: *Gaia* DR2 (Bailer-Jones et al. 2018). (10) Projected rotational velocity, $v \sin i$: the Catalog of Stellar Rotational Velocities (Glebocki & Gnacinski 2005).

2.2 Observations

We conducted high-resolution spectroscopic observations of nine PMS stars on August 12, 2021, and February 2, 2022 (Semester 21B and 22A) with the High Dispersion Spectrograph (HDS; Noguchi et al. 2002) mounted on the Subaru Telescope. We also obtained the spectrum of five PMS stars observed on September 18, 2007, by Dr. Yuhei Takagi. The spectrum was obtained using the StdNIRb mode and with the 0.6" width slit. These instrument settings achieved a wavelength coverage between 6650 Å and 9360 Å and a spectral resolution of $R \equiv \frac{\lambda}{\Delta\lambda} \sim 60,000$. The integration time for each object was between 600 s and 1500 s.

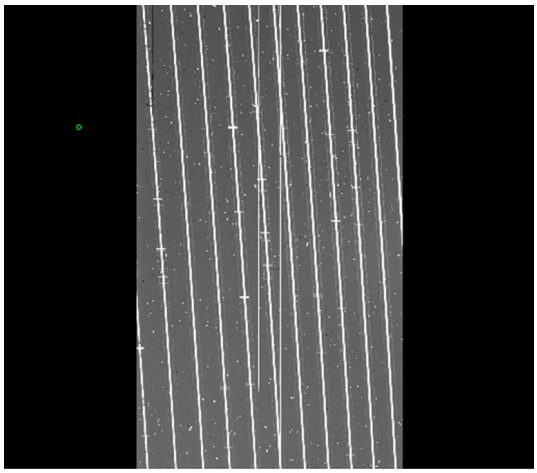

Fig. 20: Example of the raw spectra image of HDS data

The archive data of six PMS stars obtained with the UVES ($R \sim 40,000$) mounted on the Very Large Telescope (VLT) were also used. The program IDs, dates of the observations, and the integration time are listed in table 3. The wavelength coverage was between 3732 Å and 9496 Å. The integration time for each object was between 10 s and 600 s. In addition, the archive data of 63 PMS stars obtained with the X-Shooter ($R \sim 8,000$) mounted on the VLT were also used. The wavelength coverage was between 2989 Å and 10200 Å. The integration time for each object was between 2 s and 4360 s.

2.3 Datasets

The 178 PMS stars were observed in the short-cadence (120 s-exposure) mode of *TESS* Sectors 1 - 67, which extended from 2018-7-25 to 2023-6-28. These data were retrieved from the Multimission archive at the Space Telescope Science Institute.

Table 3: Details of the archive data of VLT/UVES, and VLT/X-Shooter

Program ID	Observation Date	Integration Time [s]
VLT / UVES		
075.C-0321(A)	2005-08-26	200 - 600
082.C-0005(B)	2008-10-02	10 - 150
VLT / X-Shooter		
084.C-1095(A)	2010-01-18, 19, 20	2 - 1000
085.C-0238(A)	2010-04-05, 06, 07	20 - 3600
085.C-0764(A)	2010-05-04	480 - 1800
086.C-0173(A)	2011-01-12, 13	100 - 400
088.C-0218(A)	2011-11-05	20 - 200
088.D-0556(A)	2012-02-05	48 - 96
288.C-5013(A)	2012-02-27, 2012-03-06	800 - 880
090.C-0050(A)	2012-11-13, 15, 24	10 - 1200
088.C-0218(E)	2012-12-17	8 - 60
090.C-0253(A)	2013-03-14	1200 - 1440
093.C-0506(A)	2014-05-06	480 - 880
093.C-0757(A)	2014-06-04	300 - 600
094.C-0913(A)	2014-12-05, 08, 09, 10, 2015-01-21	30 - 1720
094.C-0805(A)	2015-01-15, 2015-02-19	25 - 388
094.C-0327(A)	2015-01-16	10 - 240
095.C-0147(A)	2015-05-01	3400 - 3840
095.D-0949(A)	2015-06-12	30 - 120
096.C-0455(A)	2015-10-23	60 - 65
096.C-0979(A)	2015-10-24, 28	30 - 360
097.C-0669(A)	2016-05-03	100 - 4360
097.C-0378(A)	2016-07-25	30 - 480
101.C-0389(B)	2018-06-16	2700 - 3000
101.C-0866(A)	2018-05-19, 20	30 - 800
103.C-0887(B)	2019-06-24	20 - 300
106.20Z8.004	2021-05-02, 03	10 - 300
108.2206.001	2021-10-13, 22, 2021-11-18, 21	60 - 2800
106.20Z8.006	2021-11-24, 26, 2021-12-02	30 - 800
106.20Z8.008	2022-11-30	80 - 400

2.4 Data Reduction

2.4.1 Ground-based optical and infrared spectra

We used the Image Reduction and Analysis Facility (IRAF) software package[2] for data reduction. The HDS data was reduced with overscan subtraction, bias subtraction, flat fielding, removal of scattered light, extraction of a spectrum, wavelength calibration using a Th-Ar lamp, continuum normalization, removal of telluric absorption components, and shift to the rest radial velocity. The UVES data and X-Shooter data had already been reduced up to the point before wavelength calibration. To improve the signal to noise ratio (S/N), the multiple frames on the same day were combined and averaged for each object. We applied weights proportional to the integration time to each frame. The spectra of the targets had the contamination from the Earth's atmosphere, called the telluric absorption lines. We removed the telluric absorption lines with the TELLURIC task in the NOAO onedspec package and the Advanced Cerro Paranal Sky Model presented by ESO (Noll et al. 2012; Jones et al. 2013).

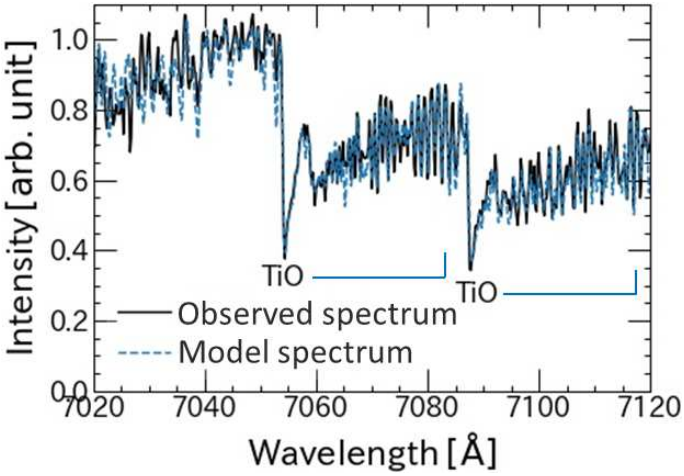

Fig. 21: Continuum-normalized spectra near the TiO molecular bands. The solid line and dashed line represent the observed spectrum of a PMS star, namely TWA 7, and the best-fitting model spectrum, respectively.

We subtracted the photospheric absorption components for all spectra with the spectral models of the stellar photosphere. In general, the photospheric absorption components of the Ca II IRT line and Mg I line are strong, especially for K-type stars. The Mg I emission component is typically buried by the photospheric absorption, as shown in figure 22b.

To detect the weak chromospheric emission lines, we determined the atmospheric parameters ($T_{\rm eff}$ and $\log g$), projected rotational velocity ($v \sin i$), and veiling value (V) of the PMS star by comparing the observed spectrum with the photospheric model spectrum. We used Phoenix-BT-Dusty models (Kulenthirarajah et al. 2019) from POLLUX database (Palacios et al. 2010). POLLUX is a

[2] IRAF software is distributed by the National Optical Astronomy Observatories, which are operated by the Association of Universities for Research in Astronomy, Inc., under a cooperative agreement with the National Science Foundation.

database of stellar spectra developed at the Laboratoire Univers et Particules de Montpellier. Phoenix-BT-Dusty models are spherical and plane-parallel models with non-LTE for atoms. They have a temperature of $2000 - 6000$ K, micro-turbulent velocity of $0.86\ \mathrm{km \cdot s^{-1}}$, resolution of $> 100,000$, and spectral range from visible to infrared. As shown in figure 21, this model includes molecular bands such as TiO, and they enable us to estimate the temperature of the cool stars. We tried to use other models, SPTool (Takeda et al. 2014) and iSpec (Blanco-Cuaresma et al. 2018), but we finally did not use them since they do not model molecular bands. Table 4 shows the investigated range of the physical parameters of the model spectrum. Initially, 280 models were obtained with effective temperature in the range $2000 - 6000$ K (in 100 K steps), $\log g$ from 2.0 to 5.0 dex (in 0.5 dex steps), and a solar iron abundance ($[\mathrm{Fe/H}] = 0$). This grid covers the wide range for our targets, and also extends to lower gravities typical of giants. The number of models was finally increased to 145600 by convolving Gaussian functions and veiling. The details will be described below. We selected six spectral regions (table 5) with reference to Frasca et al. (2017). Frasca et al. (2017) claimed that these regions are particularly suitable for the determination of T_{eff}, $\log g$, $v \sin i$, and veiling. The examples of the fitting are shown in figure 21 and 22a. $5120 - 6270$ Å is out of range for some PMS stars observed with UVES.

While we used the spectra of standard stars in Yamashita et al. (2022a), we used the model spectra in this study for three reasons. First, by using the model spectra, we can fit the model with a wider range of stellar parameters. Generally, PMS stars have lower $\log g$ than that of main-sequence stars. It is hard to observe standard stars with various $\log g$ and the same temperature as the PMS stars. Second, the grids of T_{eff} and $\log g$ can be made smaller. For the standard stars used in Yamashita et al. (2022a), the temperature difference between standard stars was typically 200 K. Third, the model spectra have a lower noise level than the observed spectra of the standard stars. In Yamashita et al. (2022a), it was difficult to determine the standard stars that fit the ZAMS stars, then we sometimes fitted a model spectrum for them, and determined a standard star whose temperature was similar to that of the model. In addition, we make the models for the PMS stars veiled, and the small difference in spectra due to the difference in $\log g$ is more likely to be buried in the noise.

For the correction of the rotational broadening, the model spectra were convolved with a Gaussian kernel. We convolved the model spectra with a Gaussian kernel in 26 steps of σ, which corresponds to $v \sin i$ of $0 - 250\ \mathrm{km \cdot s^{-1}}$. However, when we convolved a Gaussian function with large σ, the continuum level of the model spectrum became lower. This is because the wide absorption lines often blend with other strong lines. Gray (2005) and Frasca et al. (2017) had pointed out that what we actually observe is the pseudo-continuum. After convolving a Gaussian kernel, we performed continuum normalization again for all the model spectra.

Table 4: The physical parameters of the 145600 model spectra

Parameter	Range
$T_{\rm eff}$	$2000-6000$ K in 100 K steps
$\log g$	$2.0-5.0$ dex in 0.5 dex steps
Abundance	fixed on $[{\rm Fe/H}]=0$
$v\sin i$	$0-250\ {\rm km\cdot s^{-1}}$ in 26 steps
Veiling, V	$0.0-5.0$ in 20 steps

Table 5: Spectral regions for estimating $T_{\rm eff}, \log g, V$, and Gaussian σ

Wavelength [Å]	Main features
4400 - 4580	Fe I
5120 - 5220	Mg I
6050 - 6270	Ca I, Fe I, TiO
7020 - 7120	TiO
7600 - 7720	K I, Fe II
8160 - 8222	Na I, V I

An absorption line profile of a PMS spectrum might be obscured by continuum veiling. The amount of veiling, V, is defined as

$$V = \frac{W_0}{W} - 1, \tag{4}$$

where W_0 denotes the unveiled EQW of an absorption line and W is the veiled EQW. For objects indicating a significant veiling value, we made a veiled model spectrum. First, we added the veiling value V to the normalized model spectrum. Then, the continuum component was normalized again to unity by dividing by $(1+V)$. The veiled model spectrum was subtracted from that of the target star suffering significant veiling. For an object with $V=0$, the spectrum of the model which was not veiled was subtracted.

Figure 22a shows the procedure of spectral subtraction of photospheric component for PMS star. We selected the best-fitted models by measuring the standard deviation of the difference between the spectra of the PMS star and the model spectra. First, the SARITH task of IRAF was repeated, and 145600 model spectra were subtracted from the spectrum of each object. For $i-$th wavelength range in table 5, we measured the standard deviation of the count values of the residual spectrum, $F_{\rm std}(i)$. For example, $F_{\rm std}(i)$ of the residual spectrum in the bottom of figure 22a was 0.019.

To evaluate the fitting of the model spectrum in the entire wavelength ranges of table 5, we

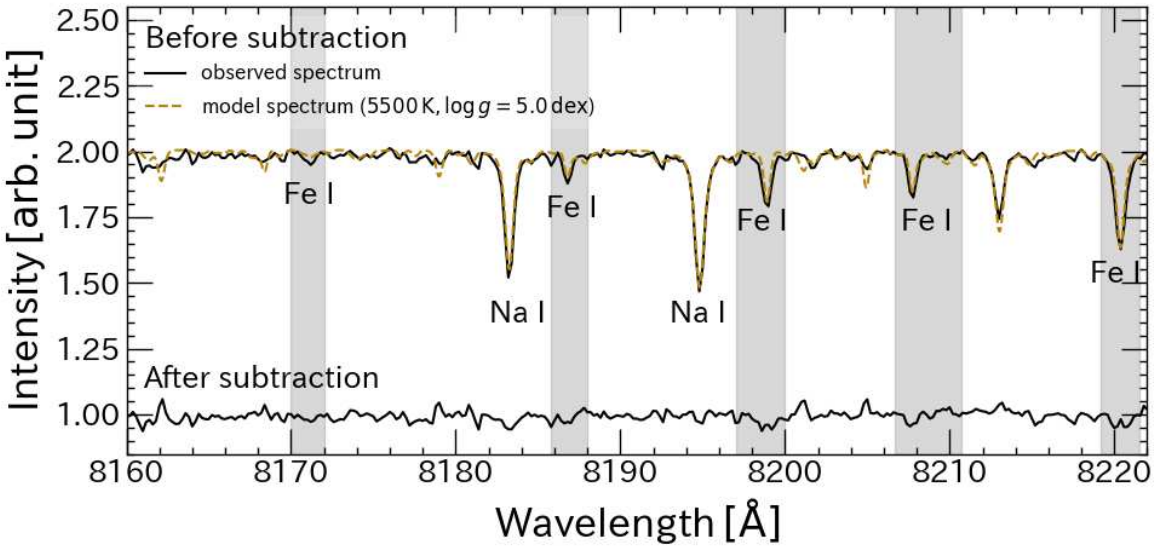

(a) Na I lines of HBC 407

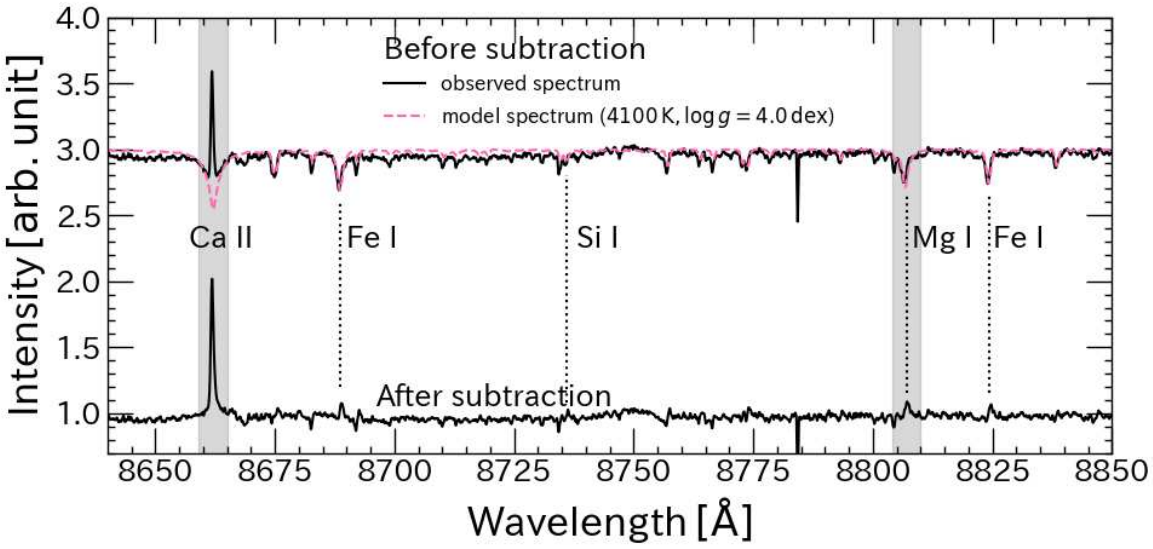

(b) Ca II and Mg I lines of AA Tau

Fig. 22: Subtraction procedure of photospheric component for PMS stars. The observed spectrum is shown in the top part of the panel with a solid line. The dashed line represents the model spectrum. Spectra of the PMS star and the model are shown shifted by $+1.0$ or $+2.0$ for display purposes. In the bottom of the panels, the difference between the spectrum of the PMS star and the model is shown. The hatched areas represent Fe I lines, Ca II line, Mg I line. We remove the wavelength in the hatched areas from the fitting range.

considered the model with the smallest $\frac{1}{n}\sqrt{\sum_{i=1}^{n} F_{\rm std}(i)^2}$ to be the best model, where n denotes the numbers of spectral regions. Here we uniquely determined $T_{\rm eff}$ and $\log g$, while V and σ depend on the wavelength. For the determination of $T_{\rm eff}$ and $\log g$, σ was fixed to the value derived through the measurement of each spectral region. We set the veiling value as a free parameter. In Frasca et al. (2017), the spectral regions in $4400-4580, 5120-5220$ Å were referenced only for the objects with a higher temperature than 3500 K. In this study, we first measured $\frac{1}{n}\sqrt{\sum_{i=1}^{n} F_{\rm std}(i)^2}$ for the spectral regions in $6050-8222$ Å. This means that $n=4$ for objects below 3500 K at the first temperature measurement. Second, for the objects above 3500 K, we included the two blue spectral regions, and recalculate $\frac{1}{n}\sqrt{\sum_{i=1}^{n} F_{\rm std}(i)^2}$. The maximum of n value is six. As described above, n of the UVES objects are two less than n of X-Shooter objects because UVES did not observe $5120-6270$ Å.

To estimate the errors of temperature and surface gravity for each object, we first examined the model with the smallest $F_{\rm std}$ in each spectral region. Then the errors were calculated by taking the standard deviations of temperature and surface gravity of those models.

Many Fe I absorption lines appeared in the spectra of the targets and photospheric model spectra as shown in the hatched area in figure 22a. The emission components of Fe I may be formed in a lower chromosphere (Vernazza et al. 1981). Actually, very active T Tauri stars show narrow Fe I and Fe II emission lines at rest velocity, which are believed to be formed in the chromosphere (Hamann & Persson 1992). The ZAMS stars also show narrow Fe I emission lines (Yamashita et al. 2022a). In this study, we refer to the iSpec database, and remove the wavelength close to the strong Fe I lines from the fitting range if its gf value is greater than $10^{-1.3}$.

Figure 22b shows the procedures of the spectral subtraction of the Ca II and Mg I line of AA Tau. In this case, the Ca II IRT lines display emission profiles over a broad absorption feature. We subtracted the model spectrum from the observed spectrum of the PMS stars. The dashed line in figure 22b represent the model spectrum with the smallest $\frac{1}{n}\sqrt{\sum_{i=1}^{n} F_{\rm std}(i)^2}$. V and σ of the model spectrum are measured in $\lambda 8420-8560$ Å for Ca II lines at $\lambda 8498, 8542$ Å, $\lambda 8560-8700$ Å for Ca II lines at $\lambda 8662$ Å, and $\lambda 8700-8850$ Å for Mg I line at $\lambda 8807$ Å. We remove the wavelength close to the strong emission lines from the fitting range, as shown with the hatched area in figure 22b. Before measuring the EQWs, the spectra after subtracting photospheric absorption components were added to unity. To obtain the EQWs of the Mg I, Ca II, and Hα emission lines, the areas of the corresponding emission profiles were directly integrated. The EQW errors were estimated by multiplying the standard deviation of the continuum by the wavelength range of the emission lines of each PMS star. We estimated the standard deviations of the continuums near the emission lines. The wavelength range

was $\lambda 8798 - 8802$ Å and $\lambda 8813 - 8819$ Å for the Mg I emission line. In these wavelength ranges, no strong features were observed.

2.4.2 *TESS* photometric data

To obtain the rotational period, spot coverage, and flare energy, we analysed the Pre-search Data Conditioning Simple Aperture Photometry (PDCSAP) fluxes observed with *TESS*. PDCSAP fluxes are derived by aperture photometry[3]. We calculated the average of PDCSAP fluxes for each star, and the standard deviation of the flux, σ_1, then removed the flux data points greater than $3\sigma_1$ above the average. We then searched for periodicity in the signals by conducting Lomb–Scargle (Scargle 1982) periodogram analysis. For each object, the period of the light curve, P, was determined. The amplitudes of the light curves were calculated by taking the 90th percentile flux and subtracting it from the 10th percentile flux.

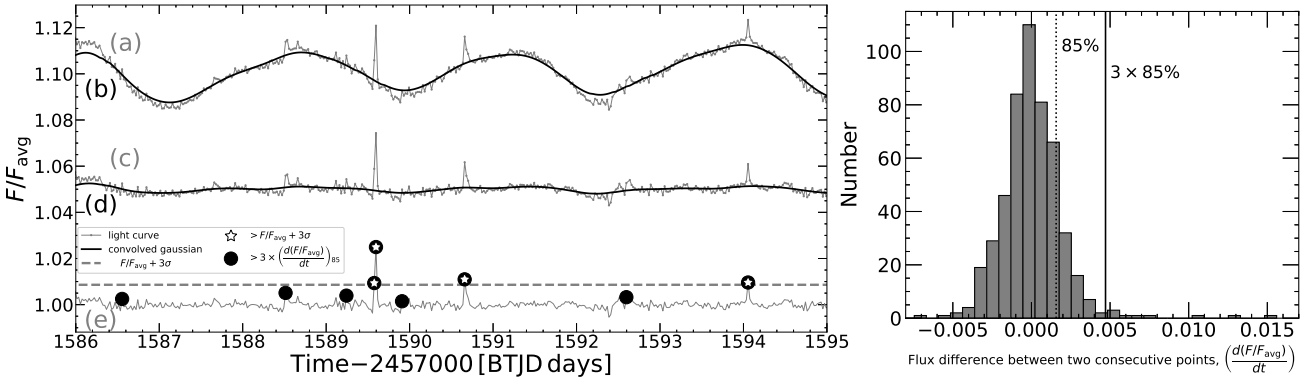

Fig. 23: Light curve of a ZAMS star, [RSP 95] 14. Horizontal and vertical axes correspond to days and normalized flux. Time is in the TESS Barycentric Julian Day (BTJD), this is a Julian day minus 2457000.0 and corrected to the arrival times at the barycenter of the Solar System. Top) The original light curve is shown with the gray solid line (a). This is divided by the median of the counts and normalized to 1. The thick black line is the Gaussian convolved light curve (b). The standard deviation of the Gaussian function is set to 300 mins. These lines are shifted by $+0.10$ for display purposes. Middle) The difference between the original light curve and the Gaussian convolved light curve shown in the top panel is presented with the gray solid line (c). The thick black line is the Gaussian convolved light curve of the gray solid line (d). The standard deviation of the Gaussian function is set to 300 mins. These lines are shifted by $+0.05$ for display purposes. Bottom) The difference between the light curve shown in the middle and the second Gaussian convolved light curve is shown with the gray solid line (e). The dashed line denotes $1 + 3\sigma_2$ of the gray line. The star symbols represent data points greater than the dashed line. The large filled circles represent data points whose brightness change is greater than the threshold of the change of brightness. The three sudden brightenings (four points) are detected as flares. The histogram in the right panel shows the number distribution of the flux differences between all pairs of two consecutive data points. The dotted line shows the top 15% of the distribution. The solid line shows the threshold of the change of the brightness, three times in the top 15% of the distribution.

[3] The details are described in the webpage of NASA; `https://heasarc.gsfc.nasa.gov/docs/tess/LightCurveFile-Object-Tutorial.html`.

Next, we detected sudden brightenings as flares. Starting from the original light curves (including $3\ \sigma_1$ outliers), first we removed the rotational light variations as described below (figure 23). *TESS* data was not obtained for several days in the middle of the observation period. We separated the light curve at the center time. Each light curve was subtracted by the median of the counts and normalized to 1 (figure 23 (a)). Each light curve was convolved with a Gaussian function (figure 23 (b)) and subtracted by the convolved light curve. We set the standard deviation of the Gaussian function to between $15\ \mathrm{mins}$ and $2.5\ \mathrm{days}$ for each light curve, which is proportional to P of the PMS stars. The derived light curve (figure 23 (c)) was again convolved with a Gaussian function (figure 23 (d)) and subtracted (figure 23 (e)). With these processes, no rotational light variation remained in the light curve, and most of the data points were set around unity. We then measured the standard deviation of the counts in the light curve, σ_2, for each PMS star.

We defined two thresholds for flare detection. The first threshold is the height of sudden brightening. After removing the rotational light variations, we searched for sudden brightenings whose relative flux exceeded $1 + 3\sigma_2$ for at least one data point. The second threshold is the change of the brightness. We calculated the brightness changes between all pairs of consecutive data points. We searched for any brightness change that occurred more than three times in the top 15% of the distribution (the solid line in the right panel of figure 23). We identified a sudden brightening that exceeded both thresholds as a flare. The time at which the flux first exceeded the first threshold, $1 + 3\sigma_2$ of the relative flux, was determined to be the flare start time. The flare end time was defined as the time at which the flux became smaller than $1 + 3\sigma_2$ of the relative flux.

3 Results

3.1 $T_{\rm eff}$ and $\log g$, $v \sin i$, and veiling

The effective temperature ($T_{\rm eff}$), surface gravity ($\log\ g$), projected rotational velocity ($v \sin i$), and veiling value (V) of 69 PMS stars were determined (table 6 and 7). Typical errors are ≈ 300 K for the effective temperature, and ≈ 0.8 dex for surface gravity.

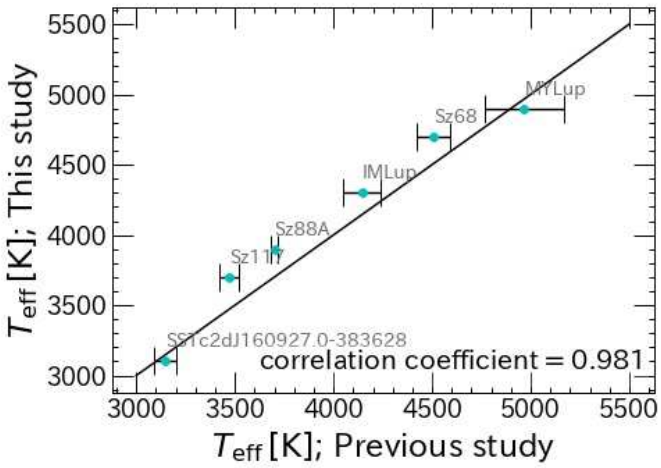

Fig. 24: Comparison between the effective temperature determined in this study and that derived from the spectroscopic study of Folsom et al. (2016).

To examine the accuracy of $T_{\rm eff}$, we compared $T_{\rm eff}$ values for the six Lupus objects determined in this study with those values reported by Folsom et al. (2016). The comparison is shown in figure 24. The $T_{\rm eff}$ values of the PMS stars in both studies are comparable. The correlation coefficient of 0.981. The result indicates that the temperatures derived in this research are consistent with those measured in Folsom et al. (2016). We concluded that the temperatures we derived for the other 69 PMS stars have a certain accuracy.

Most of the PMS stars show veiling with $V \geq 0.1$. In particular, the highly veiled 28 PMS stars have also large amounts of veiling with decreasing wavelengths. In the previous studies, the high veiling with a peak in the ultraviolet region has been observed for strongly accreting PMS stars. This is considered to be due to the heated photosphere below the mass accretion shock. Basri & Batalha (1990) investigated the wavelength dependence of optical veiling for 16 T Tauri stars. For the five T Tauri stars out of them the amounts of veiling increase with decreasing wavelengths between $\lambda 4000 - 5500$ Å and flat for $\lambda \geq 5500$ Å. This is similar to the result of this study.

$\tau_{\rm c}$ listed in table 7 represent the convective turnover time. We estimate $\tau_{\rm c}$ of the PMS stars by comparing $T_{\rm eff}$ and the luminosity with evolutionary tracks presented in Jung & Kim (2007). The details are described in section 4.1.2 and 4.3.

Table 6: Gaussian sigma and veiling values of 69 PMS stars

	4400 - 4580 Å		5120 - 5220 Å		6050 - 6270 Å		7020 - 7120 Å		7600 - 7720 Å		8160 - 8222 Å	
Object Name	σ	V	σ	V	σ	V	σ	V	σ	V	σ	V
2MASS J16123916-1859284	50	0.3	24	1.4	12	0.2	18	0.0	9	0.0	9	0.0
AA Tau	40	0.6			12	0.9	12	1.0	7	0.4	9	0.5
AB Dor					24	0.1	18	0.0	12	0.0	9	0.1
AU Mic	5	0.5			7	0.2	18	0.0	7	0.0	6	0.0
BP Tau	50	1.2			7	0.7	7	0.5	6	0.2	6	0.3
CHX22	24	0.0	30	0.2	11	0.0	15	0.0	11	0.0	12	0.0
CO Ori	40	0.0	50	0.9	40	0.4	180	0.2	24	0.0	50	0.9
COUP 1287	30	3.0	50	5.0	21	2.5	80	0.0	21	1.0	18	0.4
COUP 1423	60	0.0	24	0.9	18	0.4	15	0.1	15	0.1	15	0.0
CQ Tau	60	0.4	80	0.0	80	0.3	180	0.3	36	0.2	80	1.2
CR Cha	30	0.0	36	0.4	30	0.0	36	0.0	40	0.0	36	0.0
CV Cha	30	0.3	24	3.0	24	0.2	40	0.3	24	0.3	24	0.4
CW Cha	180	2.5	50	5.0	18	3.0	40	0.7	12	1.2	15	0.9
DE Tau	60	0.4	40	5.0	15	0.3	15	0.0	11	0.0	11	0.0
DF Tau	50	0.2			18	0.6	50	0.0	21	0.0	15	0.0
DG Tau	60	0.7	50	5.0	80	0.8	40	0.1	21	0.9	24	0.5
DK Tau	30	0.5	21	1.6	15	0.2	18	0.0	10	0.0	18	0.1
DM Tau	30	1.8	21	3.0	15	0.7	15	0.1	8	0.1	7	0.0
DN Tau	11	0.2	21	0.7	9	0.1	21	0.0	8	0.0	12	0.0
DR Tau					240	5.0	120	0.0	120	5.0	11	5.0
FP Tau	50	0.3	50	0.6	24	0.2	30	0.0	24	0.0	40	0.0
GJ 729					30	0.1	36	0.0	21	0.2	12	0.2
GM Aur	24	0.6	24	1.2	15	0.3	12	0.5	15	0.2	18	0.1
GQ Lup	24	0.6	24	1.6	11	0.3	11	0.6	12	0.2	9	0.3
GW Ori	30	0.1	30	1.0	30	0.2	120	0.1	36	0.0	40	0.3
HBC 167	15	0.0	18	0.3	15	0.0	18	0.1	15	0.2	18	0.1
HBC 407	15	0.1	15	0.3	11	0.0	12	0.1	11	0.0	12	0.0
HP Tau	80	0.3	120	1.2	120	0.5	180	0.0	7	1.4	180	0.1
IQ Tau	40	0.6	24	1.8	9	0.4	21	0.0	7	0.1	9	0.1
LkCa 04	30	0.2	30	0.8	18	0.2	24	0.0	21	0.0	21	0.0
LkCa 04	21	0.2	30	0.6	15	0.2	21	0.0	18	0.0	18	0.0
LkCa 15	24	0.4	30	1.0	18	0.1	2	5.0	18	0.0	24	0.3
LkCa 15	21	0.3	24	0.9	18	0.0	24	0.1	21	0.0	21	0.2
NLTT26194	18	0.5	30	0.8	18	0.1	40	0.0	15	0.0	15	0.1
OV Ori	30	0.3	30	0.8	18	0.2	18	0.2	24	0.0	21	0.1
RECX 04	21	0.4	24	0.9	10	0.1	9	0.0	8	0.0	6	0.0
RECX 06					21	0.3	15	0.0	15	0.0	12	0.1
RECX 07	30	0.2	30	0.6	24	0.0	36	0.0	36	0.1	30	0.1
RECX 09					30	0.3	30	0.0	18	0.2	15	0.3
RECX 10	21	0.4	30	0.7	21	0.1	36	0.0	12	0.0	6	0.0
RECX 11	30	0.2	30	0.7	15	0.0	12	0.3	15	0.0	18	0.1
RECX 15					60	0.9	21	0.0	12	0.2	11	0.1
RX J1147.7-7842	80	0.1	60	0.6	30	0.1	36	0.0	36	0.0		
RX J1204.6-7731					15	0.3	12	0.0	12	0.2	9	0.1
RY Tau	40	0.2	50	0.1	40	0.2	60	0.6	40	0.0	60	0.1
T Tau	21	0.0	18	2.0	24	0.0	30	0.0	12	0.8	18	0.2
TWA 01	18	1.0	21	2.0	12	0.5	36	0.0	8	0.2	7	0.1
TWA 06	60	0.1	50	0.7	50	0.0	60	0.0	80	0.0	50	0.0
TWA 07					15	0.3	9	0.0	8	0.0	6	0.0
TWA 14	24	0.3	30	0.8	24	0.3	36	0.0	21	0.0	24	0.0

Table 6: (Continued)

	4400 - 4580 Å		5120 - 5220 Å		6050 - 6270 Å		7020 - 7120 Å		7600 - 7720 Å		8160 - 8222 Å	
Object Name	σ	V	σ	V	σ	V	σ	V	σ	V	σ	V
TWA 22					36	0.2	18	0.0	15	0.3		
TWA 25	11	0.2	24	0.8	10	0.0			8	0.0	9	0.0
TWA 5B					40	0.4	40	0.0	36	0.0	40	0.0
TWA 5B					36	0.4	40	0.0	36	0.0	36	0.1
TWA 8A					15	0.3	21	0.0	8	0.5	6	0.1
TWA 8B					36	0.4	15	0.0	7	1.4	9	0.3
TWA 9A	10	0.1	15	0.6	12	0.0	24	0.1	11	0.0	15	0.0
TWA 9B					21	0.2	21	0.0	10	0.7	8	0.1
UX Tau	15	0.2	21	0.3	24	0.0	30	0.0	30	0.0	30	0.2
V1044 Ori	18	0.0	21	0.3	24	0.0	30	0.0	30	0.0	24	0.1
V1149 Sco	24	0.0	30	0.0	12	0.0	18	0.1	18	0.0	12	0.0
V1354 Tau	21	0.1	24	0.3	30	0.0	30	0.1	36	0.0	36	0.0
V1458 Ori	24	0.3	40	0.6	15	0.2	15	0.0	15	0.0	15	0.0
V2062 Oph	18	0.4	18	2.5	18	0.1	80	0.3	15	0.4	15	0.2
V2129 Oph	12	0.3	24	0.7	21	0.2	60	0.2	15	0.0	12	0.0
V2247 Oph	80	0.4	60	5.0	15	0.4	15	0.0	15	0.0	15	0.0

Table 7: Temperature, surface gravity, Gaussian sigma, veiling values, and convective turnover time, τ_c of 69 PMS stars

			8498 & 8542 Å		8662 Å		8807 Å		
Object Name	$T_{\rm eff}$ [K]	log g	σ	V	σ	V	σ	V	τ_c [day]
2MASS J16123916-1859284	3900 ± 310	4.0 ± 1.1	10	0.1	10	0.3	12	0.0	191
AA Tau	4100 ± 160	4.0 ± 0.8	15	0.6	15	0.9	24	0.5	72
AB Dor	3500	5.0	15	0.1	15	0.4	15	0.0	249
AU Mic	3900 ± 130	4.0 ± 0.8	8	0.0	8	0.0	8	0.0	117
BP Tau	4000 ± 180	3.5 ± 0.7	7	0.4	7	0.6	10	0.2	255
CHX22	5400 ± 400	4.5 ± 1.1	15	0.0	15	0.0	15	0.0	47
CO Ori	5800 ± 720	4.5 ± 1.1	60	0.4	60	0.5	60	0.3	
COUP 1287	3700 ± 880	3.5 ± 1.4	120	0.0	120	5.0	30	0.0	211
COUP 1423	3600 ± 120	2.0 ± 1.1	18	0.3	18	0.5	30	0.0	225
CQ Tau	6000 ± 510	2.5 ± 1.4	180	1.2	240	0.0	120	0.0	
CR Cha	5300 ± 440	4.5 ± 1.2	40	0.0	36	0.1	36	0.1	54
CV Cha	5000 ± 290	4.0 ± 1.1	36	0.2	36	0.4	36	0.2	94
CW Cha	3800 ± 940	4.5 ± 1.3	15	1.0	12	2.0	18	0.0	213
DE Tau	3800 ± 170	3.0 ± 1.1	11	0.1	9	0.4	12	0.0	233
DF Tau	3700 ± 850	2.5 ± 0.5	24	0.1	18	0.7	24	0.0	224
DG Tau	4300 ± 350	4.0 ± 1.4	36	0.4	30	1.2	40	0.4	88
DK Tau	4200 ± 170	4.0 ± 1.0	18	0.1	18	0.3	21	0.1	140
DM Tau	3700 ± 210	3.0 ± 1.0	11	0.0	9	0.2	11	0.0	240
DN Tau	3900 ± 210	2.5 ± 0.9	11	0.2	12	0.1	15	0.0	239
DR Tau	5200 ± 1020	3.0 ± 1.3	180	5.0	120	5.0	240	5.0	52
FP Tau	3700 ± 760	2.5 ± 0.9	30	0.0	24	0.3	30	0.0	237
GJ 729	3200	5.0	21	0.4	60	2.0	21	0.0	
GM Aur	4300 ± 240	4.0 ± 0.7	18	0.2	18	0.3	21	0.1	155
GQ Lup	4300 ± 200	3.5 ± 0.7	15	0.4	12	0.6	18	0.2	256
GW Ori	5600 ± 510	4.0 ± 1.1	50	0.2	40	0.5	50	0.3	42
HBC 167	5900 ± 190	3.5 ± 0.9	18	0.0	9	0.7	18	0.0	
HBC 407	5500 ± 490	5.0 ± 0.2	15	0.0	15	0.0	15	0.0	38
HP Tau	4800 ± 490	4.0 ± 1.2	180	0.0	120	0.6	120	0.3	36
IQ Tau	4000 ± 280	4.0 ± 0.9	11	0.2	10	0.5	12	0.2	120
LkCa 04	3900 ± 320	3.0 ± 1.0	24	0.1	21	0.3	24	0.0	245
LkCa 04	3900 ± 280	3.0 ± 0.9	24	0.0	24	0.0	21	0.0	245
LkCa 15	4600 ± 250	4.5 ± 0.8	24	0.1	21	0.4	24	0.3	88
LkCa 15	4600 ± 250	4.5 ± 0.8	24	0.0	21	0.3	24	0.1	88
NLTT26194	4100 ± 190	4.5 ± 0.8	18	0.2	18	0.2	18	0.2	210
OV Ori	4300 ± 350	4.0 ± 0.3	24	0.1	21	0.3	24	0.1	105
RECX 04	3900 ± 310	4.0 ± 0.7	9	0.0	9	0.1	10	0.0	253
RECX 06	3500 ± 130	4.5 ± 1.2	15	0.0	18	0.0	15	0.0	227

Table 7: (Continued)

			8498 & 8542 Å		8662 Å		8807 Å		
Object Name	$T_{\rm eff}$ [K]	log g	σ	V	σ	V	σ	V	$\tau_{\rm c}$ [day]
RECX 07	4300 ± 400	3.5 ± 1.1	36	0.3	36	0.3	36	0.2	177
RECX 09	3000 ± 380	4.0 ± 1.2	30	0.2	18	0.5	24	0.0	237
RECX 10	4100 ± 270	4.0 ± 0.7	12	0.0	12	0.2	15	0.1	119
RECX 11	4600 ± 340	4.5 ± 0.3	18	0.1	18	0.2	18	0.2	71
RECX 15	3400 ± 430	4.0 ± 1.4	30	0.0	36	0.2	15	0.0	223
RX J1147.7-7842	3600 ± 390	2.0 ± 0.8	60	0.0	50	0.3	60	0.0	228
RX J1204.6-7731	3500 ± 190	4.5 ± 0.8	15	0.0	10	0.2	12	0.0	225
RY Tau	5400 ± 330	2.5 ± 0.8	80	0.1	60	0.3	60	0.0	71
T Tau	5300 ± 420	4.0 ± 0.7	30	0.0	30	0.3	30	0.1	61
TWA 01	4100 ± 270	4.0 ± 0.6	15	0.2	15	0.4	15	0.3	151
TWA 06	4200 ± 320	4.0 ± 0.6	80	0.0	80	0.0	80	0.1	92
TWA 07	3500 ± 180	4.5 ± 0.6	10	0.0	9	0.0	9	0.0	226
TWA 14	3900 ± 360	4.0 ± 1.0	30	0.0	30	0.1	30	0.0	249
TWA 22	2800 ± 320	4.5 ± 0.5	36	0.2	21	0.7	21	0.0	178
TWA 25	4000 ± 320	3.5 ± 0.8	11	0.0	12	0.0	12	0.0	187
TWA 5B	3400 ± 210	4.5 ± 1.3	30	0.0	120	0.1	30	0.0	224
TWA 8A	3500 ± 160	4.5 ± 1.1	10	0.0	8	0.5	9	0.0	226
TWA 8B	2800 ± 1130	4.0 ± 1.2	60	0.3	120	0.6	21	0.0	178
TWA 9A	4000 ± 290	3.0 ± 0.6	11	0.0	11	0.0	12	0.0	273
TWA 9B	3400 ± 470	4.5 ± 0.6	12	0.0	10	0.1	10	0.0	222
UX Tau	5500 ± 480	5.0 ± 1.2	30	0.0	30	0.0	30	0.0	41
V1044 Ori	5800 ± 660	4.5 ± 1.1	30	0.0	30	0.0	30	0.0	
V1149 Sco	5900 ± 230	4.0 ± 0.9	15	0.0	18	0.0	18	0.0	
V1354 Tau	5300 ± 570	5.0 ± 0.3	36	0.0	40	0.0	36	0.0	32
V1458 Ori	3800 ± 340	2.5 ± 0.9	18	0.3	18	0.3	21	0.0	220
V2062 Oph	4400 ± 140	3.5 ± 1.0	21	0.2	18	0.4	21	0.2	97
V2129 Oph	4000 ± 390	2.5 ± 1.0	15	0.4	15	0.3	18	0.0	238
V2247 Oph	3800 ± 260	3.5 ± 0.6	15	0.0	15	0.4	18	0.0	242

3.2 Chromospheric emission lines

Figure 25 and 26 show the Ca II ($\lambda 8542$ Å) and Mg I line ($\lambda 8807$ Å) spectra of the PMS stars after subtracting the photospheric absorption. Ca II line and Mg I line of most of the PMS stars appear in emission. The EQWs of the chromospheric emission lines of Ca II HK ($\lambda 3934, 3968$ Å), Hα ($\lambda 6563$ Å), Ca II IRT ($\lambda 8542$ Å), and Mg I ($\lambda 8807$ Å) are listed in table 8.

The PMS stars show Ca II emission lines at $\lambda 8542$ Å whose ranges from 0.07 Å to 43 Å. In Marsden et al. (2009), the EQWs of the ZAMS stars are between 0.10 Å and 94 Å. The EQWs of the PMS stars in both studies are comparable. Mg I emission lines ($\lambda 8807$ Å) were detected from 53 out of 69 PMS stars. The PMS stars show Mg I emission lines whose range from 0.04 Å to 0.52 Å. In (Yamashita et al. 2022a), the EQWs of the Mg I emission lines range from 0.02 Å to 0.52 Å for the ZAMS stars. The EQWs of the PMS stars are comparable to those of the ZAMS stars.

Some of the chromospheric emission lines detected during a total solar eclipse (Dunn et al. 1968) are also detected in the PMS spectra after the subtraction of the absorption components in $8650 - 8850$ Å; Si I ($\lambda 8728$ Å), P12($\lambda 8750$ Å), Mg I ($\lambda 8807$ Å), and Fe I ($\lambda 8680, 8824, 8838$ Å).

Among them, P12, Mg I at λ 8807 Å, and Fe I at λ 8824 Å were also detected in the T Tauri star spectra obtained by Hamann & Persson (1992). They carried out optical spectroscopy of 34 PMSs with high accretion. Table 9 indicates the examples of the chromospheric emission lines detected from 44 PMS stars, and the number of PMS stars for which emission lines were detected. Hamann & Persson (1992) did not remove the photospheric absorption components, and detect Mg I and Fe I (λ $8807, 8824$ Å) emission lines from the eight T Tauri stars. In this study, we removed the photospheric absorption components, and detected these emission lines from more PMS stars. The detection rate is increased from 24% to 80-82%. We consider that the subtraction of the model spectrum is necessary for the detection of weak emission lines.

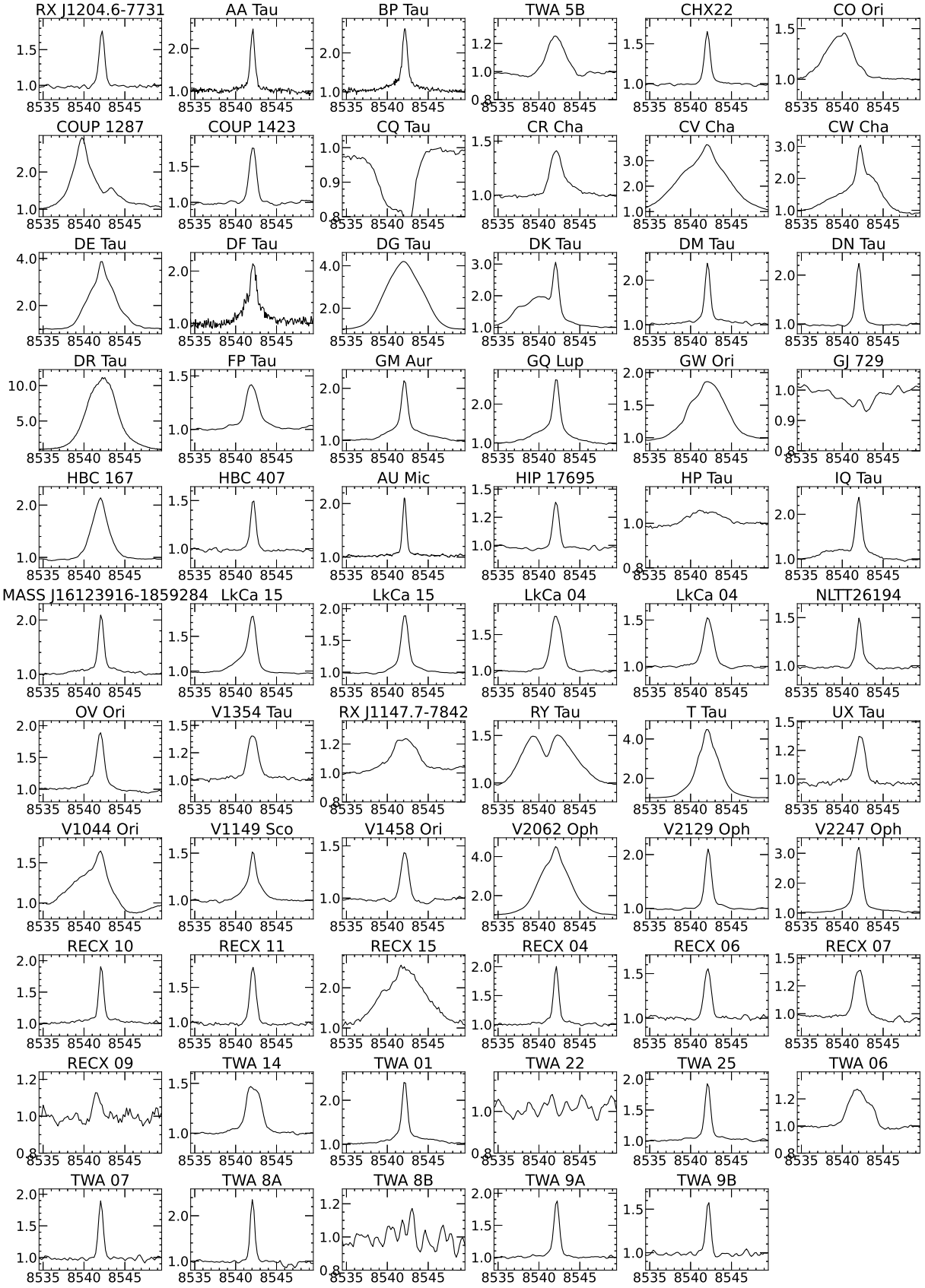

Fig. 25: Ca II (λ8542 Å) emission lines of the PMS stars. Continuum is normalized to unity. Photospheric absorption lines are already subtracted.

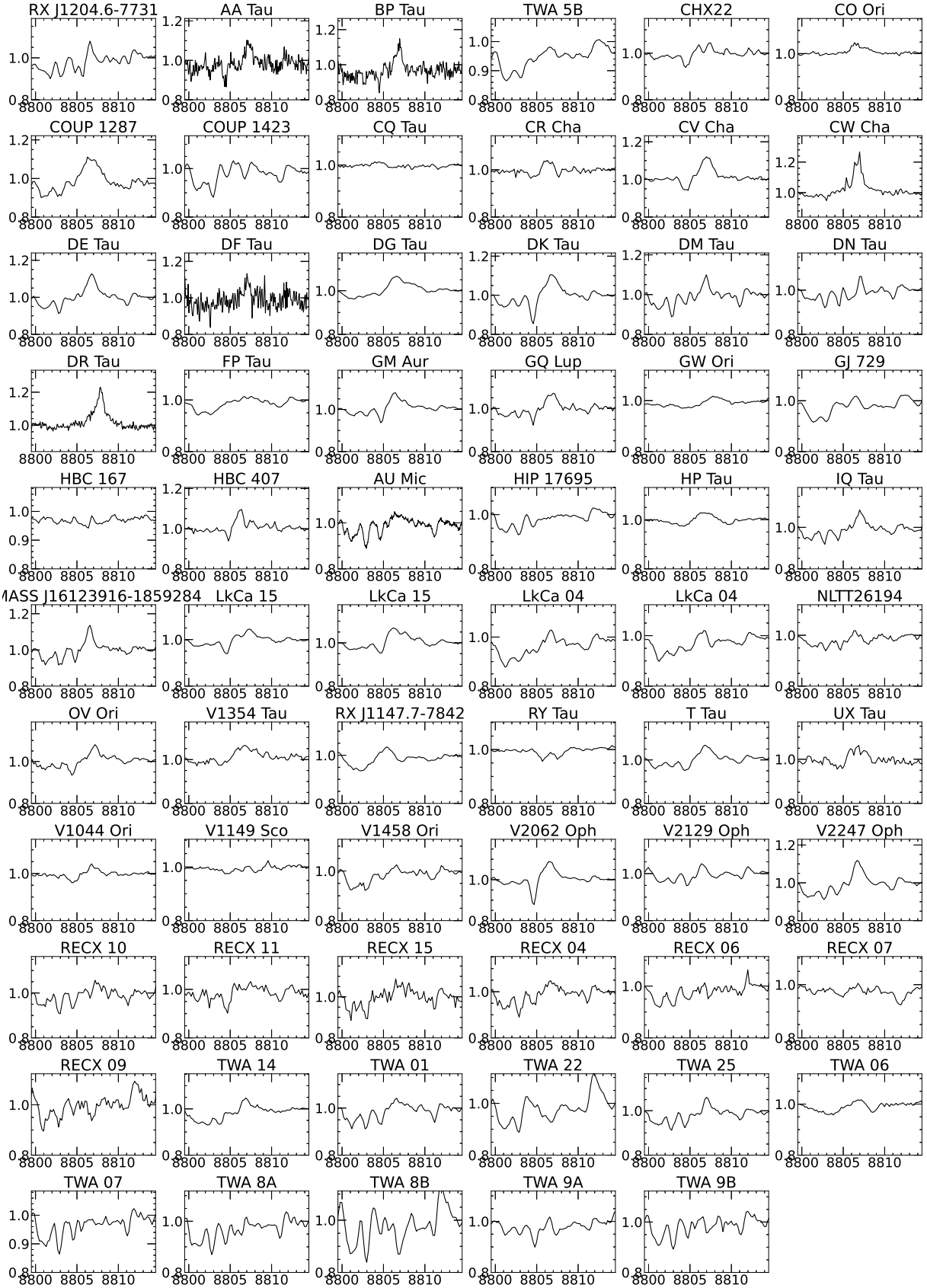

Fig. 26: Mg I (λ8807 Å) emission lines of the PMS stars. Continuum is normalized to unity. Photospheric absorption lines are already subtracted.

Table 8: EQWs of the chromospheric emission lines; Ca II HK ($\lambda 3934, 3968$ Å), Hα ($\lambda 6563$ Å), Ca II IRT ($\lambda 8542$ Å), and Mg I ($\lambda 8807$ Å)

Object Name	EQW [Å]					Flag
	3934	3968	6563	8542	8807	8807
(1)	(2)	(3)	(4)	(5)	(6)	(7)
2MASS J16123916-1859284				-1.22	-0.13 ± 0.04	TRUE
AA Tau	-8.20	-12.51	-29.16	-1.32	-0.11 ± 0.04	TRUE
AB Dor	-19.79	-19.10	-2.22	-0.40	-0.09 ± 0.05	TRUE
AU Mic				-0.69	-0.24 ± 0.06	TRUE
BP Tau	-5.08	-12.24	-50.73	-1.67	-0.15 ± 0.05	TRUE
CHX22				-0.63	-0.08 ± 0.08	FALSE
CO Ori				-1.98	-0.08 ± 0.03	TRUE
COUP 1287				-4.98	-0.45 ± 0.10	TRUE
COUP 1423				-0.96		FALSE
CQ Tau						FALSE
CR Cha				-0.97	-0.12 ± 0.04	TRUE
CV Cha				-16.30	-0.18 ± 0.03	TRUE
CW Cha				-7.57	-0.53 ± 0.10	TRUE
DE Tau				-9.61	-0.24 ± 0.07	TRUE
DF Tau	-39.44	-26.22	-52.81	-2.14	-0.10 ± 0.07	TRUE
DG Tau				-16.71	-0.21 ± 0.02	TRUE
DK Tau				-2.33	-0.33 ± 0.05	TRUE
DM Tau				-1.35	-0.13 ± 0.03	TRUE
DN Tau				-1.38	-0.06 ± 0.02	TRUE
DR Tau	-29.64	-6.57		-42.71	-0.44 ± 0.05	TRUE
FP Tau				-0.89	-0.04 ± 0.04	FALSE
GJ 729					-0.05 ± 0.02	TRUE
GM Aur				-2.01	-0.11 ± 0.03	TRUE
GQ Lup				-3.18	-0.12 ± 0.04	TRUE
GW Ori				-4.59	-0.05 ± 0.03	TRUE
HBC 167	-5.95	-3.82	-9.84	-3.11		FALSE
HBC 407	-2.13	-1.63	-0.70	-0.47	-0.10 ± 0.03	TRUE
HP Tau	-21.24	-10.83	-2.50	-0.26	-0.15 ± 0.03	TRUE
IQ Tau	-1.14	-0.42		-1.58	-0.13 ± 0.05	TRUE
LkCa 04				-0.89	-0.08 ± 0.04	TRUE
LkCa 04				-1.36	-0.09 ± 0.06	TRUE
LkCa 15				-1.24	-0.19 ± 0.05	TRUE
LkCa 15				-1.41	-0.11 ± 0.03	TRUE
NLTT26194				-0.53	-0.04 ± 0.02	TRUE
OV Ori				-1.24	-0.12 ± 0.04	TRUE
RECX 04	-23.56	-13.71	-3.86	-0.94	-0.28 ± 0.03	TRUE

Table 8: (Continued)

Object Name	EQW [Å]					Flag
	3934	3968	6563	8542	8807	8807
(1)	(2)	(3)	(4)	(5)	(6)	(7)
RECX 06	-25.97	-16.11	-3.71	-0.60	-0.06 ± 0.03	TRUE
RECX 07	-9.94	-6.75	-0.69	-0.70	-0.06 ± 0.07	FALSE
RECX 09	-20.78	-10.49	-9.55	-0.20		FALSE
RECX 10	-17.41	-10.61	-1.27	-0.70	-0.10 ± 0.03	TRUE
RECX 11	-11.02	-6.85	-10.77	-0.87	-0.29 ± 0.07	TRUE
RECX 15	-45.84		-61.27	-9.09	-0.17 ± 0.10	TRUE
RX J1147.7-7842	-22.32	-14.74	-5.05	-0.84	-0.11 ± 0.06	TRUE
RX J1204.6-7731	-29.55	-22.80	-6.92	-0.65	-0.07 ± 0.02	TRUE
RY Tau	-5.62		-14.86	-3.63	-0.03 ± 0.04	FALSE
T Tau				-10.87	-0.13 ± 0.05	TRUE
TWA 01	-8.24	-5.55	-84.71	-1.64	-0.34 ± 0.04	TRUE
TWA 06	-12.99		-4.85	-0.90	-0.14 ± 0.02	TRUE
TWA 07	-23.47	-15.93	-4.53	-0.69	0.00 ± 0.02	FALSE
TWA 14	-19.75	-12.80	-6.00	-1.02	-0.12 ± 0.04	TRUE
TWA 22	-25.18	-16.46	-9.26			FALSE
TWA 25	-21.21	-14.24	-2.32	-0.94	-0.09 ± 0.02	TRUE
TWA 5B				-0.82	-0.04 ± 0.03	TRUE
TWA 8A				-0.96	-0.01 ± 0.04	FALSE
TWA 8B				-0.07	-0.02 ± 0.10	FALSE
TWA 9A				-0.81	-0.01 ± 0.04	FALSE
TWA 9B				-0.51		FALSE
UX Tau				-0.78	-0.15 ± 0.05	TRUE
V1044 Ori				-2.74	-0.07 ± 0.04	TRUE
V1149 Sco				-0.85	-0.01 ± 0.04	FALSE
V1354 Tau				-0.65	-0.19 ± 0.04	TRUE
V1458 Ori				-0.60	-0.02 ± 0.07	FALSE
V2062 Oph				-13.26	-0.11 ± 0.02	TRUE
V2129 Oph				-1.26	-0.05 ± 0.02	TRUE
V2247 Oph				-2.84	-0.17 ± 0.04	TRUE

(7) This column shows whether the EQWs of the Mg I lines are significant or not.
TRUE: significant, FALSE: EQW is not significant or no emission line detected.

Table 9: The examples of the chromospheric emission lines detected from 64 PMS stars

Wavelength [Å]		Number of PMS stars	
		Hamann & Persson (1992)	This work
Si I	8728	-	15/64
Pa12	8750	24/34	23/64
Mg I	8807	8/34	47/64
Fe I	8824	8/34	41/64
Fe I	8838	-	27/64

3.3 Rotation, Starspots, and Flares

3.3.1 Rotation period and shape of the light curve

The rotational periods of the PMS stars range from 0.26 to 22 days. The amplitudes of the light curves range from $0.002-1.311$ mag. In table 10, we list the periods and the amplitudes of the light curves of the PMS stars that were measured multiple times in *TESS*. For the ZAMS stars, the rotational periods and the amplitudes of the light curves range $0.22-7.25$ days and $0.001-0.145$ mag (Yamashita et al. 2022b). Both of them have a wider range than that of the ZAMS stars. Some of the PMS stars especially have longer rotational periods and larger amplitudes of the light curve than the ZAMS stars.

Figure 27, 28, and 29 show three examples of the light curves. The middle column shows examples of Lomb-Scargle periodograms. In the periodograms of almost all objects (except for HD 285898), the false alarm probability of the strongest peak was less than 10^{-6}. *TESS* data was not obtained for several days in the middle of the observation period, leading to aliasing on the side of the strongest peak in the periodogram. When we split the light curve at the center time and applied the Lomb–Scargle periodogram analysis, the aliasing disappeared. In the previous space-based monitoring campaigns (Cody et al. 2014), the periodicity metric, Q, and the flux asymmetry, M were introduced and have been used to characterize the light curves of PMS stars in several star-forming regions (e.g. Cody et al. 2014, Cody & Hillenbrand 2018, Robinson, Espaillat & Rodriguez 2022).

The periodicity metric, Q is defined as

$$Q \equiv \frac{(\mathrm{rms}^2_{\mathrm{resid}} - \sigma^2)}{(\mathrm{rms}^2_{\mathrm{raw}} - \sigma^2)}, \tag{5}$$

where $\mathrm{rms}_{\mathrm{raw}}$ and $\mathrm{rms}_{\mathrm{resid}}$ are the rms values of the raw light curve and the residual light curve, respectively. First, the raw light curves (circle symbols in figure 27, 28, and 29) are folded with their period obtained by the Lomb-Scargle periodogram. Second, the folded light curves are boxcar-smoothed with sizes set to the quarter of the rotational period (magenta dashed line in figure 27, 28, and 29). The residual components are generated by subtracting the smoothed light curves from the raw light curves, and computed $\mathrm{rms}_{\mathrm{resid}}$. σ is the estimated uncertainty including the systematics. σ is estimated with the empirical relationship between *TESS* magnitudes and σ, which is provided by Handberg et al. (2021). The light curves with $Q = 0$ are periodic, and those with $Q = 1$ are aperiodic.

The flux asymmetry, M is defined as

$$M \equiv \frac{(< d_{10\%} > - d_{\mathrm{med}})}{\sigma_d}. \tag{6}$$

$< d_{10\%} >$ is the mean of all raw data at 10th and 90th percentile flux, d_{med} is the median of the entire raw light curve, and σ_d is rms of overall fluxes. The light curves with long bursting times have small M, and those with long dimming times have large M.

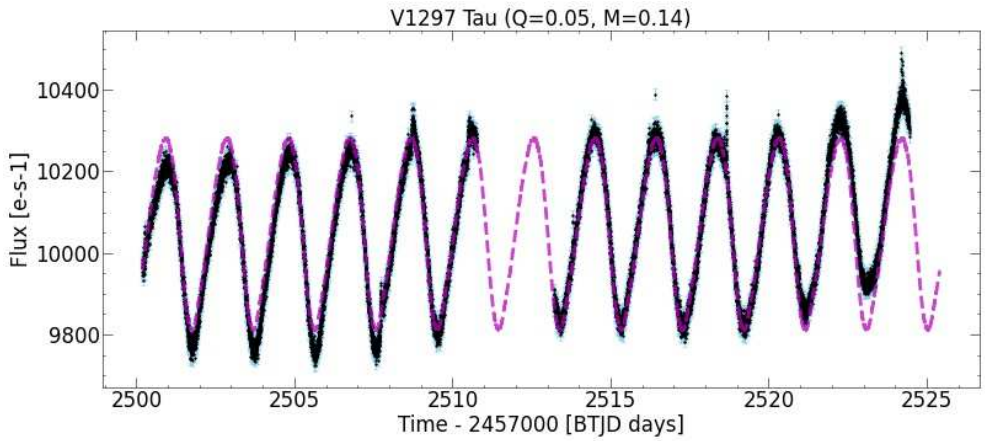

(a) Full light curve

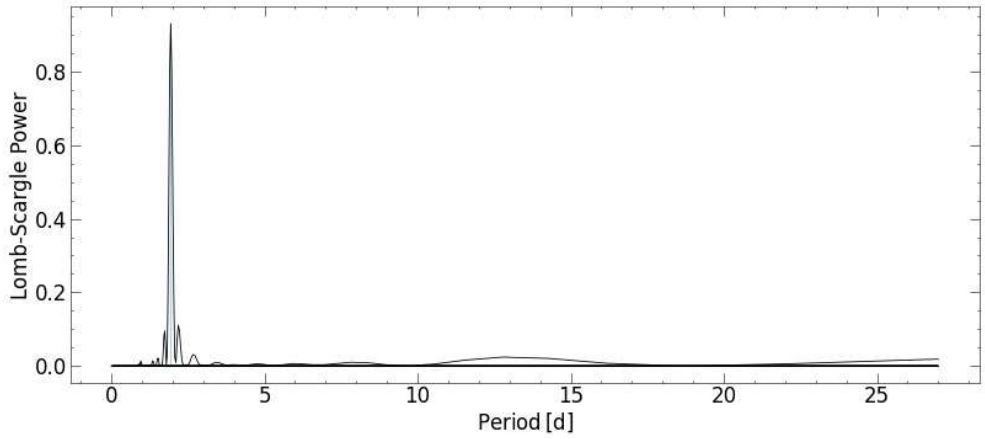

(b) Lomb-Scargle periodogram

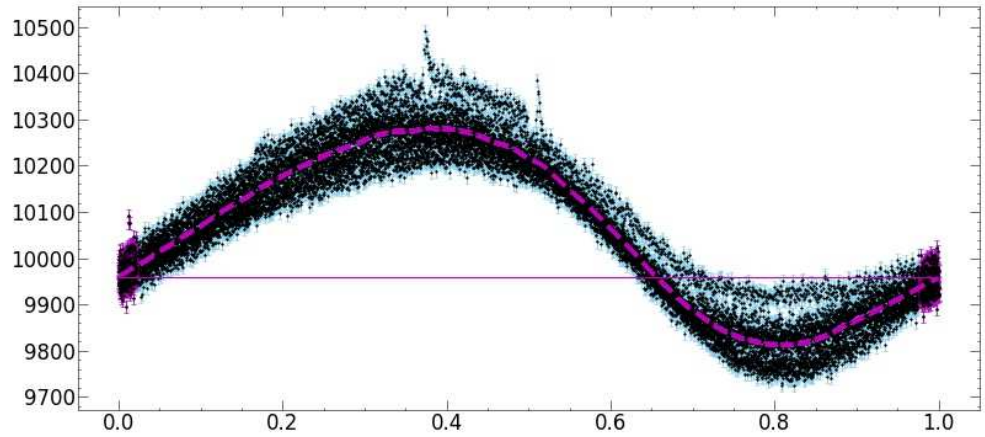

(c) Phased light curve

Fig. 27: Light curve of a PMS star with periodic variability, V1297 Tau. Top: full light curve; middle: Lomb-Scargle periodogram; bottom: phased light curve. Data points greater than $3\sigma_1$ above the average flux were removed from the phased light curve. The magenta dashed lines represent the boxcar-smoothed light curve. The horizontal solid line indicates the false alarm probability of 10^{-6}.

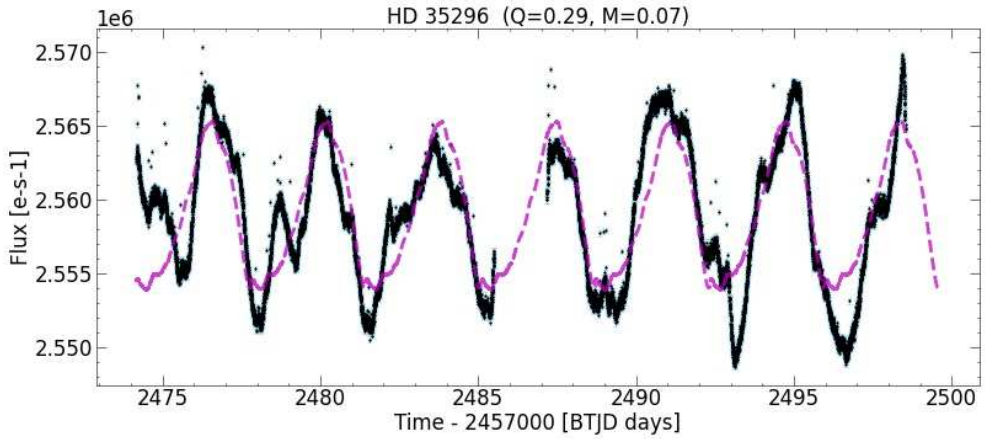

(a) Full light curve

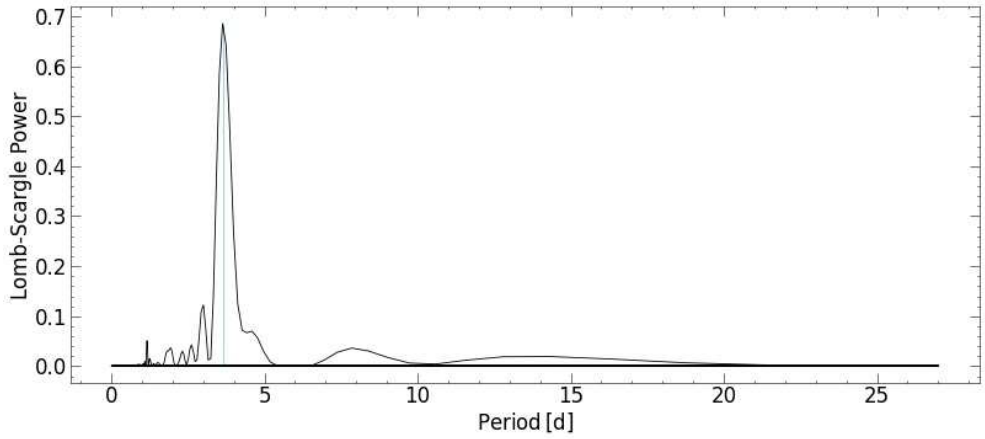

(b) Lomb-Scargle periodogram

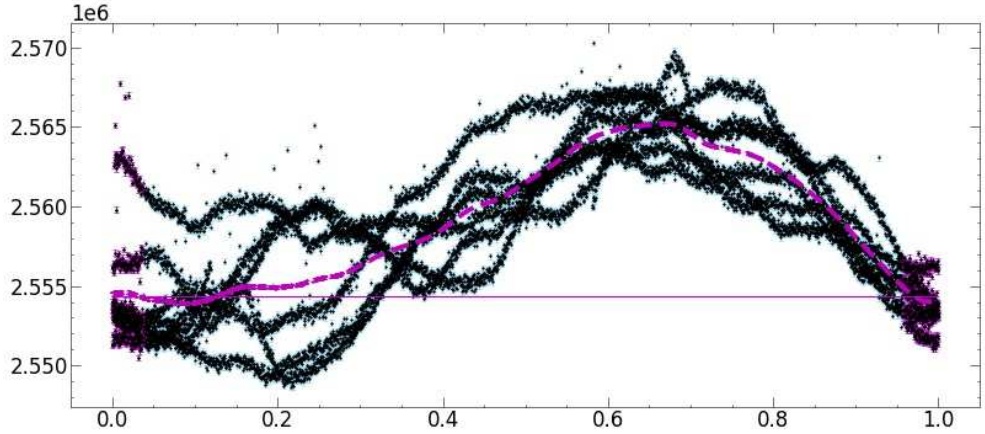

(c) Phased light curve

Fig. 28: Light curve of a PMS star with quasi-periodic stochastic variability, HD 35296. Top: full light curve; middle: Lomb-Scargle periodogram; bottom: phased light curve. Data points greater than $3\sigma_1$ above the average flux were removed from the phased light curve. The magenta dashed lines represent the boxcar-smoothed light curve. The horizontal solid line indicates the false alarm probability of 10^{-6}.

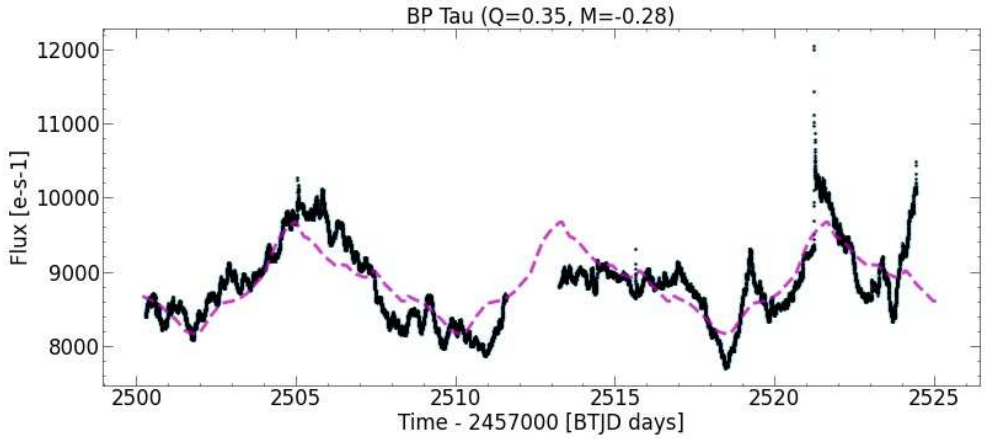

(a) Full light curve

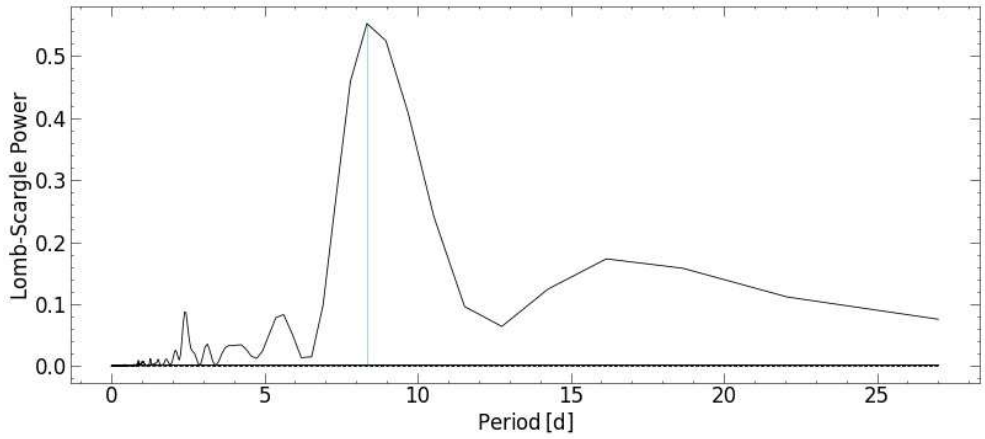

(b) Lomb-Scargle periodogram

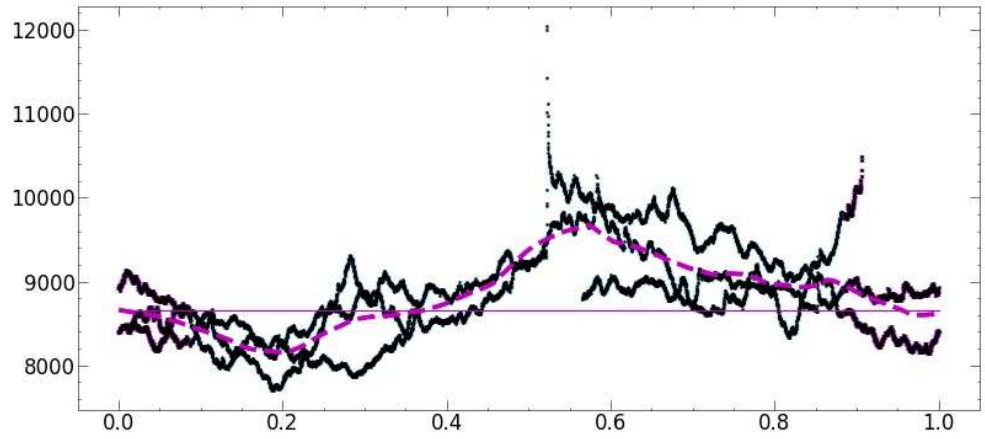

(c) Phased light curve

Fig. 29: Light curve of a burster PMS star, BP Tau. Top: full light curve; middle: Lomb-Scargle periodogram; bottom: phased light curve. Data points greater than $3\sigma_1$ above the average flux were removed from the phased light curve. The magenta dashed lines represent the boxcar-smoothed light curve. The horizontal solid line indicates the false alarm probability of 10^{-6}.

Cody & Hillenbrand (2018) classified variable stars into six classes; bursters ($M < -0.25$), purely periodic symmetric ($Q < 0.15$ and $-0.25 < M < 0.25$), quasiperiodic symmetric (QPS; $0.15 < Q < 0.85$ and $-0.25 < M < 0.25$), purely stochastic ($Q > 0.85$ and $-0.25 < M < 0.25$), quasiperiodic dippers ($0.15 < Q < 0.85$ and $M > 0.25$), and aperiodic dippers ($Q > 0.85$ and $M > 0.25$).

We measured the Q and M values for our targets using the *TESS* light curves (figure 30). We categorized the light curves into the six groups as shown in figure 30. The QM values and variability groups are listed in table 10. However, because the numbers of objects in purely stochastic, quasiperiodic dippers, and aperiodic dippers are not enough for discussion, we are going to discuss the 61 PMS stars in the purely periodic symmetric group, the 122 PMS stars in the quasi-periodic stochastic group, and the 56 PMS stars in the burster group (table 10). Actually, more than half of the PMS stars are observed by *TESS* over a few semesters. Some objects observed in several semesters are categorized into one group, and other objects are categorized into two or more groups.

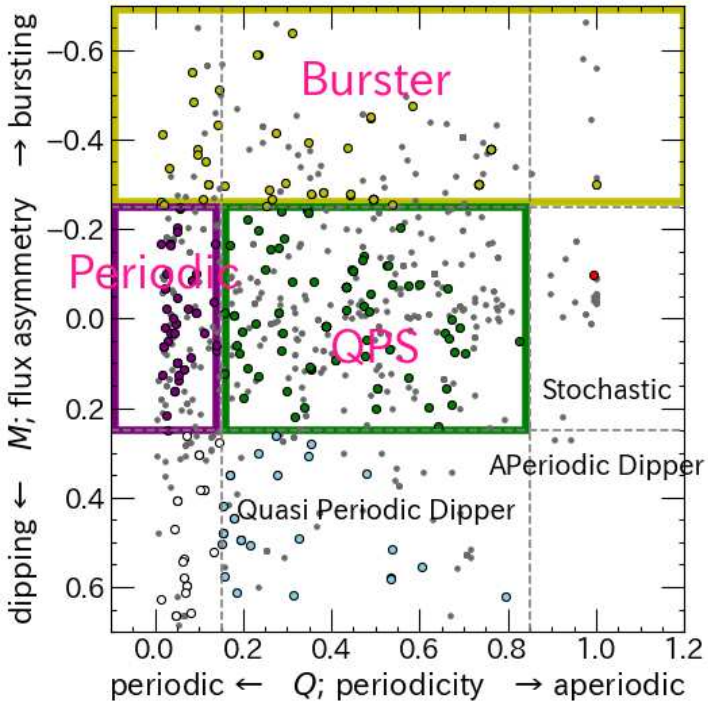

Fig. 30: Classification of the light curves of the PMS stars. The periodicity, Q, and flux asymmetry, M, are defined by Cody et al. (2014). The circles represent the PMS stars investigated in the study, and especially the PMS stars with solar-mass ($0.8 - 1.2$ $M_{\odot}$) are colored. The dashed lines show the boundaries between variability groups defined by Cody & Hillenbrand (2018).

3.3.2 Starspots

The apparent area of the spot, $A_{\rm spot}$, was estimated from the amplitude of light variation ($\Delta F/F$) using the following equation (Notsu et al. 2013):

$$A_{\rm spot} = \frac{\Delta F}{F} A_{\frac{1}{2}{\rm star}} \left[1 - \left(\frac{T_{\rm spot}}{T_{\rm eff}} \right)^4 \right]^{-1}, \tag{7}$$

where $A_{\frac{1}{2}{\rm star}}$ is the effective area of the stellar hemisphere. With the Stefan-Boltzmann law,

$$L = 4\pi {R_*}^2 \sigma {T_{\rm eff}}^4, \tag{8}$$

we estimated the stellar radius and converted it to $A_{\frac{1}{2}{\rm star}}$. $T_{\rm spot}$ and $T_{\rm eff}$ are the temperature of the starspot and photosphere of the star. The effective temperature of the solar photosphere is 5770 K. Berdyugina et al. (2005) show the temperature of sunspot is 4200 K. Temperature of the stellar spots depends on $T_{\rm eff}$. We applied eq. (4) of Notsu et al. (2019), which is an empirical equation on the temperature difference between photosphere and spot, $T_{\rm eff} - T_{\rm spot}$, deduced from Berdyugina et al. (2005). The starspot coverages, $A_{\rm spot}/A_{\frac{1}{2}{\rm star}}$, are listed in table 10.

Table 10: Amplitude, spot coverage, period, Rossby number, QM values, and variability groups measured from *TESS* light curves

Object Name	Amp [mag]	Spot coverage	Period [day]	$\log N_{\rm R}$	Q	M	Variability
2MASS J04035084+2610531	0.017	0.034	8.99	-1.40	0.95	-0.04	S
2MASS J04182147+1658470	0.015	0.022	4.98	-1.12	0.78	-0.04	QPS
2MASS J04182147+1658470	0.014	0.021	4.94	-1.13	0.78	0.00	QPS
51 Eri	0.007	0.007	1.84		0.76	-0.20	QPS
51 Eri	0.007	0.007	0.27		0.78	-0.06	QPS
AA Tau	0.230	0.383	3.47	-1.89	0.70	-0.41	B
AA Tau	0.245	0.411	4.37	-1.79	0.64	-0.10	QPS
AA Tau	0.466	0.871	4.05	-1.82	0.61	0.19	QPS
AA Tau	0.400	0.725	5.31	-1.70	0.67	0.18	QPS
AA Tau	0.376	0.673	2.91	-1.96	0.65	-0.17	QPS
AA Tau	0.446	0.825	22.07	-1.08	0.65	-0.34	B
AB Dor	0.199	0.278	0.51	-1.83	0.30	-0.04	QPS
AB Dor	0.136	0.184	0.51	-1.83	0.11	0.63	unknown
AB Dor	0.233	0.332	0.51	-1.83	0.13	0.52	unknown
AB Dor	0.216	0.304	0.51	-1.83	0.07	0.47	unknown
AB Dor	0.188	0.262	0.51	-1.83	0.10	0.38	unknown
AB Dor	0.221	0.313	0.52	-1.83	0.04	0.03	P
AB Dor	0.263	0.379	0.52	-1.83	0.20	0.06	QPS
AB Dor	0.242	0.346	0.51	-1.83	0.03	0.05	P
AB Dor	0.224	0.317	0.51	-1.83	0.15	0.50	unknown
AB Dor	0.190	0.264	0.51	-1.83	0.07	0.61	unknown
AB Dor	0.123	0.167	0.26	-2.13	0.46	-0.45	B
AB Dor	0.121	0.163	0.26	-2.13	0.46	-0.45	B
AB Dor	0.114	0.154	0.51	-1.83	0.22	-0.59	B
AB Dor	0.119	0.160	0.51	-1.83	0.22	-0.59	B
AB Dor	0.055	0.072	0.52	-1.83	0.27	0.26	QPD
AB Dor	0.060	0.078	0.52	-1.83	0.29	0.16	QPS
AB Dor	0.204	0.286	0.51	-1.83	0.05	-0.07	P
AB Dor	0.215	0.304	0.51	-1.83	0.05	-0.07	P
AB Dor	0.288	0.421	0.51	-1.83	0.06	-0.17	P
AB Dor	0.296	0.434	0.51	-1.83	0.06	-0.17	P
AB Dor	0.299	0.439	0.51	-1.83	0.07	0.16	P
AB Dor	0.308	0.455	0.51	-1.83	0.07	0.16	P
AB Dor	0.334	0.498	0.51	-1.83	0.49	-0.14	QPS
AB Dor	0.328	0.489	0.51	-1.83	0.49	-0.13	QPS
AB Dor	0.361	0.547	0.51	-1.83	0.35	0.11	QPS
AB Dor	0.376	0.573	0.51	-1.83	0.35	0.11	QPS
AB Dor	0.401	0.618	0.51	-1.83	0.45	-0.28	B
AB Dor	0.425	0.663	0.51	-1.83	0.45	-0.28	B
AB Dor	0.323	0.479	0.51	-1.83	0.28	-0.01	QPS
AB Dor	0.342	0.512	0.51	-1.83	0.28	-0.01	QPS
AB Dor	0.129	0.175	0.51	-1.83	0.02	-0.26	B
AB Dor	0.129	0.175	0.51	-1.83	0.02	-0.26	B
AB Dor	0.149	0.204	0.51	-1.83	0.04	-0.17	P
AB Dor	0.190	0.264	0.51	-1.83	0.48	-0.02	QPS
AB Dor	0.066	0.086	0.51	-1.83	0.06	0.11	P
AB Dor	0.066	0.086	0.51	-1.83	0.09	0.09	P
AB Dor	0.072	0.095	0.51	-1.83	0.01	-0.20	P
AB Dor	0.072	0.095	0.51	-1.83	0.01	-0.19	P
AB Dor	0.048	0.062	0.51	-1.83	0.09	-0.25	P

Table 10: (Continued)

Object Name	Amp [mag]	Spot coverage	Period [day]	log N_R	Q	M	Variability
AB Dor	0.048	0.062	0.51	-1.83	0.10	-0.25	P
AB Dor	0.044	0.057	0.52	-1.83	0.06	0.54	unknown
AB Dor	0.044	0.057	0.52	-1.83	0.03	0.54	unknown
AB Dor	0.069	0.091	0.51	-1.83	0.06	-0.01	P
AB Dor	0.069	0.091	0.51	-1.83	0.06	-0.01	P
AB Dor	0.084	0.111	0.51	-1.83	0.11	-0.39	B
AB Dor	0.084	0.111	0.51	-1.83	0.03	-0.39	B
AB Dor	0.093	0.123	0.52	-1.83	0.03	-0.64	B
AB Dor	0.093	0.124	0.51	-1.83	0.04	-0.59	B
AD Leo	0.048	0.092	6.24	-1.48	0.98	-0.66	B
AD Leo	0.034	0.064	6.24	-1.48	0.99	-0.44	B
AD Leo	1.095	3.530	6.22	-1.48	0.99		unknown
AD Leo	0.618	1.555	4.82	-1.59	0.97	-0.58	B
AD Leo	0.003	0.006	4.53	-1.62	0.84	-0.32	B
AD Leo	0.003	0.006	2.53	-1.87	0.90	-0.06	S
AU Mic	0.043	0.071	4.84	-1.40	0.02	-0.73	B
AU Mic	0.027	0.044	4.78	-1.40	0.11	-0.77	B
AU Mic	0.029	0.048	4.77	-1.40	0.10	-0.65	B
BD+21 584	0.014	0.016	1.19	-1.01	0.14	0.06	P
BD+21 584	0.009	0.010	1.22	-1.00	0.48	0.05	QPS
BD+21 584	0.011	0.013	1.19	-1.01	0.18	-0.06	QPS
BD-07 2388	0.032	0.042	0.33	-2.24	0.19	0.50	QPD
BD-07 2388	0.027	0.036	0.33	-2.24	0.39	0.16	QPS
BD-07 2388	0.015	0.020	0.33	-2.24	0.20	-0.01	QPS
BD-16351	0.014	0.018	3.30	-1.16	0.23	0.58	QPD
BD-16351	0.056	0.075	3.23	-1.17	0.02	-0.10	P
BP Tau	0.182	0.293	10.76	-1.08	0.50	0.07	QPS
BP Tau	0.100	0.154	2.86	-1.66	0.69	0.02	QPS
BP Tau	0.159	0.253	9.71	-1.13	0.48	0.35	QPD
BP Tau	0.155	0.245	8.35	-1.20	0.30	-0.30	B
BP Tau	0.181	0.291	8.35	-1.20	0.35	-0.28	B
BP Tau	0.126	0.197	5.10	-1.41	0.67	0.00	QPS
BP Tau	0.129	0.203	5.10	-1.41	0.66	0.03	QPS
CPD-43 7188	0.075	0.098	2.63	-1.31	0.09	-0.38	B
CPD-43 7188	0.072	0.094	2.64	-1.31	0.02	0.02	P
CQ Tau	0.513	0.844	6.95	-1.00	0.51	0.13	QPS
CQ Tau	0.560	0.943	7.35	-0.98	0.54	0.12	QPS
CQ Tau	0.718	1.309	7.33	-0.98	0.51	-0.31	B
CQ Tau	1.265	3.081	>27	-0.41	0.38	-0.11	QPS
CW Tau	1.007	2.720	9.19	-1.33	0.51	-0.09	QPS
CW Tau	0.971	2.572	9.72	-1.30	0.57	-0.50	B
CW Tau	1.021	2.777	>27	-0.86	0.73	-0.04	QPS
CX Tau	0.055	0.119	3.33	-1.82	0.04	0.04	P
CX Tau	0.054	0.117	3.31	-1.83	0.07	0.28	unknown
CY Tau	0.234	0.413	3.96	-1.65	0.37	0.43	QPD
CY Tau	0.308	0.562	4.27	-1.62	0.69	-0.03	QPS
CY Tau	0.380	0.721	14.26	-1.09	0.55	0.37	QPD
CY Tau	0.248	0.441	4.18	-1.63	0.48	0.40	QPD
CY Tau	0.212	0.371	6.90	-1.41	0.53	0.22	QPS
CZ Tau	0.167	0.251	5.17		0.72	-0.05	QPS
CZ Tau	0.153	0.228	7.34		0.59	-0.12	QPS

Table 10: (Continued)

Object Name	Amp [mag]	Spot coverage	Period [day]	log $N_{\rm R}$	Q	M	Variability
Cl* Melotte 111 AV 1693	0.005	0.006	5.80	-0.69	0.68	0.15	QPS
Cl* Melotte 111 AV 1693	0.006	0.008	4.41	-0.81	0.54	-0.25	B
Cl* Melotte 111 AV 1826	0.005	0.006	4.94	-0.85	0.52	-0.12	QPS
Cl* Melotte 111 AV 1826	0.013	0.017	9.69	-0.56	0.32	0.22	QPS
Cl* Melotte 111 AV 2177	0.005	0.007	6.06	-0.81	0.61	-0.08	QPS
Cl* Melotte 111 AV 2177	0.008	0.010	9.70	-0.60	0.34	-0.24	QPS
Cl* Melotte 111 AV 523	0.007	0.009	5.54	-0.84	0.59	-0.05	QPS
Cl* Melotte 22 PELS 031	0.029	0.037	2.97	-1.07	0.21	0.18	QPS
Cl* Melotte 22 PELS 031	0.038	0.048	4.97	-0.85	0.25	-0.11	QPS
CoKu Tau 4	0.025	0.041	1.91	-1.70	0.56	-0.22	QPS
CoKu Tau 4	0.025	0.041	1.90	-1.70	0.54	-0.10	QPS
CoKu Tau 4	0.025	0.040	1.91	-1.70	0.50	0.05	QPS
DD Tau	0.263	0.513	2.81	-1.80	0.74	-0.39	B
DD Tau	0.380	0.787	5.65	-1.50	0.58	-0.15	QPS
DD Tau	0.434	0.921	2.91	-1.79	0.76	-0.17	QPS
DE Tau	0.056	0.098	5.79	-1.61	0.40	0.08	QPS
DE Tau	0.038	0.066	5.92	-1.60	0.64	-0.05	QPS
DE Tau	0.037	0.063	5.37	-1.64	0.63	0.45	QPD
DF Tau	0.420	0.941	8.98	-1.39	0.47	-0.04	QPS
DF Tau	0.407	0.905	22.08	-1.00	0.35	-0.32	B
DF Tau	0.224	0.456	5.60	-1.59	0.70	-0.26	B
DF Tau	0.238	0.489	5.87	-1.57	0.59	-0.27	B
DG Tau	0.292	0.598	8.99	-1.41	0.54	-0.09	QPS
DG Tau	0.288	0.589	>27	-0.93	0.51	-0.56	B
DH Tau	0.226	0.444	3.96	-1.77	0.52	-0.29	B
DH Tau	0.341	0.709	>27	-0.94	0.74	-0.07	QPS
DH Tau	0.174	0.334	6.45	-1.56	0.54	-0.26	B
DH Tau	0.133	0.251	2.30	-2.01	0.77	-0.35	B
DI Tau	0.081	0.134	4.09	-1.81	0.55	-0.25	B
DI Tau	0.156	0.267	10.49	-1.40	0.38	-0.34	B
DK Tau	0.652	1.520	5.35	-1.68	0.49	0.17	QPS
DK Tau			5.35	-1.68	0.52		unknown
DK Tau	0.857	2.219	7.76	-1.52	0.27	0.26	QPD
DK Tau			7.76	-1.52	0.26		unknown
DL Tau	0.303	0.565	2.37	-2.01	0.81	-0.34	B
DL Tau	0.465	0.938	10.48	-1.36	0.63	-0.84	B
DM Tau	0.123	0.229	7.83	-1.48	0.43	-0.20	QPS
DM Tau	0.164	0.310	10.48	-1.36	0.40	-0.24	QPS
DM Tau	0.077	0.139	7.73	-1.49	0.69	-0.22	QPS
DM Tau	0.054	0.097	3.23	-1.87	0.81	-0.13	QPS
DN Tau	0.113	0.195	6.49	-1.56	0.22	-0.17	QPS
DN Tau	0.131	0.228	6.50	-1.56	0.14	-0.21	P
DO Tau	0.493	1.102	9.62	-1.38	0.27	-0.66	B
DO Tau	0.374	0.788	18.64	-1.09	0.72	-0.14	QPS
DO Tau	0.343	0.714	6.14	-1.58	0.60	-0.62	B
DO Tau	0.273	0.549	5.89	-1.59	0.53	-0.06	QPS
DQ Tau	0.227	0.380	10.57	-1.23	0.50	-0.96	B
DQ Tau	0.378	0.683	7.81	-1.36	0.56	-1.36	B
DR Tau	0.442	0.804	22.09	-1.08	0.56	-0.20	QPS
DR Tau	0.420	0.756	8.97	-1.47	0.48	0.08	QPS
DR Tau	0.513	0.966	7.80	-1.53	0.53	-0.23	QPS

Table 10: (Continued)

Object Name	Amp [mag]	Spot coverage	Period [day]	log $N_{\rm R}$	Q	M	Variability
DR Tau	0.616	1.224	>27	-1.00	0.74	-0.27	B
DS Tau	0.765	1.772	8.56	-1.47	0.32	-0.37	B
DS Tau	0.484	0.974	8.99	-1.44	0.51	-0.14	QPS
DS Tau	0.759	1.754	8.35	-1.48	0.57	-0.35	B
DX Leo	0.045	0.057	5.45	-0.73	0.21	0.13	QPS
DX Leo	0.046	0.058	5.39	-0.74	0.03	0.25	P
DX Leo	0.047	0.059	5.36	-0.74	0.05	0.13	P
DX Leo	0.020	0.025	5.41	-0.74	0.08	0.66	unknown
DX Leo	0.021	0.026	5.40	-0.74	0.12	0.90	unknown
DX Leo	0.011	0.013	5.43	-0.73	0.21	0.30	QPD
DX Leo	0.012	0.014	5.43	-0.73	0.12	0.42	unknown
DX Leo	0.010	0.013	4.87	-0.78	0.56	-0.07	QPS
DX Leo	0.010	0.013	4.82	-0.79	0.53	-0.12	QPS
EK Dra	0.022	0.027	2.63	-1.00	0.13	0.38	unknown
EK Dra	0.031	0.038	2.69	-0.99	0.07	0.60	unknown
EK Dra	0.016	0.020	2.53	-1.02	0.18	0.45	QPD
EK Dra	0.046	0.056	2.63	-1.00	0.04	0.41	unknown
EK Dra	0.032	0.039	2.62	-1.00	0.10	-0.30	B
EK Dra	0.018	0.022	2.58	-1.01	0.16	0.48	QPD
EK Dra	0.024	0.029	2.72	-0.99	0.12	-0.01	P
EK Dra	0.023	0.029	2.72	-0.99	0.11	-0.09	P
EK Dra	0.019	0.023	2.73	-0.99	0.44	-0.24	QPS
EK Dra	0.019	0.023	2.69	-0.99	0.34	-0.28	B
EK Dra	0.014	0.018	2.83	-0.97	0.41	0.09	QPS
EK Dra	0.015	0.018	2.82	-0.97	0.44	-0.11	QPS
EP Eri	0.021	0.027	7.22	-0.64	0.43	-0.02	QPS
EP Eri	0.020	0.026	6.80	-0.67	0.46	-0.11	QPS
EV Lac	0.025		4.39		0.19	-0.90	B
EV Lac	0.018		4.33		0.23	0.53	QPD
EV Lac	0.019		4.33		0.18	0.60	QPD
EV Lac	0.018		2.17		0.90	0.27	APD
EV Lac	0.019		2.20		0.92	0.22	S
FN Tau	0.012	0.018	9.16	-0.93	0.67	-0.02	QPS
FN Tau	0.015	0.022	5.40	-1.16	0.69	0.02	QPS
FN Tau	0.017	0.026	7.81	-1.00	0.63	-0.18	QPS
FO Tau	0.036	0.057	4.23	-1.32	0.59	-0.19	QPS
FO Tau	0.043	0.067	5.17	-1.23	0.42	-0.25	QPS
FO Tau	0.026	0.041	5.63	-1.19	0.74	-0.23	QPS
FP Tau	0.058	0.121	2.19	-2.01	0.03	-0.03	P
FP Tau	0.046	0.095	2.18	-2.01	0.19	0.31	QPD
FQ Tau	0.180	0.310	3.16	-1.92	0.77	-0.43	B
FQ Tau	0.120	0.201	9.69	-1.43	0.65	-0.07	QPS
FX Tau	0.262	0.525	3.22		0.68	0.56	QPD
FX Tau	1.157	3.663	3.22		0.68		unknown
FX Tau	0.281	0.568	6.17		0.34	-0.04	QPS
FX Tau	1.110	3.428	6.17		0.34	0.18	QPS
GG Tau	0.187	0.361	10.57	-1.37	0.37	0.00	QPS
GG Tau	0.233	0.459	22.04	-1.05	0.21	-0.43	B
GH Tau	0.214	0.411	3.20		0.73	0.02	QPS
GH Tau	0.242	0.470	3.12		0.72	0.17	QPS
GI Tau	1.130	3.999	>27	-0.92	0.54	0.06	QPS

Table 10: (Continued)

Object Name	Amp [mag]	Spot coverage	Period [day]	log $N_{\rm R}$	Q	M	Variability
GI Tau	0.698	1.970	3.58	-1.79	0.67	-0.01	QPS
GJ 799A	0.015	0.026	0.78	-2.32	0.95	-0.17	S
GJ 799A	0.025	0.044	1.20	-2.13	0.78	-0.14	QPS
GJ 799A	0.019	0.034	0.78	-2.32	0.60	-0.06	QPS
GK Tau	0.717	1.700	22.03	-1.03	0.54	0.09	QPS
GK Tau	0.454	0.944	4.90	-1.68	0.68	0.14	QPS
GM Aur	0.119	0.185	5.79	-1.44	0.40	0.02	QPS
GM Aur	0.137	0.215	6.57	-1.38	0.43	-0.07	QPS
GM Aur	0.114	0.176	6.21	-1.40	0.50	-0.27	B
GM Aur	0.106	0.164	4.23	-1.57	0.74	-0.30	B
GM Aur	0.097	0.149	4.37	-1.56	0.75	-0.38	B
GO Tau	0.271	0.500	>27	-0.62	0.52	0.80	QPD
GO Tau	0.110	0.188	4.74	-1.37	0.59	0.18	QPS
GO Tau	0.153	0.266	2.51	-1.65	0.62	0.36	QPD
GO Tau	0.167	0.293	5.13	-1.34	0.56	0.15	QPS
GQ Lup	0.709	1.572	10.45	-1.36	0.20	0.50	QPD
GQ Lup	0.363	0.677	11.09	-1.34	0.47	0.24	QPS
HBC 347	0.041	0.055	0.48	-1.93	0.36	-0.64	B
HBC 347	0.042	0.057	0.48	-1.93	0.08	-0.55	B
HBC 347	0.035	0.046	0.48	-1.93	0.10	-0.37	B
HBC 347	0.028	0.037	0.48	-1.93	0.12	-0.35	B
HBC 347	0.027	0.036	0.48	-1.93	0.12	-0.37	B
HBC 374	0.029	0.048	1.55	-2.20	0.23	-0.03	QPS
HBC 374	0.030	0.049	1.54	-2.20	0.26	0.01	QPS
HBC 376	0.091	0.137	0.72	-2.06	0.02	0.06	P
HBC 376	0.098	0.149	0.71	-2.06	0.05	0.10	P
HBC 376	0.097	0.148	0.71	-2.06	0.01	0.39	unknown
HBC 376	0.093	0.141	0.71	-2.06	0.04	0.32	unknown
HBC 392	0.078	0.119	3.43	-1.43	0.47	-0.03	QPS
HBC 392	0.099	0.152	3.39	-1.43	0.23	-0.20	QPS
HBC 407	0.022	0.031	3.51	-1.04	0.29	0.27	QPD
HBC 407	0.028	0.039	3.38	-1.06	0.23	-0.08	QPS
HBC 427	0.050	0.077	8.39	-1.50	0.25	0.52	QPD
HBC 427	0.096	0.152	9.72	-1.44	0.07	0.66	unknown
HBC 427	0.042	0.064	9.70	-1.44	0.56	-0.12	QPS
HBC 427	0.040	0.061	4.25	-1.79	0.65	0.14	QPS
HBC 741	0.089	0.122	3.36	-1.74	0.16	-0.29	B
HBC 741	0.065	0.089	3.45	-1.73	0.11	-0.08	P
HBC 741	0.052	0.071	3.47	-1.73	0.18	-0.47	B
HD 106506	0.025	0.030	1.44	-1.30	0.18	0.39	QPD
HD 106506	0.028	0.033	1.43	-1.30	0.20	0.02	QPS
HD 106506	0.025	0.030	1.41	-1.31	0.20	-0.38	B
HD 106506	0.054	0.066	1.42	-1.31	0.03	-0.17	P
HD 106506	0.035	0.042	1.44	-1.30	0.09	-0.03	P
HD 133938	0.011	0.014	1.01	-1.63	0.27	0.01	QPS
HD 133938	0.016	0.020	1.00	-1.64	0.32	0.05	QPS
HD 133938	0.019	0.024	1.01	-1.63	0.20	-0.06	QPS
HD 135127	0.005	0.006	0.51		0.33	0.25	QPS
HD 135127	0.004	0.005	0.53		0.49	0.11	QPS
HD 135127	0.004	0.004	0.53		0.49	-0.02	QPS
HD 141943	0.053		2.24		0.11	0.03	P

Table 10: (Continued)

Object Name	Amp [mag]	Spot coverage	Period [day]	log $N_{\rm R}$	Q	M	Variability
HD 141943	0.028		2.21		0.46	-0.09	QPS
HD 143978	0.026	0.031	1.68	-0.98	0.31	0.10	QPS
HD 147048	0.060	0.078	4.14	-1.16	0.09	0.24	P
HD 171488	0.044		1.37		0.11	0.03	P
HD 171488	0.023		1.33		0.28	-0.27	B
HD 171488	0.034		1.33		0.13	-0.17	P
HD 283572	0.083	0.111	1.53	-1.90	0.02	0.19	P
HD 283572	0.054	0.071	1.53	-1.90	0.06	0.16	P
HD 283572	0.052	0.068	1.54	-1.89	0.03	-0.23	P
HD 283572	0.084	0.112	1.54	-1.89	0.02	0.26	unknown
HD 283572	0.057	0.075	1.54	-1.89	0.04	-0.33	B
HD 285751	0.104	0.145	1.59	-1.49	0.04	0.03	P
HD 285751	0.114	0.161	1.60	-1.49	0.02	0.13	P
HD 285751	0.044	0.060	1.59	-1.49	0.08	0.77	unknown
HD 285751	0.037	0.050	1.60	-1.49	0.34	0.71	QPD
HD 285778	0.071	0.090	2.80	-1.18	0.05	0.01	P
HD 285778	0.027	0.033	2.98	-1.16	0.17	0.35	QPD
HD 285778	0.042	0.053	2.74	-1.19	0.03	0.08	P
HD 285778	0.034	0.043	2.72	-1.20	0.10	0.00	P
HD 285898	0.003	0.004	(0.01)	(-4.22)	(0.34)	-0.05	(QPS)
HD 285898	0.003	0.004	(1.63)	(-1.93)	(0.99)	-0.04	(S)
HD 286179	0.061	0.082	3.16	-1.38	0.17	0.18	QPS
HD 286179	0.030	0.040	3.16	-1.38	0.09	-0.55	B
HD 286179	0.034	0.046	3.14	-1.39	0.11	0.02	P
HD 286179	0.032	0.043	3.06	-1.40	0.14	-0.24	P
HD 29615	0.037		2.38		0.09	-0.10	P
HD 29615	0.024		2.40		0.19	0.03	QPS
HD 35296	0.006		3.64		0.29	0.03	QPS
HD 35296	0.005		3.63		0.29	0.07	QPS
HD 35296	0.007		3.85		0.29	-0.18	QPS
HD 35296	0.007		3.85		0.28	-0.16	QPS
HD 35296	0.008		3.64		0.14	-0.43	B
HD 35296	0.008		3.64		0.14	-0.51	B
HD 35296	0.011		3.61		0.14	0.01	P
HD 35296	0.011		3.60		0.12	0.07	P
HD 6569	0.020	0.026	7.37	-0.62	0.04	0.58	unknown
HH Leo	0.025	0.031	6.19	-0.64	0.15	0.28	QPD
HII 296	0.027	0.035	2.52	-1.16	0.15	-0.30	B
HII 296	0.030	0.038	2.51	-1.16	0.26	-0.29	B
HII 296	0.034	0.044	2.50	-1.16	0.17	-0.16	QPS
HII 296	0.030	0.040	2.64	-1.14	0.23	-0.03	QPS
HII 296	0.025	0.033	2.58	-1.15	0.18	-0.01	QPS
HIP 10272	0.024		6.85		0.28	0.35	QPD
HIP 10272	0.014		3.07		0.31	-0.08	QPS
HIP 10272	0.015		6.88		0.22	0.61	QPD
HIP 10272	0.009		3.42		0.56	-0.61	B
HIP 10272	0.017		6.92		0.08	0.03	P
HIP 10272	0.024		6.85		0.28	0.35	QPD
HIP 10272	0.014		3.07		0.31	-0.08	QPS
HIP 10272	0.015		6.88		0.22	0.61	QPD
HIP 10272	0.009		3.42		0.56	-0.61	B

Table 10: (Continued)

Object Name	Amp [mag]	Spot coverage	Period [day]	log $N_{\rm R}$	Q	M	Variability
HIP 10272	0.017		6.92		0.08	0.03	P
HIP 12545	0.083	0.132	4.79	-1.46	0.02	0.48	unknown
HIP 12545	0.071	0.113	4.76	-1.46	0.04	0.35	unknown
HIP 12545	0.098	0.158	4.89	-1.45	0.06	0.21	P
HIP 12545	0.121	0.196	4.79	-1.46	0.12	0.00	P
HIP 12545	0.140	0.229	4.93	-1.45	0.08	0.17	P
HIP 16853	0.010	0.011	1.28	-1.13	0.58	0.13	QPS
HIP 17695	0.031	0.057	3.81	-1.61	0.13	0.18	P
HIP 17695	0.046	0.085	3.89	-1.60	0.05	0.31	unknown
HIP 17695	0.047	0.087	3.89	-1.60	0.03	0.38	unknown
HK Tau	0.290	0.569	3.29	-1.68	0.36	0.46	QPD
HK Tau	0.291	0.572	3.29	-1.68	0.51	0.30	QPD
HK Tau	0.219	0.416	3.27	-1.69	0.39	0.50	QPD
HK Tau	0.226	0.431	3.22	-1.69	0.46	0.43	QPD
HL Tau	0.102	0.170	3.86	-1.78	0.54	-0.20	QPS
HL Tau	0.093	0.154	3.21	-1.86	0.60	-0.07	QPS
HN Tau	0.636	1.300	12.78	-0.61	0.38	-0.32	B
HN Tau			12.78	-0.61	0.38		unknown
HN Tau	0.333	0.585	2.42	-1.34	0.75	-0.37	B
HN Tau			7.29	-0.86	0.51		unknown
HV Tau	0.070	0.120	4.52	-1.74	0.07	0.31	unknown
HV Tau			4.52	-1.74	0.07		unknown
HV Tau	0.070	0.120	4.55	-1.74	0.14	0.25	unknown
HV Tau			4.55	-1.74	0.17		unknown
IP Tau	0.291	0.573	5.39	-1.64	0.32	0.08	QPS
IP Tau	0.316	0.630	5.61	-1.63	0.47	-0.16	QPS
IP Tau	0.288	0.567	5.54	-1.63	0.27	0.05	QPS
IP Tau	0.243	0.468	6.19	-1.58	0.42	-0.12	QPS
IQ Tau	1.014	3.096	6.53	-1.55	0.21	0.16	QPS
IQ Tau	1.069	3.360	6.53	-1.55	0.18	0.06	QPS
IQ Tau	1.192	4.005	6.50	-1.55	0.12	0.29	unknown
IQ Tau	1.192	4.002	6.50	-1.55	0.13	0.29	unknown
IQ Tau	1.006	3.058	6.82	-1.53	0.33	0.23	QPS
IQ Tau	0.599	1.477	6.91	-1.52	0.41	0.30	QPD
IT Tau	0.164	0.294	2.75	-1.98	0.22	0.14	QPS
IT Tau	1.311	4.237	2.75	-1.98	0.24		unknown
IT Tau	0.166	0.299	2.76	-1.98	0.28	0.03	QPS
IT Tau	1.294	4.142	2.76	-1.98	0.29		unknown
IT Tau	0.957	2.555	2.74	-1.98	0.11	0.46	unknown
IT Tau	1.043	2.915	2.77	-1.98	0.15	0.17	P
L 1551-51	0.210	0.354	2.41	-2.02	0.03	0.25	unknown
L 1551-51	0.190	0.316	2.43	-2.02	0.00	0.31	unknown
L 1551-51	0.276	0.480	2.41	-2.02	0.02	0.07	P
L 1551-51	0.279	0.486	2.45	-2.01	0.02	0.18	P
LO Peg	0.042		0.42		0.36	-0.21	QPS
LQ Hya	0.165		1.60		0.32	-0.16	QPS
LQ Hya	0.068		1.59		0.14	-0.50	B
LQ Hya	0.119		1.59		0.07	0.68	unknown
LQ Hya	0.115		1.61		0.04	0.62	unknown
LkCa 01	0.011	0.019	2.51	-1.97	0.43	0.13	QPS
LkCa 01	0.014	0.024	2.49	-1.98	0.27	-0.11	QPS

Table 10: (Continued)

Object Name	Amp [mag]	Spot coverage	Period [day]	log $N_{\rm R}$	Q	M	Variability
LkCa 03	0.037	0.054	4.27	-1.79	0.58	0.00	QPS
LkCa 03	0.043	0.064	7.37	-1.55	0.34	-0.05	QPS
LkCa 03	0.039	0.057	4.10	-1.81	0.38	0.12	QPS
LkCa 03	0.035	0.052	3.96	-1.82	0.38	0.11	QPS
LkCa 04	0.275	0.588	3.33	-1.83	0.08	-0.15	P
LkCa 04	0.282	0.603	3.33	-1.83	0.04	-0.17	P
LkCa 04	0.291	0.626	3.41	-1.82	0.03	-0.18	P
LkCa 04	0.292	0.627	3.41	-1.82	0.03	-0.18	P
LkCa 05	0.071	0.130	1.41	-2.22	0.07	0.11	P
LkCa 05	0.071	0.130	1.41	-2.22	0.03	0.14	P
LkCa 05	0.074	0.135	1.41	-2.22	0.05	0.23	P
LkCa 05	0.075	0.138	1.41	-2.22	0.05	0.17	P
LkCa 07	0.279	0.509	5.65	-1.65	0.01	0.18	P
LkCa 07	0.253	0.457	5.65	-1.65	0.07	0.19	P
LkCa 07	0.279	0.510	5.62	-1.66	0.02	0.15	P
LkCa 07	0.281	0.513	5.62	-1.66	0.01	0.14	P
LkCa 08	0.291	0.573	5.39	-1.64	0.32	0.08	QPS
LkCa 08	0.316	0.630	5.61	-1.63	0.47	-0.16	QPS
LkCa 08	0.288	0.567	5.54	-1.63	0.27	0.05	QPS
LkCa 08	0.243	0.468	6.19	-1.58	0.42	-0.12	QPS
LkCa 14	0.025	0.039	1.67	-2.20	0.29	-0.28	B
LkCa 14	0.018	0.027	1.66	-2.21	0.47	-0.46	B
LkCa 14	0.032	0.050	3.36	-1.90	0.23	-0.59	B
LkCa 14	0.032	0.049	3.40	-1.89	0.25	-0.08	QPS
LkCa 15	0.415	0.770	5.85	-1.65	0.67	0.66	QPD
LkCa 15	0.160	0.263	6.18	-1.63	0.71	0.89	QPD
LkCa 15	0.280	0.486	2.88	-1.96	0.70	0.05	QPS
LkCa 15	0.431	0.806	5.62	-1.67	0.56	0.32	QPD
LkCa 19	0.009	0.012	2.23	-1.76	0.72	0.04	QPS
LkCa 19	0.014	0.019	2.22	-1.76	0.31	0.26	QPD
LkCa 19	0.044	0.060	2.25	-1.75	0.02	-0.01	P
LkCa 19	0.019	0.025	2.21	-1.76	0.25	0.10	QPS
LkCa 19	0.019	0.025	2.22	-1.76	0.18	0.21	QPS
Mel25 151	0.009	0.011	10.08	-0.67	0.27	-0.42	B
Mel25 179	0.007	0.009	10.08	-0.66	0.37	-0.38	B
Mel25 179	0.004	0.005	4.85	-0.97	0.68	0.07	QPS
Mel25 179	0.006	0.008	11.60	-0.60	0.25	-0.25	B
Mel25 179	0.008	0.011	5.63	-0.91	0.58	-0.47	B
Mel25 179	0.005	0.006	5.15	-0.95	0.41	0.18	QPS
Mel25 179	0.003	0.005	5.15	-0.95	0.54	-0.05	QPS
Mel25 43	0.015	0.019	9.75	-0.65	0.07	-0.02	P
Mel25 43	0.005	0.007	10.53	-0.61	0.34	-0.39	B
Mel25 5	0.005	0.006	5.96	-0.81	0.65	-0.07	QPS
Mel25 5	0.004	0.006	11.17	-0.54	0.51	0.20	QPS
Mel25 5	0.005	0.006	5.94	-0.81	0.67	0.04	QPS
Mel25 5	0.005	0.006	10.59	-0.56	0.19	0.08	QPS
Mel25 5	0.003	0.004	2.79	-1.14	0.99	-0.10	S
Mel25 5	0.002	0.003	4.76	-0.91	0.83	0.05	QPS
Mel25 5	0.004	0.005	9.64	-0.60	0.47	-0.08	QPS
Mel25 5	0.003	0.004	10.51	-0.57	0.41	0.11	QPS
PAR 102	0.044	0.053	7.71		0.53	0.16	QPS

Table 10: (Continued)

Object Name	Amp [mag]	Spot coverage	Period [day]	log $N_{\rm R}$	Q	M	Variability
PAR 1391	0.003	0.003	1.88		0.99	-0.05	S
PAR 1646	0.003	0.003	0.58		0.92	-0.01	S
PW And	0.097	0.134	1.76	-1.27	0.02	0.32	unknown
PW And	0.070	0.095	1.75	-1.28	0.07	0.11	P
PW And	0.070	0.095	1.75	-1.28	0.07	0.10	P
PX Vul	0.015	0.022	5.82	-1.66	0.72	0.08	QPS
PX Vul	0.152	0.231	7.03	-1.57	0.33	0.78	QPD
PX Vul	0.675	1.328	>27	-0.99	0.18	1.03	QPD
RECX 04	0.059	0.097	7.09	-1.50	0.30	-0.32	B
RECX 04	0.041	0.067	6.92	-1.51	0.35	-0.16	QPS
RECX 04	0.041	0.066	6.90	-1.51	0.62	-0.46	B
RECX 06	0.054	0.108	1.83	-2.09	0.09	-0.24	P
RECX 06	0.064	0.130	1.83	-2.09	0.06	-0.28	B
RECX 06	0.063	0.128	1.84	-2.09	0.10	-0.20	P
RECX 06	0.034	0.068	1.85	-2.09	0.15	-0.57	B
RECX 06	0.033	0.065	1.84	-2.09	0.36	-0.28	B
RECX 06	0.032	0.063	1.83	-2.09	0.70	-0.12	QPS
RECX 06	0.054	0.109	1.84	-2.09	0.71	-0.24	QPS
RECX 06	0.052	0.106	1.84	-2.09	0.66	-0.13	QPS
RECX 06	0.052	0.104	1.83	-2.09	0.18	0.15	QPS
RECX 06	0.049	0.098	1.83	-2.09	0.09	0.21	P
RECX 06	0.053	0.108	1.84	-2.09	0.25	0.04	QPS
RECX 06	0.052	0.105	1.84	-2.09	0.13	0.07	P
RECX 09	0.059	0.099	1.95		0.55	0.33	QPD
RECX 09	0.101	0.174	1.94		0.65	0.34	QPD
RECX 09	0.085	0.146	1.94		0.71	0.20	QPS
RECX 10	0.010	0.015	5.58	-1.48	0.58	0.15	QPS
RECX 10	0.016	0.026	17.09	-1.00	0.22	-1.04	B
RECX 10	0.009	0.014	9.31	-1.26	0.77	0.24	QPS
RECX 10	0.007	0.011	1.21	-2.15	0.93	-0.13	S
RECX 10	0.009	0.014	8.74	-1.29	0.66	-0.25	QPS
RECX 10	0.023	0.036	11.48	-1.17	0.64	-0.04	QPS
RECX 10	0.008	0.012	10.36	-1.21	0.93	0.27	APD
RECX 10	0.006	0.010	6.59	-1.41	0.91	-0.10	S
RECX 10	0.017	0.027	8.34	-1.31	0.61	0.34	QPD
RECX 11	0.329	0.558	8.44	-1.14	0.56	0.88	QPD
RECX 11	0.306	0.512	2.49	-1.67	0.77	0.75	QPD
RECX 11	0.372	0.645	5.03	-1.37	0.56	0.51	QPD
RECX 11	0.304	0.509	4.64	-1.40	0.64	0.62	QPD
RECX 11	0.304	0.509	4.64	-1.40	0.64	0.62	QPD
RECX 11	0.251	0.409	5.13	-1.36	0.56	0.58	QPD
RECX 11	0.252	0.412	5.13	-1.36	0.56	0.58	QPD
RECX 11	0.326	0.553	4.66	-1.40	0.66	0.24	QPS
RECX 11	0.399	0.700	4.66	-1.40	0.62	0.55	QPD
RW Aur	0.915	1.835	7.38		0.33	-0.34	B
RW Aur	0.896	1.781	7.37		0.35	-0.38	B
RW Aur	0.574	0.967	7.35		0.47	-0.01	QPS
RW Aur	0.629	1.088	7.35		0.50	-0.22	QPS
RX J1204.6-7731	0.058	0.114	4.85	-1.67	0.07	0.28	unknown
RX J1204.6-7731	0.063	0.124	4.82	-1.67	0.02	0.11	P
RX J1204.6-7731	0.023	0.044	4.78	-1.68	0.14	-0.27	B

Table 10: (Continued)

Object Name	Amp [mag]	Spot coverage	Period [day]	log $N_{\rm R}$	Q	M	Variability
RX J1204.6-7731	0.026	0.049	4.79	-1.68	0.16	-0.06	QPS
RX J1204.6-7731	0.029	0.055	4.78	-1.68	0.32	-0.45	B
RX J1204.6-7731	0.032	0.062	4.72	-1.68	0.47	-0.31	B
RY Lup	0.756	1.483	3.62	-1.39	0.54	0.20	QPS
RY Tau	0.116	0.176	3.42	-1.87	0.75	0.29	QPD
RY Tau	0.140	0.216	4.96	-1.71	0.46	-0.07	QPS
RY Tau	0.354	0.603	7.34	-1.54	0.43	0.24	QPS
SU Aur	0.172	0.273	8.97	-1.44	0.62	0.20	QPS
SU Aur	0.034	0.050	2.68	-1.96	0.30	0.51	QPD
SU Aur	0.090	0.138	>27	-0.96	0.40	0.84	QPD
StKM 2-809	0.017	0.030	0.73	-2.55	0.46	0.24	QPS
StKM 2-809	0.014	0.026	0.73	-2.55	0.66	-0.24	QPS
StKM 2-809	0.012	0.022	0.73	-2.55	0.55	-0.32	B
StKM 2-809	0.016	0.028	0.73	-2.55	0.66	-0.28	B
StKM 2-809	0.014	0.025	0.73	-2.55	0.56	-0.39	B
T Tau	0.054	0.082	>27	-0.96	0.64	-0.30	B
T Tau	0.050	0.076	2.91	-1.92	0.71	0.53	QPD
TIC 29900813	0.002	0.002	3.41	-0.94	0.67	0.19	QPS
TIC 29900813	0.004	0.005	7.39	-0.60	0.35	-0.08	QPS
TIC 29900813	0.002	0.003	7.29	-0.61	0.50	-0.06	QPS
TIC 357019659	1.039	2.590	3.18	-1.27	0.77	-0.33	B
TIC 357019659	0.942	2.231	7.88	-0.87	0.43	-0.20	QPS
TIC 357019659	0.123	0.194	>27	-0.34	0.57	0.53	QPD
TWA 01	0.166	0.270	4.58	-1.40	0.68	-0.32	B
TWA 01	0.167	0.272	8.34	-1.14	0.66	-0.44	B
TWA 01	0.168	0.275	8.34	-1.14	0.70	-0.44	B
TWA 06	0.084	0.131	0.54	-2.20	0.24	-0.39	B
TWA 06	0.125	0.198	0.54	-2.20	0.07	-0.27	B
TWA 06	0.126	0.200	0.54	-2.20	0.08	-0.32	B
TWA 07	0.014	0.022	4.94	-1.32	0.53	-0.14	QPS
TWA 07	0.014	0.022	4.89	-1.32	0.50	-0.24	QPS
TWA 10	0.132	0.232	8.37	-1.20	0.04	-0.18	P
TWA 10	0.033	0.055	5.36	-1.40	0.47	-0.03	QPS
TWA 10	0.150	0.267	8.42	-1.20	0.01	-0.32	B
TWA 14	0.156	0.285	0.63	-2.59	0.03	0.01	P
TWA 14	0.151	0.276	0.63	-2.59	0.03	0.06	P
TWA 14	0.151	0.275	0.63	-2.59	0.08	0.00	P
TWA 14	0.146	0.265	0.63	-2.59	0.02	0.21	P
TWA 14	0.147	0.267	0.63	-2.59	0.01	0.23	P
TWA 22	0.020		0.73		0.24	0.06	QPS
TWA 22	0.022		0.73		0.17	0.08	QPS
TWA 22	0.026		0.73		0.40	-0.03	QPS
TWA 22	0.027		0.73		0.30	-0.03	QPS
TWA 22	0.032		0.73		0.29	0.00	QPS
TWA 22	0.030		0.73		0.14	0.02	P
TWA 22	0.032		0.73		0.27	-0.03	QPS
TWA 22	0.029		0.73		0.16	-0.03	QPS
TWA 23	0.024	0.049	5.61	-1.60	0.12	0.32	unknown
TWA 23	0.028	0.057	5.56	-1.61	0.18	0.42	QPD
TWA 23	0.016	0.031	5.43	-1.62	0.58	0.16	QPS
TWA 25	0.207	0.366	4.99	-1.68	0.02	0.07	P

Table 10: (Continued)

Object Name	Amp [mag]	Spot coverage	Period [day]	log $N_{\rm R}$	Q	M	Variability
TWA 25	0.104	0.176	4.97	-1.68	0.03	0.08	P
TWA 25	0.056	0.092	5.18	-1.67	0.23	-0.46	B
TWA 3A	0.039	0.065	4.25	-1.35	0.55	-0.07	QPS
TWA 3A	0.026	0.043	4.11	-1.36	0.53	-0.14	QPS
TWA 3A	0.036	0.059	4.70	-1.30	0.79	0.23	QPS
TWA 5A	0.120	0.209	0.73	-2.55	0.38	0.07	QPS
TWA 5A	0.124	0.216	0.73	-2.55	0.33	0.22	QPS
TWA 5A	0.131	0.228	0.73	-2.55	0.13	0.26	unknown
TWA 5A	0.131	0.228	0.73	-2.55	0.13	0.27	unknown
TWA 5B	0.120		0.73		0.38	0.07	QPS
TWA 5B	0.124		0.73		0.33	0.22	QPS
TWA 5B	0.131		0.73		0.13	0.26	unknown
TWA 5B	0.131		0.73		0.13	0.27	unknown
TWA 8A	0.045	0.081	4.58	-1.74	0.10	0.11	P
TWA 8A	0.079	0.143	4.70	-1.73	0.22	-0.09	QPS
TWA 8A	0.051	0.092	4.62	-1.74	0.09	-0.02	P
TWA 8B	0.146		4.57		0.17	0.05	QPS
TWA 8B	0.300		4.89		0.68	-0.11	QPS
TWA 9A	0.116	0.185	4.99	-1.47	0.02	-0.41	B
TWA 9A	0.043	0.066	4.97	-1.47	0.06	0.79	unknown
TWA 9A	0.040	0.061	5.12	-1.46	0.10	0.26	unknown
TWA 9B	0.586	1.287	4.99	-1.29	0.02	-0.41	B
TWA 9B	0.230	0.424	4.97	-1.29	0.06	0.76	unknown
TWA 9B	0.212	0.387	4.93	-1.29	0.12	0.26	unknown
TYC 0486-4943-1	0.032	0.044	3.76	-1.04	0.09	0.55	unknown
TYC 1987-509-1	0.007	0.008	4.76	-0.81	0.53	-0.08	QPS
TYC 1987-509-1	0.007	0.009	4.37	-0.85	0.34	0.20	QPS
TYC 5164-567-1	0.050	0.064	4.88	-0.79	0.23	-0.24	QPS
UX Tau	0.793	1.684	14.31	-0.95	0.69	-0.30	B
UX Tau			3.86	-1.52	0.78		unknown
UX Tau	1.156	2.970	3.82	-1.53	0.35	0.31	QPD
UX Tau			3.70	-1.54			unknown
UY Aur	0.110	0.197	3.08	-1.87	0.74	-0.36	B
UY Aur	0.074	0.131	3.52	-1.81	0.76	-0.17	QPS
UY Aur	0.066	0.116	3.06	-1.87	0.34	0.12	QPS
UY Aur	0.071	0.125	2.98	-1.89	0.45	0.15	QPS
UY Aur	0.066	0.116	2.91	-1.90	0.40	0.21	QPS
V1023 Tau	0.029	0.048	1.55	-2.20	0.23	-0.03	QPS
V1023 Tau	0.030	0.049	1.54	-2.20	0.26	0.01	QPS
V1067 Tau	0.188	0.261	0.47		0.38	0.11	QPS
V1110 Tau	0.031	0.041	1.49	-1.65	0.09	-0.48	B
V1110 Tau	0.038	0.052	1.49	-1.64	0.05	-0.05	P
V1204 Tau	0.017	0.023	3.01	-1.48	0.32	0.02	QPS
V1204 Tau	0.025	0.033	3.06	-1.47	0.14	-0.51	B
V1297 Tau	0.048	0.063	1.94	-1.31	0.05	0.14	P
V1297 Tau	0.038	0.050	1.96	-1.31	0.10	0.02	P
V1297 Tau	0.039	0.051	1.96	-1.31	0.05	0.15	P
V1298 Tau	0.021	0.028	2.94	-1.35	0.30	-0.14	QPS
V1298 Tau	0.022	0.029	2.94	-1.35	0.18	-0.08	QPS
V1298 Tau	0.026	0.034	2.92	-1.35	0.36	0.07	QPS
V1298 Tau	0.024	0.032	2.92	-1.35	0.30	0.13	QPS

Table 10: (Continued)

Object Name	Amp [mag]	Spot coverage	Period [day]	log $N_{\rm R}$	Q	M	Variability
V1299 Tau	0.020	0.024	0.82		0.43	0.20	QPS
V1299 Tau	0.018	0.021	0.81		0.32	0.04	QPS
V1304 Tau	0.110	0.206	0.30	-2.90	0.47	0.43	QPD
V1304 Tau	0.083	0.154	0.30	-2.89	0.54	0.36	QPD
V1320 Tau	0.074	0.119	5.87	-1.52	0.14	-0.13	P
V1320 Tau	0.068	0.109	5.88	-1.52	0.03	-0.11	P
V1320 Tau	0.107	0.175	5.83	-1.53	0.06	0.10	P
V1320 Tau	0.120	0.197	5.89	-1.52	0.01	0.20	P
V1321 Tau	0.044	0.071	6.23	-1.53	0.07	0.28	unknown
V1321 Tau	0.041	0.066	6.17	-1.53	0.17	-0.09	QPS
V1346 Tau	0.097	0.140	4.59	-1.12	0.03	0.22	P
V1346 Tau	0.088	0.127	4.74	-1.10	0.04	0.00	P
V1346 Tau	0.029	0.040	4.74	-1.10	0.30	-0.03	QPS
V1348 Tau	0.021	0.031	4.40	-1.35	0.21	-0.22	QPS
V1348 Tau	0.018	0.025	4.40	-1.35	0.26	-0.16	QPS
V1354 Tau	0.073	0.098	1.45	-1.54	0.03	-0.33	B
V1354 Tau	0.091	0.124	1.47	-1.53	0.03	-0.02	P
V1354 Tau	0.026	0.035	1.46	-1.54	0.16	-0.43	B
V1368 Tau	0.063	0.079	0.95	-1.60	0.08	0.21	P
V1368 Tau	0.082	0.102	0.94	-1.60	0.04	-0.06	P
V1368 Tau	0.071	0.088	0.95	-1.60	0.14	0.13	P
V1840 Ori	0.107	0.156	5.18	-1.22	0.14	0.07	P
V1840 Ori	0.108	0.157	5.15	-1.22	0.15	-0.01	QPS
V4046 SgrA	0.034	0.052	2.38	-2.04	0.53	0.10	QPS
V4046 SgrA	0.035	0.053	2.41	-2.04	0.34	-0.17	QPS
V4046 SgrB	0.034	0.052	2.38	-2.04	0.53	0.10	QPS
V4046 SgrB	0.035	0.053	2.41	-2.04	0.34	-0.17	QPS
V410 Tau	0.162	0.256	1.88	-2.16	0.08	0.30	unknown
V410 Tau	0.174	0.276	1.88	-2.16	0.05	0.66	unknown
V410 Tau	0.180	0.285	1.87	-2.16	0.03	0.71	unknown
V410 Tau	0.088	0.134	1.87	-2.16	0.02	0.32	unknown
V410 Tau	0.087	0.132	1.87	-2.16	0.02	0.12	P
V439 And	0.012	0.014	6.38	-0.52	0.20	0.11	QPS
V439 And	0.011	0.014	6.16	-0.54	0.10	-0.35	B
V439 And	0.011	0.014	6.16	-0.54	0.11	-0.27	B
V447 Lac	0.008		4.94		0.60	-0.08	QPS
V447 Lac	0.017		8.87		0.03	-0.06	P
V447 Lac	0.026		8.63		0.07	-0.29	B
V447 Lac	0.026		8.62		0.06	-0.28	B
V447 Lac	0.021		8.81		0.07	-0.37	B
V447 Lac	0.023		8.81		0.07	-0.09	P
V577 Per	0.029	0.035	3.16	-0.83	0.16	0.12	QPS
V577 Per	0.020	0.024	3.29	-0.81	0.28	0.01	QPS
V577 Per	0.025	0.030	3.29	-0.81	0.39	0.28	QPD
V773 Tau	0.089	0.144	2.61	-1.96	0.69	0.02	QPS
V773 Tau	0.129	0.213	2.60	-1.96	0.43	0.30	QPD
V819 Tau	0.059	0.100	5.53	-1.65	0.10	-0.57	B
V819 Tau	0.235	0.431	5.65	-1.64	0.04	-0.01	P
V819 Tau	0.238	0.436	5.63	-1.64	0.02	-0.09	P
V819 Tau	0.264	0.491	5.55	-1.65	0.00	0.18	P
V819 Tau	0.264	0.490	5.61	-1.64	0.02	0.17	P

Table 10: (Continued)

Object Name	Amp [mag]	Spot coverage	Period [day]	log $N_{\rm R}$	Q	M	Variability
V826 Tau	0.046	0.072	3.86	-1.82	0.15	-0.01	P
V826 Tau	0.047	0.073	3.86	-1.82	0.08	0.07	P
V826 Tau	0.045	0.070	3.81	-1.83	0.15	0.11	QPS
V826 Tau	0.045	0.070	3.81	-1.83	0.15	0.16	P
V827 Tau	0.050	0.079	3.74	-1.86	0.22	-0.25	QPS
V827 Tau	0.051	0.080	3.74	-1.86	0.11	-0.42	B
V827 Tau	0.056	0.089	3.82	-1.85	0.15	-0.21	P
V827 Tau	0.057	0.090	3.82	-1.85	0.08	-0.20	P
V830 Tau	0.172	0.298	2.76	-1.95	0.03	-0.11	P
V830 Tau	0.174	0.303	2.76	-1.95	0.02	-0.09	P
V830 Tau	0.158	0.273	2.76	-1.95	0.05	-0.06	P
V830 Tau	0.160	0.277	2.76	-1.95	0.02	-0.06	P
V830 Tau	0.079	0.131	2.74	-1.95	0.02	-0.65	B
V830 Tau	0.086	0.143	2.71	-1.96	0.07	-0.69	B
V836 Tau	0.237	0.493	6.57	-1.53	0.17	-0.10	QPS
V836 Tau	0.244	0.511	6.92	-1.51	0.14	0.03	P
V898 Per	0.028	0.033	1.85	-1.02	0.26	0.49	QPD
V898 Per	0.032	0.038	1.95	-1.00	0.35	0.11	QPS
V927 Tau	0.019	0.049	4.38	-1.70	0.64	-0.08	QPS
V927 Tau	0.015	0.040	0.61	-2.56	0.72	0.07	QPS
V928 Tau	0.027	0.047	2.24		0.39	0.03	QPS
V928 Tau	0.026	0.044	2.24		0.34	0.15	QPS
V999 Tau	0.079	0.113	2.64		0.59	-0.23	QPS
V999 Tau	0.073	0.105	2.65		0.70	-0.02	QPS
XZ Tau	0.023	0.038	3.24	-1.84	0.61	-0.08	QPS
XZ Tau	0.031	0.052	3.21	-1.85	0.37	-0.32	B
YZ CMi	0.037	0.075	2.75	-1.95	0.11	-0.20	P
YZ CMi	0.014	0.029	2.80	-1.94	0.69	0.43	QPD
YZ CMi	0.014	0.029	2.80	-1.94	0.72	0.52	QPD
ZZ Tau	0.027	0.042	4.09	-1.42	0.39	-0.15	QPS
ZZ Tau	0.038	0.061	4.22	-1.41	0.22	-0.38	B

3.3.3 Flares

We also detected 2750 flares in the light curves of 150 PMS stars. Among them, 344 flares were detected in the light curves of 37 solar-mass PMS stars ($0.8 - 1.2\ \mathrm{M}_{\odot}$). The properties of each flare are listed in table 11. Their average duration time is $840\ \mathrm{s}$. For the case of the first flare shown in figure 23, the relative flux and the duration are 2.0% and $2.4\ \mathrm{h}$, respectively. As we will discuss in section 4.4, the total bolometric energy of the flare is estimated to be $1.81 \times 10^{31}\ \mathrm{erg} - 7.72 \times 10^{35}\ \mathrm{erg}$. It is comparable to that of superflares detected in Maehara et al. (2012), in which the energy of the superflare is calculated to be 100 times larger than those of solar flares, i.e. 10^{33} to $10^{36}\ \mathrm{erg}$. The occurrence frequency of flares is estimated from the number of observed flares, the number of observed stars, and the length of the observation period. In this study, 344 flares were detected from the 37 solar-mass PMS stars in the observational period, so that the occurrence frequency of flares is calculated to be 0.91×10^{-3} flares per year per star. Maehara et al. (2012) detected 14 superflares from data collected from approximately $14,000$ slowly rotating G-type main-sequence stars over $120\ \mathrm{d}$. The occurrence frequency of superflares was 2.9×10^{-3} flares per year per star. Therefore, superflares are as likely to occur frequently on PMS stars as on main-sequence stars.

Table 11: List of detected flares

Object name	$N_{\rm flare}$	Flare rate [$\rm d^{-1}$]	Flare Energy [erg]		
			minimum	median	maximum
2MASS J04035084+2610531	6	0.276	5.27×10^{31}	1.46×10^{32}	7.01×10^{33}
2MASS J04182147+1658470	5	0.113	8.46×10^{31}	4.33×10^{32}	4.34×10^{33}
AA Tau	1	0.045	2.97×10^{33}	2.97×10^{33}	2.97×10^{33}
AB Dor	599	0.877	3.57×10^{30}	3.31×10^{32}	1.24×10^{35}
AD Leo	96	1.401	4.35×10^{29}	1.07×10^{31}	1.05×10^{33}
AU Mic	49	1.023	4.67×10^{28}	2.61×10^{31}	4.07×10^{32}
BD-07 2388	16	0.235	5.32×10^{31}	3.28×10^{32}	2.15×10^{33}
BD-16351	4	0.100	7.89×10^{31}	2.06×10^{32}	5.04×10^{33}
BP Tau	11	0.166	8.88×10^{32}	1.71×10^{33}	1.21×10^{35}
CPD-43 7188	12	0.268	6.16×10^{32}	4.02×10^{33}	3.86×10^{34}
CQ Tau	2	0.091	4.61×10^{35}	3.56×10^{36}	6.66×10^{36}
CW Tau	7	0.155	2.35×10^{32}	4.41×10^{33}	2.25×10^{35}
CY Tau	3	0.067	4.82×10^{31}	8.53×10^{32}	2.24×10^{33}
CZ Tau	3	0.138			
Cl Melotte 111 AV 1826	1	0.053			
Cl Melotte 111 AV 2177	3	0.073			
Cl Melotte 22 PELS 031	4	0.184			
DD Tau	6	0.089	5.96×10^{31}	3.22×10^{32}	2.96×10^{34}
DE Tau	9	0.199	4.77×10^{31}	2.45×10^{32}	1.28×10^{34}
DF Tau	6	0.137	4.68×10^{32}	5.34×10^{33}	5.44×10^{34}
DH Tau	8	0.183	1.17×10^{32}	8.63×10^{32}	2.84×10^{34}
DI Tau	6	0.138	9.10×10^{31}	2.50×10^{33}	1.98×10^{34}
DK Tau	2	0.046	6.39×10^{32}	2.08×10^{35}	4.16×10^{35}
DL Tau	27	0.622	2.01×10^{32}	1.54×10^{33}	3.99×10^{34}
DN Tau	7	0.317	8.34×10^{31}	4.12×10^{32}	8.20×10^{33}
DO Tau	7	0.161	9.42×10^{32}	1.14×10^{34}	1.55×10^{35}
DQ Tau	7	0.159	3.34×10^{32}	1.85×10^{34}	1.68×10^{35}
DR Tau	15	0.341	1.52×10^{32}	9.36×10^{33}	1.84×10^{35}
DS Tau	18	0.266	2.32×10^{32}	3.17×10^{33}	8.30×10^{34}
DX Leo	5	0.111	1.81×10^{31}	4.47×10^{31}	1.10×10^{32}
EK Dra	66	0.326	8.57×10^{31}	4.84×10^{32}	9.21×10^{33}
EP Eri	2	0.046	7.93×10^{32}	1.07×10^{33}	1.34×10^{33}
EV Lac	159	2.217	2.26×10^{29}	1.30×10^{30}	5.02×10^{31}
FN Tau	3	0.044	6.18×10^{31}	7.16×10^{31}	9.40×10^{33}
FP Tau	1	0.045	7.65×10^{32}	7.65×10^{32}	7.65×10^{32}
FQ Tau	3	0.134	1.34×10^{32}	3.19×10^{32}	6.98×10^{32}
FX Tau	1	0.047			
GG Tau	2	0.046	1.03×10^{32}	6.30×10^{32}	1.16×10^{33}
GI Tau	3	0.136	8.62×10^{31}	1.17×10^{32}	3.28×10^{33}
GJ 799A	48	2.059	2.66×10^{30}	9.51×10^{30}	1.29×10^{33}
GK Tau	2	0.046	2.58×10^{32}	3.39×10^{32}	4.20×10^{32}
GM Aur	5	0.075	3.46×10^{32}	7.08×10^{33}	4.41×10^{34}

Table 11: (Continued)

Object name	$N_{\rm flare}$	Flare rate [$\rm d^{-1}$]	Flare Energy [erg]		
			minimum	median	maximum
GQ Lup	11	0.247	1.55×10^{32}	8.66×10^{33}	1.20×10^{35}
Gl 799A	48	2.059	2.66×10^{30}	9.51×10^{30}	1.29×10^{33}
HBC 347	7	0.114	1.39×10^{32}	2.20×10^{32}	4.01×10^{33}
HBC 374	5	0.113	1.48×10^{32}	6.65×10^{32}	3.67×10^{33}
HBC 376	11	0.249	9.51×10^{31}	3.46×10^{32}	5.08×10^{33}
HBC 392	3	0.068	8.96×10^{31}	1.04×10^{32}	1.61×10^{32}
HBC 407	1	0.045	2.21×10^{32}	2.21×10^{32}	2.21×10^{32}
HBC 427	4	0.090	2.06×10^{33}	6.81×10^{33}	2.33×10^{34}
HBC 741	1	0.046	8.60×10^{32}	8.60×10^{32}	8.60×10^{32}
HD 106506	11	0.107	9.80×10^{32}	7.71×10^{33}	6.99×10^{34}
HD 133938	14	0.203	4.95×10^{32}	3.20×10^{33}	2.74×10^{34}
HD 135127	1	0.043	9.98×10^{32}	9.98×10^{32}	9.98×10^{32}
HD 141943	5	0.109	7.76×10^{32}	3.21×10^{33}	3.26×10^{34}
HD 147048	2	0.100	3.73×10^{32}	2.62×10^{33}	4.87×10^{33}
HD 171488	20	0.277	8.84×10^{31}	4.48×10^{32}	1.95×10^{34}
HD 283572	10	0.148	3.67×10^{32}	6.79×10^{32}	9.20×10^{33}
HD 285751	6	0.136	7.14×10^{31}	3.46×10^{32}	4.18×10^{33}
HD 285778	9	0.205	5.15×10^{32}	3.85×10^{33}	1.08×10^{34}
HD 286179	6	0.088	1.87×10^{32}	8.02×10^{32}	3.72×10^{33}
HD 29615	28	0.580	1.85×10^{32}	7.45×10^{32}	1.69×10^{34}
HD 35296	5	0.112	9.06×10^{31}	1.80×10^{32}	4.96×10^{32}
HD 6569	3	0.168	5.57×10^{31}	1.84×10^{32}	1.21×10^{33}
HH Leo	4	0.182	2.99×10^{32}	1.69×10^{33}	3.13×10^{33}
HII 296	3	0.076	1.22×10^{32}	9.45×10^{32}	2.02×10^{33}
HIP 10272	3	0.064	6.18×10^{31}	2.30×10^{32}	5.24×10^{32}
HIP 12545	22	0.350	1.77×10^{31}	8.27×10^{31}	2.21×10^{34}
HIP 17695	64	1.374	1.25×10^{30}	7.87×10^{30}	2.39×10^{32}
HK Tau	2	0.091	1.84×10^{31}	4.95×10^{31}	8.07×10^{31}
HL Tau	3	0.068	7.02×10^{33}	1.20×10^{34}	3.94×10^{35}
HN Tau	8	0.123	6.37×10^{32}	3.71×10^{34}	1.49×10^{36}
HV Tau	6	0.091	9.63×10^{31}	6.02×10^{33}	2.39×10^{35}
IP Tau	8	0.182	9.36×10^{31}	1.75×10^{32}	2.59×10^{33}
IQ Tau	2	0.093	2.32×10^{32}	5.80×10^{32}	9.28×10^{32}
IT Tau	5	0.077	3.30×10^{32}	8.09×10^{32}	1.70×10^{36}
L 1551-51	3	0.069	1.28×10^{33}	1.44×10^{33}	2.51×10^{33}
LO Peg	18	0.686	1.47×10^{31}	2.87×10^{31}	2.59×10^{33}
LQ Hya	37	0.621	1.47×10^{31}	7.33×10^{31}	4.90×10^{33}
LkCa 03	4	0.091	2.90×10^{32}	1.49×10^{33}	4.09×10^{33}
LkCa 04	3	0.068	4.30×10^{32}	7.34×10^{32}	1.02×10^{33}
LkCa 05	4	0.184	5.19×10^{31}	1.40×10^{32}	1.29×10^{33}
LkCa 07	4	0.091	9.42×10^{31}	1.75×10^{33}	9.22×10^{33}
LkCa 08	8	0.182	9.36×10^{31}	1.75×10^{32}	2.59×10^{33}
LkCa 14	1	0.045	1.20×10^{32}	1.20×10^{32}	1.20×10^{32}

Table 11: (Continued)

Object name	$N_{\rm flare}$	Flare rate [$\rm d^{-1}$]	Flare Energy [erg]		
			minimum	median	maximum
LkCa 19	9	0.135	2.65×10^{32}	1.28×10^{33}	1.21×10^{35}
LkCa 4	3	0.068	4.30×10^{32}	7.34×10^{32}	1.02×10^{33}
LkCa 5	4	0.184	5.19×10^{31}	1.40×10^{32}	1.29×10^{33}
LkCa 7	4	0.091	9.42×10^{31}	1.75×10^{33}	9.22×10^{33}
Mel25 43	1	0.046	5.19×10^{31}	5.19×10^{31}	5.19×10^{31}
Mel25 5	5	0.081	6.00×10^{31}	1.11×10^{32}	1.02×10^{33}
PW And	15	0.349	3.44×10^{31}	1.16×10^{32}	8.11×10^{33}
PX Vul	2	0.047	3.41×10^{33}	3.87×10^{35}	7.72×10^{35}
RECX 06	44	0.218	9.01×10^{30}	8.15×10^{31}	8.13×10^{33}
RECX 09	5	0.271			
RECX 10	21	0.115	6.02×10^{30}	5.81×10^{32}	2.03×10^{34}
RECX 11	8	0.086	1.21×10^{32}	1.40×10^{33}	1.08×10^{34}
RW Aur	17	0.377			
RX J1204.6-7731	36	0.250	2.04×10^{31}	1.52×10^{32}	1.12×10^{34}
RY Lup	2	0.111	5.21×10^{34}	5.21×10^{34}	5.21×10^{34}
SU Aur	3	0.066	1.15×10^{34}	9.99×10^{34}	1.40×10^{35}
StKM 2-809	69	1.143	5.36×10^{29}	2.48×10^{30}	5.61×10^{31}
T Tau	2	0.092	3.82×10^{32}	1.00×10^{33}	1.62×10^{33}
TIC 150097417	10	0.229	1.74×10^{32}	1.29×10^{33}	2.24×10^{33}
TIC 268017134	1	0.046	1.86×10^{33}	1.86×10^{33}	1.86×10^{33}
TIC 357019659	10	0.132	7.83×10^{32}	4.08×10^{33}	1.83×10^{35}
TWA 01	24	0.504	6.71×10^{31}	1.09×10^{33}	9.52×10^{34}
TWA 06	14	0.200	5.06×10^{31}	4.16×10^{32}	6.02×10^{33}
TWA 07	15	0.696	9.56×10^{30}	3.88×10^{31}	1.48×10^{33}
TWA 10	14	0.206	1.78×10^{31}	2.51×10^{32}	2.02×10^{33}
TWA 14	44	0.511	2.97×10^{31}	8.29×10^{31}	8.20×10^{33}
TWA 22	140	0.979			
TWA 23	10	0.225	1.20×10^{31}	4.15×10^{31}	1.34×10^{33}
TWA 25	22	0.317	1.69×10^{31}	7.75×10^{31}	1.08×10^{34}
TWA 3A	13	0.202	7.27×10^{30}	4.03×10^{31}	2.89×10^{32}
TWA 5A	65	0.950	2.27×10^{31}	1.39×10^{32}	2.19×10^{34}
TWA 7	15	0.696	9.56×10^{30}	3.88×10^{31}	1.48×10^{33}
TWA 8A	34	0.503	6.11×10^{30}	8.39×10^{31}	5.76×10^{33}
TWA 9A	30	0.438	2.64×10^{31}	2.25×10^{32}	4.29×10^{33}
TWA 9B	20	0.292	2.25×10^{31}	1.46×10^{32}	2.30×10^{33}
TYC 5164-567-1	1	0.075	4.85×10^{32}	4.85×10^{32}	4.85×10^{32}
UX Tau	2	0.046	3.29×10^{33}	1.51×10^{35}	2.98×10^{35}
UY Aur	6	0.089	4.71×10^{32}	2.06×10^{33}	6.75×10^{33}
V1023 Tau	5	0.113	1.48×10^{32}	6.65×10^{32}	3.67×10^{33}
V1110 Tau	20	0.461	1.23×10^{32}	5.28×10^{32}	1.20×10^{34}
V1204 Tau	5	0.114	1.45×10^{32}	1.26×10^{33}	4.77×10^{33}
V1297 Tau	4	0.184	1.58×10^{32}	5.11×10^{32}	9.59×10^{32}
V1299 Tau	4	0.092			

Table 11: (Continued)

Object name	$N_{\rm flare}$	Flare rate $[{\rm d}^{-1}]$	Flare Energy [erg]		
			minimum	median	maximum
V1304 Tau	10	0.230	5.14×10^{31}	1.29×10^{32}	4.86×10^{32}
V1320 Tau	8	0.184	6.31×10^{31}	7.74×10^{32}	3.05×10^{34}
V1346 Tau	4	0.179	7.27×10^{32}	9.01×10^{32}	1.06×10^{34}
V1348 Tau	3	0.068	4.46×10^{32}	1.32×10^{33}	6.41×10^{33}
V1354 Tau	12	0.273	1.50×10^{32}	1.22×10^{33}	6.03×10^{33}
V1368 Tau	7	0.104	2.18×10^{33}	1.39×10^{34}	5.41×10^{34}
V1840 Ori	11	0.249	2.04×10^{32}	1.66×10^{33}	1.83×10^{34}
V4046 SgrA	8	0.170	5.07×10^{31}	8.03×10^{32}	2.06×10^{34}
V4046 SgrB	8	0.170	5.07×10^{31}	8.03×10^{32}	2.06×10^{34}
V410 Tau	18	0.266	2.44×10^{32}	3.10×10^{33}	3.65×10^{34}
V577 Per	15	0.317	9.74×10^{31}	5.57×10^{32}	2.58×10^{33}
V773 Tau	11	0.249	7.88×10^{31}	2.45×10^{33}	1.30×10^{34}
V819 Tau	7	0.104	5.94×10^{31}	1.49×10^{32}	4.97×10^{33}
V826 Tau	17	0.388	2.28×10^{32}	1.81×10^{33}	3.21×10^{34}
V827 Tau	12	0.274	2.47×10^{31}	8.48×10^{32}	1.64×10^{34}
V830 Tau	11	0.254	7.92×10^{31}	3.62×10^{32}	7.32×10^{33}
V836 Tau	8	0.177	1.33×10^{32}	8.58×10^{32}	7.85×10^{33}
V898 Per	9	0.190	2.32×10^{32}	1.14×10^{33}	1.10×10^{34}
V927 Tau	4	0.188	3.73×10^{31}	2.24×10^{32}	1.97×10^{33}
V999 Tau	3	0.069			
XZ Tau	3	0.068	1.63×10^{33}	4.65×10^{33}	7.54×10^{34}
YZ CMi	120	2.604	3.35×10^{29}	1.43×10^{30}	3.67×10^{32}

4 Discussion

4.1 Stellar Rotation

4.1.1 Evolution of Rotation and Convection Zone

Figure 31 shows the evolution of the rotational periods of the target PMS stars with the mass between $0.8\ \mathrm{M}_{\odot}$ and $1.2\ \mathrm{M}_{\odot}$. We hereafter call them solar-mass PMS stars. We compared them to that of the other solar-mass PMS stars and main-sequence stars in the clusters (Gallet & Bouvier 2013). The PMS stars with $\sim 6 \times 10^6$ yr rotates every ~ 10 days, and their rotational period shortened to ~ 1 days when they are at $\sim 3 \times 10^7$ yr. The PMS stars spin up to $\sim 3 \times 10^7$ yr, and after that they spin down. Their rotation gets slower again, and the PMS stars with $\sim 4 \times 10^7$ yr rotate every ~ 10 days. The rotational distribution of our targets is consistent with Gallet & Bouvier (2013).

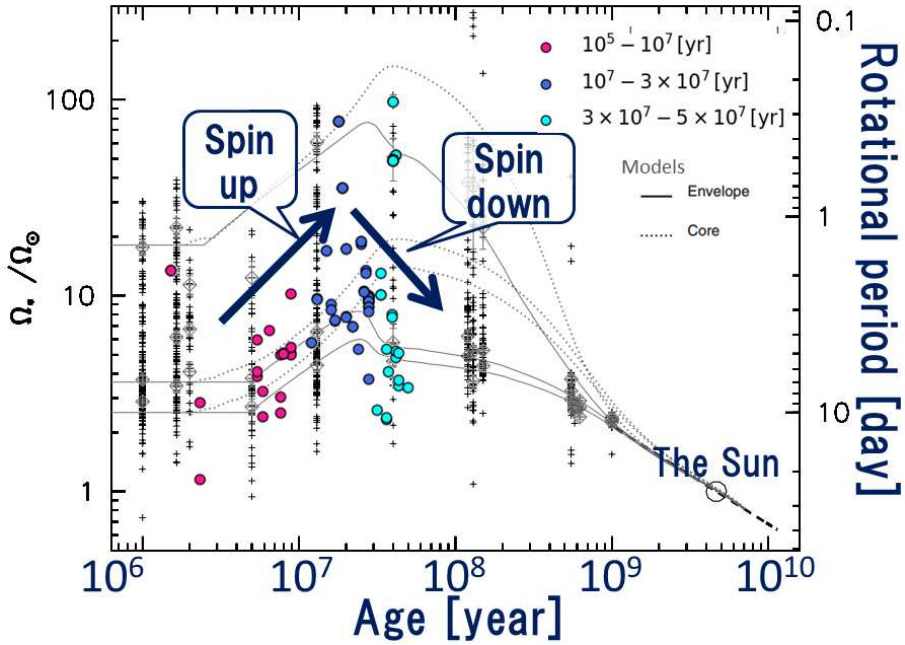

Fig. 31: The evolution of the rotational periods of the solar-mass PMS stars ($0.8 - 1.2\ \mathrm{M}_{\odot}$) as a comparison to Gallet & Bouvier (2013). The colored circles show the PMS stars, whose colors correspond to the legend in figure 19. The cross symbols represent the observation of the stars in thirteen open clusters examined in Gallet & Bouvier (2013). The gray dashed lines and solid lines are angular velocity models of the radiative core and of the convective envelope. The monochrome figure was reproduced from Gallet & Bouvier (2013).

Figure 32 plots the evolution of the rotational periods and convective turnover time, τ_{c}. We classified the solar-mass PMS stars into the three groups based on the light curve classification; periodic, quasi-periodic stochastic (QPS), and burster (the details are described in 3.3).

We believe that the main component of the period in the *TESS* light curve is due to stellar

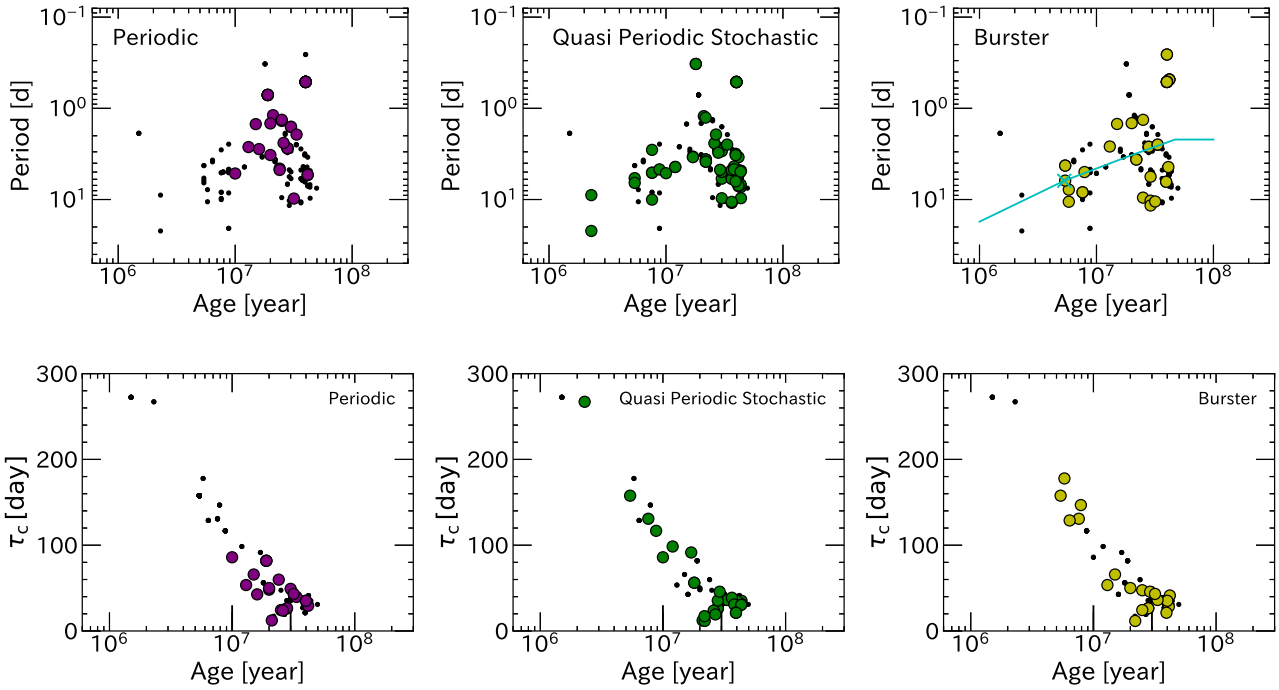

Fig. 32: The evolution of the rotational periods and convective turnover time, τ_c, for the solar-mass PMS stars in the three groups, the periodic variability, QPS variability, and bursters. The close circles denote all the PMS stars we investigated. In each panel, the PMS stars with the periodic variability (left), quasi-periodic stochastic variability (center), and bursters (right) are colored purple, green, and yellow, respectively. The upper panels and lower panels represent the rotational period and convective turnover time, τ_c, respectively. The cyan solid line in the upper right panel shows the extrapolation of the periodic evolution of GM Aur (cyan cross symbol) assuming only gravitational collapse (see section 4.1.5).

spots on their surface, not other sources such as occultation by a disk or mass accretion. First, the protoplanetary disk is flared with radial distance from the central stars (Hartmann, Herczeg & Calvet 2016). A central star would be hidden by the outer edge of the disk, if the inclination angle of the system is large. However such edge-on disk objects, which are observed from the direction of the disks, are rare. Second, the variable light caused by the obscuration of the disk could be in the order of years. The outer edge ($\sim$ 100 AU) of the Keplerian disk orbits in hundred years. A variation of hundred years is not detected during the *TESS* observation of 27 days. Third, mass accretion is predicted to be not stable, but highly-time variable, where much of the mass was accreted in short bursts (Kenyon et al. 1990, 1994). Therefore, we considered the period of all PMS stars to be caused by the spots, not only the periodic group, but also QPS and burster groups. We note that those discussions are only adopted in the cause of variation period. The amplitude of the light curves should involve spot modulation, occultation by a disk, or mass accretion.

We also reject the possibility that the PMS stars show light variation caused by pulsation. Rebull et al. (2016) identified the A-type and early F-type stars with a period of $\leq 0.3\,\mathrm{days}$ as pulsators. In this study, only AB Dor, a K0-type star, shows variable light with a period of $\leq 0.3\,\mathrm{days}$. The measured period in this study is considered to be the rotation period caused by a spot on the surface of a PMS star.

Table 12: Percentage of the solar-mass PMS stars in spin up, fastest, and spin down phases.

	spin up	fastest	spin down
	$0.1 - 10$ Myr	$10 - 30$ Myr	$30 - 50$ Myr
Periodic	0%	40%	22%
QPS	54%	34%	52%
Burster	45%	26%	26%

Table 12 shows the rates of the numbers for the PMS stars in spin up, fastest, and spin down phases. The PMS stars in the spin up phase belong to the QPS group and the burster group. No PMS stars belong to the periodic group. Almost half of the PMS stars in spin down also belong to the QPS group. In the center panels of figure 32, the PMS stars with QPS variability are plotted. The QPS group includes both spin up and spin down objects. Most of them are in the spin-down phase and have short convection periods. Their convection zone is suggested to be relatively thin. In the right panels, the burster PMS stars are plotted. In the burster group, a part of the objects are in the spin-up phase and its convection period is long. Their convection zone is suggested to be thick, perhaps fully convective.

More than half of the PMS stars in the fastest phase belong to the periodic group. In the left panels of figure 32, the PMS stars with periodic light curves are shown. Most of the objects in the periodic group are rotating faster than the objects in the other two groups. They seem to be the end of the spin up phase and just before the beginning of the spin down phase. The periodic light curves are thought to be caused by the huge spot on the stellar surface. The details will be described in section 4.3.2. The fastest-rotating PMS star shows the sinusoidal light curve. This indicates that the lifetime of the huge spot is over the *TESS* observational period, which is ~ 27 days. All of the PMS stars with periodic light curves have shorter τ_{c} than 100 days, which suggests that they have relatively thin convection zone. The PMS stars in this group are expected to have small Rossby numbers.

4.1.2 Evolution of Rossby number

When we discuss the dynamo activities, we consider not only rotation, but also the convective turnover time, $\tau_{\rm c}$. We calculated the Rossby number, $N_{\rm R}$, as follows,

$$N_{\rm R} = \frac{P}{\tau_{\rm c}} = \frac{2\pi R_*}{\tau_{\rm c} v \sin i}, \tag{9}$$

where R_* represents the stellar radius. For 188 PMS stars, we used P derived from *TESS* light curves. Unfortunately, because 23 PMS stars are not observed with *TESS*, we took $v \sin i$ from the Catalog of Stellar Rotational Velocities (Glebocki & Gnacinski 2005). We estimate $\tau_{\rm c}$ of the PMS stars with evolutionary tracks presented in Jung & Kim (2007), as shown in figure 19, We linearly interpolated that model to one-tenth of the original. The convective turnover time of a solar-mass PMS is between 300 and 100 days for the CTTS phase, and between a few hundred days and several dozens of days for the WTTS phase. The convective turnover time of an object near and on ZAMS remains stable at a few dozen days.

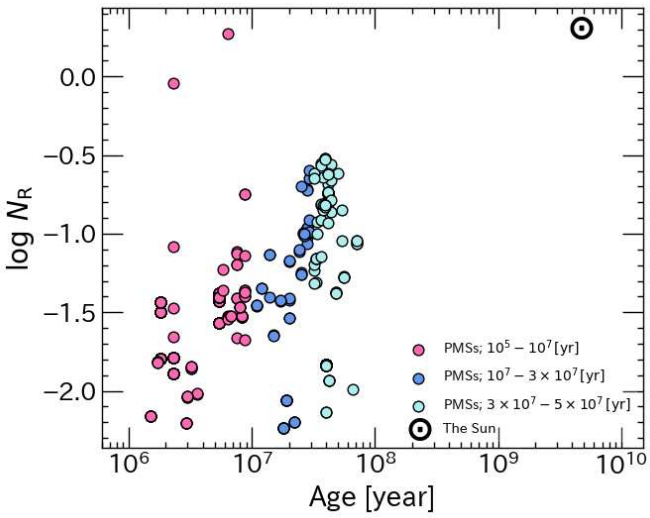

Fig. 33: Relationship between the age and the Rossby number of the PMS stars. The symbol colors correspond to the legend in figure 19. The circled dot represents the Sun.

Figure 33 plots the evolution of the Rossby numbers for our targets. The Rossby numbers of the PMS stars are about two orders of magnitude smaller than the solar one. The Rossby number remain constant at $N_{\rm R} \sim 10^{-1.4}$ during $\sim 10^6 - 2 \times 10^7$ yr, which corresponds the spin-up phase. This is because the PMS stars rotate faster, whereas, the convective turnover time $\tau_{\rm c}$ decreases with age. After reaching $\sim 10^7$ yr, the Rossby numbers increase due to the spin-down and decreasing $\tau_{\rm c}$. In the following discussion using ages or Rossby numbers, we note that the relationship between age and Rossby number is not necessarily proportional.

4.1.3 Color-color diagrams

To investigate the cause of the evolution of stellar rotation, we measured the quantities of intrinsic near-infrared excess. Figure 34 is the near-infrared color-color diagram, the relationship between the difference between $H-$ and $K-$band magnitudes, and the difference between $J-$ and $H-$band magnitudes. The intrinsic colors for CTTS were invented by Meyer, Calvet, & Hillenbrand (1997).

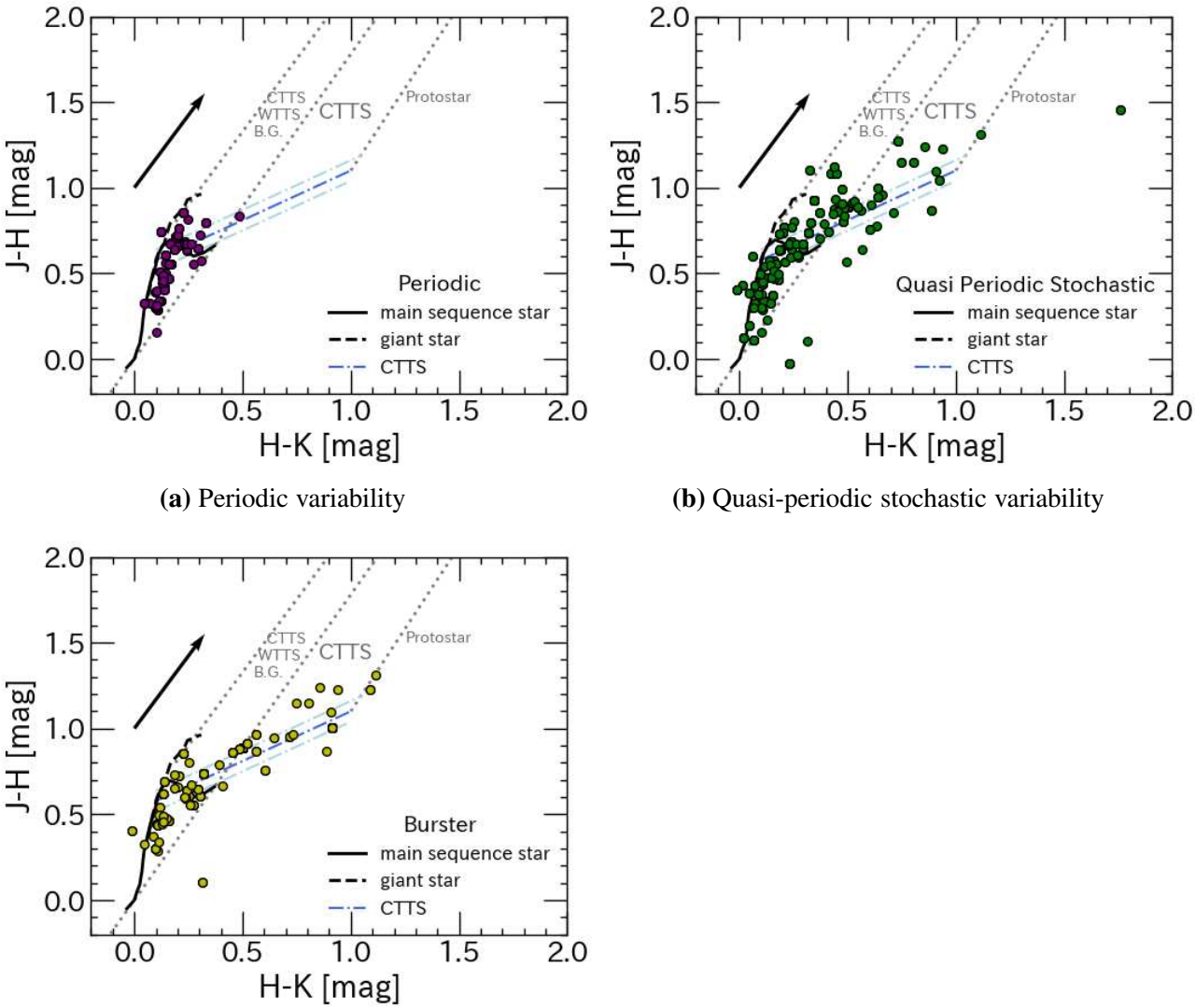

(a) Periodic variability

(b) Quasi-periodic stochastic variability

(c) Bursters

Fig. 34: Near-IR color-color diagram for the PMS stars we investigated. The purple circles, green circles, and yellow circles denote the PMS stars with periodic variability, the PMS stars with QPS variability, and the burster. The dash-dot lines represent the linear least-square fit to the intrinsic color of the CTTSs performed by Meyer, Calvet, & Hillenbrand (1997). The intrinsic colors of main-sequence stars (solid line) and giant stars (dashed line) were taken from Bessell & Brett (1988). B.G. stands for background star. The arrow and dotted lines show the interstellar reddening vector taken from Cohen et al. (1981).

We estimated the quantities of intrinsic near-infrared excess with the method described in

Hosoya et al. (2019). The intersection of the reddening vector originating from the observed JHK colors of the PMS stars and the intrinsic colors for CTTS represents the amount of the near-infrared excess of the PMS stars. The zero point of the intrinsic near-infrared excess is defined as the intersection of the line parallel to the reddening vector through an M6 dwarf color, and the intrinsic CTTS line, $(J-H, H-K) = (0.79, 0.47)$. They also defined the point of unity of the near-infrared excess as the reddest intrinsic color of CTTSs, $(J-H, H-K) = (1.0, 1.1)$ (Meyer, Calvet, & Hillenbrand 1997). The excess values are listed in table 2. The excess values of the PMS stars in this study range from -0.77 to 1.04.

Figure 34a, 34b, and 34c are the near-IR color-color diagrams for the PMS stars with the periodic variability, the PMS stars with QPS variability, and the burster, respectively. In figure 34a, the periodic PMS stars are located near the intrinsic color of the main-sequence stars. The periodic PMS stars have little near-infrared excess, and are suggested no longer to have optically thick protoplanetary disks. On the other hand, more than half numbers of bursters have near-infrared excess (figure 34c). They are suggested to have optically thick protoplanetary disks. Figure 34b also shows that the part of the PMS stars with QPS variability shows the intrinsic near-infrared excess. The PMS stars having the optically thick protoplanetary disks belong to the burster and QPS groups.

In section 4.1.1, the PMS stars in the spin up phase belong to the burster group. As described above, several researchers considered that the CTTSs have a magnetic field connecting the star to the inner edge of the disk, and it prevents the star from spinning up or reduces the spin up rate. Once the disk disappears as it ages, the magnetic field connecting the star to the inner edge of the disk also disappears, and WTTSs rotate faster than CTTSs. The PMS star is considered to be spin up after a disk disappears. Haisch, Lada & Lada (2001) indicated the overall disk lifetime is suggested to be $\sim 6 \times 10^6$ yr in the surveyed cluster sample. Gallet & Bouvier (2013) determined the disk lifetime of 5×10^6 yr. However, figure 34c suggests that more than half numbers of bursters have optically thick protoplanetary disks. These results are not consistent with the previous studies. Therefore, in the next section, we discuss the possibility that the star gains angular momentum due to mass accretion.

4.1.4 Veiling and periodic evolution

In section 3.1, we reported that some highly veiled PMS stars have also larger amount of veiling with decreasing wavelengths, which is considered to be due to the heated photosphere below the shock caused by mass accretion from a protoplanetary disk. The color-color diagram is an excellent method for examining the presence of protoplanetary disks. However, it is sometimes difficult to detect the edge-on disk. The spectroscopy enables us to detect the veiling caused by the heated photosphere, implying mass accretion from a protoplanetary disk. Actually, the six PMS stars without the excess in figure 34 also show the amount of veiling of $0.1-0.2$ for $\lambda 8813-8819$ Å. This veiling is considered to be caused by the heated photosphere below the mass accretion shock, not by near-infrared reradiation from the protoplanetary disk.

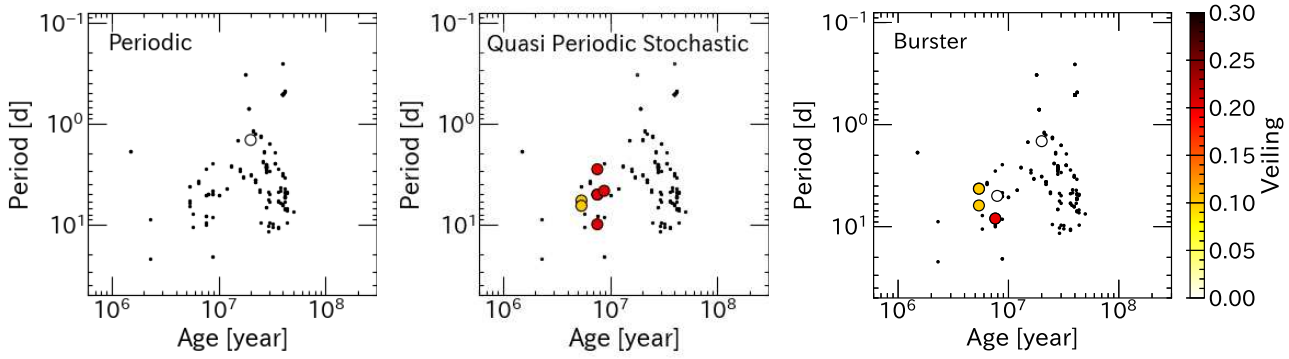

Fig. 35: The evolution of the rotational periods for the solar-mass PMS stars in the three groups, the periodic variability, QPS variability, and bursters. The large circles are the PMS stars investigated with the spectroscopy, whose color represents the amount of veiling for $\lambda 8813-8819$ Å. The dots denote all the solar-mass PMS stars we investigated.

In figure 35, we compared the rotational evolution with the amount of veiling measured in $\lambda 8700-8850$ Å (see section 2.4.1). The veiling of $0.1-0.2$ is detected from the PMS stars in the group of QPS variability and burster, which ages are $5\times10^6-10^7$ yr. These PMS stars are still considered to have protoplanetary disks even though they are spinning up. The veiling is not detected from the PMS stars with periodic variability in this study.

As described above, the previous studies have determined that the disk lifetime is $\sim5-6\times10^6$ yr and the PMS stars start to spin up after the disk disappears (Haisch, Lada & Lada 2001; Gallet & Bouvier 2013). On the other hand, our spectroscopic observations revealed objects that have a disk but are in the process of spinning up. In the following sections, we discuss whether the spinning up is the result of the gravitational collapse and mass accretion from the protoplanetary disk.

4.1.5 Gravitational collapse

In this section, we discuss the spin-up rate caused by the gravitational collapse. As described in section 1.2.1, the stellar temperature increases and luminosity decreases, and the PMS stars collapse as they evolve into the main-sequence stars. First, we estimate the stellar radius in each age of GM Aur, a burst PMS star with 2×10^7 yr and 0.9 $\mathrm{M}_\odot$. Figure 36 shows evolutional tracks on the HR diagram, in which decrease of the stellar radius with the gravitational collapse of the photosphere is explicitly depicted for a 0.9 $\mathrm{M}_\odot$ PMS star. By using the evolutionary tracks of Jung & Kim (2007) and equation 8, we calculate the radii at ages 10^6, 5×10^6, 2×10^7,5×10^7 yr. The radii of the PMS stars at $0.9\,\mathrm{M}_\odot$ contract to 2.2, 1.3, 0.9, 0.8 $\mathrm{R}_\odot$.

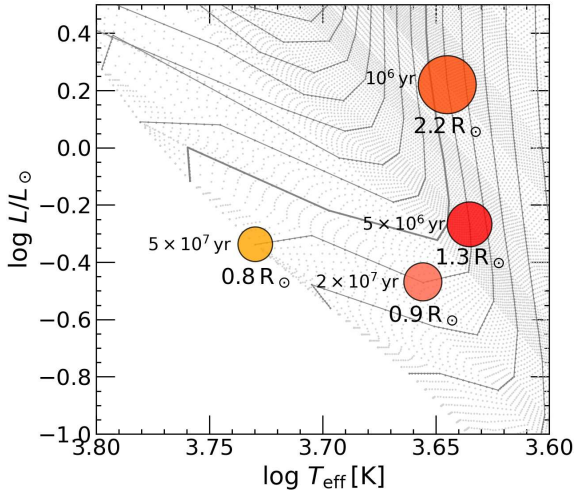

Fig. 36: The gravitational collapse of a PMS star with $0.9\,\mathrm{M}_\odot$. The solid lines and dot lines denote the evolutionary tracks and isochrones of Jung & Kim (2007). The thick solid line denotes the evolutionary track for a 1 $\mathrm{M}_\odot$ star.

In the upper right panel of figure 32, we show the periodic evolution of GM Aur. We assumed only gravitational collapse, and that the angular momentum is conserved even increasing age. With only the gravitational collapse of the stellar photosphere, the rotation period is estimated to be shortened to ≈ 3 days at the fastest. Actually, the rotational period of the fastest rotating burster is observed to be $P \approx 1$ day. In other words, the gravitational collapse alone is not enough to shorten the rotation period. The additional angular momentum to shorten the rotation period from 3 days to 1 day is calculated as below:

$$\begin{aligned} \Delta l_{\mathrm{star}} &= \frac{2}{5} M_* {R_*}^2 \times \frac{2\pi}{\Delta P} \\ &= 1.47 \times 10^{43}\,\mathrm{kg \cdot m^2 \cdot s^{-1}}. \end{aligned} \tag{10}$$

In the next section, we discuss the possibility that the star gains angular momentum due to mass accretion from a proto-planetary disk.

4.1.6 Accretion

We propose the hypothesis that the PMS stars gained angular momentum by mass accretion. In this section, we estimate the angular momentum of the photosphere gained by mass accretion. Figure 37 presents the light curve of a burster PMS star, AA Tau. We assume that the moderate and large brightening in *TESS* light curve of the burster PMS star is due to mass accretion. Figure 32 in the subsection 4.1.1 showed that many of the spin-up PMS stars belong to the burster group. Figure 34c in the subsection 4.1.3 showed that more than half of burster PMS stars have the NIR-infrared excess, and are considered to have an optically thick proto-planetary disk. Figure 39c in the subsection 4.2.2 indicate a mechanism other than sunspots as the cause of the light variation, and the figure 42c in subsection 4.3.2 suggests the other mechanism is an outburst due to mass accretion. Moreover, the previous studies have investigated that the typical timescale of the magnetic accretion is 1 day, and that of the flare is 10^{-2} days (Fisher et al. 2023).

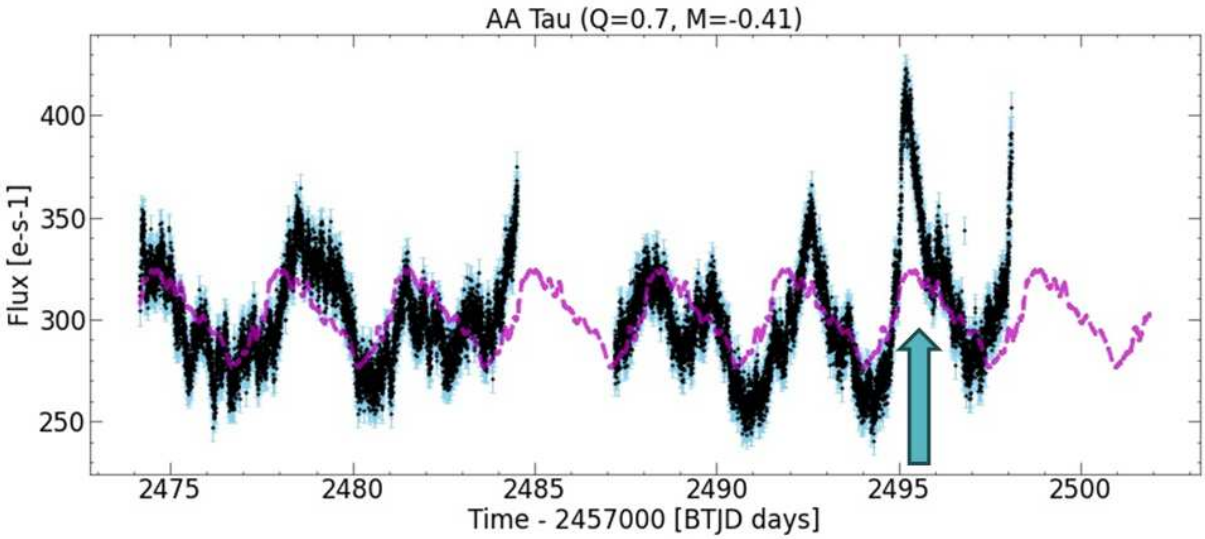

Fig. 37: The light curves of a burster PMS star, AA Tau. The filled circles with sky-blue error bars represent the raw light curve. The magenta dashed line shows the boxcar-smoothed light curve (the details are described in section 3.3). The arrow indicates the location of the outburst discussed in this section.

First, we estimated the luminosity of the outburst in $2459494.852 - 2459495.912$ BTJDdays. The radius, mass, and rotational period of AA Tau are $1.6\ \mathrm{R}_{\odot} = 1.6 \times 7.0 \times 10^{8}$ m, $0.5\ \mathrm{M}_{\odot} = 10^{30}$ kg, and 4 days. We integrated the flux of the difference between the raw light curve and the boxcar-smoothed light curve, and obtained $4 \times 10^{6}\ \mathrm{e}^{-}$. By multiplying $\frac{120\ \mathrm{s}}{60 \cdot 60 \cdot 24\ \mathrm{s \cdot day}^{-1}}$, we calculated as $5.6 \times 10^{3}\ \mathrm{e}^{-} \cdot \mathrm{s}^{-1}$ per data point.

The apparent magnitudes m_1 and m_2, of two objects and those flux f_1 and f_2 are related by (Pogson's equation):

$$m_1 - m_2 = -\frac{5}{2}\log\left(\frac{f_1}{f_2}\right). \tag{11}$$

The R-band continuum flux per unit area for a 0 mag (the AB system) object is 2.15×10^{-8} W $\cdot$ m$^{-2} \cdot \mu$m^{-1} (Fukugita et al. 1996).

The apparent magnitudes of AA Tau is $R = 11$ mag, and we obtain $F = 2.9 \times 10^{-12}$ W $\cdot$ m^{-2} by using equation 11 and the wavelength width of $R-$band, 0.3136 μm. This corresponds to the average flux during no mass accretion, ≈ 300 e$^-$ $\cdot$ s^{-1}. Then the flux of accretion, $f_{\rm acc}$, is calculated as

$$300\ \mathrm{e}^- \cdot \mathrm{s}^{-1} : 5.6 \times 10^3\ \mathrm{e}^- \cdot \mathrm{s}^{-1} = 2.9 \times 10^{-12}\ \mathrm{W} \cdot \mathrm{m}^{-2} : f_{\rm acc}, \tag{12}$$

$$f_{\rm acc} = 5.3 \times 10^{-11}\ \mathrm{W} \cdot \mathrm{m}^{-2}. \tag{13}$$

By substituting 5.3×10^{-11} W $\cdot$ m^{-2} into equation 37, the flux is converted into $L_{\rm acc} = 4\pi r^2 F = 1.1 \times 10^{28}$ kg $\cdot$ m^2 $\cdot$ s^{-3}.

Second, we estimate the angular momentum obtained by the accretion, $l_{\rm acc}$. We assume that the potential energy completely converts to the accretion luminosity. The accretion luminosity, $L_{\rm acc}$, assumes complete dissipation of the kinetic energy,

$$\begin{aligned} L_{\rm acc} &= \frac{G\dot{M}M_*}{R_*}\left(1 - \frac{R_*}{R_M}\right) \\ &\approx 0.8\frac{G\dot{M}M_*}{R_*}, \end{aligned} \tag{14}$$

where $\dot{M}$ is the rate of mass accretion onto the star (Hartmann, Herczeg & Calvet 2016). $\dot{M}$ is obtained by substituting $R_* = 1.6$ R$_\odot$, $M_* = 0.5$ M$_\odot$ and $L_{\rm acc} = 1.1 \times 10^{28}$ kg $\cdot$ m^2 $\cdot$ s^{-3} into equation 14. The mass accretion rate of AA Tau is estimated as $\dot{M} = 2.3 \times 10^{17}$ kg $\cdot$ s^{-1} $= 7.3 \times 10^{-6}$ M$_\odot$ $\cdot$ yr^{-1}. However, this accretion is not stable. We assume that interval of the burst is 10 days, and we expect $\dot{M} = 2.3 \times 10^{16}$ kg $\cdot$ s^{-1} $= 7.3 \times 10^{-7}$ M$_\odot$ $\cdot$ yr^{-1}. Assuming the burst lasts for 10^7 yr, the star is considered to gain the angular momentum of

$$\begin{aligned} l_{\rm acc} &= \dot{M}rv \\ &= (2.3 \times 10^{16}\ \mathrm{kg} \cdot \mathrm{s}^{-1}) \cdot (10^7\ \mathrm{yr}) \cdot (5\ \mathrm{R}_\odot) \cdot (140\ \mathrm{km} \cdot \mathrm{s}^{-1}) \\ &= 3.6 \times 10^{45}\ \mathrm{kg} \cdot \mathrm{m}^2 \cdot \mathrm{s}^{-1}. \end{aligned} \tag{15}$$

through mass accretion. We assumed r is 5 R$_\odot$ as the inner edge of the disk, which is consistent with the observational data (see Meyer, Calvet, & Hillenbrand 1997). v corresponds the Keplerian velocity of 140 km $\cdot$ s^{-1} at the inner edge of the disk.

Cranmer (2008) analyzed the optical spectra of jets observed with the Hubble space telescope for three T Tauri stars, CW Tau, RW Aur, and DG Tau. They obtained their angular momentum being

removed from the star. Assuming the jet lasts for 10^7 yr, the angular momentum is calculated as

$$l_{\rm jet} = 0.75 - 12.6 \times 10^{45}\ {\rm kg \cdot m^2 \cdot s^{-1}}. \tag{16}$$

They are as large as $l_{\rm acc}$. This means that most of the angular momentum gained by mass accretion is lost by the jet.

The angular momentum of AA Tau photosphere, which rotates with the period of 4 days, is calculated as

$$\begin{aligned} l_{\rm star}(4\ {\rm days}) &= \frac{2}{5} M_* {R_*}^2 \times \frac{2\pi}{T} \\ &= 9.1 \times 10^{42}\ {\rm kg \cdot m^2 \cdot s^{-1}}. \end{aligned} \tag{17}$$

The rotational period of PMS stars varies for $0.1 - 10$ days as their age (subsection 4.1.1). Then the angular momentum in cases that the star rotates with the period of $0.1\ {\rm days}, 1\ {\rm day}, 9\ {\rm days}$ are calculated as

$$l_{\rm star}(0.1\ {\rm days}) = 3.6 \times 10^{44}\ {\rm kg \cdot m^2 \cdot s^{-1}}, \tag{18}$$

$$l_{\rm star}(1\ {\rm day}) = 3.6 \times 10^{43}\ {\rm kg \cdot m^2 \cdot s^{-1}}, \tag{19}$$

$$l_{\rm star}(9\ {\rm days}) = 4.0 \times 10^{42}\ {\rm kg \cdot m^2 \cdot s^{-1}}. \tag{20}$$

Therefore, to spin up from 9 days to 0.1 days, and 1 days to 0.1 days, the PMS stars needs the angular momentum of 3.6×10^{44}, and $3.2 \times 10^{44}\ {\rm kg \cdot m^2 \cdot s^{-1}}$, respectively.

These results suggest that the spin up of the PMS stars may be transfer of angular momentum from a protoplanetary disk to a stellar photosphere via mass accretion. When a PMS star has the angular momentum $l_{\rm acc} = 3.6 \times 10^{45}\ {\rm kg \cdot m^2 \cdot s^{-1}}$ and $l_{\rm jet} = 0.75 \times 10^{45}\ {\rm kg \cdot m^2 \cdot s^{-1}}$, the difference between the angular momentum of the accretion and that of the jet is $l_{\rm acc} - l_{\rm jet} = 2.8 \times 10^{45}\ {\rm kg \cdot m^2 \cdot s^{-1}}$. Then $l_{\rm acc} - l_{\rm jet}$ exceeded by the angular momentum to spin up from 9 days, 1 days to 0.1 days. This means the PMS star obtains the angular momentum by the mass accretion and spin up.

As the cause of the spin up, Gallet & Bouvier (2013) proposed the star-disk interaction. A CTTS has an optically thick disk. The magnetic field of the star connects to the inner edge of the disk. The magnetic fields are considered to put the brakes on the rotation (magnetic braking). The radius of the inner disk is a few AU, which corresponds to the Keplarian rotation of a few days. The disks disappear as they age, and the magnetic field also be lost. We proposed that the mass accretion provides the angular momentum into the star, instead of the magnetic braking theory.

4.2 Stellar Spots

4.2.1 Evolution of Spot coverage

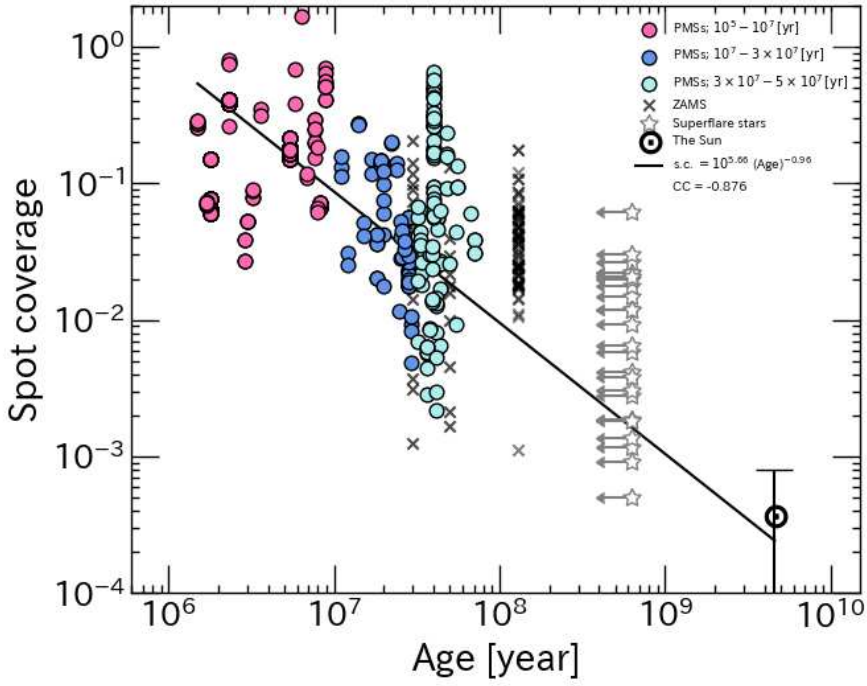

Fig. 38: Spot coverage as a function of age. The colored circles represent the PMS stars, whose colors correspond to the legend in figure 19. The circled dot represents the Sun (Toriumi & Airapetian 2022a). The solid line denotes the linear fit $\log Y = \alpha \log(\mathrm{Age}) + \beta$. The correlation coefficient including all the objects is -0.876.

Figure 38 shows the relationship between the age and spot coverage ($A_{\mathrm{spot}}/A_{\frac{1}{2}\mathrm{star}}$) of the PMS stars, ZAMS stars in IC 2391 and IC 2602 (Yamashita et al. 2022b), and the Sun (Toriumi & Airapetian 2022a). As described above, we estimated the apparent area of the spot from the amplitude of light variation by using equation 7. There is a negative correlation between the age and spot coverage. The younger PMS stars have larger spot coverage. The derived linear fit is

$$\mathrm{Spot\ coverage} = 10^{5.66} \times (\mathrm{Age})^{-0.96}, \tag{21}$$

with the correlation coefficient of -0.876. Equation 21 means the sunspot coverage decreases by a factor of 10 as the age increases by a factor of 10. This indicates that spot coverage decreases because of increasing the Rossby number associated with age. We will discuss the PMS stars whose spot coverage is over 100% in section 4.2.3.

Morris (2020) measured the spot coverage for the objects in six clusters whose ages are 10^7 yr $- 4 \times 10^9$ yr, including the two star-forming regions, namely Upper Sco (10^7 yr) and the

Upper Centaurus Lupus (1.6×10^7 yr). They found typical spot coverages in the range $1 - 10\%$, which decrease with increasing stellar age. They obtained the relationship, $\mathrm{Spot\ coverage} = 0.014 \times (\mathrm{Age})^{-0.37 \pm 0.16}$. Getman, Feigelson & Garmire (2023) investigated the spot area of late-type PMS stars ($0.7 - 1.5$ $\mathrm{M}_\odot$) in the young clusters ($7 \times 10^6 - 2.5 \times 10^7$ yr), NGC 1502, NGC 2169, NGC 869, NGC 884, h and ξ Persei, NGC 1960, and NGC 2232. They found that the spot area decreases as they age. Their results are consistent with our study.

Masuda (2022a) investigated the starspots of sun-like stars ($0.95 - 1.05$ $\mathrm{M}_\odot$) observed with *Kepler* satellite. The amplitude of light curves roughly follows $\propto t^{-2.3}$ for ages of $> 10^9$ yr, while it evolves more moderately for ages younger than 10^9 yr. The power index provided in this study, -0.96, is greater than Morris (2020). It is suggested that the thick convective zone of the PMS stars may result in a large power index.

The dispersion of spot coverage in figure 38 may be caused by the magnetic activity cycle. This is estimated from observations of the solar magnetic activity cycle and sunspot size. Many researchers have found that the large sunspots are more likely to appear in the solar maximum, and less likely to appear in the solar minimum. Moreover the previous study on the flare stars (Ikuta et al. 2023) showed that the amplitude and shape of the light curve for AU Mic and YZ CMi have varied in two years, suggesting that this can be explained by the variations of spot size and latitude.

4.2.2 The relationship between Rossby numbers and Spot coverage

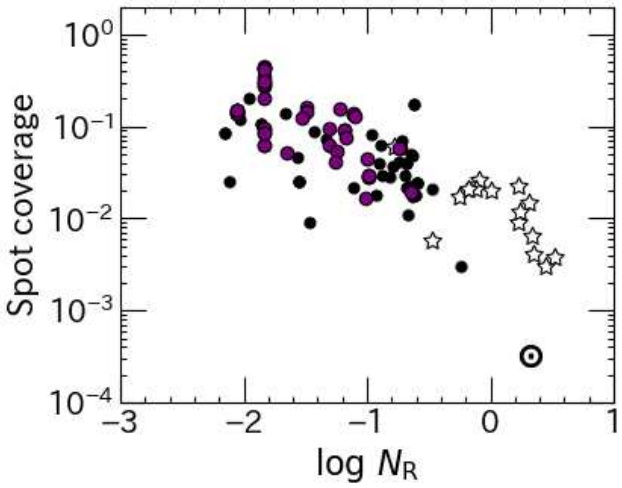

(a) Periodic variability

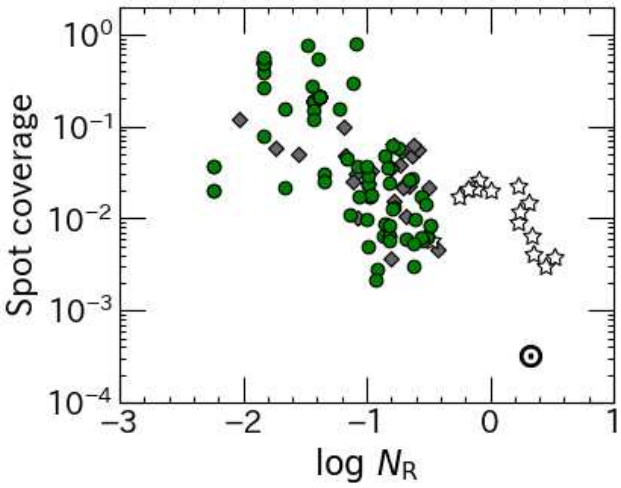

(b) Quasi-periodic stochastic variability

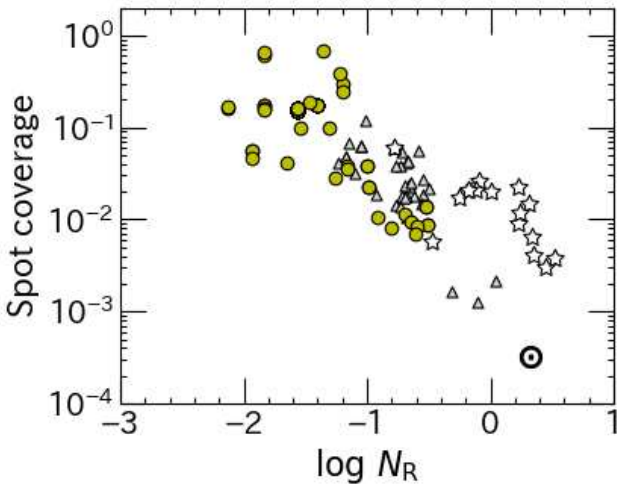

(c) Bursters

Fig. 39: Relationship between the Rossby numbers, $N_{\rm R}$, and spot coverage. The purple circles, green circles, and yellow circles denote the PMS stars with periodic variability, quasi-periodic variability, and burster. We compare them to the ZAMS stars in IC 2391, IC 2602, and the Pleiades cluster (Yamashita et al. 2022b). The filled circles in figure 39a, gray diamonds in figure 39b, open triangles in figure 39c show the ZAMS stars with a single frequency, the possible shape changer ZAMS stars, ZAMS stars and complex variability, respectively. Star marks and circled dots represent superflare stars and the Sun (Notsu et al. 2015).

The PMS stars have not only fast rotation, but also deep convection zone. It is considered that their thick convection zone generates a large magnetic flux tube, and a large stellar spot on the surface of the PMS stars. In this section, we examine the spot coverage as a function of the Rossby number. We compared the PMS stars with various main-sequence stars; the ZAMS stars in IC 2391, IC 2602,

and the Pleiades cluster (Yamashita et al. 2022b), superflare stars and the Sun (Notsu et al. 2015), and the solar-mass main-sequence stars (Masuda 2022b).

Figure 39a, 39b, and 39c show the relationship between the Rossby numbers and spot coverage for the periodic variable PMS stars, QPS variable PMS stars, and burster, respectively. The PMS stars with smaller Rossby numbers, which correspond to fast rotation and/or slower convective turnover time, show larger spot coverage. The objects with small Rossby numbers are suggested to be able to generate strong magnetic fields, and result in large stellar spots. Fritzewski et al. (2021) investigated the relationship between the Rossby numbers and $V-$band variability caused by starspot for the ZAMS stars in the $150\ \mathrm{Myr}$ open cluster NGC 2516, and cool stars in the $300\ \mathrm{Myr}$ open cluster NGC 3532. ΔV for NGC 2516 and NGC 3532 have $0.20 - 1.2\ \mathrm{mag}$ and $0.14 - 0.40\ \mathrm{mag}$, respectively. The $V-$band variability becomes larger as smaller Rossby numbers in $N_{\mathrm{R}} \lessapprox 0.06$, and saturated in $N_{\mathrm{R}} \gtrapprox 0.06$. Masuda (2022b) investigated the relation between Rossby numbers and photometric spot-modulation amplitudes for ≈ 4000 Sun-like main-sequence stars observed by Kepler. He shows the amplitude in the Santos sample appears to be constant at $N_{\mathrm{R}} \gtrsim N_{\mathrm{R}\odot} = 10^{-0.5}$.

In figure 39a, the PMS stars with the periodic variability have larger spot coverage than that of the superflare stars and the Sun. Their spot coverage is as large as that of ZAMS stars. The periodic light variations are considered to be caused by the large spot or spot groups. Yamashita et al. (2022a) indicated that $A_{\mathrm{spot}}/A_{\frac{1}{2}\mathrm{star}}$ shows a positive correlation with τ_{c} of the ZAMS stars; $A_{\mathrm{spot}}/A_{\frac{1}{2}\mathrm{star}} = 10^{-8.7} \cdot \tau_{\mathrm{c}}^{1.2}$, and obtained $D_{\mathrm{spot}} \sim 4.3{H_{\mathrm{c}}}^{1.3}$, where D_{spot} and H_{c} are the diameter of a starspot, and the thickness of the convective zone. The PMS stars are considered to be able to generate huge spots because of their thick convective zone.

In figure 39b, the burster PMS stars have smaller N_{R} and spot coverage than that of the PMS stars with the periodic variability. Their spots are suggested to become small. It is suggested that the distribution of their spots is becoming less likely to congregate in one place and more scattered in the photosphere. In the solar observation, the relatively small sunspots result in irregular light variation. Masuda (2023, Autumn Annual Meeting of the Astronomical Society of Japan, Z409r) claimed that the main-sequence stars with smaller N_{R} show sinusoidal light curves, and that with larger N_{R} show irregular light curves. Yamashita et al. (2022b) show that the ZAMS stars with irregular variability have smaller N_{R} than the ZAMS stars with single frequency. In this study, these results are also consistent with the PMS stars.

In figure 39c, the burster PMS stars and ZAMS stars do not have small N_{R}. The spot coverages of a part of burster PMS stars are as that of ZAMS stars, and others are more than that of ZAMS stars. For the latter, there are other causes of light variation besides stellar spots, such as mass accretion from the protoplanetary disks. This is consistent with figure 34c which suggests the burster PMS

stars have optically thick disks.

4.2.3 Spot coverage as a function of Magnetic strength

The spot coverage against magnetic flux is plotted in figure 40. We refereed the mean magnetic strength, $< B >$ [G], measured for the PMS stars with Zeeman-Doppler imaging (Folsom et al. 2016, Folsom et al. 2018, MAPP, MaTYSEE, and Villebrun et al. 2019). The magnetic flux, Φ [Mx], is calculated by multiplying $< B >$ [G] by the surface area of the hemisphere. The solar magnetic flux and spot coverage (Toriumi & Airapetian 2022a) are also plotted.

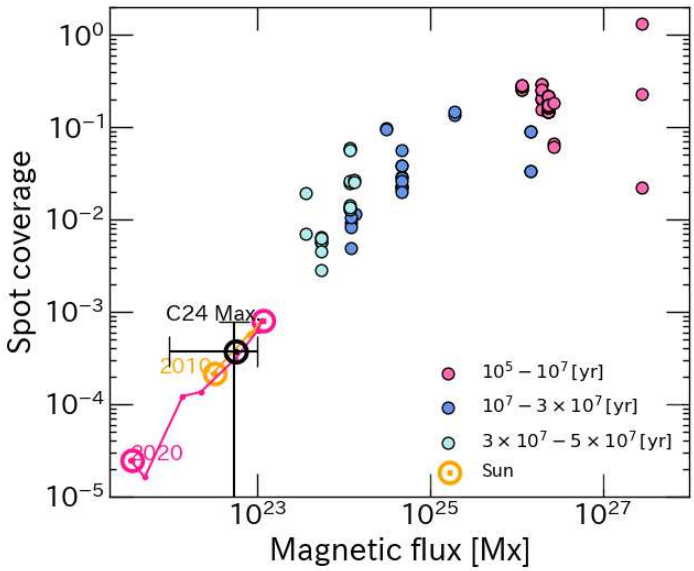

Fig. 40: Relationship between the strength of surface magnetic fields and spot coverage, $A_{\rm spot}/A_{\frac{1}{2}{\rm star}}$. The colored circles represent the PMS stars. The symbol colors correspond to the legend in figure 19. For the PMS stars, the strength of surface magnetic fields are refereed from Folsom et al. (2016), Folsom et al. (2018), MAPP, MaTYSEE, and Villebrun et al. (2019); the details are described in section 4.6. With the Stefan-Boltzmann law (equation 8), we estimated the stellar radius and converted it into the surface area. The solar magnetic flux and spot coverage are refereed from Toriumi & Airapetian (2022a).

The magnetic flux and spot coverage show a positive correlation. Their relationship appears to be continuous from the PMS stars to the sun. A positive correlation between the magnetic field strength and the spot coverage raises the possibility that the PMS stars have huge groups of spots/spot groups.

Actually, the large light variations do not necessarily result from large spot coverage. First, a single PMS star has a spot coverage larger than 100%. The idea is that large light variations result in different sources than in spots. In this study, the 16 PMS stars show the light variation suggesting the spot coverage over 100%. Most of their light curves are categorized as the burster group or quasi-periodic stochastic group. Moreover, the 10 PMS stars out of the 16 PMS stars also have a

near-infrared excess of $0.04 - 1.04$, and other 2 PMS stars do not show any near-infrared excess. The PMS stars are suggested to have not only spots but also protoplanetary disks (Also see section 4.3.2).

Second, except for a single PMS star whose spot coverage is over 100%, the positive correlation makes the existence of sunspots more certain. The maximum spot coverage of PMS stars appears as $\approx 30\%$ in this study. This is consistent with Stelzer et al. (2003) in which WTTS, V410 Tau show large light variation, and is considered to have huge spot/spot groups of $\sim 29\%$. The spot coverage seems to be saturated in 10^{-1} whereas the magnetic flux is not saturated in $> 10^{25}$ Mx.

Over 11 years, which corresponds to the single Solar activity cycle, both the magnetic field strength and coverage of sunspots vary by about two orders of magnitude. In the boundary of the ages of the PMS stars, objects with different ages have similar magnetic field strength and spot coverage. This may be because the observation date corresponds to the different phases of their magnetic activity cycles are either active or quiescent.

4.3 Chromospheric emission lines

We calculate the strength of the emission lines, F', for the Ca II line at $\lambda 8542$ Å and Mg I line at $\lambda 8807$ Å. A bolometric continuum flux per unit area at a stellar surface, F, was calculated at first. We used the i-band mag (the AB system) of the UCAC4 Catalogue (Zacharias et al. 2013) and the ATLAS All-Sky Stellar Reference Catalog (Tonry et al. 2018). F is given as

$$\log \frac{f}{f_0} = -\frac{2}{5} \times \left(m_{i\mathrm{star}} - \frac{1}{(1+V)} A_I \right), \tag{22}$$

$$F = f \times \left((1+V) \frac{d}{R_{\mathrm{star}}} \right)^2, \tag{23}$$

where f is the bolometric continuum flux of the object per unit area as observed on Earth. $m_{i\mathrm{star}}$ is the apparent magnitude of the object in the $i-$band. V is the veiling value measured near each of the emission lines (see 2.4.1). The bolometric continuum flux per unit area for an $m_i = 0$ mag (the AB system) star, f_0, is 1.852×10^{-12} W $\cdot$ m$^{-2} \cdot$ Å^{-1} (Fukugita et al. 1996). A_I is the interstellar extinction of the I-band, which has the relationship with the interstellar extinction of the $V-$band, A_V (van de Hurst 1968):

$$A_I = A_V \times 0.482. \tag{24}$$

A_V is referred from the previous studies (Herczeg & Hillenbrand 2014; Wahhaj et al. 2010; Gontcharov & Mosenkov 2017; Yu et al. 2023; Furlan et al. 2009; Yang et al. 2012; Da Rio et al. 2012; Michel et al. 2021). d denotes the distance from an object to Earth (*Gaia* DR2: Bailer-Jones et al. 2018).

R_{star} is the stellar radius estimated using Stefan-Boltzmann's law (equation 8) with the photospheric luminosity and temperature. In this study, the photometric luminosity, L_{star}, is estimated from $i-$band magnitude. The $i-$band magnitude was converted from the AB magnitude system to Vega magnitude system. The zero point, $U-B = B-V = 0$, of Vega magnitude is defined as the averaged brightness of the six A0-type main-sequence stars including Vega (α Lyrae). The AB magnitude is a system of magnitudes with 3630 Jy (1 Jy $= 10^{-23}$ erg $\cdot$ s$^{-1} \cdot$ cm$^{-2} \cdot$ Hz^{-1}) as zero magnitude for all wavelengths. Fukugita et al. (1996) presented this empirical law:

$$m_{\mathrm{I,Vega}} = m_{\mathrm{i,AB}} - 0.377, \tag{25}$$

where $m_{\mathrm{I,Vega}}$ and $m_{\mathrm{i,AB}}$ are apparent magnitude in Vega system and AB system.

The apparent magnitude is needed to correct for the difference in brightness depending on distances. The absolute magnitude is defined as the magnitude of the object at a distance of 10 percec from the observer. Then the apparent magnitude, m of the object at a distance of r pc is converted into the absolute magnitude, M, with this equation;

$$m_{\mathrm{I,Vega}} - M_{\mathrm{I}} = 5\log\left(\frac{r}{10}\right). \tag{26}$$

To obtain the luminosity, we need to estimate the bolometric absolute magnitude, M_{bol}, which is the total luminosity over all wavelengths. The difference between the $V-$band magnitude and M_{bol} is called bolometric correction. We referred the empirical relationship between T_{eff} and $(V-R), (R-I), M_{\mathrm{V}}$ and bolometric correction (BC) for main-sequence stars from Allen's Astrophysical Quantities (2000);

$$M_{\mathrm{V}} = M_{\mathrm{I}} + (V-R) + (R-I). \tag{27}$$

$$M_{\mathrm{bol}} = M_{\mathrm{V}} + BC. \tag{28}$$

Then M_{bol} is converted into the luminosity, L_{star}, with the below equation;

$$M_{\mathrm{bol}} = 4.74 - 2.5\log\left(\frac{L_{\mathrm{star}}}{L_{\odot}}\right). \tag{29}$$

However, since the $i-$band magnitude is measured both of the photospheric continuum and the veiling from the disk, we need to correct the radius with the veiling value; $R_{\mathrm{star,new}} = \frac{1}{\sqrt{1+V}} R_{\mathrm{star}}$.

F was multiplied by the EQW of the emission lines, W.

$$F'_{\mathrm{IRT}} = F \times W, \tag{30}$$

With $F_{\lambda 8542}$ and T_{eff}, we calculated $R'_{\lambda 8542}$ for the PMS stars as

$$R'_{\lambda 8542} = \frac{F_{\lambda 8542}}{\sigma T_{\mathrm{eff}}^4}, \tag{31}$$

where σ is Stefan-Boltzmann's constant. R'_{IRT} is similar to the parameter R'_{HK} derived for the Ca II H and K lines, as described by Noyes et al. (1984). $R'_{\lambda 8542}$, the ratio of the surface flux of the $\lambda 8542$ Å line to the stellar bolometric luminosity, has been previously used by Soderblom et al. (1993) and James & Jeffries (1997). The R' values for the chromospheric emission lines of Ca II HK ($\lambda 3934, 3968$ Å), Hα ($\lambda 6563$ Å), Ca II IRT ($\lambda 8542$ Å), and Mg I ($\lambda 8807$ Å) are listed in table 13.

Table 13: Rossby number, and R' of the chromospheric emission lines; Ca II HK ($\lambda 3934, 3968$ Å), Hα ($\lambda 6563$ Å), Ca II IRT ($\lambda 8542$ Å), and Mg I ($\lambda 8807$ Å)

Object Name	$\log N_{\rm R}$	$\log R'$			
		HK	6563	8542	8807
2MASS J16123916-1859284	-1.80			-3.63	-4.60
AA Tau	-1.01	-3.30	-3.15	-3.45	-4.51
AB Dor	-1.81	-2.75	-3.86	-4.22	-4.86
AU Mic	-1.39	-2.61	-3.85	-3.98	-4.45
BP Tau	-1.55	-2.69	-2.22	-3.43	-4.48
CHX22	-0.80			-3.74	-4.65
CO Ori				-3.11	-4.53
COUP 1287	-2.43			-2.91	-3.95
COUP 1423	-2.14			-3.73	
CQ Tau					
CR Cha	-1.38			-3.74	-4.64
CV Cha	-1.50			-2.45	-4.42
CW Cha	-2.30			-2.94	-4.10
DE Tau	-1.61			-2.77	-4.37
DF Tau	-1.32	-2.26	-2.35	-3.48	-4.82
DG Tau	-0.69			-2.15	-4.06
DK Tau	-1.33			-3.28	-4.13
DM Tau	-1.52			-3.68	-4.70
DN Tau	-1.57			-3.57	-4.92
DR Tau	-0.50	-1.48		-1.38	-3.37
FP Tau	-2.03			-3.76	-5.15
GJ 729					-5.19
GM Aur	-1.46			-3.43	-4.68
GQ Lup	-1.38			-2.94	-4.37
GW Ori	-0.87			-2.87	-4.85
HBC 167		-3.05	-3.05	-3.34	
HBC 407	-1.04	-3.45	-4.18	-4.06	-4.75
HP Tau	-1.91			-3.72	-3.97
IQ Tau	-1.26			-3.38	-4.46
LkCa 04	-1.86			-3.80	-4.85
LkCa 04	-1.86			-3.62	-4.82
LkCa 15	-1.23			-3.65	-4.45
LkCa 15	-1.23			-3.52	-4.62
NLTT26194					
OV Ori	-1.66			-3.49	-4.49
RECX 04	-1.56	-2.55	-3.54	-3.85	-4.38

Table 13: (Continued)

Object Name	$\log N_{\rm R}$	$\log R'$			
		HK	6563	8542	8807
RECX 06	-2.09	-2.59	-3.65	-4.06	-5.06
RECX 07	-1.95	-2.82	-4.20	-3.90	-4.96
RECX 09	-2.09	-2.86	-3.37	-4.60	
RECX 10	-1.13	-2.62	-3.97	-3.93	-4.79
RECX 11	-1.15	-2.70	-2.92	-3.82	-4.30
RECX 15	-2.36		-2.37	-2.89	-4.62
RX J1147.7-7842		-2.44	-3.31	-3.90	-4.79
RX J1204.6-7731	-1.67	-2.43	-3.31	-4.02	-5.02
RY Tau	-1.13		-3.05	-2.97	-5.09
T Tau	-0.61			-2.56	-4.49
TWA 01	-1.33	-2.76	-1.97	-3.49	-4.18
TWA 06	-2.23		-3.26	-3.82	-4.64
TWA 07	-1.66	-2.48	-3.42	-4.00	-6.44
TWA 14	-2.60	-2.60	-3.33	-3.79	-4.73
TWA 22	-2.39	-2.59	-3.24		
TWA 25	-1.57	-2.47	-3.66	-3.84	-4.88
TWA 5B	-2.49			-3.92	-5.19
TWA 8A	-1.69			-3.84	-5.66
TWA 8B	-1.57			-5.06	-5.68
TWA 9A	-1.73			-3.91	-5.89
TWA 9B	-1.65			-4.14	
UX Tau	-0.80			-3.87	-4.59
V1044 Ori				-3.09	-4.71
V1149 Sco				-3.90	-5.81
V1354 Tau	-1.35			-3.99	-4.52
V1458 Ori	-1.29			-3.93	-5.33
V2062 Oph	-1.23			-1.90	-3.96
V2129 Oph	-1.67			-3.67	-5.04
V2247 Oph	-2.34			-2.00	-3.21

4.3.1 Evolution of Chromospheric Emission Lines

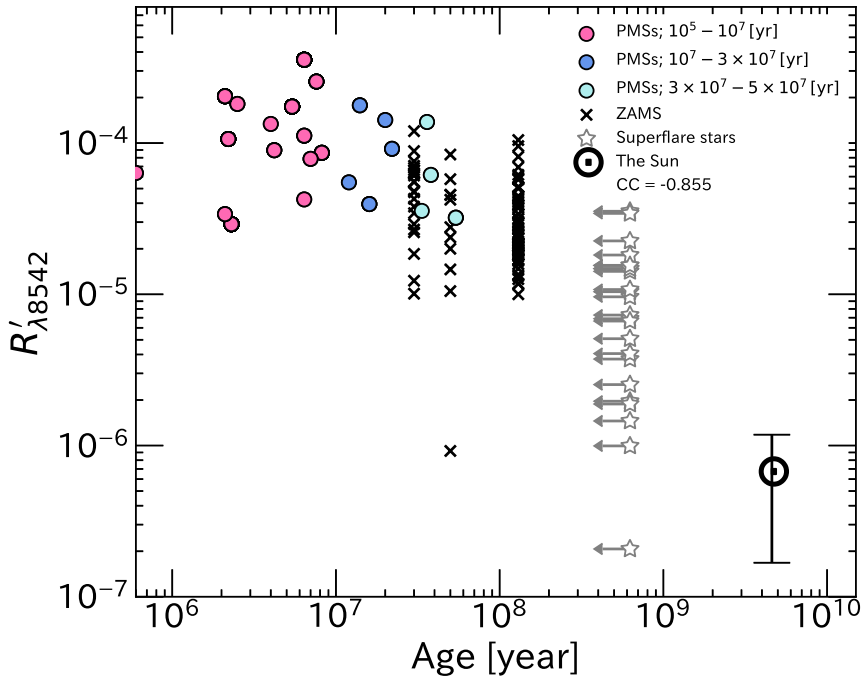

Fig. 41: The ratio of the surface flux of the Ca II IRT emission line ($\lambda 8542$ Å) to the stellar bolometric luminosity, $R'_{\lambda 8542}$ as a function of age. The colored circles represent the PMS stars, whose colors correspond to the legend in figure 19. The cross symbols show low-mass stars in the young open clusters IC 2391, IC 2602 (Marsden et al. 2009), and the Pleiades (Soderblom et al. 1993). The circled dot represents the Sun. The solid line denotes the linear fit $\log\ Y = \alpha \log\ (\mathrm{Age}) + \beta$. The correlation coefficient including all the objects is -0.855.

Figure 41 shows the relationship between the age and the emission line strength, $R'_{\lambda 8542}$, detected from the PMS stars, ZAMS stars in IC 2391, IC 2602 (Marsden et al. 2009) and the Pleiades (Soderblom et al. 1993), and the Sun (Notsu et al. 2015). The objects show a negative correlation whose a coefficient of -0.855. This result means that the younger stars have brighter Ca II emission lines. The derived linear fit is

$$R'_{\lambda 8542} = 10^{0.78} \times (\mathrm{Age})^{-0.73}. \tag{32}$$

The power index is a little smaller than that of spot coverage evolution shown in figure 38. This indicates that the area of the chromospheric emitting region decreases because of increasing the Rossby number associated with age. Our previous work suggests the chromosphere of the PMS stars are filled with the emitting region (Yamashita et al. 2020). On the other hands, the ratio of solar plage area is $1 - 8\%$ (Chatzistergos et al. 2022).

Skumanich et al. (1972) showed that the strength of Ca II HK emission lines decay as $\propto t^{-\frac{1}{2}}$,

for the main-sequence stars whose ages are $t = 10^9 - 10^{10}$ yr. This is considered to result in spin-down and is not able to generate a strong magnetic field. Hartmann et al. (1984) also provided the strength of Ca II HK emission lines as a function of age for T Tauri stars.

As same as Skumanichi's law, the strength of Ca II IRT emission lines of PMS stars decay as they age. The decay rate for the PMS stars is greater slope than Skumanichi's law. This is considered to result in decreasing the convective turnover time, $\tau_{\rm c}$. In the PMS stage, they show not only increasing the rotational period, but also decreasing $\tau_{\rm c}$, as their age. While $\tau_{\rm c}$ during main-sequence remains constant, it is possible that the activity of the PMS stars has decayed more rapidly than that of main-sequence stars.

We note the collelation between the Ca II HK emission lines and Ca II IRT emission lines. Mittag et al. (2017) observed the Ca II HK emission lines and Ca II IRT emission lines for the late-type stars. The strength of Ca II IRT emission lines is roughly correlated with the strength of Ca II HK emission lines. However, the correlation became less clear for objects with weak emission lines. Actually the correlation is not clear in the observation of the Sun, which generally has weak emission lines.

4.3.2 Starspots and Chromospheric Ca II Emission Lines

Notsu et al. (2015) indicated that the Sun and superflare stars show a rough positive correlation between the amplitude of the light curve and the $r_0(8542)$ index, the residual core flux normalized by the continuum level at the line core of the Ca II IRT. They claimed that the magnetic field strengths of superflare stars are higher than that of the Sun.

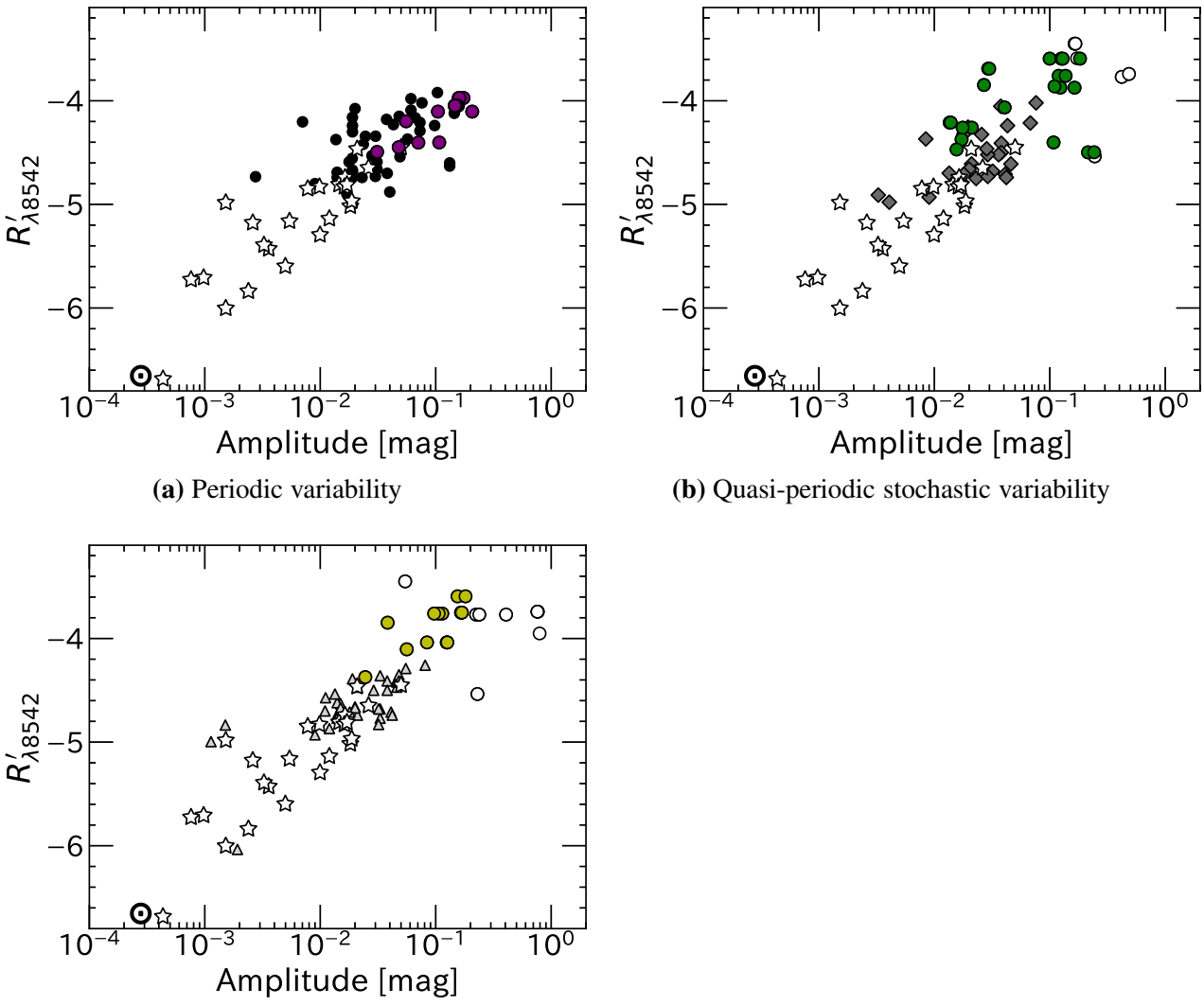

(a) Periodic variability

(b) Quasi-periodic stochastic variability

(c) Bursters

Fig. 42: Relationship between the amplitude of the light curve and the ratio of the surface flux of the Ca II IRT emission line ($\lambda 8542$ Å) to the stellar bolometric luminosity, $R'_{\lambda 8542}$ of the PMS stars. The circle symbols represent the PMS stars. The colored circles are the PMS stars without excess, and the open circles are those with excess. The other symbols correspond to the legend in figure 39.

For the PMS stars, we investigated the relationship between the amplitude of the light curve and the strength of the Ca II IRT emission line ($\lambda 8542$ Å). We compare the relationship with the ZAMS stars studied in Yamashita et al. (2022b), the superflare stars, and the Sun studied in Notsu et

al. (2015). In figure 42a, 42b, and 42c, the PMS stars are categorized according to their lightcurve shape.

Figure 42 shows that the PMS stars with a large light curve amplitude have large $R'_{\lambda 8542}$. Objects with different types of light curves seem to be plotted at different locations in figure 42a, 42b, and 42c, as represented by the colors of the symbols.

Periodic variability

Figure 42a plots the PMS stars with the periodic variability and the ZAMS stars with a single frequency. The PMS stars with periodic variability have relatively small light curve amplitudes and larger $R'_{\lambda 8542}$ compared with other types. The maximum values of them are ~ 0.2 mag and $R' \sim 10^{-4.2}$, which are comparable to maximum values of ZAMS stars. This indicates that the maximum variability induced by the large starspot is ~ 0.2 mag. As we discuss in 4.3.4, the maximum of R' from active chromosphere is considered to be $\sim 10^{-4.2}$.

We will discuss why we consider stellar cool spots cause periodic light variation. Perhaps it is possible that an accretion generates a hot spot on the stellar surface, and the hot spot is hidden and appears by the rotation. It may show periodic light variations. It is rejected for the following two reasons. First, the color-color diagram (figure 34) indicated that the PMS stars with periodic variability no longer have an optically thick disk. Therefore, an accretion from a protoplanetary disk is not considered to cause the light variation. Second, as discussed in 4.1.1, several previous studies show an accretion is a highly-time variable. Then it is hard to consider that a hot spot causes a periodic light variation.

The Sun, the superflare stars, the ZAMS stars, and the PMS stars in figure 42a show a positive correlation; all the objects with larger spots show brighter chromospheric emission lines. This is consistent with the distribution of solar spots surrounded by emitting regions (figure 12). The light curve amplitudes and $R'_{\lambda 8542}$ of PMS stars are approximately two orders of magnitude larger than those of the Sun. This is considered to be due to the smaller Rossby number of PMS stars than the Rossby number of solar stars (figure 33). We claim that the PMS stars with periodic variability have similar magnetic activity (spot and chromosphere) to main-sequence stars.

The youngest PMS star in the periodic group is CX Tau. Its age is 6×10^5 yr. The result of this study suggests that the PMS stars and ZAMS stars whose ages are between 0.6 and 120 Myr link the properties of the Sun and the superflare stars. Haisch, Lada & Lada (2001) indicates that protoplanetary disks begin to dissipate at about 10^6 yr. It is suggested that the PMS stars show periodic variation due to the cool spots before the end of the disk dissipation.

Burster

In figure 42c, we compared the burster PMS stars with the ZAMS stars with the complex variability. Compared with not only ZAMS stars but other types of PMS stars, the burster PMS stars tend to have larger light curve amplitudes and larger $R'_{\lambda 8542}$. Most of the buster PMS stars are located in the upper of the graph. A part of the burster PMS stars show NIR-excess in figure 42c. This indicates that an optically thick disk and the mass accretion from their disks caused the irregular variability. The large amplitude of light curves and bright Ca II emission lines may be attributed to the accretion from the proto-planetary disks. Moreover, several researchers have pointed out that broad components of Ca II IRT emission lines are emitted not only from the active chromosphere but also from the accretion flows (Hamann & Persson 1992; Muzerolle et al. 1998, Ghosh et al. 2022).

QPS variablity

The PMS stars with QPS variability (figure 42b) tend to be located between the PMS stars with periodic variability and the burster PMS stars. In this study, we see two types of PMS stars with quasi-periodic variability. First, a part of PMS stars are located near the ZAMSs. They have small spots. Yamashita et al. (2022b) investigated that the ZAMS stars with complex variability have smaller light curve amplitudes and smaller $R'_{\lambda 8542}$ compared with other types, suggesting that they have small spot coverage like a sunspot.

Second, the PMS stars with NIR-excess are located in the upper of the graph, like the bursters. They may have optically thick disks yet, and the mass accretion from their disks results in irregular variability. The QPS group included young PMS stars with ages of $5 \times 10^4 - 6 \times 10^5$ yr. Among the PMS stars in the QPS group, the younger PMS stars show slightly irregular light variation due to mass accretion.

4.3.3 The relationship between Rossby numbers and emission lines of Ca II and Hα

Figure 43 and 44 shows the relationship between Rossby numbers and R' of chromospheric Hα ($\lambda 6563$ Å) and Ca II IRT ($\lambda 8542$ Å) lines. The Rossby numbers and R' are listed in table 13. $\tau_{\rm c}$ of the PMS stars are estimated with $T_{\rm eff}$ obtained in this work, and the luminosity estimated in section 4.3. The PMS stars have fast rotation and slow convective turnover time, then all the PMS stars have small Rossby numbers. Hα and Ca II emission lines are known as the optically thick emission lines (e.g. Batalha & Basri 1993). The chromospheric emission lines of more than half of the PMS stars have $N_{\rm R} < 10^{-1.1}$, and show saturation in figure 43 and 44.

Ca II IRT emission lines

Marsden et al. (2009) investigated the Ca II IRT emission lines of ZAMS stars in the young open clusters, IC 2391, IC 2602, and the Pleiades cluster. For the ZAMS stars with $N_{\rm R} > 10^{-1.1}$, $R'_{\lambda 8542}$ increases with decreasing $N_{\rm R}$ until it saturates. For the ZAMS stars with $N_{\rm R} < 10^{-1.1}$, $R'_{\lambda 8542}$ reaches a constant level.

Figure 43 shows R' of the Ca II IRT emission line ($\lambda 8542$ Å) as a function of the Rossby number. The color of the symbols represents the veiling value measured in $\lambda 8420 - 8560$ Å. In figure 43, most PMS stars without veiling have $N_{\rm R}$ and $R'_{\rm IRT}$, which is similar to those of the ZAMS stars in the saturated regime. We claim that these chromosphere of the PMS stars are activated by the magnetic field generated by the dynamo process and that the chromosphere of these stars are completely filled by the emitting region. It is consistent with the previous studies indicating that PMS stars have optically thick Ca II IRT emission lines (e.g. Batalha & Basri 1993; Hamann & Persson 1992). A part of the PMS stars shows larger R' than the ZAMS stars with the same Rossby numbers. These PMS stars have veiling. The Ca II emission lines are suggested to be formed by mass accretion. The emission feature of Ca II IRT of PMS stars is thought to originate from the active chromospheres and the magnetospheric accretion funnels (Hamann & Persson 1992; Muzerolle et al. 1998).

Hα emission lines

Yamashita et al. (2022a) investigated the relationship between $R'_{\rm H\alpha}$ and $N_{\rm R}$ of the ZAMS stars. The ZAMS stars tend to show larger $R'_{\rm H\alpha}$ as $N_{\rm R}$ becomes smaller. In contrast, the ZAMS stars with $N_{\rm R} < 10^{-1.1}$ have constant $R'_{\rm H\alpha}$ at $10^{-3.9\pm0.5}$.

Figure 44 shows R' of the Hα emission line as a function of the Rossby number. More than half of the PMS stars show R' similar to the ZAMS stars. A part of the PMS stars shows larger R' than that of the ZAMS stars with the same Rossby number, which suggests mass accretion.

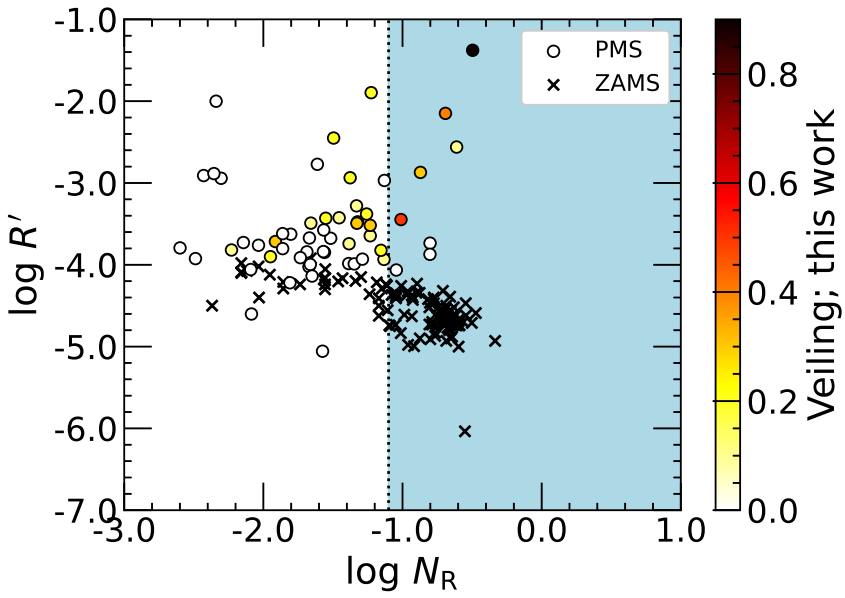

Fig. 43: Relationship between the Rossby number, $N_{\rm R}$, and the ratio of the surface flux of the chromospheric Ca II IRT emission line at λ8542 Å to the stellar bolometric luminosity, R'. The circles show the PMS stars. The crosses denote the ZAMS stars (Marsden et al. 2009). The color of the circles represents the amount of the veiling. The sky blue region bounded by the vertical dotted line shows the unsaturated region of the ZAMS stars.

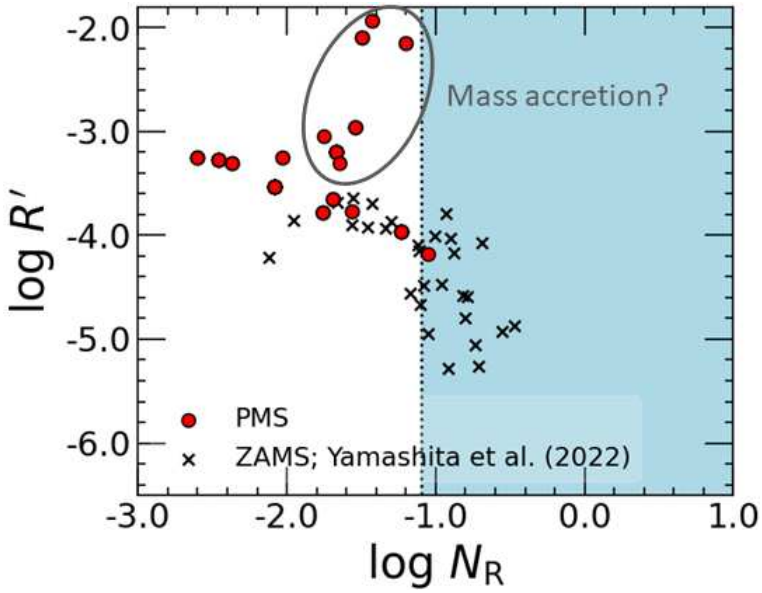

Fig. 44: Relationship between the Rossby number, $N_{\rm R}$, and the ratio of the surface flux of the chromospheric Hα emission line at λ6563 Å to the stellar bolometric luminosity, R'. The circles show the PMS stars. The crosses denote the ZAMS stars (Yamashita et al. 2022a). The sky blue region bounded by the vertical dotted line shows the unsaturated region of the ZAMS stars.

4.3.4 The relationship between Rossby numbers and Mg I emission lines

In this section, we investigate the strength of the Mg I emission lines, and determine whether the chromosphere of the PMS stars is activated by the dynamo process or accretion. Figure 45 shows the ratio of the surface flux of the Mg I emission lines at $\lambda 8807$ Å line to the stellar bolometric luminosity, R', as a function of the Rossby number. We compared the PMS stars with the ZAMS stars examined in Yamashita et al. (2022a). We colored the PMS stars to represent the amount of veiling measured in $\lambda 8700 - 8850$ Å, and the near-infrared excess (see section 2.4.1 and 4.1.3).

Compared to the ZAMS stars with the same Rossby number, some PMS stars have R' comparable to those of ZAMS stars, and other PMS stars have larger R' than those of ZAMS stars. The PMS stars with no veiling show the emission line strength comparable to those of ZAMS stars with the same Rossby numbers. The Mg I emission lines of such stars are considered to be formed by general dynamo activity similar to the ZAMS stars. Among the PMS stars, R' of the Mg I emission lines are not roughly saturated against the Rossby numbers.

On the other hand, the PMS stars with larger R' than ZAMS stars with the same Rossby number show veiling (e.g. CV Cha, TWA 01). More than half of them, such as DK Tau, GQ Lup, and IQ Tau, also show near-IR excess measured in section 4.1.3. These objects are thought to have protoplanetary disks. For such stars, the chromosphere is activated not only by the dynamo process but also by mass accretion from a protoplanetary disk.

The veiling is formed in the accretion shock column. Figure 18 shows the schematic view of an accretion shock structure. The column is generally divided into three subregions: the preshock region, the postshock (cooling) region, and the heated photosphere. The stellar photospheric pressure at the depth of continuum formation is calculated as $\log\ g \approx 3.5 \sim 10^4\ \mathrm{dyn \cdot cm^{-2}}$, indicating that the shock forms near the photosphere (Calvet & Gullbring 1998). The Mg I emission lines are known to be formed from the lower chromosphere to the upper photosphere (Fleck et al. 1994). It is considered that the Mg I emission lines are induced by accretion because the height forming Mg I is consistent with the shock region.

With the completion of this study, we propose the use of Mg I chromospheric emission lines as a new and excellent method to examine the activity of fast-rotating PMS stars and ZAMS stars. Noyes et al. (1984), the remarkable previous study for the activity of the main-sequence stars, introduced the five observational indicators of the dynamo activity, i.e. the rotation, the stellar mass (M_{star}), the spectral type ($= T_{\mathrm{eff}}$), the thickness of the convective zone, and the convective turnover time (τ_{c}). They proposed the use of the Rossby numbers, which involves the five parameters, as the indicator of stellar activity.

We add mass accretion as the new mechanism for chromospheric activity in PMS stars.

Yamashita et al. (2020) studied the Ca II emission lines of PMS stars and suggested that the PMS stars with high mass accretion rates show the Ca II emission lines stronger than the ZAMS. However, that conclusion was not strongly confirmed because R' of the Ca II emission lines were saturated against the Rossby numbers. Yamashita et al. (2022a) showed that the Mg I emission lines are the good indicator of the activity of the fast-rotating and active ZAMS stars. We conclude that the Mg I emission lines are more suitable than the Ca II emission lines for examining chromospheric activity for active objects like the PMS stars.

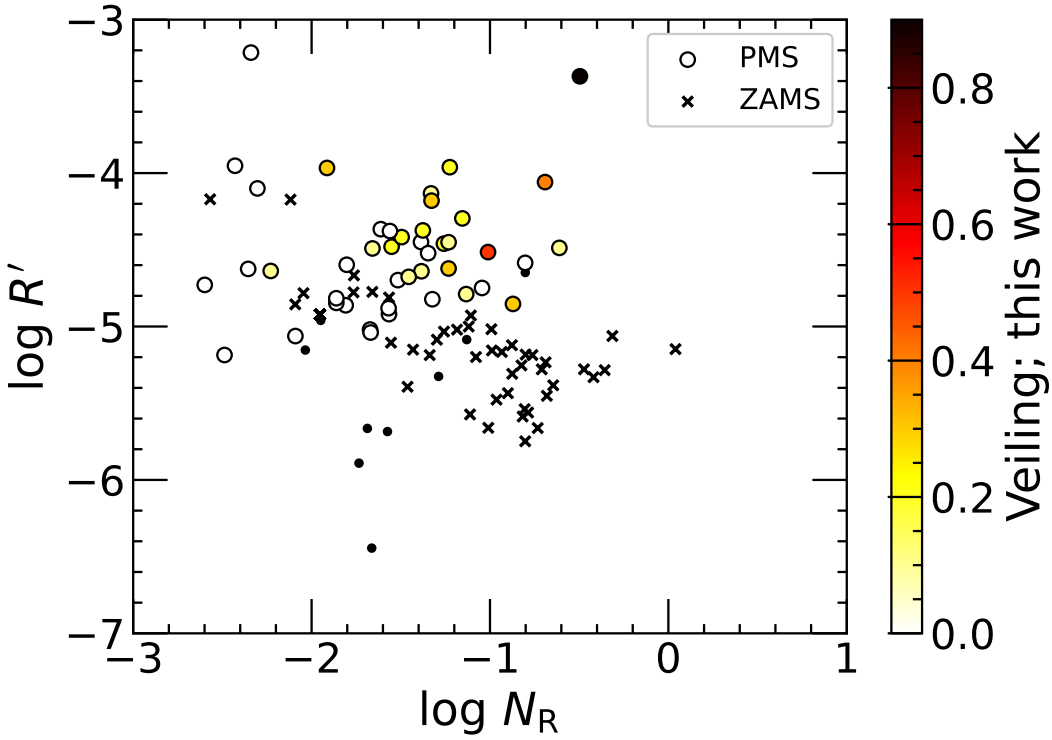

(a) Veiling

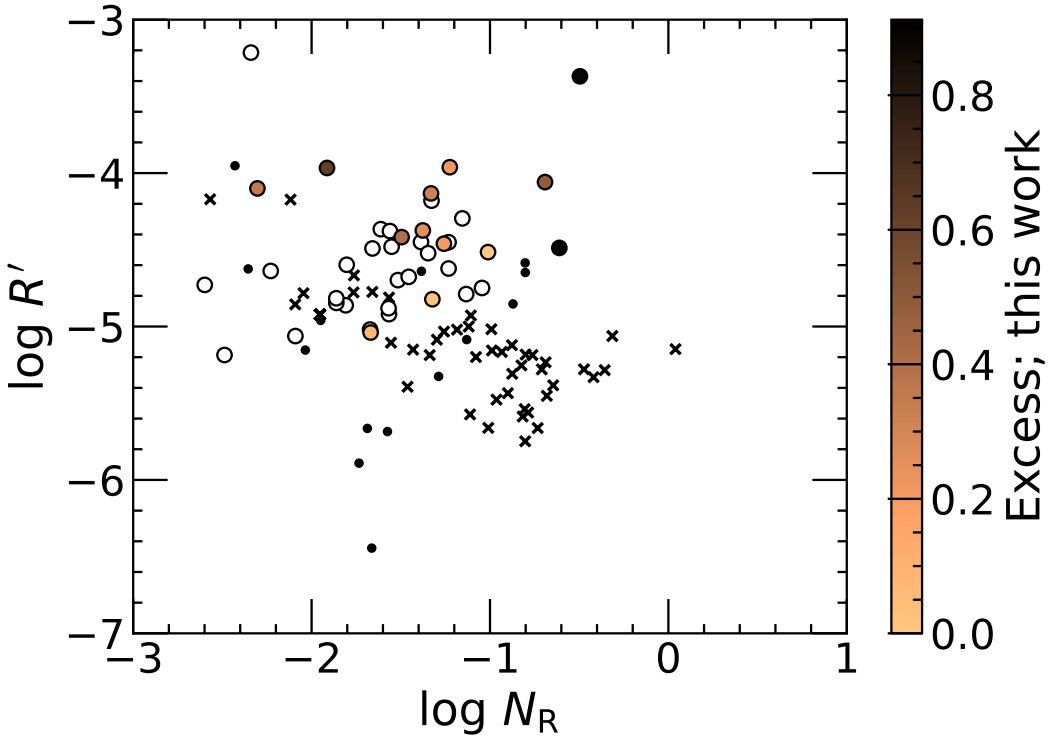

(b) Excess

Fig. 45: Relationship between the ratio of the surface flux of the chromospheric emission lines to the stellar bolometric luminosity, R', and the Rossby number, $N_{\rm R}$, of the PMS stars (large circles). The color of the large circles represents the amount of the veiling (figure 45a) or excess (figure 45b) of the PMS stars. The tiny circles show the PMS stars without significant detection of the Mg I emission line. The ZAMS stars examined in Yamashita et al. (2022a) are shown with the cross symbols.

4.3.5 Chromospheric activity and the shape of the light curves

The relationship between $N_{\rm R}$ and the ratio of the surface flux of the Ca II IRT emission line to the stellar bolometric luminosity, $R'_{\lambda 8542}$, is shown in figure 46. We compared the PMS stars with the ZAMS stars (Yamashita et al. 2022b) and main-sequence stars including the Sun (Notsu et al. 2015).

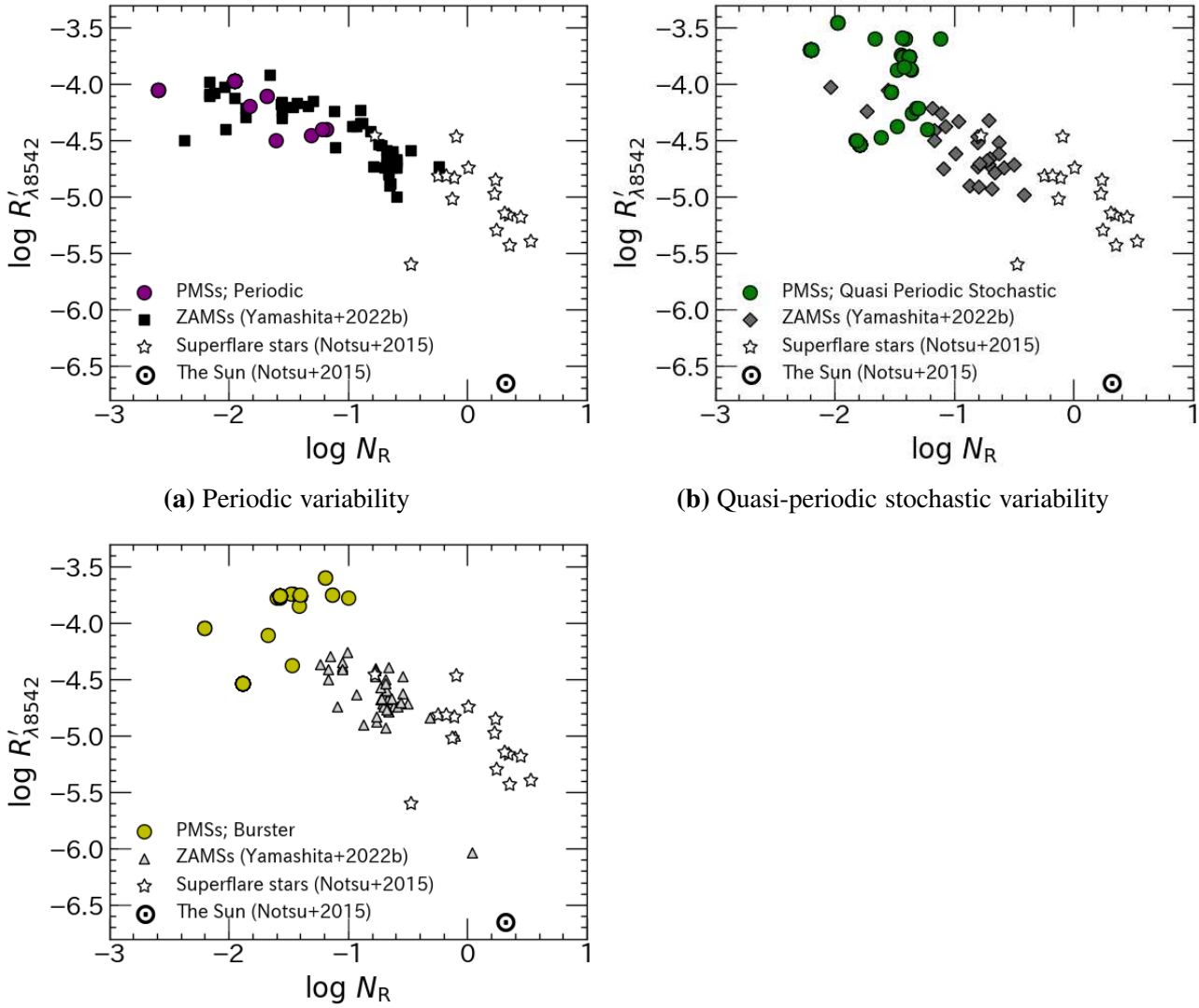

(a) Periodic variability

(b) Quasi-periodic stochastic variability

(c) Bursters

Fig. 46: The ratio of the surface flux of the Ca II emission line (λ8542 Å) to the stellar bolometric luminosity, $R'_{\lambda 8542}$, as a function of the Rossby number, $N_{\rm R}$ of PMS stars (the colored circles; this work), ZAMS stars (the black circles, gray diamonds, and gray triangles; Yamashita et al. 2022b), superflare stars (star marks; Notsu et al. 2015), and the Sun (circled dot; Notsu et al. 2015). The symbols correspond to the legend in figure 39.

Periodic variability

In figure 46a, we plot the PMS stars with periodic variability. First, we noticed that the PMS

stars with periodic variability have as large $R'_{\lambda 8542}$ as that of the ZAMS stars with single frequency. This is attributed to the small Rossby numbers of the PMS stars. This is consistent with figure 32, which indicates that the PMS stars with periodic variability are at the end of the spin-up phase.

Second, the PMS stars with periodic variability show relatively smaller $R'_{\lambda 8542}$ than the other two groups. The color-color diagram (figure 34) indicated that the PMS stars with periodic variability no longer have the optically thick disk. Thus, these objects are considered not to have accretion. By combining with figure 42a, the PMS stars with periodic variability are suggested to have large chromospheric emitting regions around huge spot / spot groups.

Marsden et al. (2009) suggest that the chromosphere is completely filled by the emitting region for stars in the saturated regime. We claim that the chromospheres of the PMS stars with periodic variability are activated by the magnetic field generated by the dynamo process. The chromosphere of these stars are completely filled by the emitting region of Ca II IRT. It is consistent with the previous studies indicating that PMS stars have optically thick Ca II IRT emission lines (e.g. Batalha & Basri 1993; Hamann & Persson 1992).

QPS variablity

Figure 46b plots the PMS stars with QPS variability and ZAMS stars with the possible shape changer. The half of the PMS stars show as large $R'_{\lambda 8542}$ as that of the ZAMS stars. These objects are similar to the PMS stars with periodic variability. The other half of the PMS stars with QPS variability show larger $R'_{\lambda 8542}$ than that of ZAMS stars.

Burster

Figure 46c plots the burster PMS stars. The burster PMS stars have large $R'_{\lambda 8542}$. As described above (figure 32), the QPS group and burster group include both spin-up and spin-down objects. Figure 34b and 34c show that the PMS stars having the optically thick protoplanetary disks belong to the burster and QPS groups. Then the large $R'_{\lambda 8542}$ could result in the accretion from the disk.

4.4 Flares

After removing the rotational light variations in the *TESS* light curves, we detected 344 flares from 37 solar-mass PMS stars. The light curve of these flares shows characteristics similar to those of solar-type main-sequence stars; sudden brightening and gradual decay. We estimated the energy of a flare from the amplitude of a flare ($\Delta F_{\rm flare}/F$) and the duration time. A detailed description is presented in Shibayama et al. (2013) and their related studies. $\Delta F_{\rm flare}/F$ is written as

$$\frac{\Delta F_{\rm flare}}{F} = \frac{A_{\rm flare}}{A_{\frac{1}{2}{\rm star}}} \frac{\int B(T_{\rm flare}, \lambda) S(\lambda) d\lambda}{\int B(T_{\rm eff}, \lambda) S(\lambda) d\lambda}, \tag{33}$$

where $A_{\rm flare}/A_{\frac{1}{2}{\rm star}}$ is the fraction of the flare-emitting area normalized by the effective area of the stellar hemisphere. With the Stefan-Boltzmann law (equation 8), we estimated the stellar radius and converted it to $A_{\frac{1}{2}{\rm star}}$. $T_{\rm flare}$ is the temperature of a flare component. We assumed that the spectral energy distribution of the flare component is similar to blackbody radiation, with the temperature of 10000 K (e.g., Hawley & Pettersen 1991; Hawley & Fisher 1992). $B(T_{\rm flare}, \lambda)$ is the Plank function, and $S(\lambda)$ is the spectral response function of the TESS detector ($\lambda 6000 - 10000$ Å; Ricker et al. 2015). We estimated $A_{\rm flare}$ with equation 33 and substituted it into equation 34, then we obtained the bolometric luminosity of the flare, $L_{\rm flare}$,

$$L_{\rm flare} = \sigma T_{\rm flare}^4 A_{\rm flare}. \tag{34}$$

The total bolometric energy of a flare, $E_{\rm flare}$, is an integral of $L_{\rm flare}$ over the flare duration,

$$E_{\rm flare} = \int L_{\rm flare}(t) dt. \tag{35}$$

In this study, $E_{\rm flare}$ for the solar-mass PMS stars ($0.8 - 1.2$ $\rm M_\odot$) range from 3.57×10^{30} erg to 7.72×10^{35} erg. Table 14 listed the occurrence frequency and averaged energy of the flares for each variability group.

Table 14: Flare frequency and averaged energy

	Frequency [day^{-1}]	$\overline{E_{\rm flare}}$ [erg]
Periodic	0.35	1.87×10^{33}
QPS	0.14	3.59×10^{33}
Burster	0.25	1.77×10^{34}

4.4.1 Evolution of Flare Energy

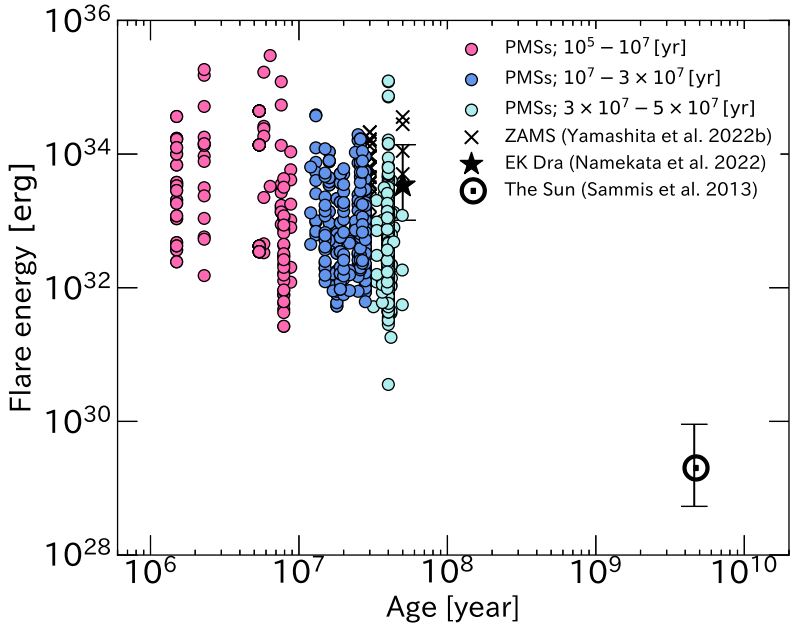

Fig. 47: Flare energy as a function of age. The colored circles represent the solar-mass PMS stars ($0.8 - 1.2$ $M_\odot$), whose colors correspond to the legend in figure 19. The cross symbols show low-mass ZAMS stars in the young open clusters IC 2391 and IC 2602 (Yamashita et al. 2022b). The star symbol represents the flare distribution of EK Dra detected by *TESS* (Namekata et al. 2022). The circled dot represents the Sun (Sammis et al. 2000).

Figure 47 shows the relationship between the age and the energy of the flares detected from the PMS stars, ZAMS stars in IC 2391 and IC 2602 (Yamashita et al. 2022b), EK Dra (Namekata et al. 2022), and the Sun (Sammis et al. 2000). EK Dra is known as an active G-type ZAMS star that exhibits frequent flares. A flare with larger energy was detected from the younger stars.

This may be related to the fact that the spot coverage decreases with age (figure 38), because solar flares are detected mainly above active regions. The high energy flares more than 10^{34} erg were also detected from the PMS stars of $\leq 10^7$ yr. Young pre-main-sequence stars with protoplanetary disks have large magnetic fields connecting the star and the disk, which may be the cause of the high-energy flares. This is beyond the scope of this study and not be discussed here.

Davenport et al. (2019) construct an empirical model on the star whose ages are $1, 2, 3, 4$ Myr, and showed that a flare with large energy occurs on the younger objects. The result of our study provides an observational reference to the model calculations of Davenport et al. (2019), and strengthens their conclusion.

4.4.2 Occurrence rate of flares

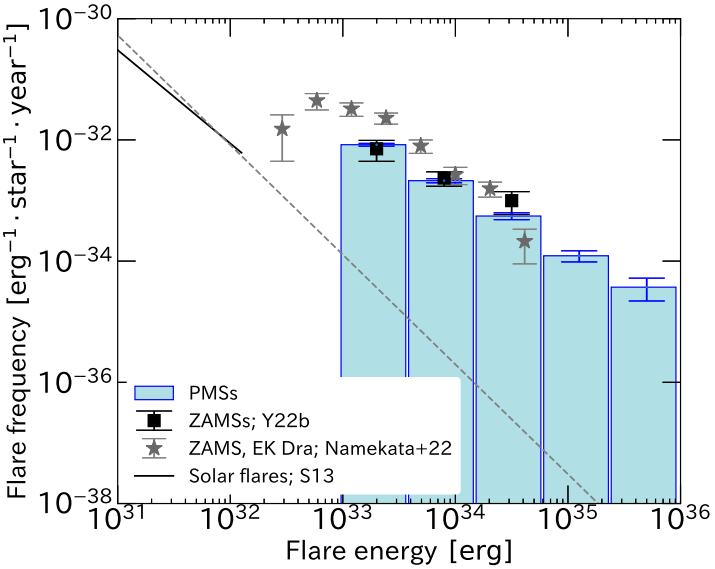

Fig. 48: Occurrence rate of flares on the PMS stars, ZAMS stars, and the Sun. The histogram shows the frequency distribution of 2750 flares on the 150 PMS stars on which flares were detected. The square symbols represent the flare distribution of ZAMS stars in IC 2391 and IC 2602 detected by *TESS* (Yamashita et al. 2022b). The star symbols represent the flare distribution of EK Dra detected by *TESS* (Namekata et al. 2022). The solid line indicates the power-law distribution of solar flares observed in hard X-rays (Crosby et al. 1993), with the distribution $dN/dE \propto E^{-\alpha}$ with index $\alpha \sim 1.8$. The dashed line corresponds to the power-law distribution estimated from superflares in Sun-like stars and solar flares (Shibayama et al. 2013).

We compare the occurrence rate of flares on the PMS stars with those of solar flares and ZAMS superflares (figure 48). For the PMS stars, flares with larger energy have a lower occurrence rate, the same as solar flares. For the 12 ZAMS stars from which flares were detected, we obtained the distribution $dN/dE \propto E^{-\alpha}$ with index $\alpha \sim 0.7$. We found that the flare frequency on EK Draconis is similar to that of our ZAMS stars (Yamashita et al. 2022b). In this study, the flares occur on the PMS stars as frequently as the ZAMS stars.

4.4.3 The relationship between Spot coverage and Flare energy

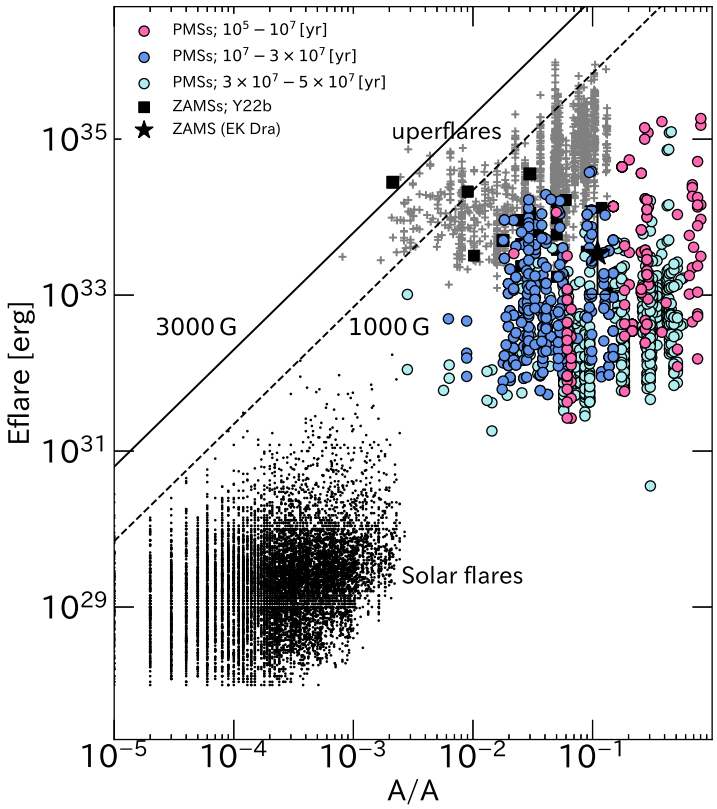

Fig. 49: Relationship between spot coverage, $A_{\rm spot}/A_{\frac{1}{2}{\rm star}}$, and flare energy, $E_{\rm flare}$. The colored circles represent the PMS stars, and the color shows their age (the details are described in the legend in figure 19). The square symbols denote flares on the ZAMS stars in IC 2391 and IC 2602. The star symbol represents the flare distribution of EK Dra detected by *TESS* (Namekata et al. 2022). The tiny circles show solar flares (Sammis et al. 2000 and private communication), and the cross symbols show superflares on Sun-like stars (Okamoto et al. 2021). The black solid and dashed lines correspond to the analytical relationship between $E_{\rm flare}$ and $A_{\rm spot}$ for $B = 3000$ G and 1000 G, respectively.

Figure 49 is a scatter plot of the flare energy, $E_{\rm flare}$, as a function of spot coverage, $A_{\rm spot}/A_{\frac{1}{2}{\rm star}}$, of the PMS stars. In the figure, solar flares and superflares, including those of EK Dra and ZAMS stars in IC 2391 and IC 2602, are also shown. For EK Dra, we referenced the spot coverage from Strassmeier & Rice (1998), and the flare energy from Namekata et al. (2022). We found that the spot coverage of the PMS stars and ZAMS stars is similar to that of superflare stars. The energy of the flares is estimated to be $\sim 10^{33} - 10^{35}$ erg, which is comparable with the energy of a superflare.

4.5 Coronal X-ray

We used the data set of the 90 PMS stars analyzed by Mr. Takashi Ito, a second-year master student at Nagoya University. The photometric data are obtained by the X-ray satellite ROSAT (ROentgen SATellite) all-sky survey in 1990-1991 and by XMM (X-ray Multi-Mirror Mission)-Newton telescope. The spectra obtained by XMM-Newton are also analyzed. The details are described in section 6.1.

4.5.1 Age vs X-ray

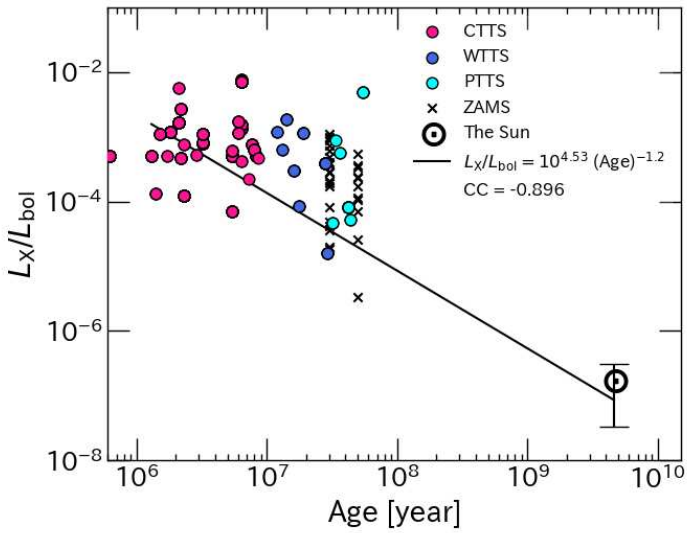

Fig. 50: The X-ray luminosity divided by the stellar bolometric luminosity, $L_{\rm X}/L_{\rm bol}$ as a function of age. The colored circles represent the solar-mass PMS stars ($0.8 - 1.2$ $\rm M_{\odot}$), whose colors corresponds to the legend in figure 19. The cross symbols show low-mass stars in the young open clusters IC 2391 and IC 2602 (Marsden et al. 2009). The circled dot represents the Sun (Tu et al. 2015). The solid line denotes the linear fit $\log Y = \alpha \log({\rm Age}) + \beta$. The correlation coefficient, CC is shown in the legend.

In figure 50, we compared the evolution of the X-ray luminosity, $L_{\rm X}$ of the target PMS stars, and ZAMS stars, and the Sun. In figure 50, we normalized $L_{\rm X}$ by the stellar bolometric luminosity in order to remove the dependence on the temperature. The younger PMS stars have large X-ray luminosity, and this is consistent with the X-ray spectroscopic study on the solar-mass PMS stars with $10^6 - 10^7$ yr by Ito, Nakazawa & Mitsuishi (in prep. and private communication). The correlation coefficient is -0.896. It suggests that with age, the corona becomes less active, thus the active region on the corona decreases. This may be related to the fact that the spot coverage and the chromospheric emission strength decrease with age (also see figure 38 and 41).

4.5.2 The relationship between Rossby number and X-ray luminosity

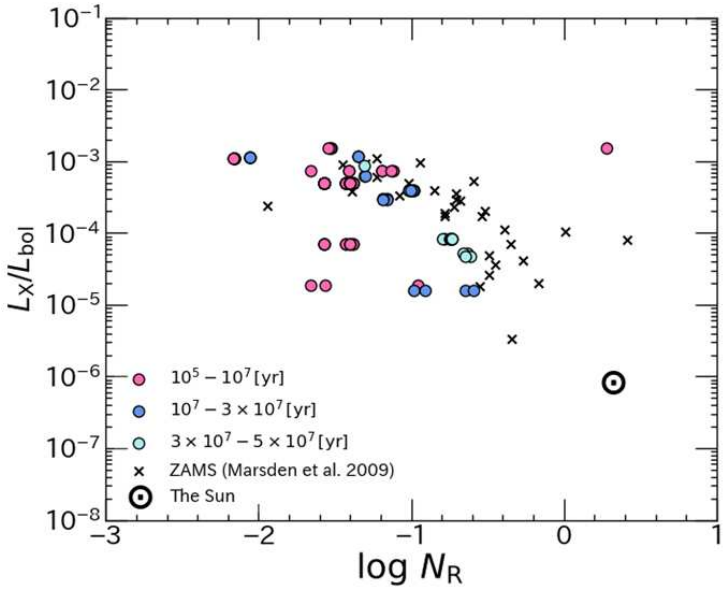

Fig. 51: The X-ray luminosity divided by the stellar bolometric luminosity, $L_{\rm X}/L_{\rm bol}$ as a function of the Rossby number. The colored circles represent the PMS stars, whose colors corresponds to the legend in figure 19. The cross symbols show low-mass stars in the young open clusters IC 2391 and IC 2602 (Marsden et al. 2009). The circled dot represents the Sun (Tu et al. 2015).

Figure 51 shows the relationship between the Rossby number, $N_{\rm R}$, and X-ray luminosity divided by the stellar bolometric luminosity, $L_{\rm X}/L_{\rm bol}$. We plotted the PMS stars, ZAMS stars (Marsden et al. 2009), and the Sun (Tu et al. 2015).

Almost half of the PMS stars show saturation, as same as the Ca II emission line (figure 43). Many researchers have studied the relationships between $N_{\rm R}$ and X-ray (e.g. Wright et al. 2011). Bouvier 1990 studied the rotation-activity relationship for T Tauri stars.

For the ZAMS stars in IC 2391, IC 2602, and Pleiades cluster, Marsden et al. (2009) presented the relationship between the Rossby numbers and $L_{\rm X}/L_{\rm bol}$. We plotted them in figure 51. Their $L_{\rm X}/L_{\rm bol}$ show saturation in $\log N_{\rm R} \sim -1.0$, which is consistent with Ca II emission lines. They claimed that both saturation of the chromosphere and corona have the same mechanism, such as dynamo saturation. They introduced Stepien et al. (2001), who suggest that coronal saturation is the result of the coronal emitting regions of a star being completely filled.

4.5.3 Spot coverage and X-ray luminosity

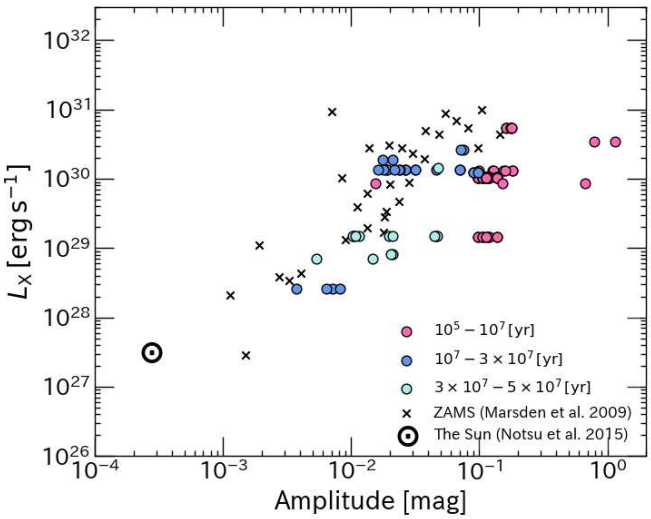

Fig. 52: $L_{\rm X}$ as a function of the amplitude of the *TESS* light curve. The colored circles represent the PMS stars, whose colors correspond to the legend in figure 19. The cross symbols show low-mass stars in the young open clusters IC 2391 and IC 2602 (Yamashita et al. 2022b; Marsden et al. 2009). The circled dot represents the Sun (Notsu et al. 2015; Tu et al. 2015).

Figure 52 plots the relationship between the amplitude of the lightcurve, and $L_{\rm X}$. The amplitude of the light curves is measured in this study for the PMS stars, in Yamashita et al. (2022b) for the ZAMS stars in the young open clusters IC 2391 and IC 2602, and Notsu et al. (2015) for the Sun. We refereed $L_{\rm X}$ from Marsden et al. (2009) for the ZAMS stars, and Tu et al. (2015) for the Sun.

The objects with larger amplitude of the light curves also show large $L_{\rm X}$, as same as the chromospheric emission line strength (figure 42). As described above, figure 42 suggests that the large-scale magnetic activity which generates huge spots and active chromosphere continues from the PMS stage. In figure 52, the light curve amplitudes and $L_{\rm X}$ of PMS stars are approximately two or three orders of magnitude larger than those of the Sun. Then the PMS stars are considered to have active coronae, and continue from the PMS stage. We note that the PMS stars whose amplitudes are $> 10^{-1}$ mag show the saturation of $L_{\rm X}$.

Getman, Feigelson & Garmire (2023) shows that X-ray luminosity, $L_{\rm X}$, and starspot area of the late-type PMS stars ($0.7 - 1.5$ M$_\odot$, $7 - 25$ Myr) are strongly correlated as $L_{\rm X} \propto A_{\rm spot}^{0.4}$. In addition to this, we first confirmed the saturation of $L_{\rm X}$ against the amplitude of the light curves. The large amplitude of the light curves is considered to result from large spots, which result from a strong magnetic field. We provide the relationship between the magnetic flux and X-ray irradiance in the next subsection.

4.5.4 The scaling law of chromospheric and coronal emission as a function of Magnetic flux

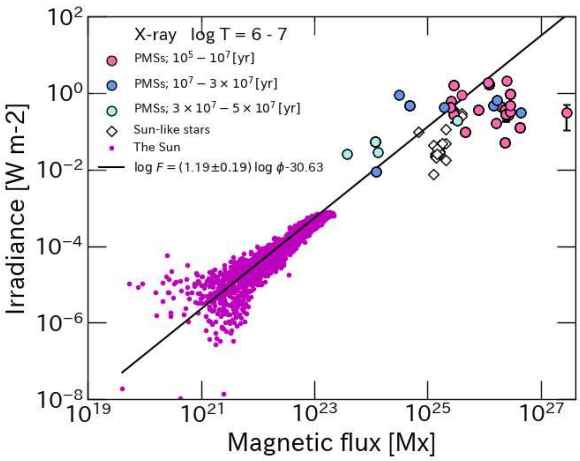

(a) coronal X-ray

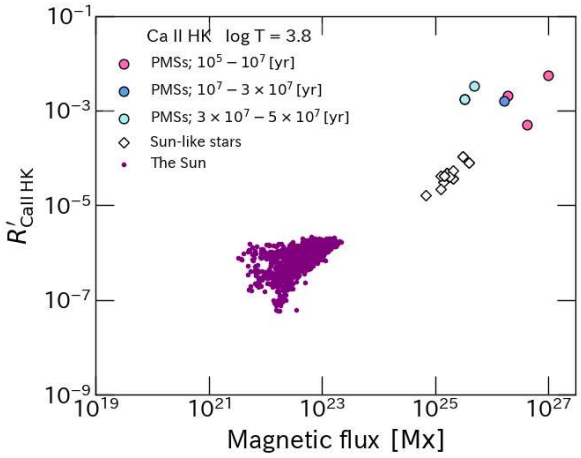

(b) chromospheric Ca II HK emission line at $\lambda 3968, 3934$ Å

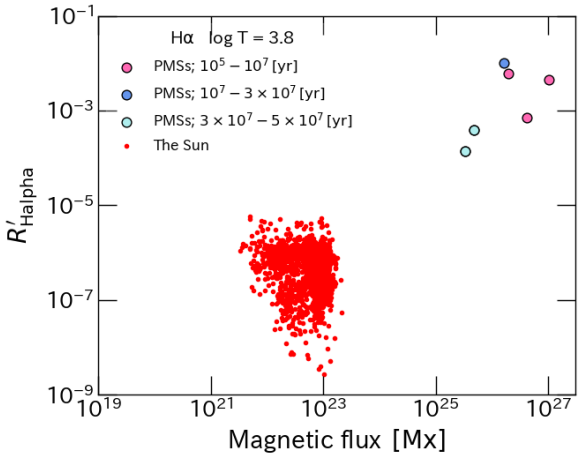

(c) chromospheric Hα emission line at $\lambda 6563$ Å

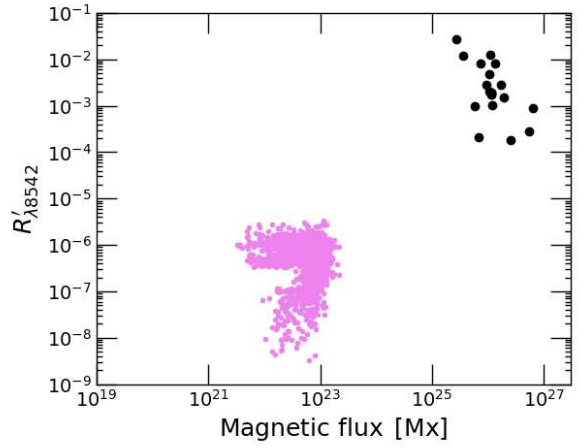

(d) chromospheric Ca II emission line at $\lambda 8542$ Å

Fig. 53: Irradiance as a function of the magnetic flux. The circles located in the top right of each panel represent the PMS stars, whose colors correspond to the legend in figure 19. The diamond symbols and tiny circles in the bottom left shows the Sun-like stars, and the Sun (Kochukhov et al. 2020; Toriumi & Airapetian 2022a). The solid line represents a linear fitting to the solar data.

The magnetic flux on the surface transports the energy upwards and heats the chromosphere, transition region, and corona. For the Sun and 14 Sun-like stars, Toriumi & Airapetian (2022a) constructed the power-law scalings, $\log F = \alpha \log \Phi + \beta$, between the total magnetic flux, Φ, and spectral irradiances, F. They showed the power-law scalings at various wavelengths, which correspond to the chromosphere (Mg II h+k), the transition region (C II, Lyα), and the corona (X-ray, Fe XV). The coronal X-ray has $\alpha > 1$ and the chromospheric emission lines have $\alpha \leq 1$. They found that solar-type stars have a common atmospheric heating mechanism.

The PMS stars are expected to generate strong magnetic fields and have active chromosphere

and corona, because PMS stars have fast rotation and thick convective zone. Several researchers pointed out that low-mass dwarfs showing strong Ca II emission lines also have strong X-ray emissions (Hodebine et al. 2017), strong magnetic fields (Linsky 2017; Valenti & Johns-Krull 2001), and that the flux variation of the Ca II lines is related to the coverage of their faculae or spots. Pevtsov et al. (2003) studied the relationship between Φ and $L_{\rm X}$ of the Sun and active stars (main-sequence stars and six PMS stars). They found that Φ and $L_{\rm X}$ exhibit a clear linear relationship over 12 orders of magnitude. However, five of the six PMS stars are CTTS, which means that the number of WTTS is not sufficient.

Figure 53 are scatter plots of the irradiance of chromospheric emission lines and coronal emission continuum as a function of the magnetic flux. First, in order to discuss each age, we analyzed a few dozen PMS and ZAMS stars. Second, we measured not only the strength of the X-ray, but also chromospheric emission lines (Ca II HK, Hα, Ca II at $\lambda 8542$ Å). The X-ray irradiance is calculated by dividing $L_{\rm X}$ by the unit area of a sphere, whose radius is 1 AU. The X-ray irradiance and R' of chromospheric emission lines are compared with the magnetic flux obtained with Zeeman broadening or Zeeman-Doppler imaging in the previous studies (the details are described in 4.6). We refereed the unsigned magnetic flux on the visible hemisphere, X-ray irradiance, and $R'_{\rm HK}$ of the solar-like stars.

In figure 53, the irradiance of X-ray and chromospheric emission lines are located in the extension of the power-law scalings of the Sun. The solar-type stars including the PMS stars are suggested to have a common atmospheric heating mechanism. However, a part of the PMS stars show saturation of X-ray irradiance against the magnetic flux. Figure 53a is similar to figure 52.

Shoda et al. (2020) discussed the prediction that the flux expansion is suppressed with the large filling factor. Based on observations from the Hinode solar satellite and the Chromospheric LAyer Spectropolarimeter (CLASP2), Ishikawa et al. (2021) showed that the plage magnetic field is narrow in the photosphere, and spreads horizontally in the upper chromosphere. This is consistent with coronal saturation discussed in 4.5.2.

4.6 Magnetic field strength

We analyzed the photospheric magnetic field. The PMS stars and ZAMS stars have huge spots and bright chromospheric emission lines, which means their surface magnetic fields are strong. Brown et al. (2022) confirmed that the main-sequence stars and PMS stars with $T_{\rm eff} = 3200 - 6700$ K show as larger $R'_{\rm HK}$ as stronger mean magnetic fields. The theoretical maximum value of the magnetic strength of PMS is 3000 G (Shu et al. 1994). In fact, the strong magnetic fields of a few thousand G are observed from PMS stars with Zeeman broadening or Zeeman-Doppler imaging in the previous studies. We note that measurement of the magnetic fields is difficult, and currently mainly the group using the polarization spectroscopy with Canada France Hawaii Telescope (CFHT) / ESPaDOnS, have succeeded. Moreover, their magnetic strength varies with the rotational phase.

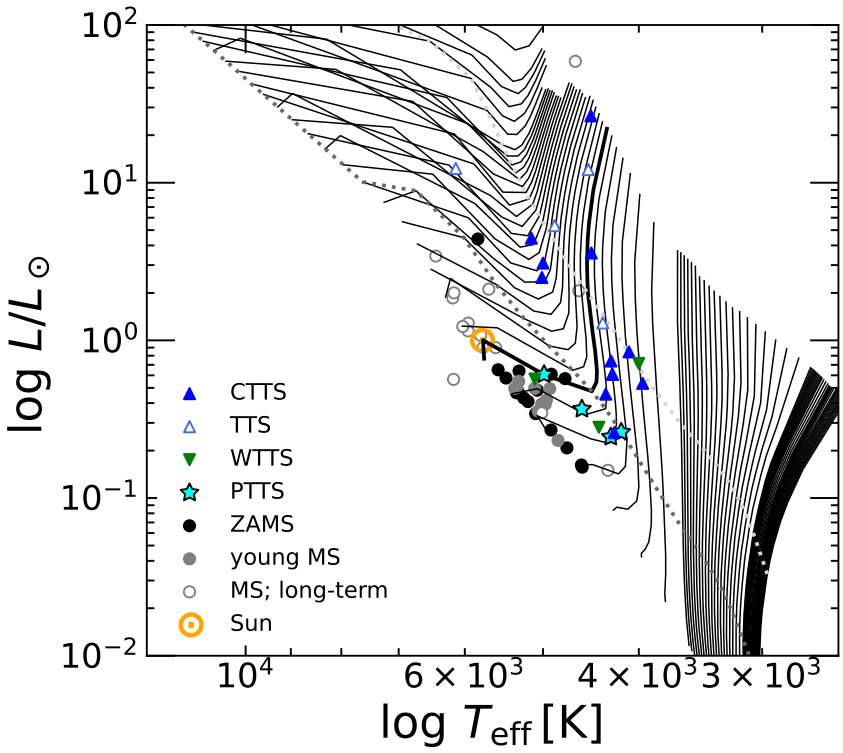

Fig. 54: HR diagram of the investigated PMS stars, ZAMS stars, main-sequence stars. The solid lines and dot lines denote the evolutionary tracks and isochrones of 10 Myr and 100 Myr of Jung & Kim (2007). The blue triangles, white triangles, green inverted triangles, and cyan star symbols represent CTTSs, T Tauri stars, WTTSs, and post T Tauri stars. The filled circles, gray circles, open circles, and circled dots show ZAMS stars, young main-sequence stars, and long-term main-sequence stars, and the Sun.

We investigated the average magnetic field strength $< B >$ (in the line-of-sight direction) and the variation of magnetic field strength $\Delta B = B_{\rm max} - B_{\rm min}$. The targets are the 28 PMS stars, belonging to the four molecular clouds (Tau, Lup, Ori, Sco), and three moving groups (β Pic, TWA,

AB Dor). Their masses and ages range $\sim 0.5 - 2.0\ \mathrm{M}_{\odot}$, and $\sim 10^5 - 10^7\ \mathrm{yr}$. We also studied the 42 main-sequence stars including the Sun. The main-sequence stars except the Sun and background stars belong to the open clusters; Pleiades, Her-Lyr, Coma Ber, and Hyades. Figure 54 presents the HR diagram of the objects investigated.

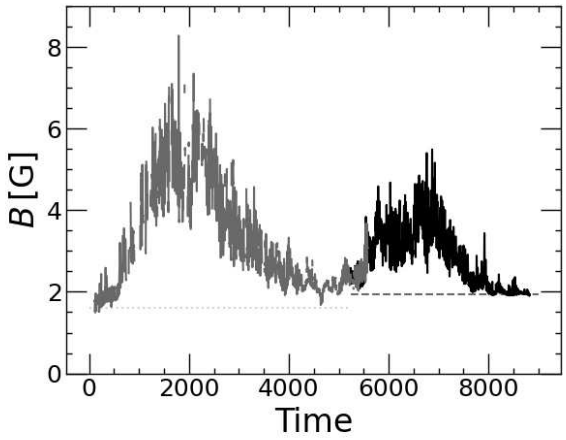

Fig. 55: Time series of total unsigned magnetic flux of the Sun. The gray solid line and the gray dotted line denote the data obtained by SDO/HMI, and the basal flux. The black solid line and black dashed line denote the data obtained by SOHO/MDI and the basal flux.

We analyzed the time series of the total unsigned magnetic flux of the Sun from 1996 to 2019 (figure 55; Toriumi & Airapetian 2022a, Namekata et al. 2023). The total unsigned magnetic flux from Apr. 1996 to May 2010 is obtained by Michelson Doppler Imager (MDI) installed to *Solar and Heliospheric Observatory (SOHO)*, and that from May 2010 to Feb. 2020 is obtained from Helioseismic and Magnetic Imager (HMI) installed to *Solar Dynamics Observatory (SDO)*. The data from the two satellites covers two solar cycles; Solar cycle 23 from Aug. 1996 to Dec. 2008, and Solar cycle 24 from Dec. 2008 to Dec. 2019. The regular period of greatest solar activity during the solar cycle is called as "solar maximum", which is defined as the period when the average sunspot number in 13 month bin is the highest. In solar circles 23 and 24, the solar maxima are at Sep. 2001 and Feb. 2014. However, the periods with the highest number of sunspots without averaging are Nov. 2001 and Apr. 2014. The regular period of least solar activity in the solar cycle is called as "solar minimum".

Figure 56 shows the examples of the analysis. We subtracted the basal flux of $\sim 2\ \mathrm{G}$, which is magnetic field strength generated from the quiescent region. Now what we want to compare with stars is the variation in magnetic field strength resulting in sunspots. The solar rotation period is about 30 days. Then in order to cover about a dozen rotational periods, the data are divided approximately every year. We calculated the magnetic field variability amplitude, $\Delta B\ [\mathrm{G}]$, by taking the 90th percentile

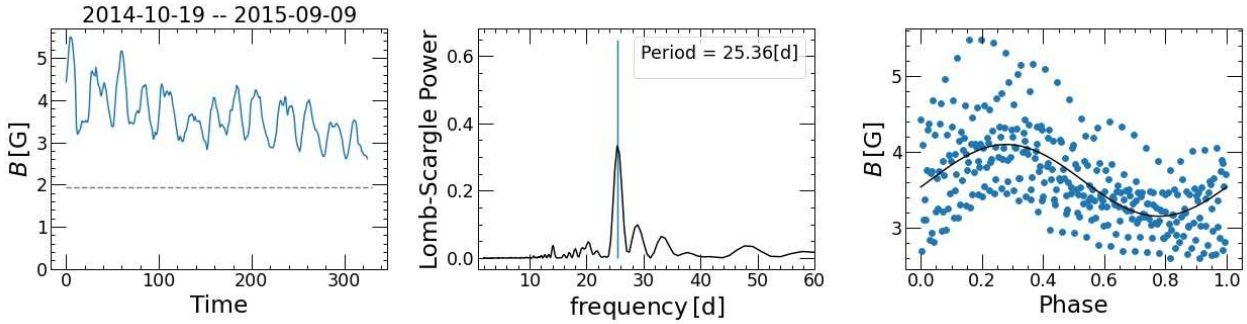

Fig. 56: The examples of the analysis for the solar total magnetic flux. In this figure, the period near the solar maximum (August 2014) observed with SDO/HMI is shown. Left column: full light curve; middle column: Lomb-Scargle periodogram; right column; phased light curve.

flux and subtracting it from the 10th percentile flux. The result is described in table 15.

Table 15: Total unsigned magnetic flux, $< B >$, and their variation, ΔB, of the Sun in approximately year bin.

start date	$< B >$ [G] - basal flux	ΔB [G]
1996-01-01	0.214	0.583
1996-12-19	0.536	0.906
1997-12-07	1.575	1.299
1998-11-25	2.901	1.660
1999-11-13	3.627	1.830
2000-10-31	3.276	1.872
2001-10-19	3.712	1.936
2002-10-07	2.562	1.831
2003-09-25	1.889	1.408
2004-09-12	1.510	1.008
2005-08-31	1.004	0.750
2006-08-19	0.784	0.620
2007-08-07	0.611	0.371
2008-07-25	0.467	0.442
2009-07-13	0.632	0.574
2010-07-01	0.691	1.027
2011-06-19	1.400	1.006
2012-06-06	1.394	1.275
2013-05-25	1.704	1.281
2014-05-13	1.808	1.520
2015-05-01	1.171	1.070
2016-04-18	0.480	0.754
2017-04-06	0.273	0.585
2018-03-25	0.085	0.198
2019-03-13	0.060	0.151

Figure 57 show the relationship between the mean magnetic strength, $< B >$, and their variation, ΔB of the PMS stars and main-sequence stars. We refereed the mean magnetic strength, $< B >$ from MaPP (2008), MaTYSSE (2014), Yang (2008), and Villebrun et al. (2019) for CTTS, Villebrun et al. (2019) for TTS and WTTS, Yang (2008), Yang (2011), and Folsom et al. (2016) for PTTS, Folsom et al. (2016) and Folsom et al. (2018) for ZAMS, Folsom et al. (2018) for young main-sequence stars and long-term main-sequence stars. We note that the Zeeman-Doppler imaging for stars not being resolved spatially obtained the longitudinal components of the magnetic fields, whereas the solar data are obtained with the radial component.

$< B >$ and ΔB show a positive correlation over three orders of magnitude. This suggests that the mechanism driving the magnetic field is common to the Sun, main-sequence stars, and PMS stars; the higher $< B >$ means that the spots are more huge, and result in the larger ΔB. The strength of the magnetic field in the solar and stellar spots is only a few kilogauss at most, due to the balance with the gas pressure on the stellar surface. Therefore, by assuming that sunspots are responsible for most of the magnetic field, it is suggested that a large total magnetic flux means a large sunspot area. Isik et al. (2020) assumed that the active regions are inhomogeneously distributed on the surface of an active solar-type star, and this assumption was supported by the result in Yamashita et al. (2022b). The positive correlation between $< B >$ and ΔB is also shown in Brown et al. (2022) for main-sequence and PMS stars of $T_{\rm eff} = 3200 - 6700$ K. Similarly, the intensity of the Ca II HK emission lines, $R'_{\rm HK}$, show a positive correlation with $\Delta R'_{\rm HK}$ in Brown et al. (2022) and Radick (2018) for the Sun and 72 Sun-like stars.

Comparing the main-sequence stars with each other (ZAMS, young main-sequence stars, long-term main-sequence stars, and the Sun), $< B >$ and ΔB are larger for the younger objects. The ZAMS stars are plotted in the upper right in figure 57, followed by the young MS, and the Sun is plotted in the lower left. The rotation of main-sequence stars gets slower as they age, and it becomes difficult to generate a strong magnetic field.

In Folsom et al. 2018, the dispersion of $< B >$ in long-term MS was considered to be due to differences in magnetic activity cycles. Figure 57b show $< B >$ and ΔB of the Sun. $< B >$ and ΔB vary over the solar cycle. In the solar maximum, $< B >$ and ΔB are the largest in the circles, and in the solar minimum they are the smallest. However, the long-term MS was observed for six months to six years, and PMS and ZAMS stars were observed for a few days to a few months, which is not enough to observe the activity circles. PMS and ZAMS stars also show a positive correlation between $< B >$ and ΔB. Therefore, the difference in activity cycle is considered to be not the only parameter expected to influence $< B >$ and ΔB.

The PMS stars (CTTS, TTS, WTTS, and PTTS) are the group with the strongest magnetic

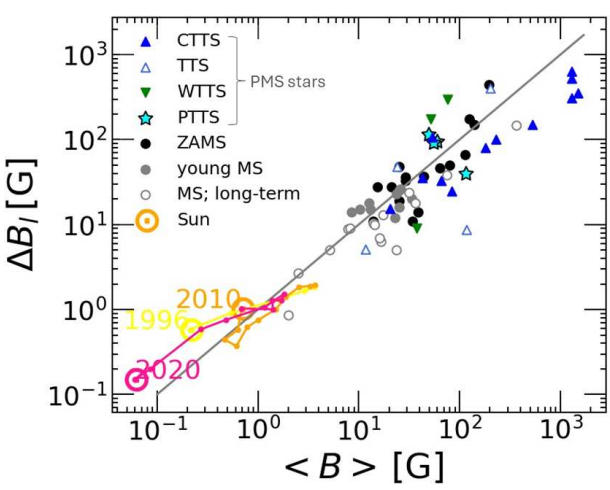

(a) All objects

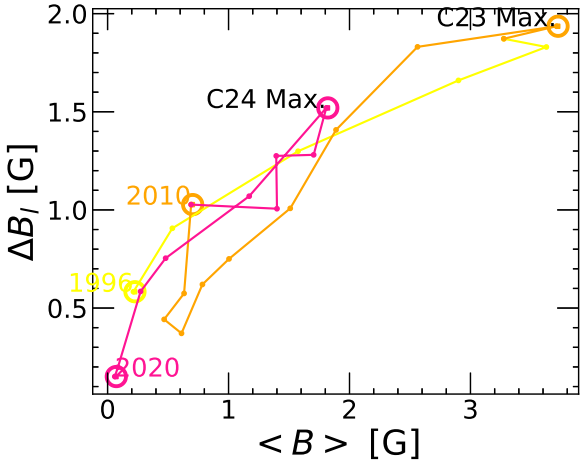

(b) Enlarged view of the solar data in figure 57a

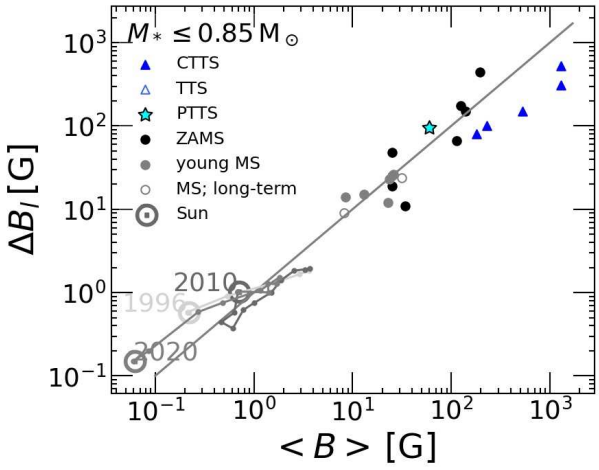

(c) $M_* \leq 0.85$ $M_\odot$; 21 objects

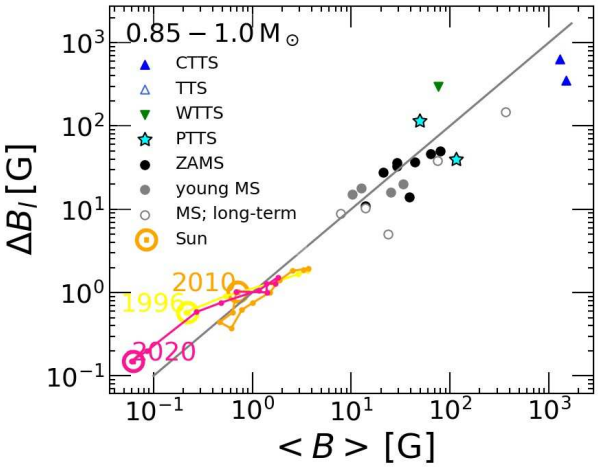

(d) $0.85 < M_* \leq 1.0$ $M_\odot$; 23 objects

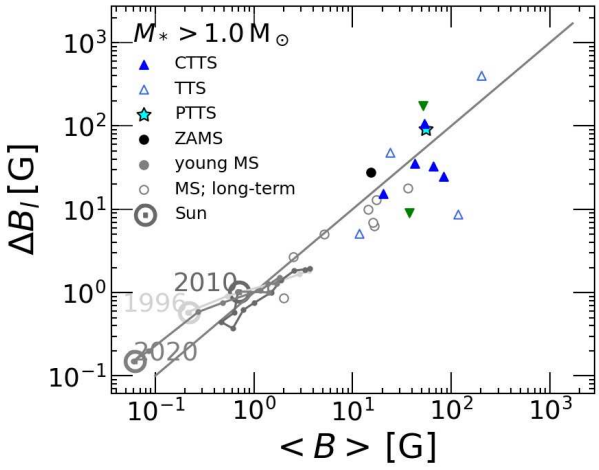

(e) $M_* \geq 1.0$ $M_\odot$; 21 objects

Fig. 57: The relationship between the mean magnetic strength, $< B >$, and their variation, ΔB of the PMS stars and main-sequence stars. The symbols correspond to figure 54. In figure 57c, 57d, and 57e, all objects in figure 54 are categolized by their mass, M_*. The solid line indicates 1:1.

field of all the objects. CTTSs ($\approx 10^6$ yr) have especially large $< B >$ and ΔB. Their $< B >$ and ΔB are smaller than 1:1. There are two possible reasons for this. First, the magnetic flux expansion is expected to be suppressed when the filling factor is large (Shoda et al. 2020). The other possibility is that ΔB is underestimated due to the smaller number of observations, because CTTSs are fainter than main-sequence stars. Brown et al. (2022) also found that ΔB are smaller for objects with fewer observations. On the other hand, $< B >$ and ΔB of PTTSs ($\approx 3 \times 10^7$ yr) are relatively small in the PMS stars. Saar (2001) shows the magnetic field strength decay with their age, $|B| \propto \mathrm{age}^{-0.655}$.

In figure 57c, 57d, and 57e, the objects with higher mass show smaller $< B >$ and ΔB. This is considered to be because the objects with higher mass are expected to have thinner convection zones. Mullan (1973) discussed the relationship between the thickness of the convection zone and the size of a starspot. They predicted that the lower limit of sunspot size, D_{spot}, becomes higher as the convective layer is thicker. They considered that the depth of the spot, H_{s}, is equal to the depth of the convection zone, H_{c}, which yields $2.04 < D_{\mathrm{spot}}/H_{\mathrm{c}} < 6.75$. Yamashita et al. (2022b) showed that the spot coverage is also larger for longer τ_{c} for ZAMS stars, and derived $D_{\mathrm{spot}}/H_{\mathrm{c}} \sim 4.3$.

5 Conclusion

We investigated light variation and chromospheric activities of 220 G, K, and M-type PMS stars in one molecular cloud and six moving groups. We analyzed the high-resolution optical spectra of the 69 PMS stars obtained with VLT/UVES and VLT/X-Shooter, then examined the Hα ($\lambda 6563$ Å), Ca II IRT ($\lambda 8542$ Å), and infrared Mg I ($\lambda 8807$ Å) emission lines.

To detect the weak chromospheric emission lines, we determined the atmospheric parameters ($T_{\rm eff}$ and $\log g$), projected rotational velocity, and the amount of veiling of the PMS star by comparing the observed spectrum with the photospheric model spectrum. After subtracting the photospheric model spectrum from the PMS spectrum, Hα, Ca II, and Mg I were detected as the emission lines.

The previous study for the activity of the main-sequence stars (Noyes et al. 1984) introduced five observational indicators of the dynamo activity, i.e., the rotation, the stellar mass ($M_{\rm star}$), the spectral type ($= T_{\rm eff}$), the thickness of the convective zone, and the convective turnover time ($\tau_{\rm c}$). Noyes et al. (1984) proposed the use of the Rossby number, which involves the rotation period and convective turnover time, as the indicator of stellar activity. They investigated the relationship between the Rossby numbers and the strength of the chromospheric Ca II emission lines for main-sequence stars.

On the other hand, PMS stars are active and show saturated Ca II emission lines. We found out that the faint Mg I emission line is a useful indicator of stellar activity even for such active stars.

The strengths of the Mg I emission lines of the PMS stars with no veiling are comparable to those of ZAMS stars if both kinds of stars have similar Rossby numbers. The Mg I emission lines are considered to be formed by the dynamo activity similar to the ZAMS stars.

The strengths of Mg I emission lines of the PMS stars with veiling are larger than those of the ZAMS stars. These objects are thought to have protoplanetary disks. The mass accretion from the protoplanetary disk makes a shock near the photosphere, and heats the chromosphere. We propose that the chromosphere of the PMS stars are activated not only by the dynamo process but also by mass accretion.

We analyzed the *TESS* light curves for the 178 PMS stars. We categorize the PMS stars into three groups, i.e., the periodic variables, the quasi-periodic variables, and the bursters. The rotational periods of the PMS stars range from 0.26 to 22 days. The amplitudes of the light curves range from $0.002 - 1.311$ mag. The 344 flares are also detected in the light curves of 37 solar-mass PMS stars. The total bolometric energy of the flare is estimated to be $10^{31} - 10^{36}$ erg.

Gallet & Bouvier (2013) proposed the star-disk interaction scenario for the stellar rotation of PMS stars. A CTTS has an optically thick disk. The magnetic field of the star connects to the inner edge of the disk. The magnetic fields are considered to put the brakes on the rotation. Because

the radius of the inner disk is ~ 10 solar radius, its Keplarian rotation is several days. Once the disk disappears as their age, and the magnetic field also dissappears. They claimed that, as a result, WTTSs rotate faster than CTTSs.

All the PMS stars with periodic variability show no near-infrared excess, and their spot coverage and strength of the Ca II emission line are comparable to those of the ZAMS stars. They are $> 10^7$ yr in age, and are considered to no longer have the optically thick disk and mass accretion, and their dynamo processes are like that of the ZAMS stars.

A part of the burster PMS stars show near-infrared excess, larger light variation, and stronger Ca II emission lines than those of the ZAMS stars. It is suggested that these PMS stars have optically thick disks and the mass accretion from the disk induces the outburst and bright emission lines. We showed that the PMS stars obtained the angular momentum by the mass accretion while they have the protoplanetary disks, and the angular momentum is enough to spin up the star.

A series of my works during the Ph.D. course and this doctoral thesis showed the following things:

1. Mass accretion directly heats the chromosphere by shock and induces the emission lines.
2. Mass accretion transports angular momentum to the star and indirectly activates the chromosphere by accelerating the stellar rotation.

The PMS stars and the ZAMS stars have strong chromospheric emission lines, huge sunspots, and high-energy flares. This indicates that the PMS stars and the ZAMS stars have strong magnetic fields originating, at least partially, from the dynamo process.

Acknowledgments

Before entering University of Hyogo, I was an ordinary high school student who was slightly good at mathematics and physics. In the next spring, I will successfully become an astronomer. It is never thought that I could become an astronomer. I cannot thank my teachers enough —Prof. Yoichi Itoh, Prof. Satoshi Honda, and Prof. Toshihito Ishida— to make me realize my potential. At Itoh laboratory, I am the third student to graduate from the doctoral program, and the first student who has been from an undergraduate student to a doctoral course. I want to continue my research for as long as possible.

The author would like to thank Prof. Koji Kawabata, Prof. Satoshi Takeuchi, Prof. Yoshihito Tanaka, and Prof. Satoshi Honda, the vice chairpersons. I am grateful to them for their very careful screening process despite the different fields of materials science and astronomy. Thanks to them, I have acquired the ability to explain to people in different fields. Now I think if I review students' work in other fields in the future, I should try to understand it properly.

I am especially indebted to my co-researchers of the three papers (Yamashita et al. 2020, 2022ab), Prof. Yoichi Itoh, Prof. Yumiko Oasa, and Dr. Yuhei Takagi. Dr. Takagi is well-versed in the temperature measurements of PMS stars and is reliably senior to me. They taught me their attitude toward astronomical observation and observing results, i.e., we must not waste a second while we observe. I will not forget the spirit of optical and infrared astronomy after my graduation.

To acquire the knowledge needed to write the introduction (section 1), I would like to thank all the members of the Nishi-Harima Astronomical Observatory who always engaged in heated discussions at the seminar. Thank you to the young researchers in other institutions for encouraging me; Misaki Sagawa, Dr. Masayuki Yamaguchi, Dr. Mayuko Mori, Takahiro Kanai, Hibiki Miura, and everyone else.

To section 2, I appreciate Prof. Jung and Prof. Kim for sending me the numerical results of the evolution tracks of Jung & Kim (2007) through private communication (see figure 19). Also, I would like to thank Dr. Yuhei Takagi (for Semester 21B) and Dr. Akira Arai (for Semester 22A) for the service observations of the Subaru Telescope / HDS (figure 19). I would like to express my great appreciation to Dr. Morihana and Dr. Kudo at Hawaii Observatory for consulting with me on every occasion. This paper includes data collected with the TESS mission, from the MAST data archive at the Space Telescope Science Institute (STScI). When we conducted solar observations at Hida Observatory of Kyoto University, we received kind support from Prof. Kiyoshi Ichimoto and Dr. Satoru UeNo for observations, Dr. Daiki Yamasaki for recommending the observation at Hida Observatory, and Ms. Haruhi Shirato, Mr. Hashimoto, and Mr. Matsuda for teaching me the analysis

of the Domeless Solar Telescope. Analyzing solar data was challenging for me, and I hope to resume analysis after graduation.

When I wrote Yamashita et al. (2022b), I wished to thank Dr. Yuta Notsu and Dr. Kosuke Namekata. They taught me how to analyze the *TESS* satellite data. I would also like to thank Prof. Nogami, Prof. Maehara, and everyone else who always asked questions and gave meaningful comments at the conference. Their technique and comments were helpful in writing the discussion about the stellar spot and flare (section 4.2 and 4.4).

About the section 4.5, 4.6, and 6.1, I would also like to thank Prof. Shin Toriumi, Prof. Ikuyuki Mitsuishi, Mr. Takashi Ito, and Mr. Kota Nakazawa. Mr. Ito not only obtained the X-ray intensities but also analyzed X-ray spectra in between his master's theses. They will be co-authors of the papers I plan to write. After my graduation, I would like to continue to promote interesting collaborative research.

This work would not have been possible without the financial support of the JSPS KAKENHI grant number 23KJ1855. During the third grade of the PhD course, I am also supported as JSPS Research Fellow (DC2). For attending the international research meeting, COOL STARS 21, I was also supported by a grant from the Hayakawa Satio Fund awarded by the Astronomical Society of Japan. Also, I was supported by a scholarship from the Japan Association of University Women and would like to acknowledge them. It was an invaluable experience to participate in national and international conferences and workshops such as APRIM and PPVII and interact with astronomers from around the world; Vietnam, Hawaii, India, Netherlands, France, Australia, Russia... I would like to continue my research in the future, keeping in mind that the time available for our research is limited.

Last, I thank my family and all my ancestors for giving me your talents. I'm enjoying my research.

References

Allen's Astrophysical Quantities, 4th edition, Springer

Arnaud, K.A., 1996, Astronomical Data Analysis Software and Systems V, eds. Jacoby G. and Barnes J., p17, ASP Conf. Series volume 101.

Bailer-Jones, C. A. L., Rybizki, J., Fouesneau, M., Mantelet, G., & Andrae, R. 2018, ApJ, 156, 58

Baliunas, S., Sokoloff, D., & Soon, W. 1996, Astrophys. J., 457, L99

Basri, G., & Batalha, C. 1990, Astrophys J, 363, 654

Batalha, C. C., & Basri, G. 1993, ApJ, 412, 363

Bessell, M. S., & Brett, J. M. 1988, Publ Astron Soc Pacific, 100, 1134

Batalha, C. C., Stout-Batalha, N. M., Basri, G., & Terra, M. A. O. 1996, ApJS, 103, 211.

Berdyugina, S. V. 2005, Living Rev Sol Phys, 2, 1

Blanco-Cuaresma, S., Soubiran, C., Heiter, U., & Jofre, P. 2014, Astron Astrophys, 569, 111

Boro Saikia, S., Marvin, C. J., Jeffers, S. V., et al. 2018, Astron Astrophys, 616, 108

Bouvier, J. 1990, Astron J, 99, 946

Bouvier, J., Cabrit, S., Fernandez, M., Martin, E. L., & Matthews, J. M. 1993, Astron Astrophys, 272, 176

Brickhouse, N. S., Cranmer, S. R., Dupree, A. K., Luna, G. J. M., & Wolk, S. 2010, Astrophys J, 710, 1835

Brown, E. L., Jeffers, S. V., Marsden, S. C., et al. 2022, Mon Not R Astron Soc, 514, 4300

Calvet, N., Basri, G., & Kuhi, L. V. 1984, Astrophys J, 277, 725

Calvet, N., & Gullbring, E. 1998, Astrophys J, 509, 802

Camenzind. 1990, Rev Mod Astron, 3, 234

Carlsson, M., De Pontieu, B., & Hansteen, V. H. 2019, Annu Rev Astron Astrophys, 57, 189

Chatzistergos, T., Ermolli, I., Krivova, N. A., et al. 2022, Astron Astrophys, 667, 167

Cody, A. M., Stauffer, J., Baglin, A., et al. 2014, AJ, 147

Cody, A. M., & Hillenbrand, L. A. 2018, Astron J, 156, 71

Coffey, D., Bacciotti, F., & Podio, L. 2008, Astrophys J, 689, 1112

Cohen, J. G., Persson, S. E., Elias, J. H., & Frogel, J. A. 1981, Astrophys J, 249, 481

Cranmer, S. R. 2008, Astrophys. J., 689, 316

Crosby, N. B., Aschwanden, M. J., & Dennis, B. R. 1993, SoPh, 143, 275C

Cutri, R. M., Skrutskie, M. F., van Dyk, S., et al. 2003, VizieR Online Data Catalog: II/246

Da Rio, N., Robberto, M., Hillenbrand, L. A., Henning, T., & Stassun, K. G. 2012, Astrophys J, 748

Davenport, J. R. A., Covey, K. R., Clarke, R. W., et al. 2019, ApJ, 871, 241

Deinzer, W. 1965, Astrophys. J., 141, 548

Dunn, R. B., Evans, J. W., Jefferies, J. T., et al. 1968, ApJS, 15, 275

Fisher et al., 2023 Protostars and Planets VII, p.355

Fleck, B., Deubner, F.-L., Maier, D., & Schmidt, W. 1994, IAU Symp, 154, 65

Folsom et al. 2016, MNRAS, 457, 580

Folsom et al. 2018, MNRAS, 474, 4956

Fontenla, J. M., Stancil, P. C., & Landi, E. 2015, Astrophys J, 809 , 157

Fontenla, J. M., Linsky, J. L., Garrison, J., et al. 2016, Astrophys J, 830, 154

Furlan, E., Watson, D. M., McClure, M. K., et al. 2009, Astrophys J, 703, 1964

Frasca, A., Biazzo, K., Alcala, J. M., et al. 2017, A&A, 602, 33

Fritzewski, D. J., Barnes, S. A., James, D. J., Jrvinen, S. P., & Strassmeier, K. G. 2021, A&A, 656

Frohlich, C., & Lean, J. 2004, Astron Astrophys Rev, 12, 273

Fukugita, M., Ichikawa, T., Gunn, J. E., et al. 1996, ApJ, 111, 1748

Fuhrmeister, B., Schmitt, J. H. M. M., & Hauschildt, P. H. 2010, Astron Astrophys, 511, 293

Gaia Collaboration, 2018, A&A, 616, 1

Gallet, F., & Bouvier, J. 2015, A&A, 577, 1

Getman, K. V., Feigelson, E. D., & Garmire, G. P. 2023, Astrophys J, 952, 63

Ghez, A. M., Neugebauser, G., & Matthews, K. 1993, ApJ, 106, 2005

Ghosh, A., Sharma, S., Ninan, J. P., et al. 2022, Astrophys J, 926, 68

Gilliland, R. L. 1986, Astrophys J, 300, 339

Gilman, P. A. 1980, in IAU Colloquium Stellar Tublence, ed. D. Gray, & J. L. Linsky, Vol. 51 (Springer, New York, NY), 19

Glebocki, R., & Gnacinski, P. 2005, VizieR Online Data Cat, 3244

Gontcharov, G. A., & Mosenkov, A. V. 2017, Mon Not R Astron Soc, 472, 3805

Gray, D. F. 2005, The observation and analysis of stellar photospheres, Cambridge (third)

Haisch, Jr., K. E., Lada, E. A., & Lada, C. J. 2001, Astrophys J, 553, L153

Hale, G.E., Ellerman, F., Nicholson, S.B., Joy, A.H. 1919, Astrophys J, 49, 153

Hartmann, L., Soderblom, D. R., Noyes, R. W., Burnham, N., & Vaughan, A. H. 1984, Astrophys J, 276, 254

Hartmann, L., Herczeg, G., & Calvet, N. 2016, Annu Rev Astron Astrophys, 54, 135

Handberg, R., Lund, M. N., White, T. R., et al. 2021, Astron J, 162, 170

Hamann, F., & Persson, S. E. 1992, ApJS, 82, 247

Herczeg, G. J., & Hillenbrand, L. A. 2014, Astrophys J, 786, 97

Hosoya, K, Itoh, Y., Oasa, Y., Gupta, R., & Sen, A. K. 2019, Int J Astron Astrophys, 09, 154

Honda, S., Notsu, Y., Maehara, H., et al. 2015, Publ Astron Soc Japan, 67, 1

Houdebine, E. R., Mullan, D. J., Bercu, B., Paletou, F., & Gebran, M. 2017, ApJ, 837, 96

Hussain, G. A. J., & Alecian, E. 2014, Proc Int Astron Union, 9, 25

Ikuta, K., Namekata, K., Notsu, Y., et al. 2023, Astrophys J, 948, 64

Ishikawa, R., Bueno, J. T., Del Pino Aleman, T., et al. 2021, Sci Adv, 7, 1

Ito, T., Nakazawa, K. & Mitsuishi, I., in prep., Master thesis of the University of Nagoya

Ilin, E., Schmidt, S. J., Davenport, J. R. A., & Strassmeier, K. G. 2019, Astron Astrophys, 622, 133

Isik, E., Shapiro, A. I., Solanki, S. K., & Krivova, N. A. 2020, ApJL, 901, L12

James, D. J., & Jeffries, R. D. 1997, MNRAS, 291, 252

Jones, A., Noll, S., Kausch, W., Szyszka, C., & Kimeswenger, S. 2013, Astron Astrophys, 560

Jung, Y. K., & Kim, Y.-C. 2007, J. Astron. Space Sci., 24, 1

Kenyon S. J., Gomez M., Marzke R. O., Hartmann L. 1994. Astron. J. 108, 251

Kenyon S. J., Hartmann L., Strom K. M., Strom S. E. 1990. Astron. J. 99, 869

Koch, D. G., Borucki, W. J., Basri, G., et al. 2010, ApJL, 713, 79

Kochukhov, O., Hackman, T., Lehtinen, J. J., & Wehrhahn, A. 2020, Astron Astrophys, 635

Konigl. 1991, Astrophys J, 370, 39

Kraus, S., Hofmann, K.-H., Malbet, F., et al. 2009, A&A, 508, 787

Kraus, A. L., Ireland, M. J., Hillenbrand, L. A., & Martinache, F. 2012, ApJ, 745, 19

Kulenthirarajah, L., Donati, J. F., Hussain, G., Morin, J., & Allard, F. 2019, Mon Not R Astron Soc, 487, 1335

Lanza, A. F., Rodon, M., Pagano, I., Barge, P., & Llebaria, A. 2003, A&A, 403, 1135

Leinert, C., Zinnecker, H., Weitzel, N., et al. 1993, A&A, 278, 129

Linsky, J. L. 2017, Annu Rev Astron Astrophys, 55, 159

Maehara, H., Shibayama, T., Notsu, S., et al. 2012, Nature, 485, 478

Marsden, S. C., Carter, B. D., & Donati, J.-F. 2009, MNRAS, 399, 888

Donati J.-F. et al., 2008, MNRAS, 386, 1234; Magnetic Protostars and Planets (MaPP)

Masuda, K. 2022, Astrophys J, 937, 94

Masuda, K. 2022, ApJ, 933, 195

Donati J.-F. et al., 2014, MNRAS, 444, 3220; Magnetic Topologies of Young Stars and the Survival of massive close-in Exoplanets (MaTYSSE)

Meyer, M., Calvet, N., & Hillenbrand, L. 1997, Astron Jounal, 114, 288

Michel, A., van der Marel, N., & Matthews, B. C. 2021, Astrophys J, 921, 72

Mittag, M., Hempelmann, A., Schmitt, J. H. M. M., et al. 2017, Astron Astrophys, 607, 1

Mohanty, S., Jayawardhana, R., & Basri, G. 2005, ApJ, 626, 498

Morris, B. M. 2020, ApJ, 893, 67

Mullan, D. J. 1973, ApJ, 186, 105

Muzerolle, J., Hartmann, L., & Calvet, N. 1998, ApJ, 116, 455

Namekata, K., et al. 2022, ApJ, 926, L5

Namekata, K., Toriumi, S., Airapetian, V. S., et al. 2023, Astrophys J, 945, 147

Neuhauser, R., Strerzik, M. F., Schmitt, J. H. M. M., Wichmann, R., & Krautter, J. 1995, A&A, 297, 391

Noguchi, K., Aoki, W., Kawanomoto, S., et al. 2002, PASJ, 54, 855

Noll, S., Kausch, W., Barden, M., et al. 2012, Astron Astrophys, 543, A92

Notsu, Y., Shibayama, T., Maehara, H., et al. 2013, ApJ, 771

Notsu, Y., Honda, S., Maehara, H., et al. 2015b, PASJ, 67, 33

Notsu, Y., Maehara, H., Honda, S., et al. 2019, ApJ, 876, 58

Noyes, R. W., Hamann, F. W., Baliunas, S. L., & Vaughan, A. H. 1984, AJ, 279, 763

Okamoto, S., Notsu, Y., Maehara, H., et al. 2021, AJ, 906, 72

Palacios A., Gebran M., Josselin E., Martins F., Plez B., Belmas M., Lebre A., 2010, A&A 516, A13

Pevtsov, A. A., Fisher, G. H., Acton, L. W., et al. 2003, Astrophys J, 598, 1387

Radick, R. R., Lockwood, G. W., Henry, G. W., Hall, J. C., & Pevtsov, A. A. 2018, Astrophys J, 855, 75

Rebull, L. M., Stauffer, J. R., Bouvier, J., et al. 2016a, AJ, 152, 113

Ricker, G. R., et al. 2015, J. Astron. Telesc., Instrum. Syst., 1, 014003

Robinson, C. E., Espaillat, C. C., & Rodriguez, J. E. 2022, Astrophys J, 935, 54

Robrade, J., & Schmitt, J. H. M. M. 2006, Astron Astrophys, 449, 737

Saar 2001, CoolStars, 223, 292

Sammis, I., Tang, F., & Zirin, H. 2000, Astrophys J, 540, 583

Scargle, J. D. 1982, AJ, 263, 835

Shibayama, T., Maehara, H., Notsu, S., et al. 2013, ApJS, 209, 5

Shoda et al. 2020, ApJ, 896, 123

Shu, F., Najita, J., Ostriker, E., & Wilken, F. 1994, Astrophys J, 429, 781

Skumanich, A. 1972, ApJ, 171, 565

Soderblom, D. R., Stauffer, J. R., & Hudon, J. D. 1993, ApJ, 85, 315

Stahler, S. W., & Palla, F. 2004, The Formation of Stars (Wiley-VCH)

Stauffer, J., Rebull, L., Bouvier, J., et al. 2016, AJ, 152, 115

Stepien, K., Schmitt, J.H.M.M., Voges, W., 2001, A&A,370, 157

Strassmeier, K. G., Rice, J. B., 1998, A&A, 330, 685

Stelzer, B., Fernandez, M., Costa, V. M., et al. 2003, A&A, 411, 517

Takagi, Y., Itoh, Y., & Oasa, Y. 2014, Publ Astron Soc Japan, 66, 1

Takeda, Y., Ohkubo, M., Sato, B., Kambe, E., & Sadakane, K. 2005, Publ Astron Soc Japan, 57, 27

Toriumi, S., & Airapetian, V. S. 2022, ApJ, 927, 179

Toriumi, S., Airapetian, V. S., Namekata, K., & Notsu, Y. 2022, ApJS, 262, 46

Toriumi, S., & Wang, H. 2019, Living Reviews in Solar Physics, 16, 3

Tonry, J. L., Denneau, L., Flewelling, H., et al. 2018, Astrophys J, 867, 105

Tout, C. A., Livio, M., & Bonnell, I. A. 1999, Mon Not R Astron Soc, 376, 360

Tu, L., Johnstone, C. P., Gudel, M., & Lammer, H. 2015, 3, 1

Uchida, Y., & Shibata, K. 1985, Publ Astron Soc Japan, 37, 515

Valenti J. A., Johns-Krull C. 2001. In Magnetic Fields Across the timeprung-Russell Diagram, ed. G. Mathys, S. K. Solanki, D. T. Wickramasinghe. ASP Conf. Ser. 248:179. San Francisco: ASP

van de Hurst, 1968, Nebulae and Interstellar Matter

Vernazza, J. E., Avrett, E. H., & Loeser, R. 1981, ApJS, 45, 635

Villebrun, F., Alecian, E., Hussain, G. A. J., et al. 2019, A&A, 622, 72

Voges, W., Aschenbach, B., Boller, T., et al. 1999, A&A, 349, 389

Wahhaj, Z., Cieza, L., Koerner, D. W., et al. 2010, ApJ, 724, 835

Webb, N. A., Coriat, M., Traulsen, I., et al. 2020, Astron Astrophys, 641, 136

Wright, N. J., Drake, J. J., Mamajek, E. E., & Henry, G. W. 2011, Astrophys J, 743

Wright, N. J., & Drake, J. J. 2016, Nature, 535, 526

Yamashita, M., Itoh, Y., & Takagi, Y. 2020, PASJ, 72, 80

Yamashita, M., & Itoh, Y. 2022a, PASJ, 74, 557

Yamashita, M., Itoh, Y., & Oasa, Y. 2022b, PASJ, 74, 1295

Yang, H., Johns-Krull, C. M., & Valenti, J. A. 2008, Astron J, 136, 2286

Yang, H., & Johns-Krull, C. M. 2011, Astrophys J, 729

Yang, H., Herczeg, G. J., Linsky, J. L., et al. 2012, Astrophys J, 744

Yu, J., Khanna, S., Themessl, N., et al. 2023, Astrophys J Suppl Ser, 264, 41

Zacharias, N., Finch, C. T., Girard, T. M., et al. 2013, ApJ, 145, 1

Zuckerman, B., & Song, I. 2004, A&A, 42, 685

6 Appendix

6.1 Data Reduction for X-ray data

We used the data set of the 90 PMS stars analyzed by Mr. Takashi Ito, a second-year master's student at Nagoya University. The photometric data are obtained by the X-ray satellite ROSAT (ROentgen SATellite) all-sky survey in 1990-1991 and by XMM (X-ray Multi-Mirror Mission) - Newton telescope. The spectra obtained by XMM-Newton are also analyzed.

ROSAT observed an energy band of $0.1-2.4\,\mathrm{keV}$, which corresponds to a wavelength of $5.2-124$ Å. The photometric counts are converted into the Hardness Ratio, flux, and X-ray luminosity, L_{X}. The detail is described in Voges et al. (1999). The Hardness Ratio is defined and calculated as $\equiv (H-S)/(H+S)$, in which H is the hard X-ray ($0.5-2.0\,\mathrm{keV}$) count value and S is the soft X-ray ($0.1-0.4\,\mathrm{keV}$) count value. In 3.3.5 of Voges et al. (1999), they constructed an empirical law for converting the counts of the main-sequence stars are converted to fluxes with the Hardness Ratio;

$$\mathrm{flux} = (5.3 \cdot \mathrm{HR} + 8.31) \cdot 10^{-12} \cdot \mathrm{counts} \cdot \mathrm{s}^{-1}\ [\mathrm{erg\ cm^{-2}\ s^{-1}}] \tag{36}$$

The luminosity, L, is the total energy from a star per unit of time. The solar absolute luminosity is $L_{\odot} = 3.828 \times 10^{26}\ \mathrm{J \cdot s^{-1}}$. Considering a spherically symmetric object, luminosity L is equal to the energy per unit time flowing through a sphere of radius r. The flux, f, is converted into L with r;

$$L = 4\pi r^2 f \tag{37}$$

The XMM-Newton telescope is equipped with three detectors mos1, mos2, and pn. The energy band of the CCD camera covers $0.15-15\,\mathrm{keV}$, corresponding to a wavelength $0.83-83$ Å. The photometric values of $mos1\ [\mathrm{cts}], mos2\ [\mathrm{cts}], pn\ [\mathrm{cts}]$ and three total $epic\ [\mathrm{cts}]$ were obtained. In this study, the fluxes in $0.20-12\,\mathrm{keV}$ converted from $epic\ [\mathrm{cts}]$ are refereed from the 4XMM-Data Release12 catalog (Webb et al. 2020). This is because the CCDs have low sensitivity in the energy bands $0.15-0.20\,\mathrm{keV}$ and $12-15\,\mathrm{keV}$. Then the fuxes are converted into the luminosity, L_{X}, by equation 37. Some PMS stars were observed several times. The spatial resolution is $0.1" - 8.0"$.

Newton spectroscopic data were also analyzed for the eight PMS stars. The PMS stars were selected on the following conditions: I) the magnetic field strength B has been investigated in previous studies, II) high-dispersion spectroscopic observations in the optical to near-infrared including the wavelength of chromospheric emission lines such as Ca II, Hα, Mg I are obtained, and III) they are not observed as binary stars. The eight PMS stars are at various evolutionary stages, and their magnetic field strengths range from $20-3100$ G. Xspec (Arnaud 1996), which is a package developed by NASA for the analysis of high-energy spectra, is used for data reduction. For those stars with high S/N ratio and multi-temperature structures, the multi-temperature model was fitted. In this study, the

thermal collisional ionization equilibrium plasma model of Robrade & Schmitt 2005, a previous spectroscopic analysis for TTS, was applied. The model was divided into at most three components, each of which is determined by the $L_{\rm X}$, Emission Measure ($\equiv \int n_{\rm e} n_{\rm H} dV$), coronal temperature, hydrogen column density, $N_{\rm H}$, and metal abundance in the corona (table 16). $L_{\rm X}$ including the extinction was corrected by $N_{\rm H}$. The best-fit values were obtained by the χ-square test by using Xspec. The fitting error was calculated with a 90% confidence interval by the χ-square test. The χ value is shifted until it increases to (optimal value) + (90% confidence interval of the χ-square distribution with 1 degree of freedom), and the error is considered to be the difference between the value of the physical quantity at the best fitting.

All the above analyses were performed by Mr. Takashi Ito.

Table 16: Magnetic strength, and X-ray luminosity of the PMS stars.

		ROSAT	XMM-Newton					
		phot.	phot.	spec.				
Object Name	$< B >$	$L_{\rm X}$	$L_{\rm X}$	$L_{\rm X}$	EM	kT	$N_{\rm H}$	Abund.
	[G]	[erg · s^{-1}]	[erg · s^{-1}]	[erg · s^{-1}]	[cm^{-3}]	[keV]	[$\times 10^{22}$ cm^{-2}]	
2MASS J03442257+3201536			1.1×10^{29}					
AA Tau	2780		3.5×10^{29}					
AU Mic			2.6×10^{29}					
BP Tau	2170		1.3×10^{30}					
CHX22			3.9×10^{30}	4.6×10^{30}	1.3×10^{54}	0.46	0.43	0.55
COUP 1350			6.5×10^{30}	4.1×10^{30}	9.1×10^{53}	3.24	0.14	1.26
CPD-43 7188	31	2.6×10^{30}						
CY Tau	1160		1.7×10^{29}					
Cl* Melotte 22 PELS 031	44	5.1×10^{29}						
Cl* NGC 6530 SCB 7	12		1.1×10^{29}					
Cl* NGC 6530 SCB 739			3.3×10^{28}					
DG Tau	2550		2.9×10^{29}	2.3×10^{34}	1.8×10^{60}	0.05	2.06	0.84
DH Tau	2680		5.9×10^{30}					
DK Tau	2640		4.6×10^{29}					
DN Tau	540		1.0×10^{30}	4.9×10^{29}	2.0×10^{53}	0.86	0.11	0.15
DR Tau			5.3×10^{29}					
DS Tau		1.4×10^{29}						
DX Leo	29		1.5×10^{29}					
EK Dra	75		1.4×10^{30}					
EP Eri	34		8.2×10^{28}					
EV Lac	4000		5.0×10^{28}					
FN Tau			6.3×10^{29}					
GG Tau	1240		2.7×10^{29}					
GJ 729	2000		1.5×10^{34}					
GK Tau	2280		7.5×10^{29}					
GM Aur	2220		1.1×10^{30}	3.7×10^{29}	1.0×10^{53}	1.54	0.14	0.31
GO Tau			1.7×10^{29}					
HBC 374			2.7×10^{30}					
HBC 376		1.2×10^{30}						
HBC 427			4.0×10^{30}					
HBC 741	64	1.7×10^{30}						
HD 133938	29	3.6×10^{30}						
HD 135127	4000	8.8×10^{29}						
HD 137059	400	1.7×10^{30}						
HD 143978	300	7.3×10^{29}						
HD 147048	300	2.5×10^{30}						
HD 285778	1500		1.4×10^{30}	1.0×10^{30}	1.4×10^{53}	0.87	0	0.14
HIP 10272	21	1.8×10^{29}						
HIP 17695	3100		5.5×10^{29}					
J12156+526 StKM 2-809	4500		1.3×10^{29}					
LO Peg	140		5.8×10^{29}					
LkCa 04	1500	7.8×10^{29}						
LkCa 14		1.2×10^{30}						
LkCa 15			1.9×10^{30}					
LkCa 19		5.0×10^{30}	4.9×10^{30}					
LkHa 86			7.5×10^{29}					
Mel25 179	26	2.6×10^{28}						
Mel25 43	9	7.1×10^{28}						

Table 16: (Continued)

		ROSAT	XMM-Newton					
		phot.	phot.	spec.				
Object Name	$< B >$	$L_{\rm X}$	$L_{\rm X}$	$L_{\rm X}$	EM	kT	$N_{\rm H}$	Abund.
	[G]	[erg · s^{-1}]	[erg · s^{-1}]	[erg · s^{-1}]	[cm^{-3}]	[keV]	[$\times 10^{22}$ cm^{-2}]	
NGC 2264 108	28		1.1×10^{31}					
NGC 2264 121	166		5.2×10^{31}					
NGC 2264 84	450		1.0×10^{30}					
PAR 1394	350		7.7×10^{29}					
PAR 1455	300		2.0×10^{30}					
PAR 1736	1500		6.1×10^{32}					
PAR 2244	860		8.5×10^{30}					
PX Vul	1400		8.7×10^{29}					
RECX 04			8.6×10^{29}					
RECX 06		9.7×10^{28}	2.7×10^{29}					
RECX 07			1.9×10^{30}					
RECX 09			4.6×10^{29}					
RECX 10			5.2×10^{29}					
RECX 11			3.2×10^{30}					
RECX 15			3.3×10^{28}					
RX J1204.6-7731		8.4×10^{29}						
RY Lup			7.6×10^{29}					
RY Tau			3.2×10^{30}					
SU Aur		5.2×10^{30}	5.6×10^{30}					
T Tau	2370	8.9×10^{29}	4.8×10^{30}					
TAP 10	700		7.5×10^{30}					
TAP 26	380	1.2×10^{30}						
TWA 01	3000		1.8×10^{30}					
TWA 22		6.1×10^{28}						
TWA 5A	4900	1.4×10^{30}	9.4×10^{29}					
UX Tau		3.5×10^{30}						
V 1001 Sco	35	9.4×10^{29}						
V 1002 Sco	24	4.1×10^{30}						
V 1152 Sco	86	2.2×10^{30}						
V1023 Tau	2500		2.7×10^{30}	2.1×10^{30}	1.0×10^{54}	0.72	0.37	0.17
V1044 Ori			3.8×10^{30}	6.2×10^{30}	1.8×10^{53}	2.18	0	0.79
V1204 Tau		1.7×10^{30}						
V1297 Tau		1.5×10^{30}						
V1321 Tau			4.2×10^{29}					
V1348 Tau		1.9×10^{30}						
V1840 Ori		5.4×10^{30}						
V410 Tau	490		5.4×10^{30}					
V447 Lac	39	5.0×10^{28}						
V819 Tau	300		1.2×10^{30}	9.5×10^{29}	3.4×10^{53}	0.97	0.27	0.24
V830 Tau	250	7.8×10^{29}	4.6×10^{30}	1.8×10^{30}	9.7×10^{53}	1.65	0.08	0.07
V836 Tau		1.8×10^{30}						
YY Ori			1.5×10^{30}					

The magnetic field strength, $< B >$, is refereed from MaPP (2008), MaTYSSE (2014), Villebrun et al. (2019), Yang (2008), Yang (2011), Folsom et al. (2016), and Folsom et al. (2018).

6.2 Papers

1. ◯**Mai Yamashita, Yoich Itoh, Yuhei Takagi, "Measurements of the Ca II infrared triplet emission lines of pre-main-sequence stars", PASJ, Vol. 72, id. 80 (pp. 1-17), August 2020**
   https://academic.oup.com/pasj/article-abstract/72/5/80/5889941

2. ◯**Mai Yamashita, Yoich Itoh, "Measurements of chromospheric Mg I emission lines of zero-age main-sequence stars", PASJ, Vol. 74, id. 557 (pp. 1-12), April 2022**
   https://academic.oup.com/pasj/article-abstract/74/3/557/6575674

3. ◯**Mai Yamashita, Yoich Itoh, Yumiko Oasa, "Starspots, chromospheric emission lines, and flares of Zero-Age Main-Sequence Stars", PASJ, Vol. 74, id. 1295 (pp. 1-14), September 2022**
   https://academic.oup.com/pasj/article-abstract/74/6/1295/6694273

Continued on the next page.

Publ. Astron. Soc. Japan (2020) 72 (5), 80 (1–17)
doi: 10.1093/pasj/psaa073
Advance Access Publication Date: 2020 August 8

Measurements of the Ca II infrared triplet emission lines of pre-main-sequence stars

Mai YAMASHITA,[1,*] Yoichi ITOH,[1] and Yuhei TAKAGI[2]

[1]Nishi-Harima Astronomical Observatory, Center for Astronomy, University of Hyogo, 407-2 Nishigaichi, Sayo, Sayo, Hyogo 679-5313, Japan
[2]Subaru Telescope, National Astoronomical Observatory of Japan, 650 North A'ohoku Place, Hilo, HI 96720, USA

*E-mail: yamashita@nhao.jp

Received 2020 March 19; Accepted 2020 July 3

Abstract

We investigated the chromospheric activity of 60 pre-main-sequence (PMS) stars in four molecular clouds and five moving groups. It is considered that strong chromospheric activity is driven by the dynamo processes generated by stellar rotation. In contrast, several researchers have pointed out that the chromospheres of PMS stars are activated by mass accretion from their protoplanetary disks. In this study, the Ca II infrared triplet (IRT) emission lines were investigated utilizing medium- and high-resolution spectroscopy. The observations were conducted with Nayuta/MALLS and Subaru/HDS. Additionally, archive data obtained by Keck/HIRES, VLT/UVES, and VLT/X-Shooter were used. The small ratios of the equivalent widths indicate that Ca II IRT emission lines arise primarily in dense chromospheric regions. Seven PMS stars show broad emission lines. Among them, four PMS stars have more than one order of magnitude brighter emission line fluxes compared to the low-mass stars in young open clusters. The four PMS stars have a high mass accretion rate, which indicates that the broad and strong emission results from a large mass accretion. However, most PMS stars exhibit narrow emission lines. No significant correlation was found between the accretion rate and flux of the emission line. The ratios of the surface flux of the Ca II IRT lines to the stellar bolometric luminosity, $R'_{\rm IRT}$, of the PMS stars with narrow emission lines are as large as the largest $R'_{\rm IRT}$ of the low-mass stars in the young open clusters. This result indicates that most PMS stars, even in the classical T Tauri star stage, have chromospheric activity similar to zero-age main-sequence stars.

Key words: stars: activity — stars: chromospheres — stars: pre-main sequence — techniques: spectroscopic

1 Introduction

The chromosphere of a star is the region between the photosphere and corona. The temperature of the chromosphere gradually increases with radial distance from the photosphere; in the case of the Sun, it is from almost 4000 K at the bottom to 8000 K at the top (Vernazza et al. 1981). Because of these high temperatures, atoms emit some permitted lines like Hα and Ca II. Several high-spatial-resolution observations of the Sun have shown that in the chromosphere the abovementioned emission lines form under the influence of strong magnetic fields, such as faculae and plages near dark spots (Linsky 2017). The Hinode satellite has

obtained space- and time-resolved images of the solar chromosphere and revealed its energetic activity (Katsukawa et al. 2007). Over a 30 yr period, Livingston (2007) showed that the fluxes of the Ca II K, Hα, and He I lines were strong when the solar magnetic activity was high. These observations revealed the relationship between the emission line strengths and the chromospheric activity induced by the magnetic field.

For main-sequence stars, chromospheric activity is often discussed in relation to stellar rotation. It is claimed that chromospheric activity is driven by the magnetic field, which is generated by the dynamo process. Wilson (1978) showed that chromospheric activity analogous to that associated with the solar magnetic activity cycle is ubiquitous in stars along the lower main sequence. As mentioned in Noyes et al. (1984), rotation is not the only parameter related to the dynamo process: the stellar mass, spectral type, depth of convection zone, and convective turnover time (τ_c) are also related. These five parameters are included in the Rossby number (N_R), which is defined as P_{obs}/τ_c, where P_{obs} is the stellar rotational period. According to the standard dynamo theory in Parker (1955), the magnetic activity at the stellar surface becomes stronger with increasing rotation speed and strength of differential rotation.

It is well established that young stars are fast rotators (e.g., Bouvier et al. 1990). Skumanich (1972) found that the luminosity of the Ca II emission lines and the rotational velocity of solar-mass stars with an age of 10^7 yr are one order of magnitude larger than those of stars with age 10^{10} yr. Soderblom et al. (1993) revealed strong emission lines of the Ca II infrared triplet (IRT; $\lambda\lambda$8498, 8542, 8662 Å) of low-mass stars in a young open cluster, M45 (age 130 $\pm$ 20 Myr, 0.6–1.4 $M_\odot$). Marsden, Carter, and Donati (2009) observed low-mass stars in young open clusters, IC 2391 and IC 2602, including rapidly rotating stars. The ages of IC 2391 and IC 2602 are 50 $\pm$ 5 Myr and 30 $\pm$ 5 Myr, respectively (Stauffer et al. 1997; Barrado y Navascués et al. 2004). The cluster members are considered to be on the zero-age main sequence (ZAMS) or in the last phase of evolving to ZAMS with a mass between 0.8 $M_\odot$ and 1.5 $M_\odot$. Soderblom et al. (1993) and Marsden, Carter, and Donati (2009) calculated R'_{IRT} from the equivalent widths (EQWs). R'_{IRT} describes the ratio of the surface flux of the Ca II IRT emission lines to the stellar bolometric luminosity. They found that R'_{IRT} is constant at levels of around $\log R'_{\lambda 8498} \sim -4.4$, $\log R'_{\lambda 8542} \sim -4.2$, and $\log R'_{\lambda 8662} \sim -4.3$ for stars with $\log N_R \leq -1.1$. These regions are called the saturated regime. For stars with $\log N_R \geq -1.1$, R'_{IRT} decreases with increasing N_R. This region is called the unsaturated regime. Marsden, Carter, and Donati (2009) suggested that the chromosphere is completely filled by the emitting region for stars in the saturated regime.

The idea that the activity of the chromospheres is driven by the dynamo process is widely accepted not only for low-mass main-sequence stars but also for pre-main-sequence (PMS) stars. However, several previous studies showed that a certain proportion of T Tauri stars (TTSs) are slow rotators. Vogel and Kuhi (1981) found that low-mass PMS stars ($\leq$1.5 $M_\odot$) generally rotate at less than 25 km s^{-1}. White and Basri (2003) revealed that all of the low-mass TTSs in the Taurus–Auriga star-forming region are slowly rotating ($v \sin i < 30$ km s^{-1}). Hartmann et al. (1986) confirmed and extended the findings of Vogel and Kuhi (1981); they found that about 30% of the 0.5–1.0 $M_\odot$ TTSs in Taurus have rotational velocities at or below 10 km s^{-1}, and half have $v \sin i$ values between 10 and 15 km s^{-1}. However, previous studies also showed that a fraction of TTSs exhibit strong Ca II emission lines (Hartmann et al. 1986). Batalha and Basri (1993) constructed models of photosphere and chromosphere to fit the observed profiles of the Ca II IRT emission line for TTSs with low accretion rates but null veiling. Those deep chromosphere models explain the emission characteristics of TTSs, showing a narrow emission profile over a broad absorption feature (Calvet et al. 1984; Batalha et al. 1996). Calvet and Gullbring (1998) found that shock heating of the photosphere by emission of chromosphere results in a temperature inversion and the temperature increases in the chromosphere, as shown by deep chromospheric models. In contrast, Moto'oka and Itoh (2012) found no clear correlation between the EQWs of the Ca II IRT emission lines and stellar rotation velocity. As mentioned above, the rotation velocity is not the only parameter expected to be related to the dynamo process. The effective temperature (T_{eff}), τ_c, and the spectral distribution of the continuum flux change as PMS stars evolve.

Another indicator for chromospheric activity of PMS stars is mass accretion from their protoplanetary disks. Moto'oka and Itoh (2012) found that the EQWs of the Ca II IRT emission lines decrease with stellar evolution from classical TTSs (CTTSs), transitional disk objects, weak-line TTSs (WTTSs), to ZAMS stars. They also revealed that PMS stars with high mass accretion rates have strong Ca II emission lines. Mohanty, Jayawardhana, and Basri (2005) investigated the chromospheric activity of CTTSs, very low-mass young stars ($0.075 \leq M_* < 0.15\,M_\odot$), and young brown dwarfs ($M_* \leq 0.075\,M_\odot$). The surface flux of the Ca II emission line at λ8662 Å, $F'_{\lambda 8662}$, exhibited correlation with the associated mass accretion rate, $\dot{M}$, for approximately four orders of magnitude. Hence, Mohanty, Jayawardhana, and Basri (2005) claimed that the Ca II emission line is an excellent quantitative measure for the accretion rate. Hamann and Persson (1992) carried out optical

spectroscopy for 53 TTSs and 32 Herbig Ae/Be stars. They interpreted narrow emission lines such as Ca II and Mg I generated in the stellar chromosphere. The Ca II IRT emission lines of several TTSs and Herbig Ae/Be stars also have a broad line component. This profile can be explained well by the magnetospheric accretion model (e.g., Muzerolle et al. 1998).

In this study we investigate the Ca II IRT emission lines of 60 PMS stars with medium- and high-resolution spectral data. We compare the rotation–activity relationship of the PMS stars with that of low-mass stars in young open clusters. The chromospheric activity of the cluster members is considered to be induced by dynamo activity. In the next section we describe the observation and the data reduction procedures. In section 3 we present the results, and in section 4 we discuss the origin of the Ca II IRT emission lines and the emitting region on the stellar surface.

2 Observations and data reduction

2.1 Stellar parameters

All the targets investigated in this study are listed in table 1. These 60 objects are associated with four molecular clouds or five moving groups; the Taurus–Auriga molecular cloud, the Orionis OB 1c association, the Upper Scorpius association, the Perseus molecular cloud, the TW Hydrae association, the η Chamaeleontis cluster, the "Cha-Near" region, the β Pictoris moving group, and the AB Doradus moving group. Hereafter, objects belonging to both molecular clouds and moving groups are called "low-mass PMS stars." We did not observe binaries or triplets listed in Ghez, Neugebauer, and Matthews (1993), Leinert et al. (1993), Neuhauser et al. (1995), Kraus et al. (2009, 2012), Zuckerman and Song (2004), and Wahhaj et al. (2010).

Figure 1 presents the Hertzsprung–Russell (HR) diagram of the PMS stars investigated. The filled circle symbols indicate PMS stars in molecular clouds. The open circles represent PMS stars in moving groups. The luminosity, $T_{\rm eff}$, and distance of the objects were taken from Gaia DR2 (Bailer-Jones et al. 2018). For objects whose $T_{\rm eff}$ is not listed in Gaia DR2 (Bailer-Jones et al. 2018), we referred to other sources: Palla and Stahler (2002) for AA Tau, Kenyon and Hartmann (1995) for GH Tau, and Pecaut and Mamajek (2013) for HD 197481, RECX 09, and TWA 22. The solid lines indicate Canuto and Mazzitelli Alexander evolutionary tracks (D'Antona & Mazzitelli 1994). The stellar masses, M_*, masses of the bottom of the convective zone, $M_{\rm conv}$, and ages of the target stars were estimated from their evolutionary tracks. For example, objects with $M_{\rm conv} = 0\,M_\odot$ are fully convective.

2.2 Observations

The observations were conducted with the Medium And Low Long slit Spectrograph (MALLS) mounted on the 2.0 m Nayuta Telescope at the Nishi-Harima Astronomical Observatory (NHAO), Japan. The data for four PMS stars were obtained between 2017 December 5 and 2019 February 6 with the 0.″8-width slit or the 1.″2-width slit using the 1800 l mm^{-1} grating. These instrument settings achieved a wavelength coverage between 8350 Å and 9360 Å and a spectral resolution between 7500 and 9000. The integration time for each object was between 600 s and 1200 s.

High-resolution spectroscopic observations of five PMS stars were conducted on 2007 September 18 with the High Dispersion Spectrograph (HDS; Noguchi et al. 2002) mounted on the Subaru Telescope. The data were obtained using the StdNIRb mode and with the 0.″6-width slit. These instrument settings achieved a wavelength coverage between 6650 Å and 9360 Å and a spectral resolution of 60000. The integration time for each object was between 600 s and 1500 s.

Archive data of 26 PMS stars and 5 standard stars obtained with HIRES mounted on the Keck Telescope was also used. The observer, date of the observations, wavelength coverage, and integration times are listed in table 2. The spectral resolution was 70000. The archive data of six PMS stars obtained with the UVES ($R \sim 40000$) mounted on the Very Large Telescope (VLT) was also used. The program IDs, principal investigators, and dates of the observations are listed in table 2. The wavelength coverage was between 5655 Å and 9496 Å. The integration time for each object was between 10 s and 600 s. In addition, the archive data of 19 PMS stars obtained with the X-Shooter ($R \sim 8000$) mounted on the VLT was also used. The wavelength coverage was between 5337 Å and 10200 Å. The integration time for each object was between 2 s and 600 s.

2.3 Data reduction

The Image Reduction and Analysis Facility (IRAF) software package[1] was used for data reduction. Overscan subtraction, dark subtraction, flat fielding, wavelength calibration using an Fe–Ne–Ar lamp, removal of scattered light, extraction of a spectrum, and continuum normalization were conducted for all the spectra obtained by MALLS.

The HDS data was reduced with overscan subtraction, bias subtraction, flat fielding, removal of scattered light, extraction of a spectrum, wavelength calibration using a

[1] IRAF is distributed by the National Optical Astronomy Observatories, which are operated by the Association of Universities for Research in Astronomy, Inc., under cooperative agreement with the National Science Foundation.

Table 1. Physical parameters of the PMS stars.*

Object name	i	$(B-V)_0$	A_V	$L/L_\odot$	$T_{\rm eff}$	Dist	$v\sin i$	$\tau_{\rm c}$	$\log \dot{M}$	M_*	$M_{\rm conv}$	Age	Telescope
	[mag]	[mag]	[mag]		[K]	[pc]	[km s^{-1}]	[$\times 10^6$ s]	[$M_\odot$ yr^{-1}]	[$M_\odot$]	[$M_\odot$]	[Myr]	
(1)	(2)*	(3)*	(4)*	(5)*	(6)*	(7)*	(8)*	(9)	(10)*	(11)	(12)	(13)	(14)†
Taurus–Auriga molecular cloud													
AA Tau	12.7	0.82	0.74	0.74	4060	136	12.7	20	−8.48	0.5	0.0	1.0	V
BP Tau	11.0	1.01	0.34	0.46	4320	128	10.9	14	−7.54	0.9	0.2	5.0	V
CX Tau	11.9	1.31	0.80	0.28	3417	127	19.1	19	−8.97	0.3	0.0	1.0	K
CoKu Tau4	12.6	1.30	1.75	0.11	4070	170	25.8	11	−10.0	0.6	0.2	20.0	K
DF Tau	10.4	0.75	0.45	0.93	3665	124	18.4	19	−7.62	0.3	0.0	0.3	V
DG Tau	11.5	0.54	1.30	0.34	3731	120	21.7	19	−6.30	0.4	0.0	1.0	N
DL Tau	11.6	0.53	2.00	0.44	3998	158	19.0	21	−6.79	0.6	0.0	2.0	N
DM Tau	12.6	0.82	1.10	0.18	3769	144	10.0	22	−7.95	0.5	0.0	5.0	K
DR Tau	10.8	0.46	0.61	0.86	4327	194	10.0	21	−6.50	0.7	0.0	1.0	V
DS Tau	11.3	0.78	0.34	0.43	4040	158	11.2	21	−7.89	0.6	0.0	2.0	K
FN Tau	11.8	1.27	1.40	0.14	4250	130	6.4	7	—	0.7	0.5	30.0	K
FP Tau	12.0	1.55	0.20	0.24	3486	128	27.9	19	−9.45	0.3	0.0	1.0	K
GH Tau	11.5	1.41	0.40	0.79	3580	140	25.2	19	−7.92	0.3	0.0	0.5	K
GM Aur	11.2	1.10	0.31	0.55	4338	158	12.6	14	−8.02	0.9	0.2	5.0	K
GO Tau	13.1	1.10	1.20	0.08	3984	143	19.2	4	−7.93	0.6	0.5	70.0	K
HBC 374	11.0	1.65	0.00	0.43	4007	125	12.9	21	—	0.6	0.0	2.0	S
HBC 376	11.4	1.08	0.00	0.28	4389	121	68.0	5	−8.92	0.8	0.6	30.0	S
HBC 407	11.9	1.03	0.00	0.16	4649	125	8.8	3	—	0.7	0.6	70.0	V
HBC 427	10.7	1.21	0.20	0.87	4249	148	10.0	21	—	0.7	0.0	1.0	K
HD 285778	9.7	0.72	0.23	1.18	5358	119	17.6	6	−8.03	1.3	1.0	7.0	S
HP Tau	—	1.55	0.39	0.29	3688	176	100.0	20	−8.47	0.4	0.0	2.0	V
IT Tau	12.5	1.18	3.10	0.18	3913	161	—	13	—	0.7	0.2	10.0	K
LkCa 04	11.3	1.38	0.35	0.40	3621	129	26.1	19	−8.73	0.4	0.0	1.0	K
LkCa 14	10.8	1.21	0.00	0.58	4218	127	21.9	22	−8.85	0.7	0.0	2.0	K
LkCa 15	11.0	1.08	0.60	0.64	4201	158	12.5	22	−8.87	0.7	0.0	2.0	K
LkCa 19	10.0	0.96	0.00	1.63	4784	158	19.8	16	−10.0	1.2	0.2	2.0	K
RY Tau‡	9.3	0.86	1.50	6.30	5750	133	48.8	3	−7.11	1.8	1.7	5.0	N
SU Aur	8.9	0.58	0.90	4.31	4359	157	65.0	20	−8.25	0.6	0.0	0.2	V
UX Tau	10.0	0.92	0.36	0.59	4427	139	9.9	19	−9.00	0.9	0.1	3.0	K
V1023 Tau	11.0	1.24	1.35	0.43	4007	125	12.9	21	−7.78	0.6	0.0	2.0	N
V1204 Tau	10.1	0.88	0.31	1.05	4800	138	22.5	9	—	1.2	0.6	5.0	S
V1297 Tau	10.8	0.72	0.28	0.44	5039	117	17.5	2	—	0.9	0.9	50.0	K
V1321 Tau	12.0	1.35	0.70	0.22	4042	146	11.2	7	—	0.7	0.5	30.0	K
V1348 Tau	11.3	1.09	0.00	0.41	4441	155	4.8	12	—	0.9	0.3	7.0	K
V1840 Ori	11.1	0.97	0.20	0.59	4617	149	14.5	10	—	1.0	0.5	7.0	S
V830 Tau	11.1	1.22	0.30	0.44	4020	130	26.6	21	−8.10	0.6	0.0	2.0	K
V836 Tau	12.4	1.00	1.70	0.40	3631	168	13.4	19	−8.98	0.4	0.0	1.0	K
ZZ Tau	11.9	1.22	1.00	0.16	4130	134	21.4	7	—	0.7	0.5	30.0	K
Orionis OB 1c association													
HBC 167	10.4	0.70	0.00	7.32	5504	406	18.0	13	—	2.0	0.6	1.0	V
Upper Scorpius association													
1RXS J161951.4−215431	11.1	1.40	0.00	—	3746	—	—	2	—	—	—	—	K
Perseus molecular cloud													
LkHα 86	14.4	1.44	0.00	0.14	3657	321	6.8	20	—	0.4	0.0	5.0	K
LRL 72§	—	2.24	0.00	0.51	3488	249	9.3	19	—	0.3	0.0	0.7	K
AB Doradus moving group													
HIP 17695	9.8	1.51	0.00	0.04	3349	16	18.0	19	—	0.2	0.0	20.0	V
β Pictoris moving group													
HD 197481	7.4	1.46	0.04	0.10	3652	9	8.0	21	—	0.4	0.0	10.0	V
η Chamaeleontis cluster													
RECX 04	11.4	1.43	0.00	0.21	4023	99	6.0	13	—	0.7	0.2	10.0	V
RECX 06	12.4	1.42	0.00	0.10	3525	97	20.9	19	—	0.3	0.0	5.0	V
RECX 07	10.0	1.15	0.00	0.71	4325	98	30.0	22	—	0.8	0.0	3.0	V
RECX 09	12.8	1.46	0.00	0.10	3933	97	—	9	−10.4	0.6	0.3	30.0	V
RECX 10	11.3	1.42	0.00	0.21	4088	97	9.0	7	—	0.8	0.5	20.0	V
RECX 11	10.3	1.18	0.00	0.45	4392	98	13.0	12	−9.77	0.9	0.3	7.0	V
RECX 15	12.7	0.83	0.00	0.06	3719	91	28.0	11	−9.09	0.5	0.2	30.0	V
"Cha-Near" region													
RX J1147.7−7842	11.6	1.54	0.00	0.16	3881	106	—	9	—	0.7	0.4	20.0	V
RX J1204.6−7731	11.8	1.52	0.00	0.16	3584	100	6.0	20	—	0.4	0.0	3.0	V

Table 1. (Continued)

Object name	i	$(B-V)_0$	A_V	$L/L_\odot$	$T_{\rm eff}$	Dist	$v\sin i$	τ_c	$\log \dot{M}$	M_*	$M_{\rm conv}$	Age	Telescope
	[mag]	[mag]	[mag]		[K]	[pc]	[km s^{-1}]	[$\times 10^6$ s]	[$M_\odot$ yr^{-1}]	[$M_\odot$]	[$M_\odot$]	[Myr]	
(1)	(2)*	(3)*	(4)*	(5)*	(6)*	(7)*	(8)*	(9)	(10)*	(11)	(12)	(13)	(14)†
TW Hydrae association													
TWA 01	10.0	0.89	0.27	0.26	4235	59	14.0	9	−8.74	0.9	0.5	10.0	V
TWA 06	10.3	1.23	0.27	0.21	4268	65	—	7	—	0.8	0.5	20.0	V
TWA 07	10.0	1.46	0.00	0.08	4017	33	4.4	9	—	0.6	0.3	30.0	V
TWA 14	11.3	1.27	0.10	0.20	3852	91	—	20	—	0.6	0.0	7.0	V
TWA 22	11.3	1.73	0.00	0.01	2843	19	9.7	2	—	0.0	0.0	0.7	V
TWA 23	10.6	1.50	0.05	0.14	3508	55	—	19	—	0.3	0.0	3.0	K
TWA 25	9.9	1.34	0.24	0.22	4019	53	12.9	7	—	0.8	0.5	20.0	V

*References of parameters. (2) i-mag: UCAC4 Catalogue (Zacharias et al. 2013). (3) $B-V$: van Leeuwen (2007), Mayne et al. (2007), Manoj et al. (2006), Henden et al. (2016), Herbig and Bell (1988), Hanson (2003), and Davies et al. (2014). (4) A_V: Kraus et al. (2009), Manoj et al. (2006), and Wahhaj et al. (2010). (5) and (6) Luminosity and $T_{\rm eff}$: Gaia DR2 (Gaia Collaboration 2018), Palla and Stahler (2002), Kenyon and Hartmann (1995), and Pecaut and Mamajek (2013). (7) Distance: Gaia DR2 (Bailer-Jones et al. 2018). (8) $v\sin i$: Glebocki and Gnacinski (2005), Nguyen et al. (2012), Torres et al. (2006), and Messina et al. (2011). (10) $\dot{M}$: Najita, Strom, and Muzerolle (2007), Gullbring et al. (1998), White and Ghez (2002), Hartmann et al. (1998), Lawson, Lyo, and Muzerolle (2004), Calvet et al. (2004), and Ingleby et al. (2013).

†(14) The telescopes used for the observations. N: Nayuta Telescope; S: Subaru Telescope; K: Keck Telescope; V: VLT.

‡For RY Tau, A_V, $L/L_\odot$, $T_{\rm eff}$, and the distance were taken from Garufi et al. (2019).

§The original name is "Cl* IC 348 LRL 72."

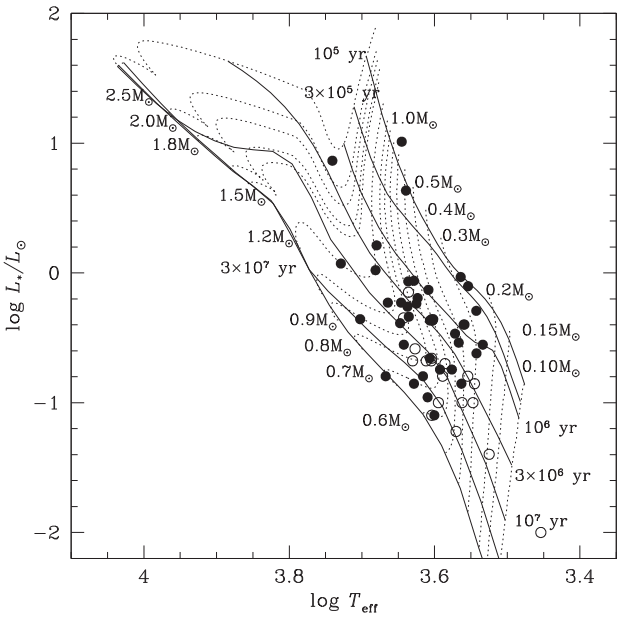

Fig. 1. HR diagram of the PMS stars investigated. The solid lines are Canuto and Mazzitelli Alexander evolutionary tracks (D'Antona & Mazzitelli 1994). The filled circle symbols and the open circles indicate PMS stars in molecular clouds and moving groups, respectively.

Th–Ar lamp, and continuum normalization. A detailed description of the data reduction methods used here is presented in Takagi et al. (2011). The HIRES data was reduced with the Mauna Kea Echelle Extraction (MAKEE) package. The UVES data and X-Shooter data had already been reduced.

All object spectra were shifted to match the rest radial velocity. Therefore, we measured the wavelengths of two unblended Fe I absorption lines (λλ8468.404, 8621.598 Å), then shifted the wavelength of all spectra by the average of the difference between the measured wavelengths and laboratory wavelength.

The Ca II IRT emission lines are often located on the broad photospheric absorption lines of Ca II. In general, the photospheric absorption of the Ca II IRT line is strong, especially for K-type stars. Also, the PMS stars investigated have late spectral type. An absorption line profile of a PMS spectrum could be obscured by continuum veiling. The amount of veiling, V, is defined as

$$V = \frac{W^0}{W} - 1, \tag{1}$$

where W^0 denotes the unveiled EQW and W is the veiled EQW.

In this study, inactive stars with a spectral type similar to that of the target object were used as template stars (the inactive stars library; Yee et al. 2017; Passegger et al. 2018). We obtained the Keck archive data of five inactive stars, ι Psc (F7), 16 Cyg (G3), HD 166 (G8), HD 88230 (K6), and GJ 412a (M1). For the correction of the rotational broadening, the spectra of the template stars were convolved with a Gaussian kernel to match the width of the absorption lines of each object. To estimate the amount of veiling, we measured the EQWs of Ti I, Fe I, and Cr I photospheric absorption lines between 8420 and 8700 Å (table 3). In table 3, absorption lines of several stars could not be measured because of the varying wavelength ranges of the individual data archives. If the amount of the veiling was estimated for more than five absorption lines, we calculated their mean values and residuals. Basri and Batalha (1990) claimed that the veiling is constant around 8500 Å. We assumed that each of the Ca II IRT emission

Table 2. Details of the archive data from Keck/HIRES, VLT/UVES, and VLT/X-Shooter.

Program ID	PI-observers	Observation dates	Wavelength [Å]	Integration time [s]
Keck / HIRES				
C05H	N. Reid	1999-06-16	7600–9910	100
C77H	L. Hillenbrand	1999-12-06, 07	6240–8680	1200–1500
C109H	L. Hillenbrand	2000-01-10, 11	6240–8680	300–900
C240Hr	S. E. Dahm	2007-11-30	4880–9380	460–1800
C095Hr	S. E. Dahm	2008-12-03, 04	4450–8900	10–1200
N107Hr	I. Pascucci	2012-12-01	4880–9380	300–3710
C252Hr	L. Hillenbrand	2013-12-26, 27	4880–9380	150–600
C247Hr	J. Carpenter	2015-06-01, 02	4880–9380	305–424
C250Hr	L. Hillenbrand	2016-05-17	4880–9380	22
C226Hr	L. Hillenbrand	2017-01-13	4880–9380	130
VLT/UVES				
075.C-0321(A)	M. Hempel	2005-08-26	5655–9496	200
082.C-0005(B)	A. Scholz	2008-10-02, 2009-01-08, 18	5655–9496	10–600
VLT/X-Shooter				
084.C-1095(A)	G. Herczeg	2010-01-19, 2010-01-20	5337–10200	2–388
085.C-0238(A)	J. M. Alcala	2010-04-06, 07	5337–10200	20–480
086.C-0173(A)	J. M. Alcala	2010-01-12, 13	5337–10200	100–400
094.C-0327(A)	S. Alencar	2015-01-16	5337–10200	120
094.C-0805(A)	G. Herczeg	2015-01-15, 2015-03-07	5337–10200	24–600
094.C-0913(A)	C. F. Manara	2014-12-05	5337–10200	320–400

Table 3. Absorption lines for estimating the amount of veiling.

	Wavelength [Å]
Ti I	8426.497
Ti I	8450.871
Cr I	8455.288
Fe I	8468.404
Fe I	8621.598
Fe I	8632.412
Ti I	8682.988
Fe I	8688.600
Ti I	8692.326

lines has the same veiling value as all the others. We substituted the EQW of the lines of the PMS spectrum for W, that of the template star for W^0, and then obtained the amount of veiling for each absorption line. The average value of V and standard deviation σ_V were calculated (table 4). In the case that $V - \sigma$ was negative or the veiling values were measured for less than five absorption lines, we regarded V as 0.

For objects indicating a significant veiling value, we made a veiled spectrum of the template star. First, we added the veiling value V to the normalized spectrum of the template star. Then, the continuum component was normalized again to unity by dividing by $(1 + V)$. The veiled spectrum of the template star was subtracted from that of the target star indicating a significant veiling value. For objects indicating $V = 0$, the spectrum of the template star which was not veiled was subtracted.

Figure 2 shows the procedures of the spectral subtraction of the Ca II IRT lines of AA Tau. The solid line at the top of the panel shows the observed spectrum of AA Tau before subtraction of the spectrum of the template star. In this case, the Ca II IRT lines display emission profiles over a broad absorption feature. The dotted line is the fitted spectrum of the veiled template star. The continuum components of both spectra were normalized to unity. The solid line in the bottom of the panel represents the observed spectrum of AA Tau after subtracting the spectrum of the template star. Any broad absorption feature was removed completely, and only the emission component remained. Unfortunately, any absorption lines (table 3) to measure the veiling value are not shown in figure 2. The spectra of most objects only contain emission components after this subtraction has been performed. The subtraction of the template spectrum is necessary for correct measurement of the EQWs for the Ca II IRT emission lines.

Before measuring the EQWs, the continuum component of the spectra was added to unity. To obtain the EQWs of the Ca II IRT emission lines, the area of the emission profile was directly integrated. We also measured their full width at half maximum (FWHM) by fitting with a Gaussian function. The EQW errors were estimated by multiplying the standard deviation of the continuum by the wavelength range of the emission line. The wavelength range for

Table 4. EQWs, FWHMs of the Ca II IRT emission lines (λλ8498, 8542, 8662 Å) and the veiling value.

Object name	W_{IRT} [Å]			FWHM [km s^{-1}]			Veiling
	λ8498	λ8542	λ8662	λ8498	λ8542	λ8662	
Taurus–Auriga molecular cloud							
AA Tau	0.65 ± 0.04	0.77 ± 0.04	0.61 ± 0.04	20	23	20	1.29 ± 1.20
BP Tau	1.05 ± 0.07	1.68 ± 0.12	1.15 ± 0.11	24	32	26	0.56 ± 0.40
CX Tau	0.59 ± 0.03	0.77 ± 0.04	0.72 ± 0.05	31	35	36	−0.11 ± 0.20
CoKu Tau4	0.53 ± 0.03	0.83 ± 0.04	0.6 ± 0.04	37	42	38	—
DF Tau	1.14 ± 0.15	2.02 ± 0.25	1.38 ± 0.19	33	55	45	—
DG Tau	49.49 ± 1.58	46.83 ± 1.74	51.39 ± 2.50	185	221	211	—
DL Tau	53.88 ± 8.14	50.65 ± 9.21	39.37 ± 7.89	249	271	250	—
DM Tau	1.02 ± 0.06	1.29 ± 0.09	1.07 ± 0.09	16	22	19	−0.19 ± 0.18
DR Tau	53.1 ± 0.73	59.83 ± 0.75	49.03 ± 0.30	126	163	153	2.64 ± 1.48
DS Tau	0.75 ± 0.04	1.19 ± 0.06	1.05 ± 0.04	26	35	35	0.35 ± 0.32
FN Tau	1.32 ± 0.10	—	1.49 ± 0.14	20	—	28	−0.18 ± 0.29
FP Tau	0.55 ± 0.04	—	0.55 ± 0.06	45	—	41	—
GH Tau	0.62 ± 0.04	0.72 ± 0.04	0.56 ± 0.03	38	40	37	—
GM Aur	0.73 ± 0.02	1.41 ± 0.02	1.15 ± 0.02	27	42	38	0.31 ± 0.16
GO Tau	0.62 ± 0.04	0.86 ± 0.05	0.72 ± 0.05	19	23	22	−0.20 ± 0.16
HBC 374	0.57 ± 0.03	0.97 ± 0.06	—	23	33	—	—
HBC 376	0.67 ± 0.08	0.90 ± 0.08	—	95	111	—	—
HBC 407	0.26 ± 0.01	0.33 ± 0.01	0.27 ± 0.01	24	27	25	—
HBC 427	0.44 ± 0.02	0.58 ± 0.03	0.52 ± 0.04	25	32	31	0.07 ± 0.17
HD 285778	0.24 ± 0.02	0.39 ± 0.04	—	26	41	—	—
HP Tau	0.56 ± 0.04	0.84 ± 0.05	0.72 ± 0.03	84	110	90	—
IT Tau	0.81 ± 0.03	1.05 ± 0.03	0.88 ± 0.06	55	61	58	0.12 ± 0.23
LkCa 04	0.62 ± 0.05	0.92 ± 0.06	0.83 ± 0.07	51	68	67	—
LkCa 14	0.54 ± 0.04	0.74 ± 0.04	0.62 ± 0.04	29	32	29	—
LkCa 15	0.56 ± 0.02	0.58 ± 0.02	0.56 ± 0.05	22	26	23	0.25 ± 0.17
LkCa 19	0.37 ± 0.02	0.51 ± 0.03	0.38 ± 0.03	32	36	31	0.40 ± 0.18
RY Tau	6.53 ± 1.57	4.94 ± 1.47	4.21 ± 1.17	222	220	170	—
SU Aur	1.11 ± 0.16	1.87 ± 0.19	1.51 ± 0.26	117	179	113	—
UX Tau	0.37 ± 0.02	0.49 ± 0.02	0.43 ± 0.03	40	41	45	—
V1023 Tau	0.88 ± 0.24	1.32 ± 0.29	—	43	53	—	—
V1204 Tau	0.37 ± 0.04	0.39 ± 0.03	—	35	36	—	—
V1297 Tau	0.30 ± 0.04	0.36 ± 0.04	0.28 ± 0.05	29	30	28	—
V1321 Tau	0.54 ± 0.02	0.73 ± 0.04	0.62 ± 0.04	19	24	22	−0.32 ± 0.16
V1348 Tau	0.40 ± 0.04	0.54 ± 0.05	0.42 ± 0.05	18	25	20	0.31 ± 0.33
V830 Tau	0.75 ± 0.04	1.17 ± 0.06	0.79 ± 0.04	43	46	40	−0.37 ± 0.14
V836 Tau	0.68 ± 0.05	0.84 ± 0.05	0.81 ± 0.06	28	40	34	0.08 ± 0.35
ZZ Tau	0.62 ± 0.07	0.84 ± 0.07	0.56 ± 0.08	28	33	35	—
Orionis OB 1c association							
HBC 167	1.93 ± 0.05	3.28 ± 0.08	2.43 ± 0.05	67	85	80	0.13 ± 0.26
Upper Scorpius association							
1RXS J161951.4−215431	0.55 ± 0.06	0.84 ± 0.07	0.69 ± 0.06	43	52	43	—
Perseus molecular cloud							
LkHα 86	0.62 ± 0.04	0.85 ± 0.06	0.68 ± 0.06	15	20	18	−0.24 ± 0.18
LRL 72	0.47 ± 0.04	0.58 ± 0.08	0.44 ± 0.07	15	20	21	−0.21 ± 0.19
AB Doradus moving group							
HIP 17695	0.42 ± 0.03	0.58 ± 0.06	0.41 ± 0.07	29	33	32	—
β Pictoris moving group							
HD 197481	0.57 ± 0.02	0.69 ± 0.03	0.56 ± 0.03	15	19	18	—
η Chamaeleontis cluster							
RECX 04	0.61 ± 0.07	0.84 ± 0.11	0.63 ± 0.08	23	31	25	0.08 ± 0.38

Table 4. (Continued)

Object name	W_{IRT} [Å]			FWHM [km s^{-1}]			Veiling
	λ8498	λ8542	λ8662	λ8498	λ8542	λ8662	
RECX 06	0.59 ± 0.08	0.71 ± 0.12	0.51 ± 0.10	38	43	40	—
RECX 07	0.58 ± 0.05	0.83 ± 0.07	0.67 ± 0.04	54	58	59	—
RECX 09	0.49 ± 0.11	0.92 ± 0.15	0.66 ± 0.11	57	85	78	—
RECX 10	0.52 ± 0.08	0.67 ± 0.09	0.51 ± 0.07	54	62	52	0.02 ± 0.21
RECX 11	0.59 ± 0.03	0.87 ± 0.05	0.72 ± 0.05	52	63	61	0.41 ± 0.83
RECX 15	9.28 ± 0.58	9.46 ± 0.58	7.32 ± 0.52	204	226	222	0.11 ± 0.40
"Cha-Near" region							
RX J1147.7−7842	0.57 ± 0.08	0.94 ± 0.09	0.63 ± 0.05	104	112	94	—
RX J1204.6−7731	0.64 ± 0.05	0.87 ± 0.07	0.64 ± 0.05	21	27	22	—
TW Hydrae association							
TWA 01	1.03 ± 0.07	1.96 ± 0.08	1.72 ± 0.10	26	38	35	0.37 ± 0.55
TWA 06	0.56 ± 0.03	0.90 ± 0.04	0.72 ± 0.05	80	85	83	—
TWA 07	0.62 ± 0.04	0.73 ± 0.05	0.55 ± 0.06	19	24	20	—
TWA 14	0.75 ± 0.05	1.15 ± 0.07	0.85 ± 0.07	66	81	76	0.03 ± 0.33
TWA 22	0.55 ± 0.12	1.06 ± 0.18	0.80 ± 0.18	32	56	74	—
TWA 23	0.36 ± 0.04	0.48 ± 0.06	0.29 ± 0.04	18	22	19	−0.22 ± 0.19
TWA 25	0.62 ± 0.02	0.82 ± 0.03	0.72 ± 0.03	24	27	26	—

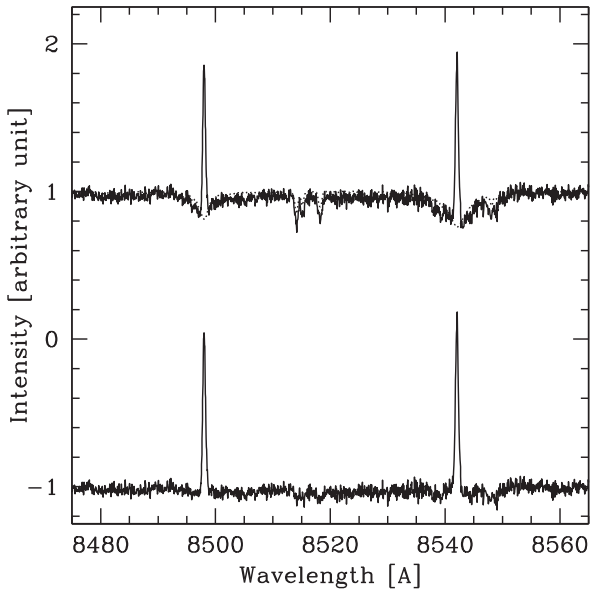

Fig. 2. Emission profiles of the Ca II IRT lines (λλ8498, 8542 Å). The observed spectrum of AA Tau is shown in the top of the panel with a solid line. The dotted line is the fitted inactive star, a K6 template star. The difference between the observed and template spectra is shown in the bottom of the panel, where the Ca II IRT narrow lines appear in the emission. The difference between the AA Tau spectrum and the template star's spectrum is shown shifted by −1.0 for display purposes. Note that all nine absorption lines used for estimating the amount of the veiling (table 3) are out of range for this figure.

measuring standard deviation is λλ8483–8492 Å for the Ca II λλ8498, 8542 Å lines and λλ8623–8632 Å for the Ca II λ8662 line. These ranges are free from any emission and absorption lines. Also, for our discussion we only consider emission profiles with S/N larger than 3 for calculating EQWs, FWHMs, etc.

3 Results

The EQWs of the Ca II IRT emission lines and their errors are listed in table 4. Seven objects have broad emission lines of Ca II λ8498 Å (FWHM >100 km s^{-1}), while most PMS stars exhibit narrow emission lines (FWHM ≤100 km s^{-1}). Figure 3 shows the spectra of the λ8498 Å emission line after subtracting the photospheric absorption. The emission lines of DG Tau, DL Tau, and DR Tau are broad and strong ($W_{IRT} \sim 50$ Å), while those of RY Tau, SU Aur, RECX 15, and RX J1147.7−7842 are broad but not strong ($W_{IRT} < 10$ Å). All EQWs of narrow emission lines are weaker than 5 Å. We note that part of the narrow emission component of the PMS stars could be buried by the photospheric absorption before removal. In our sample, most objects that belong to the moving group only have absorption lines before removal of the photospheric absorption.

We obtained the amount of veiling for 27 objects. Among them, the amount of veiling was measured in the previous studies for 13 objects. The correlation coefficient between the literature values and our measured values is 0.84. The literature value was found to be within the uncertainty of the measured V for eight objects. We note that on multiple occasions variation of the veiling value has been reported (Basri & Batalha 1990; Batalha et al. 1996; Hartigan et al. 1989, 1991).

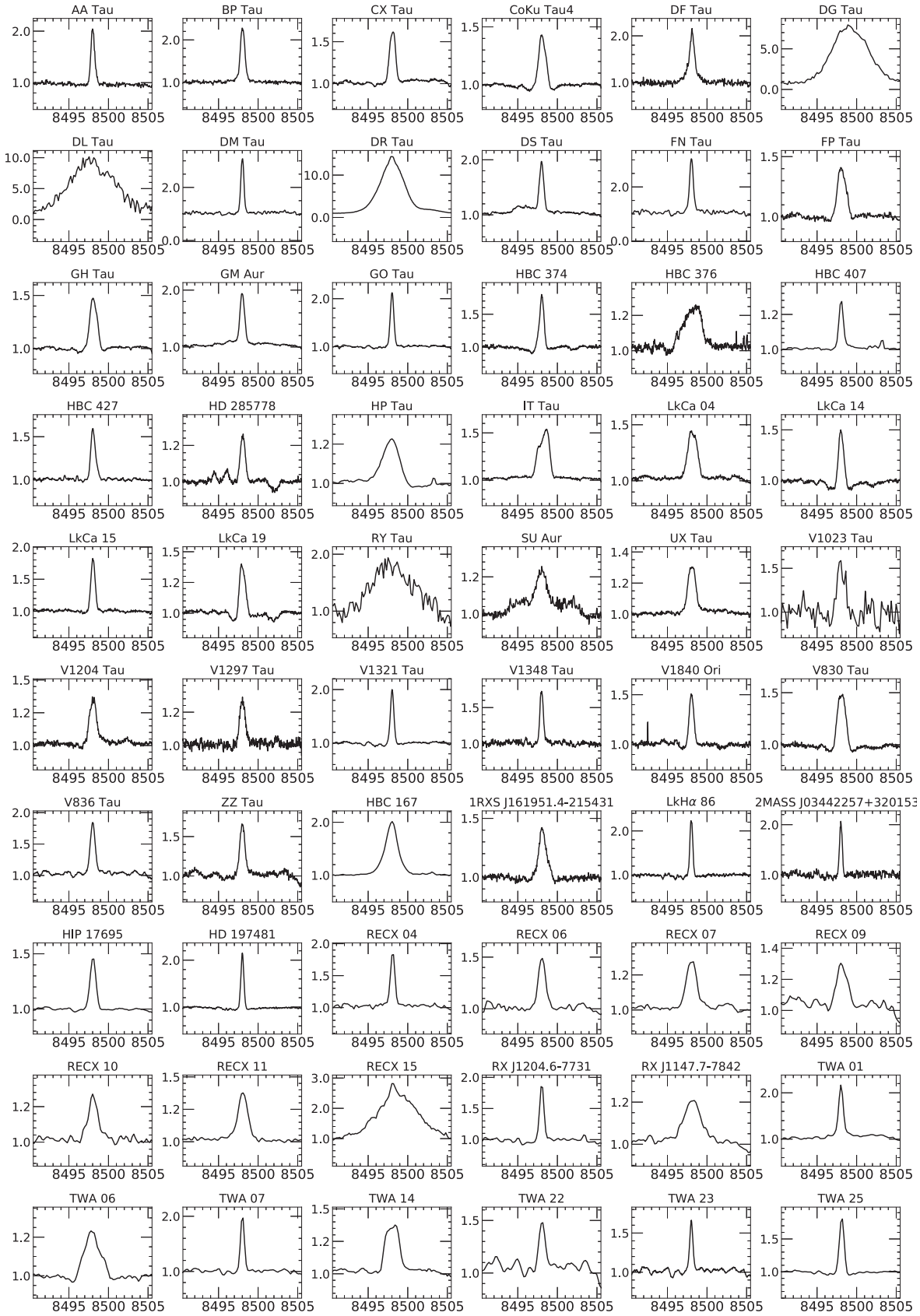

Fig. 3. Ca II IRT emission lines (λ8498 Å) of all the PMS stars. The spectra are normalized to unity. Photospheric absorption lines have already been subtracted.

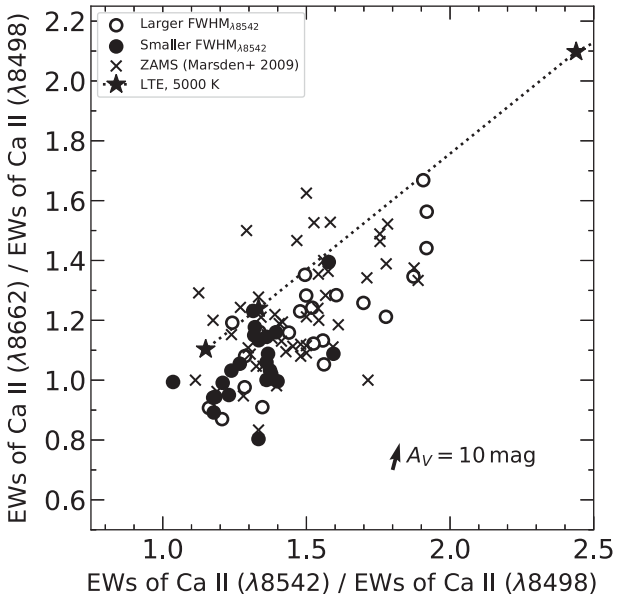

Fig. 4. Ratios of the EQWs of the Ca II IRT emission lines. The circle symbols represent the PMS stars in the molecular clouds and moving groups. The PMS stars are separated into two groups by the median of their FWHM$_{\lambda8542}$; the open circles show the group of PMS stars with a broader FWHM$_{\lambda8542}$ than the median. The filled circles represent the narrower group. The low-mass stars in the young open clusters IC 2391 and IC 2602 are plotted as cross symbols (Marsden et al. 2009). The dotted line represents isothermal slabs ($T = 5000$ K) in LTE (Herbig & Soderblom 1980; Hamann & Persson 1992). The black star symbols on the line correspond to slab optical depths of 10, 100, and 1000, beginning from the upper right. The arrow in the lower right is the redding vector with $A_V = 10$ mag.

4 Discussion

4.1 Emission line ratios of the Ca II IRT lines

The ratios of the EQWs $W_{\lambda8542}/W_{\lambda8498}$ and $W_{\lambda8662}/W_{\lambda8498}$ are sensitive to the conditions of the emitting plasma. It has been shown that solar chromospheric plages and flares have the ratio of $1 \leq W_{\lambda8542}/W_{\lambda8498} \leq 2$ (Herbig & Soderblom 1980). In contrast, optically thin emission sources such as solar prominences have a high value of this ratio, $W_{\lambda8542}/W_{\lambda8498} > 4$. In several studies (Herbig & Soderblom 1980; Hamann & Persson 1992), TTSs showed small line ratios of the Ca II IRT emission lines, indicating dense chromospheric regions such as plages and flares.

The ratios of the EQWs of the Ca II IRT emission lines are plotted in figure 4. The circle symbols represent the PMS stars in the molecular clouds and the moving groups. The PMS stars are separated into two groups by the median of their FWHM$_{\lambda8542}$; the open circles represent the group of PMS stars with a broader FWHM$_{\lambda8542}$ than the median. The filled circles represent the narrower group. For comparison, we also plotted the low-mass stars in the young open clusters IC 2391 and IC 2602 studied in Marsden, Carter, and Donati (2009) using cross symbols. The dotted line indicates isothermal slabs ($T = 5000$ K) in local thermal equilibrium (LTE; Herbig & Soderblom 1980; Hamann & Persson 1992). The black star symbols on the line correspond to the slab optical depths of 10, 100, and 1000. The arrow in the lower right is the reddening vector calculated by the equation below (Tokunaga 2000) with $A_V = 10$ mag,

$$\frac{A_\lambda}{A_V} = 0.41 \times (\lambda[\mu\mathrm{m}])^{-1.75}. \quad (2)$$

As shown in figure 4, the values of $W_{\lambda8542}/W_{\lambda8498}$ are 1.0–2.0 and $W_{\lambda8662}/W_{\lambda8498}$ are 0.7–1.7 for both the PMS samples and cluster members. This suggests that the emission originates from regions such as chromospheric plages and flares. Moreover, there is a tendency for emission lines showing relatively large $W_{\lambda8542}/W_{\lambda8498}$ to be broad. The large FWHM of the line suggests a large turbulent velocity (Hamann & Persson 1992).

Our results for the PMS stars are consistent with Herbig and Soderblom (1980), Hamann and Persson (1992), and Frasca et al. (2017). Frasca et al. (2017) investigated the ratio of the line flux, $F_{\lambda8542}/F_{\lambda8498}$, of Class II and Class III objects in the Lupus star-forming region. These objects have a low ratio of $1 < F_{\lambda8542}/F_{\lambda8498} < 2$. Not only the PMS stars in our sample but also the cluster members in IC 2391 and IC 2602 show a ratio of $W_{\lambda8542}/W_{\lambda8498}$ of 1.0–2.0, indicating that the Ca II IRT emission lines are emitted from regions analogous to solar plages and flares.

The relationship between optical thickness and line broadening has been studied for the Ca II HK emission lines. Hamann and Persson (1989, 1992) noticed that the Ca II HK emission lines of the TTSs are stronger and broader than the Ca II IRT emission lines. Their interpretation was that the Ca II HK emission lines are optically thicker than the Ca II IRT emission lines because the Ca II HK emission lines are generally stronger than the Ca II IRT emission lines. Cram and Giampapa (1987) calculated the Ca II K line profile in the non-LTE chromospheric model. According to this model, with a small chromospheric mass column density, the Ca II K line shows a narrow and weak emission. In the case where the mass column density increases, the Ca II K line exhibits not only stronger but also broader emissions. Batalha and Basri (1993) constructed photospheric and chromospheric models to match the Ca II HK and IRT emission line profiles of six PMS stars. They found that the lines are shaped by the mass and temperature of the photosphere, the chromospheric temperature and microturbulence, and the temperature gradient of the lower chromosphere. A broad absorption line with a narrow emission core at the line center was successfully reproduced in both CTTSs and WTTSs with the chromospheric models.

4.2 Chromospheric activity and mass accretion rate

We compared the strengths of the Ca II IRT emission lines and mass accretion rates to discuss whether the chromosphere is activated by mass accretion from the protoplanetary disk.

Mohanty, Jayawardhana, and Basri (2005) investigated the chromospheric activity of CTTSs, very low-mass young stars ($0.075 \leq M_* < 0.15\,M_\odot$) and young brown dwarfs ($M_* \leq 0.075\,M_\odot$). They selected "accretors" by applying a number of accretion diagnostics, such as an Hα 10% width $\geq$200 km s^{-1}. For the accretors, the surface flux of the Ca II emission line, $F'_{\lambda 8662}$, showed a positive correlation with their mass accretion rate, $\dot{M}$, for approximately four orders of magnitude. Hence, they claim that the mass accretion rate can be estimated using the strength of the broad components of the Ca II IRT emission lines. In Mohanty, Jayawardhana, and Basri (2005), the mass accretion rates of CTTSs were taken from Muzerolle, Hartmann, and Calvet (1998) and White and Basri (2003), in which the rates were estimated from the amount of veiling in the U, V, and R_C bands. For the very low-mass young stars and the young brown dwarfs, the mass accretion rates were taken from Muzerolle et al. (2003), in which the rates were estimated from the EQWs of the Hα emission lines.

For calculating $F'_{\rm IRT}$, a bolometric continuum flux per unit area at a stellar surface, F, was first calculated. We used the i-band mag (the AB system) of the UCAC4 Catalogue (Zacharias et al. 2013), the stellar radius, and the distance of the objects (table 1). F is given as

$$\log \frac{f}{f_0} = -\frac{2}{5} \times (m_{i*} - A_I), \tag{3}$$

$$F = f \times \left(\frac{d}{R_*}\right)^2, \tag{4}$$

where f is the bolometric continuum flux of the object per unit area as observed on Earth, and m_{i*} is the apparent magnitude of the object in the i band. The bolometric continuum flux per unit area under $m_i = 0$ mag (the AB system) condition, f_0, is 1.852×10^{-12} W m^{-2} Å $^{-1}$ (Fukugita et al. 1996). A_I is the absorption coefficient for I mag, which is established with the absorption coefficient for V mag, A_V (Rieke & Lebofky 1985):

$$A_I = A_V \times 0.482. \tag{5}$$

Above, d denotes the distance from an object to Earth (Gaia DR2; Bailer-Jones et al. 2018). Unfortunately, the distance from GH Tau is not listed in Gaia DR2, so we substituted

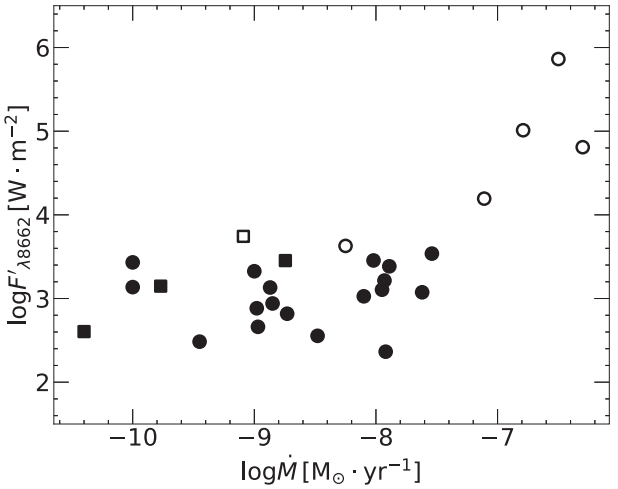

Fig. 5. Surface flux of the Ca II emission line, $F'_{\lambda 8662}$, as a function of mass accretion rate, $\dot{M}$. The circle symbols represent the PMS stars in the molecular clouds, and the square symbols are the PMS stars in the moving groups. The open symbols show the objects with a broad Ca II IRT emission line (FWHM $>$ 100 km s^{-1}), and the filled symbols represent the objects with a narrow Ca II IRT emission line (FWHM $\leq$ 100 km s^{-1}).

that of the Taurus molecular cloud (140 pc). R_* is the stellar radius estimated using the Stefan–Boltzmann law with the photospheric luminosity, $T_{\rm eff}$, and the distance of the objects in Gaia DR2 (Gaia Collaboration 2018; Bailer-Jones et al. 2018). For objects whose $T_{\rm eff}$ is not listed in Gaia DR2, we used the luminosity and $T_{\rm eff}$ listed in other papers: Palla and Stahler (2002) for AA Tau, Kenyon and Hartmann (1995) for GH Tau, and Pecaut and Mamajek (2013) for HD 197481, RECX 09, and TWA 22. F was multiplied by the EQW of the Ca II IRT lines,

$$F'_{\rm IRT} = F \times W_{\rm IRT}, \tag{6}$$

and the $F'_{\rm IRT}$ are listed in table 6. The relation between the mass accretion rate, $\dot{M}$, and the surface flux of the Ca II line, $F'_{\lambda 8662}$, is shown in figure 5. The $\dot{M}$ listed in table 1 were taken from several studies, in which the rates were estimated from the amount of veiling: Najita, Strom, and Muzerolle (2007) and Calvet et al. (2004) estimated $\dot{M}$ with a continuum component between the visible and UV wavelengths, Gullbring et al. (1998), White and Ghez (2002), Hartmann et al. (1998), and Ingleby et al. (2013) determined $\dot{M}$ from the amount of continuum veiling in the U band. For objects whose veiling had not been determined, we used $\dot{M}$ estimated with the EQW of the Hα emission line (Lawson et al. 2004).

In figure 5, the circle symbols represent the PMS stars in the molecular clouds and the square symbols are the PMS stars in the moving groups. The open symbols show objects with a broad Ca II IRT emission line (FWHM $>$100 km s^{-1}) and the filled symbols represent the objects with a narrow

Table 5. Time variation of the profiles of the CTTS, BP Tau.

Observation date	Profiles	$W_{\lambda 8662}$ [Å]	Reference*
1993	Narrow emission (λ8498)	Not measured	[1]
1996	Broad emission + narrow emission (λ8542)	7.8	[2]
2006	Broad emission + narrow emission (λλ8498, 8542, 8662)	6.44	[3]
2008	Narrow emission + photospheric abrorption (λλ8498, 8542, 8662) + Photospheric abrorption (λλ8498, 8542, 8662)	1.15	[4]

*References: [1] Ardila et al. (2002); [2] Muzerolle, Hartmann, and Calvet (1998); [3] Moto'oka and Itoh (2012); [4] This work.

Ca II IRT emission line (FWHM $\leq 100\,\mathrm{km\,s^{-1}}$). As mentioned above, the broad line components are explained well by the magnetospheric accretion model in Muzerolle, Hartmann, and Calvet (1998), while the narrow Ca II lines are generated in the stellar chromosphere (Hamann & Persson 1992).

We can see two groups among the PMS stars. High mass accretion rate PMS stars ($\dot{M} \gtrsim 10^{-7}\,M_\odot\,\mathrm{yr^{-1}}$) have a broad Ca II IRT emission line. DG Tau, DL Tau, and DR Tau belong to this group. Those are classified as accretors based on the accretion diagnosis of Mohanty, Jayawardhana, and Basri (2005). The relationship between the mass accretion rate and the surface flux of the Ca II IRT emission line is consistent with that for the accretors (Mohanty et al. 2005). The mass accretion rate does not show any correlation with $F'_{\lambda 8662}$ for the objects with a narrow emission and almost all objects have $\log F'_{\lambda 8662} \sim 3$ with a flat distribution to $\dot{M}$. Those do not meet the accretor criteria presented by Mohanty, Jayawardhana, and Basri (2005). Most objects in our sample, including CTTSs, belong to this group. All the investigated PMS stars with a low mass accretion rate, except SU Aur and RECX 15, do not show broad Ca II IRT emission lines. The difference in F'_{IRT} between the two groups is more than one order of magnitude. We found that there is a significant difference between the group of objects with a broad Ca II IRT emission line and the group of objects with a narrow Ca II IRT emission line. This is a well-established difference between accretors and non-accretors reported by some studies, and our results support that.

The Ca II IRT emission lines of PMS stars vary with time (e.g., Johns-Krull & Basri 1997). We present the EQWs and profiles of the Ca II IRT emission lines of BP Tau in table 5. In this work, BP Tau shows narrow emissions superposed on broad absorption features. The $W_{\lambda 8662}$ of BP Tau in this study is 1.15 Å. In contrast, the Ca II IRT lines in Mohanty, Jayawardhana, and Basri (2005) are broad and $W_{\lambda 8662}$ is 7.8 Å. Mohanty, Jayawardhana, and Basri (2005) referred to the EQWs of the Ca II IRT emission lines in Muzerolle, Hartmann, and Calvet (1998); BP Tau as observed in 1996 has strong $F'_{\lambda 8662}$, similar to DG Tau, DL Tau, and DR Tau. In Mohanty, Jayawardhana, and Basri (2005), objects with broad Ca II IRT emission lines as classified by Muzerolle, Hartmann, and Calvet (1998) show a positive correlation with the mass accretion rate. Most objects in this study have narrow components, so that their $F'_{\lambda 8662}$ has no correlation with the mass accretion rate.

4.3 Rotation–activity relation

The narrow Ca II IRT emission lines in most of our samples are not correlated with the mass accretion rate. Noyes et al. (1984) used the Rossby number, N_{R}, as an indicator of stellar dynamo activity. We calculated N_{R} as follows,

$$N_{\mathrm{R}} = \frac{2\pi R_*}{\tau_{\mathrm{c}} v \sin i}, \tag{7}$$

where $v \sin i$ is taken from the Catalog of Stellar Rotational Velocities (Glebocki & Gnacinski 2005), Torres et al. (2006), Messina et al. (2011), and Nguyen et al. (2012). For objects whose $v \sin i$ was not measured, we took the rotation period from Messina et al. (2010, 2011), Heinze et al. (2018), and the AAVSO International Variable Star Index (Watson et al. 2006). The rotation periods of IT Tau, TWA 06, TWA 14, TWA 23, and RECX'09 are 7.56 d, 0.54 d, 0.63 d, 1.03 d, and 1.71 d, respectively. R_* represents the stellar radius and τ_{c} is the convective turnover time.

We estimate τ_{c} of our PMS stars using the pre-main-sequence evolutionary tracks and convective turnover time of stars with 0.065–5.0 $M_\odot$ presented in Jung and Kim (2007). The convective turnover time of a solar-mass PMS is between 300 and 100 d for the CTTS phase, and between a few hundred days and several dozens of days for the WTTS phase. The convective turnover time of an object near and on ZAMS remains stable at a few dozen days. In Jung and Kim (2007), the τ_{c} of low-mass stars near the main sequence was not calculated. For objects whose τ_{c} was not calculated in Jung and Kim (2007), we apply the approximation from Noyes et al. (1984) when calculating τ_{c} with $(B-V)_0$. $(B-V)_0$ was calculated from $B-V$ (Herbig & Bell 1988; Hanson 2003; Manoj et al. 2006;

Table 6. $F'_{\rm IRT}$ and $R'_{\rm IRT}$ of the Ca II IRT emission lines (λλ8498, 8542, 8662 Å).

Object name	$\log F'_{\lambda 8498}$ [W m^{-2}]	$\log F'_{\lambda 8542}$ [W m^{-2}]	$\log F'_{\lambda 8662}$ [W m^{-2}]	$\log R'_{\lambda 8498}$	$\log R'_{\lambda 8542}$	$\log R'_{\lambda 8662}$	$\log N_{\rm R}$	Note*
Taurus–Auriga molecular cloud								
AA Tau	2.58	2.65	2.55	−4.61	−4.54	−4.63	−1.71	NC
BP Tau	3.50	3.70	3.54	−3.80	−3.59	−3.76	−1.57	NC
CX Tau	2.57	2.69	2.66	−4.32	−4.20	−4.23	−1.75	NC
CoKu Tau4	3.38	3.57	3.43	−3.81	−3.62	−3.76	−2.00	NC
DF Tau	2.99	3.24	3.07	−4.02	−3.77	−3.94	−1.53	NC
DG Tau	4.79	4.77	4.81	−2.25	−2.27	−2.23	−1.85	BC
DL Tau	5.15	5.12	5.01	−2.01	−2.04	−2.15	−1.83	BC
DM Tau	3.08	3.19	3.11	−3.98	−3.87	−3.95	−1.71	NC
DR Tau	5.90	5.95	5.86	−1.40	−1.35	−1.44	−1.81	BC
DS Tau	3.24	3.44	3.38	−3.94	−3.74	−3.79	−1.68	NC
FN Tau	3.78	—	3.83	−3.49	—	−3.44	−1.17	NC
FP Tau	2.49	—	2.48	−4.44	—	−4.44	−1.97	NC
GH Tau	2.41	2.47	2.36	−4.56	−4.50	−4.61	−1.68	NC
GM Aur	3.26	3.54	3.45	−4.04	−3.76	−3.85	−1.55	NC
GO Tau	3.15	3.29	3.21	−4.00	−3.86	−3.94	−1.57	NC
HBC 374	2.85	3.08	—	−4.32	−4.08	—	−1.67	NC
HBC 376	3.50	3.63	—	−3.82	−3.69	—	—	NC
HBC 407	2.82	2.91	2.83	−4.61	−4.52	−4.60	−1.03	NC
HBC 427	2.83	2.95	2.90	−4.44	−4.32	−4.37	−1.45	NC
HD 285778	3.06	3.27	—	−4.61	−4.40	—	−1.33	NC
HP Tau	—	—	—	—	—	—	−2.54	NC
IT Tau	3.57	3.67	3.60	−3.56	−3.45	−3.52	−1.33	NC
LkCa 04	2.69	2.86	2.82	−4.30	−4.13	−4.17	−1.87	NC
LkCa 14	2.88	3.02	2.94	−4.37	−4.24	−4.31	−1.90	NC
LkCa 15	3.13	3.15	3.13	−4.11	−4.10	−4.12	−1.66	NC
LkCa 19	3.13	3.27	3.14	−4.34	−4.21	−4.34	−1.68	NC
RY Tau	4.38	4.26	4.19	−3.41	−3.53	−3.60	−1.19	BC
SU Aur	3.49	3.72	3.63	−3.82	−3.59	−3.68	−1.92	BC
UX Tau	3.26	3.39	3.33	−4.08	−3.95	−4.01	−1.52	NC
V1023 Tau	3.30	3.47	—	−3.87	−3.69	—	−1.67	NC
V1204 Tau	3.08	3.11	—	−4.40	−4.37	—	−1.54	NC
V1297 Tau	3.04	3.11	3.02	−4.52	−4.45	−4.55	−1.01	NC
V1321 Tau	2.99	3.12	3.04	−4.19	−4.06	−4.13	−1.28	NC
V1348 Tau	2.95	3.08	2.98	−4.39	−4.26	−4.37	−1.09	NC
V830 Tau	3.00	3.20	3.03	−4.17	−3.97	−4.14	−1.98	NC
V836 Tau	2.81	2.90	2.88	−4.19	−4.09	−4.11	−1.58	NC
ZZ Tau	3.24	3.37	3.20	−3.98	−3.85	−4.02	−1.65	NC
Orionis OB 1c association								
HBC 167	3.96	4.19	4.06	−3.75	−3.52	−3.65	−1.26	NC
Upper Scorpius association								
1RXS J161951.4−215431	—	—	—	—	—	—	—	NC
Perseus molecular cloud								
LkHα 86	2.65	2.79	2.69	−4.36	−4.22	−4.32	−1.54	NC
LRL 72	—	—	—	—	—	—	−1.32	NC
AB Doradus moving group								
HIP 17695	2.21	2.36	2.21	−4.64	−4.49	−4.64	−2.15	NM
β Pictoris moving group								
HD 197481	2.56	2.64	2.56	−4.44	−4.36	−4.45	−1.70	NM
η Chamaeleontis cluster								
RECX 04	2.83	2.97	2.85	−4.34	−4.20	−4.33	−1.30	NM

Table 6. (Continued)

Object name	$\log F'_{\lambda 8498}$ [W m^{-2}]	$\log F'_{\lambda 8542}$ [W m^{-2}]	$\log F'_{\lambda 8662}$ [W m^{-2}]	$\log R'_{\lambda 8498}$	$\log R'_{\lambda 8542}$	$\log R'_{\lambda 8662}$	$\log N_{\rm R}$	Note*
RECX 06	2.50	2.58	2.44	−4.44	−4.36	−4.51	−2.04	NM
RECX 07	2.94	3.10	3.00	−4.36	−4.20	−4.29	−2.01	NM
RECX 09	2.48	2.75	2.60	−4.66	−4.39	−4.53	−1.79	NM
RECX 10	2.80	2.91	2.79	−4.40	−4.29	−4.41	−1.22	NM
RECX 11	3.06	3.23	3.15	−4.27	−4.10	−4.18	−1.50	NM
RECX 15	3.85	3.85	3.74	−3.19	−3.18	−3.29	−2.11	BM
"Cha-Near" region								
RX J1147.7−7842	2.85	3.07	2.90	−4.26	−4.04	−4.21	—	BM
RX J1204.6-7731	2.62	2.76	2.62	−4.35	−4.22	−4.35	−1.44	NM
TW Hydrae association								
TWA 01	3.23	3.51	3.45	−4.03	−3.75	−3.81	−1.53	NM
TWA 06	3.03	3.24	3.14	−4.24	−4.04	−4.13	−2.21	NM
TWA 07	2.89	2.96	2.84	−4.28	−4.21	−4.33	−1.20	NM
TWA 14	2.87	3.05	2.92	−4.23	−4.05	−4.18	−2.57	NM
TWA 22	1.99	2.27	2.15	−4.58	−4.30	−4.42	−1.05	NM
TWA 23	2.34	2.46	2.24	−4.60	−4.47	−4.69	−2.34	NM
TWA 25	2.95	3.07	3.01	−4.22	−4.10	−4.16	−1.36	NM

*This column shows the groups based on the FWHM of the Ca II emission lines (λ8498 Å) and the membership of the objects. NC: Narrow emission objects belonging to the molecular clouds. BC: Broad emission objects belonging to the molecular clouds. NM: Narrow emission objects belonging to the moving groups. BM: Broad emission objects belonging to the moving groups.

van Leeuwen 2007; Mayne et al. 2007; Davies et al. 2014; Henden et al. 2016) and A_V in Kraus et al. (2009), Manoj et al. (2006), and Wahhaj et al. (2010).

We calculated the ratio of the surface flux of the Ca II IRT lines to the stellar bolometric luminosity, $R'_{\rm IRT}$, for each Ca II IRT line. $R'_{\rm IRT}$ is similar to the parameter $R'_{\rm HK}$ derived from the Ca II H and K lines, as described by Noyes et al. (1984). $R'_{\lambda 8542}$, the ratio of the surface flux of the λ8542 Å line to the stellar bolometric luminosity, has previously been used by Soderblom et al. (1993) and James and Jeffries (1997). In addition to $R'_{\lambda 8542}$, $R'_{\lambda 8498}$ and $R'_{\lambda 8662}$ were used by Marsden, Carter, and Donati (2009). In their study, $R'_{\lambda 8498}$ and $R'_{\lambda 8662}$ showed qualitatively similar results to $R'_{\lambda 8542}$. $R'_{\rm IRT}$ involves $R'_{\lambda 8498}$, $R'_{\lambda 8542}$, and $R'_{\lambda 8662}$, which are determined individually for each of the Ca II IRT lines. For calculating $R'_{\rm IRT}$, the $F'_{\rm IRT}$ are divided by $\sigma T_{\rm eff}^4$,

$$R'_{\rm IRT} = \frac{F'_{\rm IRT}}{\sigma T_{\rm eff}^4}, \tag{8}$$

where σ is the Stefan–Boltzmann constant. The dependence of the surface flux upon the $T_{\rm eff}$ of the objects is eliminated by this calculation. The $R'_{\rm IRT}$ are listed in table 6.

The chromospheric activity of ZAMS stars is considered to be induced by dynamo activity. Marsden, Carter, and Donati (2009) investigated the Ca II IRT emission lines of low-mass stars in the young open clusters IC 2391 and IC 2602. For stars with $\log N_{\rm R} \leq -1.1$, $R'_{\rm IRT}$ is constant at levels of $\log R'_{\lambda 8498} \sim -4.4$, $\log R'_{\lambda 8542} \sim -4.2$, and $\log R'_{\lambda 8662} \sim -4.3$. These regions are called the saturated regime. For stars with $\log N_{\rm R} \geq -1.1$, $R'_{\rm IRT}$ decreases with increasing $N_{\rm R}$. This region is called the unsaturated regime. Marsden, Carter, and Donati (2009) suggested that the chromosphere is completely filled by the emitting region for stars in the saturated regime.

Figure 6 shows $R'_{\rm IRT}$ as a function of $N_{\rm R}$. The circle symbols represent PMS stars in molecular clouds, and the square symbols are PMS stars in moving groups. The open circles and squares show objects with a broad Ca II IRT emission line, and the filled circles and squares represent objects with a narrow Ca II IRT emission line. The cross symbols represent low-mass stars in IC 2391 and IC 2602, as studied in Marsden, Carter, and Donati (2009).

Most PMS stars have $N_{\rm R}$ and $R'_{\rm IRT}$ similar to those of the cluster members in the saturated regime. We claim that the chromospheres of the PMS stars are activated by the magnetic field generated by the dynamo process, and that the chromospheres of these stars are completely filled by the emitting region. This is consistent with the previous studies indicating that PMS stars have optically thick Ca II IRT emission lines (e.g., Hamann & Persson 1992; Batalha & Basri 1993), and our results support them. In contrast, three PMS stars with strong and broad emission lines (DG Tau, DL Tau, and DR Tau) have $R'_{\rm IRT}$ two orders of magnitude larger than the cluster members. We consider that strong emission lines are caused by heavy mass accretion from their protoplanetary disks.

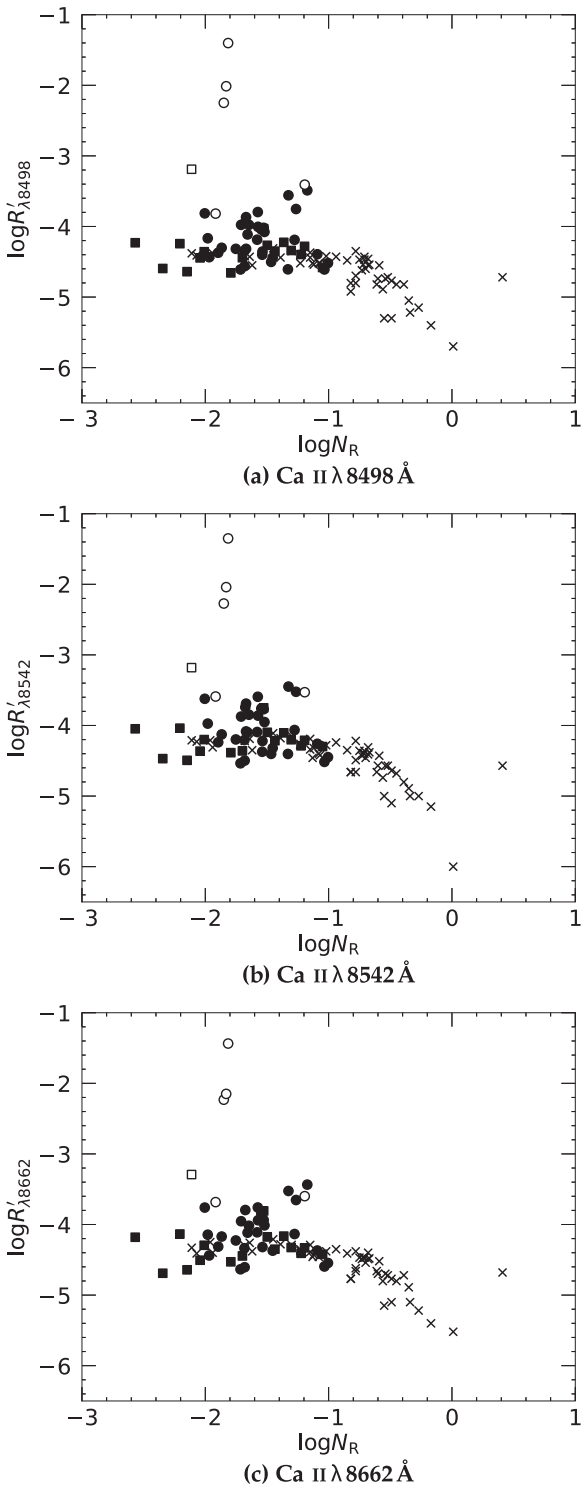

Fig. 6. Relation between the ratio of the surface flux of the Ca II IRT line to the stellar bolometric luminosity, $R'_{\rm IRT}$, and the Rossby number, $N_{\rm R}$. The circle symbols represent PMS stars in molecular clouds, and the square symbols indicate PMS stars in moving groups. The filled symbols represent PMS stars with narrow Ca II IRT emission lines, and the open symbols show PMS stars with broad Ca II IRT emission lines. The cross symbols represent low-mass stars in the young open clusters IC 2391 and IC 2602, as studied in Marsden, Carter, and Donati (2009).

Several researchers have pointed out that low-mass dwarfs showing strong Ca II emission lines also have strong X-ray emissions (Hodebine et al. 2017) and strong magnetic fields (Valenti & Johns-Krull 2001; Linsky 2017), and that the flux variation of the Ca II lines is related to the coverage of their faculae or spots. Some of these features have already been found in low-mass PMS stars. Furthermore, it has to be investigated whether low-mass PMS stars have these other features.

5 Conclusion

We have investigated the Ca II infrared triplet lines (λλ8498, 8542, 8662 Å) of 60 PMS stars. The observations were conducted with Nayuta/MALLS and Subaru/HDS. Archived data obtained from Keck/HIRES, VLT/UVES, and VLT/X-Shooter were also used.

(1) The ratios of the equivalent widths of the Ca II IRT emission lines $W_{\lambda 8542}/W_{\lambda 8498}$ are 1.0–2.0 and $W_{\lambda 8662}/W_{\lambda 8498}$ are 0.7–1.7 for both PMS stars and the low-mass stars in the young open clusters (Marsden et al. 2009). This suggests that the Ca II IRT emission lines originate from the regions analogous to solar plages and flares.

(2) Seven PMS stars (DG Tau, DL Tau, DR Tau, RY Tau, SU Aur, RECX 15, and RX J1147.7−7842) have broad Ca II IRT emission lines. It is suggested that their broad emissions result from heavy mass accretion from their protoplanetary disks.

(3) Most PMS stars have narrow Ca II IRT emission lines similar to low-mass stars in young open clusters. The emissions of these objects indicate no correlation with the mass accretion rate. The ratio of the surface flux of the Ca II IRT emission lines to the stellar bolometric luminosity, $R'_{\rm IRT}$, of these objects is as large as the largest $R'_{\rm IRT}$ of the cluster members. Most PMS stars have chromospheric activity similar to zero-age main-sequence stars. The chromospheres of these stars are completely filled by the Ca II emitting region.

Acknowledgment

This research has made use of the Keck Observatory Archive (KOA), which is operated by the W. M. Keck Observatory and NASA Exoplanet Science Institute (NExScI), and it is under contract with the National Aeronautics and Space Administration, and is based on observations made with ESO Telescopes at La Silla Paranal Observatory under programmes ID 075.C-0321, 082.C-0005, 084.C-1095, 085.C-0238, 086.C-0173, 094.C-0327, 094.C-0805, and 094.C-0913. Y. I. is supported by JSPS KAKENHI grant number 17K05390.

References

Ardila, D. R., Basri, G., Walter, F. M., Valenti, J. A., & Johns-Krull, C. M. 2002, ApJ, 567, 1013

Bailer-Jones, C. A. L., Rybizki, J., Fouesneau, M., Mantelet, G., & Andrae, R. 2018, ApJ, 156, 58

Barrado y Navascués, D., Stauffer, J. R., & Jayawardhana, R. 2004, ApJ, 614, 386

Basri, G., & Batalha, C. 1990, ApJ, 363, 654

Batalha, C. C., & Basri, G. 1993, ApJ, 412, 363

Batalha, C. C., Stout-Batalha, N. M., Basri, G., & Terra, M. A. O. 1996, ApJS, 103, 211

Bouvier, J. 1990, AJ, 99, 946

Calvet, N., Basri, G., & Kuhi, L. V. 1984, ApJ, 277, 725

Calvet, N., & Gullbring, E. 1998, ApJ, 509, 802

Calvet, N., Hartmann, L., Wilner, D., Walsh, A., & Sitko, M. L. 2004, in ASP Conf. Ser., 324, Debris Disks and the Formation of Planets, ed. L. Caroff et al. (San Francisco: ASP), 205

Cram, L. E., & Giampapa, M. S. 1987, ApJ, 323, 316

D'Antona, F., & Mazzitelli, I. 1994, ApJS, 90, 467

Davies, A. G., Veeder, G. J., Hill, S. I., Matson, D. L., & Johnson, T. V. 2014, Icarus, 241, 190

Frasca, A., Biazzo, K., Alcalá, J. M., Manara, C. F., Stelzer, B., Covino, E., & Antoniucci, S. 2017, A&A, 602, A33

Fukugita, M., Ichikawa, T., Gunn, J. E., Doi, M., Shimasaku, K., & Schneider, D. P. 1996, AJ, 111, 1748

Gaia Collaboration 2018, A&A, 616, A1

Garufi, A., et al. 2019, A&A, 628, A68

Ghez, A. M., Neugebauer, G., & Matthews, K. 1993, ApJ, 106, 2005

Glebocki, R., & Gnacinski, P. 2005, VizieR Online Data Catalog, III/244

Gullbring, E., Hartmann, L., Briceño, C., & Calvet, N. 1998, ApJ, 492, 323

Hamann, F., & Persson, S. E. 1989, ApJ, 339, 1078

Hamann, F., & Persson, S. E. 1992, ApJS, 82, 247

Hanson, M. M. 2003, ApJ, 597, 957

Hartigan, P., Hartmann, L., Kenyon, S., Hewett, R., & Stauffer, J. 1989, ApJS, 70, 899

Hartigan, P., Kenyon, S. J., Hartmann, L., Strom, S. E., Edwards, S., Welty, A. D., & Stauffer, J. 1991, ApJ, 382, 617

Hartmann, L., Calvet, N., Gullbring, E., & D'Alessio, P. 1998, ApJ, 495, 385

Hartmann, L., Hewett, R., Stahler, S., & Mathieu, R. D. 1986, ApJ, 309, 275

Hartmann, L. W., Soderblom, D. R., & Stauffer, J. R. 1987, AJ, 93, 907

Heinze, A. N., et al. 2018, AJ, 156, 241

Henden, A. A., Templeton, M., Terrell, D., Smith, T. C., Levine, S., & Welch, D. 2016, VizieR Online Data Catalog, II/336

Herbig, G. H., & Bell, K. R. 1988, Lick Obs. Bull., No. 1111

Herbig, G. H., & Soderblom, D. R. 1980, ApJ, 242, 628

Houdebine, E. R., Mullan, D. J., Bercu, B., Paletou, F., & Gebran, M. 2017, ApJ, 837, 96

Ingleby, L., et al. 2013, ApJ, 767, 112

James, D. J., & Jeffries, R. D. 1997, MNRAS, 291, 252

Johns-Krull, C. M., & Basri, G. 1997, ApJ, 474, 433

Jung, Y. K., & Kim, Y.-C. 2007, J. Astron. Space Sci., 24, 1

Katsukawa, Y., et al. 2007, Science, 318, 1594

Kenyon, S. J., & Hartmann, L. 1995, ApJS, 101, 117

Kraus, A. L., Ireland, M. J., Hillenbrand, L. A., & Martinache, F. 2012, ApJ, 745, 19

Kraus, S., Hofmann, K.-H., Malbet, F., Meilland, A., Natta, A., Schertl, D., Stee, P., & Weigelt, G. 2009, A&A, 508, 787

Lawson, W. A., Lyo, A.-R., & Muzerolle, J. 2004, MNRAS, 351, L39

Leinert, C., Zinnecker, H., Weitzel, N., Christou, J., Ridgway, S. T., Jameson, R., Haas, M., & Lenzen, R. 1993, A&A, 278, 129

Linsky, J. L. 2017, ARA&A, 55, 159

Livingston, W., Wallace, L., White, O. R., & Giampapa, M. S. 2007, ApJ, 657, 1137

Manoj, P., Bhatt, H. C., Maheswar, G., & Muneer, S. 2006, ApJ, 653, 657

Marsden, S. C., Carter, B. D., & Donati, J.-F. 2009, MNRAS, 399, 888

Mayne, N. J., Naylor, T., Littlefair, S. P., Saunders, E. S., & Jeffries, R. D. 2007, MNRAS, 375, 1220

Messina, S., Desidera, S., Lanzafame, A. C., Turatto, M., & Guinan, E. F. 2011, A&A, 532, A10

Messina, S., Desidera, S., Turatto, M., Lanzafame, A. C., & Guinan, E. F. 2010, A&A, 520, A15

Mohanty, S., Jayawardhana, R., & Basri, G. 2005, ApJ, 626, 498

Moto'oka, K., & Itoh, Y. 2013, Res. Astron. Astrophys., 13, 1189

Muzerolle, J., Hartmann, L., & Calvet, N. 1998, AJ, 116, 455

Muzerolle, J., Hillenbrand, L., Calvet, N., Briceño, C., & Hartmann, L. 2003, ApJ, 592, 266

Najita, J. R., Strom, S. E., & Muzerolle, J. 2007, MNRAS, 378, 369

Neuhauser, R., Strerzik, M. F., Schmitt, J. H. M. M., Wichmann, R., & Krautter, J. 1995, A&A, 297, 391

Nguyen, D. C., Brandeker, A., van Kerkwijk, M. H., & Jayawardhana, R. 2012, ApJ, 745, 119

Noguchi, K., et al. 2002, PASJ, 54, 855

Noyes, R. W., Hartmann, L. W., Baliunas, S. L., Duncan, D. K., & Vaughan, A. H. 1984, ApJ, 279, 763

Palla, F., & Stahler, S. W. 2002, ApJ, 581, 1194

Parker, E. N. 1955, ApJ, 122, 293

Passegger, V. M., et al. 2018, A&A, 615, A6

Pecaut, M. J., & Mamajek, E. E. 2013, ApJS, 208, 9

Rieke, G. H., & Lebofky, M. J. 1985, ApJ, 288, 618

Skumanich, A. 1972, ApJ, 171, 565

Soderblom, D. R., Stauffer, J. R., Hudon, J. D., & Jones, B. F. 1993, ApJS, 85, 315

Stauffer, J. R., Hartmann, L. W., Prosser, C. F., Randich, S., Balachandran, S., Patten, B. M., Simon, T., & Giampapa, M. 1997, ApJ, 479, 776

Takagi, Y., Itoh, Y., Oasa, Y., & Sugitani, K. 2011, PASJ, 63, 677

Tokunaga, A. T. 2000, in Allen's Astrophysical Quantities, 4th ed., ed. A. N. Cox (New York: AIP Press), 143

Torres, C. A. O., Quast, G. R., da Silva, L., de La Reza, R., Melo, C. H. F., & Sterzik, M. 2006, A&A, 460, 695

Valenti, J. A., & Johns-Krull, C. 2001, in ASP Conf. Ser., 248, Magnetic Fields Across the Hertzsprung–Russell Diagram, ed. G. Mathys et al. (San Francisco: ASP), 179

van Leeuwen, F. 2007, A&A, 474, 653

Vernazza, J. E., Avrett, E. H., & Loeser, R. 1981, ApJS, 45, 635

Vogel, S. N., & Kuhi, L. V. 1981, ApJ, 245, 960

Wahhaj, Z., et al. 2010, ApJ, 724, 835

Watson, C. L., Henden, A. A., & Price, A. 2006, J. Am. Assoc. Variable Star Obs., 35, 318
White, R. J., & Basri, G. 2003, ApJ, 582, 1109
White, R. J., & Ghez, A. M. 2002, ApJ, 556, 265
Wilson, O. C. 1978, ApJ, 226, 379
Yee, S. W., Petigura, E. A., & von Braun, K. 2017, ApJ, 836, 77
Zacharias, N., Finch, C. T., Girard, T. M., Henden, A., Bartlett, J. L., Monet, D. G., & Zacharias, M. I. 2013, AJ, 145, 44
Zuckerman, B., & Song, I. 2004, A&A, 42, 685

Publ. Astron. Soc. Japan (2022) 74 (3), 557–568
https://doi.org/10.1093/pasj/psac013
Advance Access Publication Date: 2022 April 28

Measurements of chromospheric Mg I emission lines of zero-age main-sequence stars

Mai YAMASHITA* and Yoichi ITOH

Nishi-Harima Astronomical Observatory, Center for Astronomy, University of Hyogo, 407-2 Nishigaichi, Sayo, Sayo, Hyogo 679-5313

*E-mail: yamashita@nhao.jp

Received 2021 November 16; Accepted 2022 February 4

Abstract

The chromosphere is the active atmosphere in which energetic eruption events, such as flares, occur. Chromospheric activity is driven by the magnetic field generated by stellar rotation and convection. The relationship between chromospheric activity and the Rossby number, the ratio of the rotational period to the convective turnover time, has been extensively examined for many types of stars, by using narrow chromospheric emission lines, such as the Ca II lines and the Mg II H and K lines. However, the stars with small Rossby numbers, i.e., stars with rapid rotations and/or long convective turnover times, show constant strengths of such lines against the Rossby number. In this study, we investigate the infrared Mg I emission lines at 8807 Å of 47 zero-age main-sequence (ZAMS) stars in IC 2391 and IC 2602 using the archive data of the Anglo-Australian Telescope at the University College London Echelle Spectrograph. After subtracting the photospheric absorption component, the Mg I line is detected as an emission line for 45 ZAMS stars, the equivalent widths of which are between 0.02 Å and 0.52 Å. A total of 42 ZAMS stars show the narrower Mg I emission lines instead of the Ca II infrared triplet emission lines, suggesting that they are formed at different depths. The ZAMS stars with smaller Rossby numbers show stronger Mg I emission lines. The Mg I emission line is not saturated even in the saturated regime of the Ca II emission lines, i.e., Rossby number $<10^{-1.1}$. The Mg I emission line is considered to be a good indicator of chromospheric activity, particularly for active objects.

Key words: stars: activity — stars: chromospheres — techniques: spectroscopic

1 Introduction

The chromosphere is the active atmosphere in which flares and other energetic eruption phenomena occur. It is claimed that chromospheric activity is driven by the magnetic fields induced by the dynamo process. In the dynamo process, the Coriolis force (=rotational moment × convection velocity) balances the Lorentz force (= current × magnetic strength/density of plasma) (Baliunas et al. 1996). Stellar rotation and convection are considered to be the main processes that drive the evolution of magnetic activities. Noyes et al. (1984) used the Rossby number, N_R, as an indicator of stellar activity. It is defined as P/τ_c, where P is the stellar rotational period and τ_c is the convective turnover time. N_R can be approximated as the inverse square of the dynamo number, N_D, the wave solution of the dynamo equation. Magnetic fields develop when $|N_D| > 1$.

The relationship between chromospheric line strength and the Rossby number has been extensively examined

for main-sequence stars. Skumanich (1972) found that the luminosity of the Ca II emission lines and rotational velocity of a solar-type star with an age of 10^8 yr are one order of magnitude larger than those of stars with an age of 10^{10} yr. Linsky et al. (1979) obtained profiles of the Ca II infrared triplet (IRT) line at λ8542 Å in 49 main-sequence or giant stars of spectra type F9–K3. For active chromospheric stars, they found that the line cores are filled in compared to quiet chromospheric stars of the same spectral type. They claimed that a better way of testing for chromospheric emission in the photospheric absorption is to subtract the profiles of similar spectral type stars. As a result, they showed strong evidence of a chromospheric emission component beyond the line core for active stars. Soderblom et al. (1993) revealed strong Ca II IRT (λ8498, 8542, 8662 Å) emission lines of low-mass stars in the young open cluster M45. Marsden, Carter, and Donati (2009) also detected Ca II IRT emission lines of low-mass stars in young open clusters IC 2391 and IC 2602. The cluster members are considered to be on the zero-age main-sequence (ZAMS) or in the last evolution phase to the ZAMS. Soderblom et al. (1993) and Marsden, Carter, and Donati (2009) calculated $R'_{\rm IRT}$ from the equivalent widths (EQWs), where $R'_{\rm IRT}$ describes the ratio of the surface flux of the Ca II IRT emission lines to the stellar bolometric luminosity. They found that for stars with $N_{\rm R} \geq 10^{-1.1}$, $R'_{\rm IRT}$ decreases with increasing $N_{\rm R}$. This region is called the unsaturated regime. In contrast, $R'_{\rm IRT}$ is constant at levels of approximately $10^{-4.2}$ for stars with $N_{\rm R} \leq 10^{-1.1}$. This region is called the saturated regime. Marsden, Carter, and Donati (2009) suggested that the chromosphere is completely filled by the emitting regions for the stars in the saturated regime.

Yamashita, Itoh, and Takagi (2020) investigated the relation between $N_{\rm R}$ and the Ca II IRT emission lines of 60 pre-main sequence (PMS) stars. Only three PMS stars showed broad and strong emissions, indicative of large mass accretion. Most of the PMS stars present narrow and weak emissions, suggesting that their emission lines are formed in the chromosphere. All their Ca II IRT emission lines have $R'_{\rm IRT} \sim 10^{-4.2}$, which is as large as the maximum $R'_{\rm IRT}$ of ZAMS stars. The PMS stars show $N_{\rm R} < 10^{-0.8}$ and constant $R'_{\rm IRT}$ against $N_{\rm R}$, i.e., their Ca II IRT emission lines are saturated.

In this study, we examined the infrared Mg I emission line at λ8807 Å (3d–3p transition) as a representative unsaturated chromospheric emission line. This Mg I emission line was isolated from other strong absorption lines. It was detected with numerous chromospheric emission lines during a total solar eclipse in 1962 (Dunn et al. 1968). The solar imaging with the infrared Mg I emission line suggested that the emission line is formed in the chromosphere 500 km above the photosphere (Fleck et al. 1994). As another example, the prominent infrared Mg I emission line was detected from eight T Tauri stars (Hamann & Persson 1992).

Specifically, we investigated the infrared Mg I emission lines of 47 ZAMS stars using high-resolution spectral data. We examined the relationship between the Rossby number and the Mg I emission line strength. In the next section, we describe the observations and the data reduction procedure. In section 3, we present the results, and in section 4, we discuss the origin of the Mg I emission line and the correlation of the line strength and the Rossby number.

2 Observations and data reduction

2.1 Stellar parameters

Our targets are F-, K-, and G-type ZAMS stars in IC 2391 (50 ± 5 Myr; Barrado y Navascues et al. 2004) and IC 2602 (30 ± 5 Myr; Stauffer et al. 1997). The metallicity of both clusters has been determined to be close to that of the Sun, at $[{\rm Fe/H}] = -0.01 \pm 0.02$ for IC 2391 (D'Orazi & Randich 2009) and $[{\rm Fe/H}] = 0.00 \pm 0.01$ for IC 2602 (Randich et al. 2001).

A total of 52 ZAMS stars are confirmed as single stars in the IC 2391 and IC 2602 members based on the strength of the lithium 6708 Å absorption line (Marsden et al. 2009). We examined the proper motion and radial velocity of these stars. The proper motion and the radial velocity are taken from Gaia Data Release 2 (DR2) (Gaia Collaboration 2018). For IC 2391, the mean proper motion in RA and Dec are $-23.6 \pm 4.7\,{\rm km\,s^{-1}}$ and $22.0 \pm 4.4\,{\rm km\,s^{-1}}$, respectively. For IC 2602, the corresponding values are $-17.3 \pm 1.0\,{\rm km\,s^{-1}}$ and $10.8 \pm 1.3\,{\rm km\,s^{-1}}$. Based on the observations in Gaia DR2 (Soubiran et al. 2018), for 51 objects in IC 2391 and 325 objects in IC 2602, Gutierrez Albarran et al. (2020) obtained mean radial velocities of $14.9 \pm 0.6\,{\rm km\,s^{-1}}$ and $17.8 \pm 0.7\,{\rm km\,s^{-1}}$, respectively. VXR PSPC 02A, VXR PSPC 31, VXR PSPC 78, and [RSP95] 96 have both proper motion and radial velocity that deviated by more than 3σ from the mean values. [RSP95] 42C has both proper motion and parallax that deviated by more than 3σ from the mean values. They were removed from our target list. A total of 47 targets were investigated in this study, which are presented in table 1.

2.2 Data reduction

2.2.1 Photometry

To obtain the rotational period, P, we analyzed the light curves of 39 ZAMS stars. The members of IC 2391 and IC 2602 were observed in Transiting Exoplanet Survey Satellite (TESS) Sectors 8 and 10, respectively. All 39 stars were observed in the long-cadence (1800-second exposure) mode, which continued for 27 days. These data were

Table 1. Physical parameters of the ZAMS stars in IC 2391 and IC 2602.*

Object name	r	i	$L/L_\odot$	$T_{\rm eff}$	$(B-V)_0$	Distance	Period	$v\sin i$	M_*	$\tau_c \times$
	[mag]	[mag]		[K]	[mag]	[pc]	[d]	[km s^{-1}]	[$M_\odot$]	10^5 [s]
(1)	(2)	(3)	(4)	(5)	(6)	(7)	(8)	(9)	(10)	(11)
IC 2391										
Cl* IC2391 L32	9.7	9.2	3.27	6590	0.43	150	–	68	1.5	1
VXR PSPC 3A	10.8	10.6	0.83	5607	0.67	150	3.93	10	1.0	15
VXR PSPC 7	9.5[a]	9.4	2.43	6472	0.45	146	–	21	1.4	2
VXR PSPC 12	11.6	11.4	0.41	5042	0.83	152	3.69	10	0.9	25
VXR PSPC 14	10.3	10.2	1.42	5768	0.56	158	1.35	43	1.1	11
VXR PSPC 16A	11.5	11.3	0.44	5093	0.87	152	–	21	0.9	25
VXR PSPC 22A	10.8	10.6	0.76	5587	0.73	148	2.31	8	1.0	15
VXR PSPC 35A	12.2	11.8	0.25	4982	0.99	150	0.26	89	0.8	25
VXR PSPC 44	9.7	9.4	2.64	6536	0.41	151	0.57	79	1.4	1
VXR PSPC 45A	10.5[a]	9.8[b]	1.19	5125	0.80	151	0.22	235	1.2	25
VXR PSPC 50A	–	11.6	0.21[b]	5210[b]	0.84	145[c]	–	56	0.8	20
VXR PSPC 52	10.2	10.1	1.48	5949	0.56	156	2.15	10	1.2	11
VXR PSPC 62A	11.6	11.3	0.45	4914	0.85	151	0.503[d]	49	0.9	25
VXR PSPC 66	9.7	9.5	2.36	6382	0.46	150	0.92	52	1.3	2
VXR PSPC 67A	11.4	11.1	0.55	5004	0.95	149	3.41	9	1.0	25
VXR PSPC 69A	11.3	11.1	0.43	5062	0.83	149	2.22	19	0.9	25
VXR PSPC 70	10.6	10.4	0.99	5737	0.63	152	2.61	16	1.0	15
VXR PSPC 72	11.3	11.1	0.54	5336	0.72	151	3.05	13	0.9	20
VXR PSPC 76A	12.4	12.0	0.22	4776	1.04	150	4.58	7	0.8	25
VXR PSPC 77A	9.9	9.6	2.14	6163	0.49	152	0.65	93	1.3	7
VXR PSPC 80A	–	11.0[b]	0.38[b]	4880[b]	0.96	145[c]	–	145	0.9	25
IC 2602										
Cl* IC2602 W79	11.3	11.1	0.48[b]	5500[b]	0.79	150	6.55	8	0.9	31
[RSP95] 1	11.3	11.0	0.56	5198	0.87	149	3.85	7	0.9	31
[RSP95] 7	9.4	9.0	3.74	6610	0.40	150	–	58	1.5	1
[RSP95] 8A	–	9.8[b]	1.27[b]	6190[b]	0.61	145[c]	–	27	1.2	7
[RSP95] 10	–	11.6[b]	0.22[b]	4520[b]	1.19	145[c]	3.16	14	0.8	42
[RSP95] 14	11.4	11.2	0.45	5071	0.83	149	2.73	11	0.9	31
[RSP95] 15A	–	10.7[b]	0.48[b]	4920[b]	0.89	145[c]	3.6[e]	7	1.0	31
[RSP95] 29	12.2	11.9	0.23	4779	1.07	150	2.22	21	0.8	42
[RSP95] 35	10.4[a]	9.9[b]	1.16	5838	0.36	152	2.46	21	1.1	11
[RSP95] 43	11.8[a]	11.1[b]	0.37	4994	0.91	150	0.78	47	0.9	31
[RSP95] 45A	–	10.1[b]	0.97[b]	5960[b]	0.62	145[c]	–	14	1.1	11
[RSP95] 52	12.0	11.6	0.25	4828	1.03	136	0.39	122	0.8	31
[RSP95] 58	10.4	10.2	1.37	5502	0.61	160	0.57	92	1.1	18
[RSP95] 59	11.6	11.3	0.44	4961	0.78	151	1.31	31	0.9	31
[RSP95] 66	10.8	10.6	0.77	5476	0.64	150	3.28	11	1.0	18
[RSP95] 68	10.9	10.6	0.58	4908	0.82	135	0.99	51	1.1	31
[RSP95] 70	10.7	10.6	0.83	5755	0.65	148	4.25	9	1.1	11
[RSP95] 72	10.6	10.5	0.99	5557	0.60	156	1.05	49	1.1	18
[RSP95] 79	9.0[a]	8.6[b]	4.26	6383	0.40	155	0.75	78	1.5	1
[RSP95] 80	10.3	10.1	1.27	4980	0.89	145	7.25	13	1.3	31
[RSP95] 83	10.5	10.5	1.02	5588	0.58	149	1.74	30	1.0	18
[RSP95] 85	9.7	9.7	2.11	6171	0.48	151	1.33	45	1.3	7
[RSP95] 88A	–	11.4[b]	0.25[b]	4350[b]	1.16	145[c]	0.204[e]	255	0.8	65
[RSP95] 89	12.5	12.0	0.19	4510	1.20	146	4.73	9	0.8	42
[RSP95] 92	10.0	9.9	0.65	5740	0.63	145[c]	1.93	16	1.1	11
[RSP95] 95A	12.3	11.1	0.55	5071	0.83	153	1.22	14	0.9	31

*References for parameters in each column: (2),(3) r [mag] and i [mag]: UCAC4 Catalogue (Zacharias et al. 2013), [a]ATLAS All-Sky Stellar Reference Catalogue (Tonry et al. 2018) and [b]Marsden, Carter, and Donati (2009). (4),(5) $L/L_\odot$ and $T_{\rm eff}$: Gaia DR2 (Gaia Collaboration 2018) and [b]Marsden, Carter, and Donati (2009). (6) $(B-V)_0$: Marsden, Carter, and Donati (2009). (7) Distance: Gaia DR2 (Bailer-Jones et al. 2018) and [c]van Leeuwen (2007). (8) Period: [d]Patten and Simon (1996) and [e]Barnes et al. (1999). (9) $v\sin i$: Marsden, Carter, and Donati (2009). (10) Canuto and Mazzitelli [CM] Alexander model (D'Antona & Mazzitelli 1994). (11) Landin, Mendes, and Vaz (2010) model and Noyes et al. (1984) model.

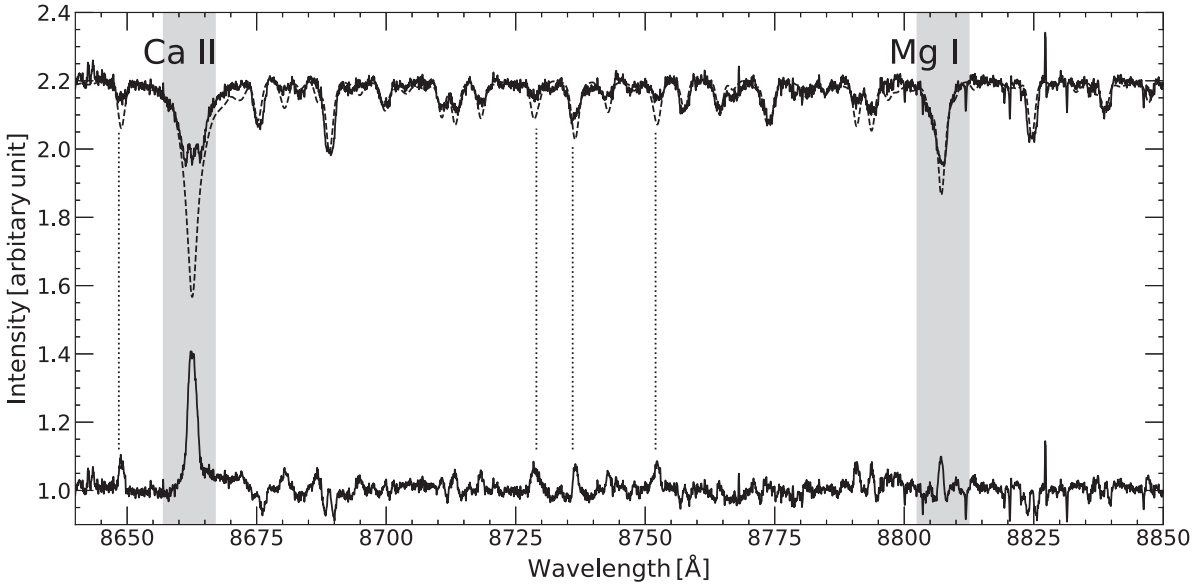

Fig. 1. Procedure of spectral subtraction of photospheric component for ZAMS star. The observed spectrum of [RSP95] 43 is shown in the top part of panel with a solid line. The dotted line represents the spectrum of the fitted inactive template star. The spectra of [RSP95] 43 and template star are shown shifted by +1.2 for display purposes. The difference between the spectra of [RSP95] 43 and template star is shown in the bottom of the panel, which is shifted by +1. The Ca II line (λ8662 Å) and the Mg I line (λ8808 Å) appear in emission. Other emission lines such as Si I (λ8648, 8729, 8752 Å) and Mg I (λ8736 Å) are also detected.

retrieved from the Multimission Archive at the Space Telescope Science Institute. We conducted principal component analysis using eleanor, an open-source tool for extracting light curves from TESS full-frame images (Feinstein et al. 2019). After the photometric measurements, we searched for periodic signals by conducting Lomb–Scargle (Scargle 1982) periodogram analysis. For each object, the period of the light curve was determined. VXR PSPC 44 presented beating signatures in its light curve; therefore, we adopted the second maximum of the power. We calculated the amplitudes of the light curves by taking the 90th percentile flux and subtracting it from the 10th percentile flux. For three objects that had amplitude/mean flux error <10 (Cl* IC2391 L32, VXR PSPC 7, and [RSP95] 7), we used the periods listed in Marsden, Carter, and Donati (2009). We also used the periods or $v \sin i$ listed in Marsden, Carter, and Donati (2009) for three objects not observed by TESS. The derived periods are listed in table 1. They show good correlation with the periods measured by Patten and Simon (1996) and Barnes et al. (1999), with a correlation coefficient of 0.997.

2.2.2 Spectroscopy

We investigated the Mg I line, the Hα line, and the Ca II IRT lines of the 47 considered ZAMS stars using the 3.9 m Anglo-Australian Telescope (AAT) and the University College London Echelle Spectrograph (UCLES) archived spectra. The principal investigator was S. C. Marsden. The dates of the observations were 2000 March 17–19, 2001 January 6–8, and 2001 February 11–12. The wavelength coverage was between 3522 Å and 9386 Å ($R \equiv \lambda/\Delta\lambda \sim$ 40000–120000). The integration time for each object was between 300 s and 1200 s. The number of frames obtained for each ZAMS star ranged from two to six. A detailed description of the observations is presented in Marsden, Carter, and Donati (2009).

We used the Image Reduction and Analysis Facility (IRAF) software package for data reduction.[1] Overscan subtraction, bias subtraction, flat-fielding, removal of scattered light, removal of cosmic rays and OH airgrow, extraction of a spectrum, wavelength calibration using a Tr–Ar lamp, and continuum normalization were conducted for all UCLES spectra. After the wavelength calibration, only 12 orders (orders 64–67, 75–76, 84–87, and 94–95) were reduced.

To improve the signal to noise (S/N) ratio, we combined and averaged multiple frames for each object. Moreover, the UCLES spectrum overlaps with the next order over several tens of Angstroms. The average ratio of the intensity to the next order was 1.8, which was independent of the wavelength. We applied a weight of 1.8 to each short spectrum.

We subtracted the photospheric absorption component for all spectra. The Mg I emission component is typically

[1] IRAF software is distributed by the National Optical Astronomy Observatories, which are operated by the Association of Universities for Research in Astronomy, Inc., under a cooperative agreement with the National Science Foundation.

buried by the photospheric absorption, as shown in figure 1. Inactive stars with a spectral type similar to that of the target were used as template stars. We reduced the UCLES spectra of HD 16673 (F6V), α Cen A (G2V), and α Cen B (K1V). We also obtained the VLT archive spectra of 10 inactive stars chosen from the inactive stars library (Yee, Petigura & von Braun 2017) and the UVES POP library: ζ Ser (F2IV), HD 3861 (F8V), HD 1388 (G0V), HD 156846 (G1V), HD 109749 (G3V), HIP 94256 (G5V), HD 190360 (G7V), HD 217107 (G8V), HD 16160 (K3V), and HD 165341B (K4V). According to Yee, Petigura, and von Braun (2017) and Nordstom et al. (2004), the metallicity of these stars is $-0.11 \leq [\mathrm{Fe/H}] \leq 0.31$. Their surface gravity is $4.01 \leq \log g \leq 4.64\,\mathrm{cm\,s^{-2}}$. The differences in the surface gravities of the target and template stars were sufficiently small, and were therefore not expected to change the strengths of the photospheric absorption lines. For each template star, we reduced several frames, followed by averaging. The spectrum of an inactive star was shifted to match the radial velocity of the target star. To correct the rotational broadening, the spectra of the template stars were convolved with a Gaussian kernel to match the widths of the absorption lines of each target. Using the high-S/N spectra of the inactive stars, we carefully subtracted the photospheric absorption component. We considered the photospheric subtraction to be reliable if the photospheric absorption lines did not show any emission or absorption component. Many Fe I absorption lines appeared in the spectra of the targets and templates. However, the emission components of Fe I may be formed in a lower chromosphere (Vernazza et al. 1981). Actually, T Tauri stars show narrow Fe I and Fe II emission lines at rest velocity, which are believed to be formed in the chromosphere (Hamann & Persson 1992). In contrast, we used Ni I (6644, 6728, 7525 Å), Mn I (6014, 6017, 6022 Å), V I (6039 Å), and Ti I (7523 Å) as the photospheric absorption lines. These absorption lines were isolated and relatively deep. We measured the standard deviation of the counts at Ni I (λ6644 Å) after the subtraction of the spectrum of the inactive star, $\sigma_{\mathrm{Ni\,I}}$. The wavelength range was set as the wing width of the Ni I absorption line before the subtraction. σ_{cont} is the standard deviation of the counts between λ6683 and 6693 Å, where there was no strong feature. $\sigma_{\mathrm{Ni\,I}}/\sigma_{\mathrm{cont}} \sim 1$ represents the appropriate subtraction of the photospheric absorption. $\sigma_{\mathrm{Ni\,I}}/\sigma_{\mathrm{cont}}$ of the ZAMS stars were between 0.59 and 2.51. In principle, $\sigma_{\mathrm{Ni\,I}}$ is greater than σ_{cont}, because the number of photons in the Ni I absorption line is smaller than that in the continuum. We considered that the photospheric subtraction was reliable if $\sigma_{\mathrm{Ni\,I}}/\sigma_{\mathrm{cont}} < 1.2$. A total of 30 ZAMS stars showed $\sigma_{\mathrm{Ni\,I}}/\sigma_{\mathrm{cont}} < 1.2$, and the remaining 17 ZAMS stars showed $\sigma_{\mathrm{Ni\,I}}/\sigma_{\mathrm{cont}} \geq 1.2$.

Before measuring the EQWs, the continuum components of the spectra were added to unity. To obtain the EQWs of the Mg I and Hα emission lines, the areas of the corresponding emission profiles were directly integrated. The EQW errors were estimated by multiplying the standard deviation of the continuum by the wavelength range of the emission lines of each ZAMS star. We estimated the standard deviations of the continuums near the Mg I and Hα emission lines. The wavelength range was λ8798–8802 Å and λ8813–8819 Å for the Mg I emission line, and that for the Hα emission line was λ6615–6623 Å. In these wavelength ranges, no strong features were observed. We also measured the full widths at half maximum (FWHMs) of the Mg I and Ca II IRT emission lines by fitting with a Gaussian function. The Ca II IRT lines at λ8542 Å of some template stars were out of range, and we did not measure their FWHMs.

3 Results

Figures 2 and 3 show the Hα, Ni I, and Mg I line spectra of the ZAMS stars after subtracting the photospheric absorption. Before subtracting the photospheric absorption component, the Mg I emission component is typically buried by the photospheric absorption, 11 ZAMS stars show Hα as an emission line, and all ZAMS stars show the Ni I line as an absorption component. After the subtraction, the Mg I line is detected as an emission line in 45 ZAMS stars. The Mg I lines of these ZAMS stars show narrow emission, indicative of a chromospheric origin. Their EQWs range from 0.02 to 0.52 Å. A total of 44 ZAMS stars show the Hα emission line. The Ni I line does not present any emission component. The EQWs of the Mg I and Hα emission lines and the FWHMs of the Mg I, Hα, and Ca II IRT emission lines are listed in table 2.

Some of the chromospheric emission lines detected during a total solar eclipse (Dunn et al. 1968) are also detected in the ZAMS spectra after the subtraction of the absorption components in the order of 64–67 and 84–87, P12 (λ8750 Å), P14 (λ8598 Å), He I (λ6678 Å), O I (λ8446 Å), Mg I (λ8736 Å), Si I (λ6721, 8557, 8648, 8728, 8742, 8752 Å), Ca I (λ6573 Å), and Fe I (λ6518, 6575, 6634, 6713, 6753, 8680, 8686, 8713, 8790, 8824 Å). Among them, P12, P14, He I (λ6678 Å), and O I (λ8446 Å) were also detected in the T Tauri star spectra obtained by Hamann and Persson (1992).

The emission line of Mg I at λ8807 Å is the most frequently detected line in the ZAMS spectra. Out of the 47 ZAMS stars, 45 show the emission lines of Mg I at λ8807 Å. The second most frequently detected line is the Mg I at λ8736 Å, which is detected in 40 ZAMS stars. However, this line blends with nearby Si I emission lines (λ8728, 8742 Å). The Fe I (λ8689, 8790 Å) and Si I (λ8728 Å) lines are detected in 35 ZAMS stars, 37 ZAMS stars, and

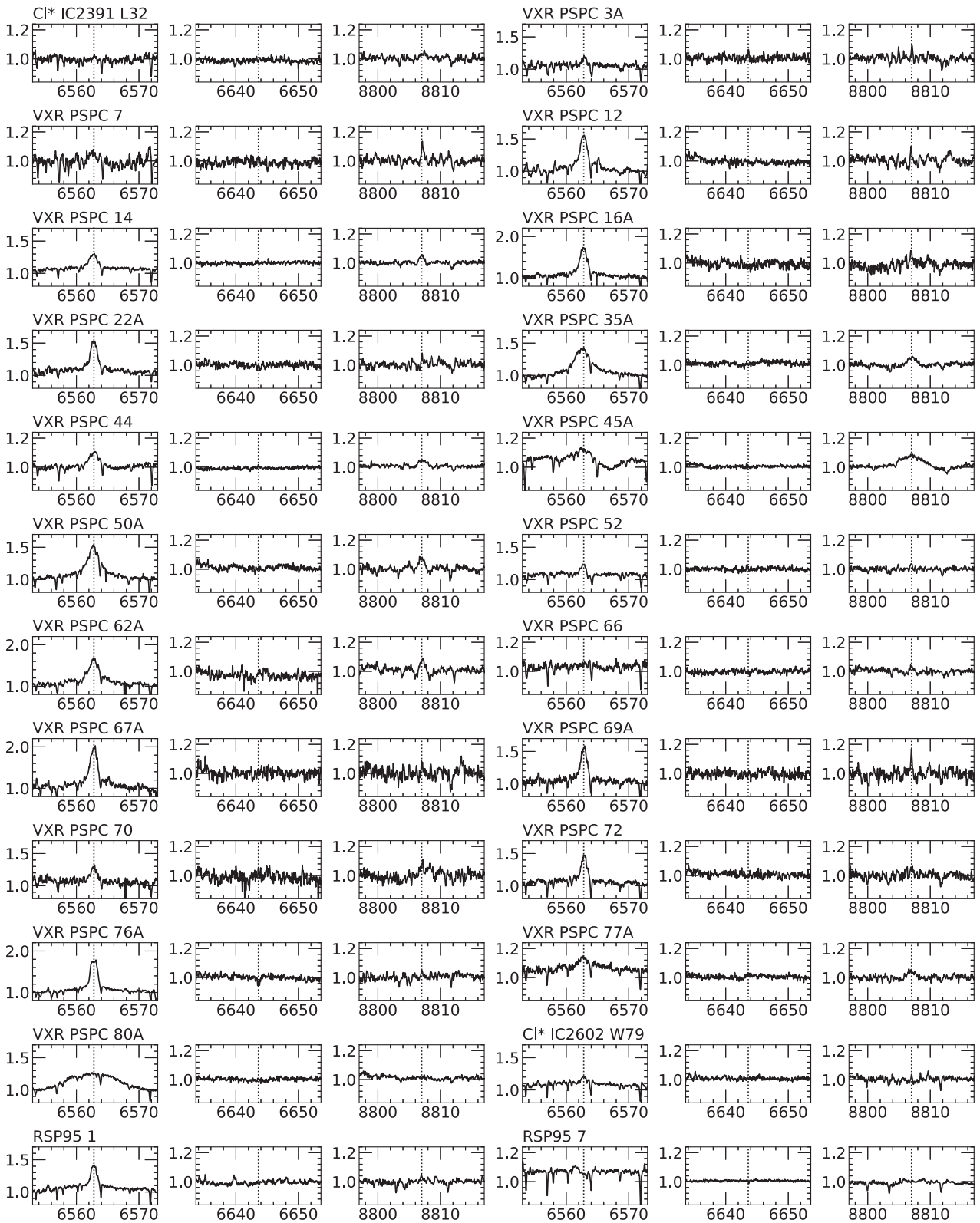

Fig. 2. Hα (6563 Å), Ni I (6644 Å), and Mg I (λ8807 Å) emission lines of ZAMS stars belonging to IC 2391 and IC 2602. The continuum is normalized to unity. Photospheric absorption lines are already subtracted.

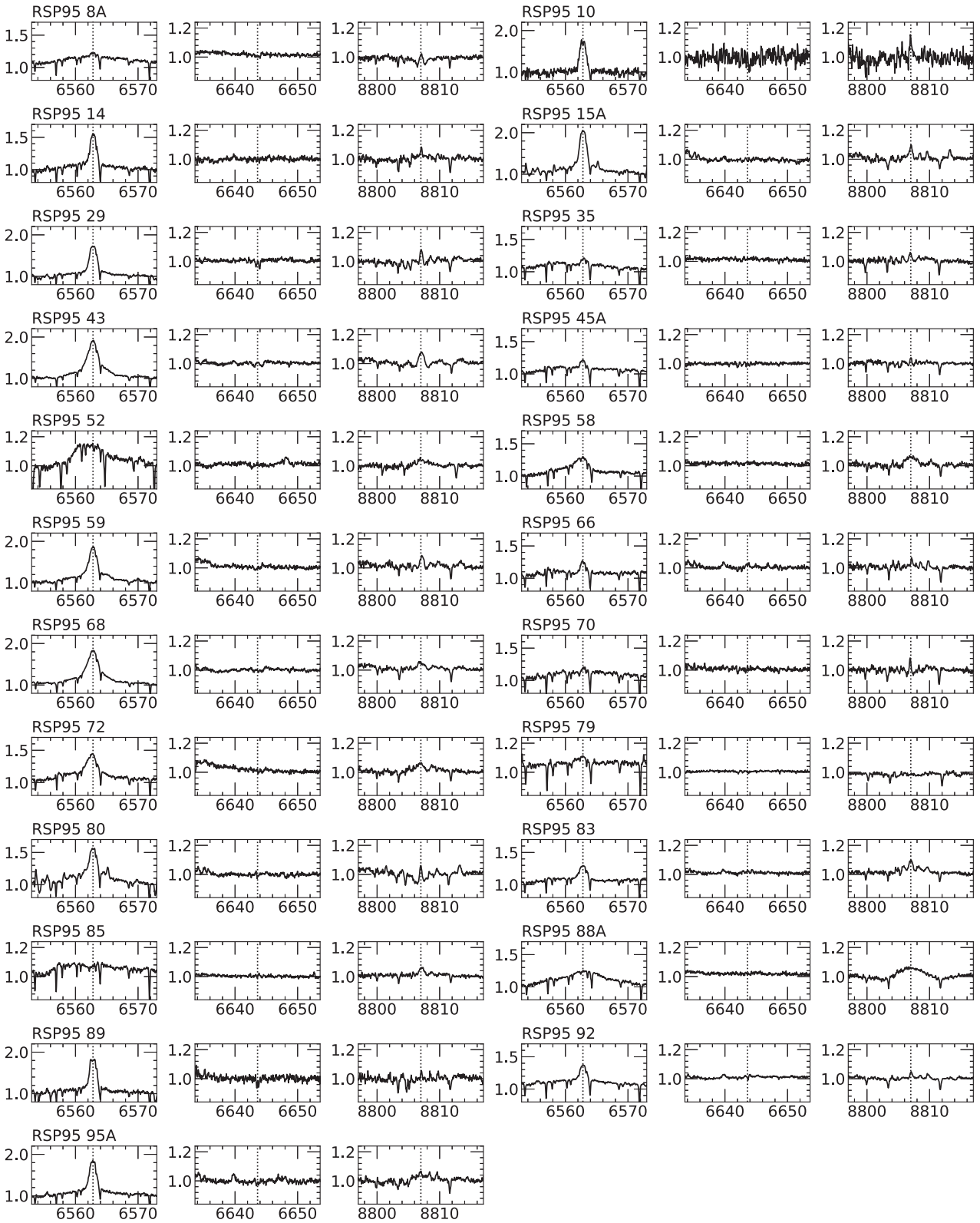

Fig. 3. Hα (6563 Å), Ni I (6644 Å), and Mg I (λ8807 Å) emission lines of ZAMS stars belonging to IC 2602. The continuum is normalized to unity. Photospheric absorption lines are already subtracted.

Table 2. EQWs, FWHMs, and R' of ZAMS stars belonging to IC 2391 and IC 2602.

Object name	EQW [Å]		FWHM [km s^{-1}]							log R'	
	Mg I λ8807	Hα λ6563	Mg I λ8807	Hα λ6563	Ca II λ8498	Ca II λ8542	Ca II λ8662	$\frac{\sigma_{\rm Ni\,I}}{\sigma_{\rm cont}}$	log $N_{\rm R}$	Mg I λ8807	Hα λ6563
IC 2391											
Cl* IC2391 L32	0.08 ± 0.07	<0.41*	61	—	78	129	76	0.88	− 0.31	− 5.17	—
VXR PSPC 3A	0.05 ± 0.02	0.10 ± 0.05	9	38	18	27	17	1.22	− 0.65	− 5.38	− 4.92
VXR PSPC 7	0.10 ± 0.03	0.10 ± 0.07	17	81	52	118	51	0.90	0.04	− 5.02	− 4.92
VXR PSPC 12	0.04 ± 0.03	0.86 ± 0.09	9	60	24	28	24	0.71	− 0.90	− 5.43	− 4.03
VXR PSPC 14	0.08 ± 0.02	0.34 ± 0.06	31	71	52	56	51	1.08	− 0.99	− 5.16	− 4.38
VXR PSPC 16A	0.10 ± 0.04	0.93 ± 0.13	22	62	34	—	33	0.91	− 1.26	− 5.03	− 3.98
VXR PSPC 22A	0.08 ± 0.03	0.57 ± 0.09	39	58	21	26	21	1.06	− 0.88	− 5.12	− 4.17
VXR PSPC 35A	0.17 ± 0.07	1.53 ± 0.14	65	148	141	—	138	1.04	− 2.05	− 4.78	− 3.81
VXR PSPC 44	0.12 ± 0.04	0.27 ± 0.05	56	79	64	162	63	0.97	− 0.36	− 4.98	− 4.55
VXR PSPC 45A	0.50 ± 0.09	0.55 ± 0.10	140	222	174	—	171	0.92	− 2.12	− 4.17	− 4.21
VXR PSPC 50A	0.16 ± 0.06	1.27 ± 0.12	41	117	77	—	75	1.14	− 1.76	− 4.67	—
VXR PSPC 52	0.03 ± 0.01	0.21 ± 0.05	13	48	21	29	20	1.05	− 0.79	− 5.56	− 4.59
VXR PSPC 62A	0.18 ± 0.05	1.07 ± 0.16	35	85	61	71	60	1.25	− 1.76	− 4.78	− 3.96
VXR PSPC 66	0.06 ± 0.03	<0.39*	29	—	74	72	72	0.85	− 0.42	− 5.28	—
VXR PSPC 67A	0.08 ± 0.06	1.65 ± 0.19	25	68	27	30	27	1.19	− 0.93	− 5.17	− 3.79
VXR PSPC 69A	0.09 ± 0.03	0.59 ± 0.09	12	50	30	—	29	0.74	− 1.22	− 5.00	− 4.09
VXR PSPC 70	0.06 ± 0.04	0.28 ± 0.10	28	56	39	35	38	0.59	− 0.82	− 5.25	− 4.48
VXR PSPC 72	0.05 ± 0.03	0.47 ± 0.06	22	52	25	—	24	1.06	− 0.88	− 5.31	− 4.27
VXR PSPC 76A	0.03 ± 0.02	1.60 ± 0.06	14	59	18	—	18	1.96	− 0.81	− 5.54	− 3.78
VXR PSPC 77A	0.13 ± 0.05	0.21 ± 0.04	60	68	72	105	71	1.22	− 1.11	− 4.93	− 4.66
VXR PSPC 80A	0.10 ± 0.10	2.22 ± 0.20	140	362	220	247	216	1.16	− 2.09	− 4.86	—
IC 2602											
Cl* IC2602 W79	0.02 ± 0.01	0.08 ± 0.02	11	48	19	27	18	0.65	− 0.73	− 5.66	− 5.06
RSP95 1	0.04 ± 0.02	0.34 ± 0.04	12	53	19	—	19	0.94	− 0.96	− 5.48	− 4.47
RSP95 7	<0.10*	0.06 ± 0.02	–	58	—	—	—	1.02	− 1.11	—	− 5.29
RSP95 8A	0.06 ± 0.02	0.09 ± 0.19	20	582	33	42	33	1.10	− 0.76	− 5.19	—
RSP95 10	0.07 ± 0.06	0.85 ± 0.17	12	52	25	—	24	1.16	− 1.18	− 5.02	—
RSP95 14	0.03 ± 0.02	0.60 ± 0.06	9	51	23	—	23	0.71	− 1.11	− 5.57	− 4.15
RSP95 15A	0.07 ± 0.04	1.81 ± 0.05	22	67	22	30	22	1.99	− 0.99	− 5.02	—
RSP95 29	0.07 ± 0.02	1.09 ± 0.06	15	67	34	—	34	2.51	− 1.34	− 5.19	− 3.93
RSP95 35	0.04 ± 0.02	0.05 ± 0.02	17	41	39	56	38	0.81	− 0.71	− 5.28	− 5.26
RSP95 43	0.13 ± 0.03	2.01 ± 0.07	33	112	63	92	62	1.96	− 1.66	− 4.77	− 3.69
RSP95 45A	0.03 ± 0.01	0.23 ± 0.02	12	42	24	38	23	1.29	− 0.68	− 5.45	—
RSP95 52	0.13 ± 0.07	1.38 ± 0.10	85	217	190	—	187	1.07	− 1.95	− 4.92	− 3.86
RSP95 58	0.17 ± 0.07	1.07 ± 0.09	68	163	96	165	94	0.97	− 1.57	− 4.81	− 3.90
RSP95 59	0.08 ± 0.03	1.95 ± 0.07	22	84	46	60	45	1.35	− 1.43	− 5.15	− 3.70
RSP95 66	0.02 ± 0.01	0.14 ± 0.03	9	41	26	36	25	1.25	− 0.80	− 5.75	− 4.79
RSP95 68	0.08 ± 0.03	2.01 ± 0.06	43	110	67	96	66	1.47	− 1.55	− 5.11	− 3.64
RSP95 70	0.06 ± 0.01	0.11 ± 0.02	12	44	27	53	27	1.64	− 0.47	− 5.28	− 4.87
RSP95 72	0.09 ± 0.04	1.15 ± 0.08	50	111	64	82	63	1.19	− 1.30	− 5.09	− 3.87
RSP95 79	<0.09*	0.10 ± 0.02	–	92	60	—	59	1.10	− 0.24	—	− 4.94
RSP95 80	0.07 ± 0.02	0.76 ± 0.06	16	77	23	26	22	1.34	− 0.69	− 5.23	− 4.08
RSP95 83	0.08 ± 0.02	0.28 ± 0.03	25	52	45	51	44	1.20	− 1.08	− 5.20	− 4.48
RSP95 85	0.07 ± 0.02	<0.20*	29	—	52	203	51	1.08	− 0.80	− 5.25	—
RSP95 88A	0.52 ± 0.09	1.56 ± 0.18	159	456	157	—	154	0.78	− 2.57	− 4.17	—
RSP95 89	0.02 ± 0.02	1.03 ± 0.08	10	56	18	—	17	1.80	− 1.01	− 5.66	− 4.01
RSP95 92	0.03 ± 0.01	0.23 ± 0.02	15	50	25	31	24	1.86	− 0.82	− 5.59	− 4.58
RSP95 95A	0.04 ± 0.02	1.06 ± 0.08	16	62	24	—	23	1.34	− 1.46	− 5.39	− 3.92

*3σ upper limit.

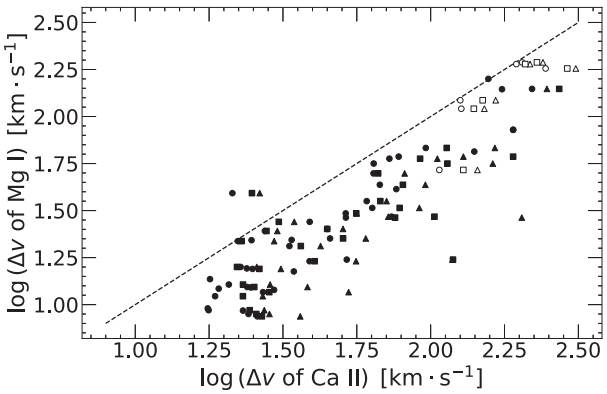

Fig. 4. Relationships between line widths Δv of Ca II IRT emission lines and line width of Mg I emission line (λ8807 Å). Filled symbols represent ZAMS stars in this study and open symbols represent T Tauri stars cited in Hamann and Persson (1992). Circles, triangles, and squares show Ca II IRT emission lines (λ8498, 8542, 8662 Å), respectively. The dashed line represents Δv of Ca II = Δv of Mg I.

30 ZAMS stars, respectively. Other chromospheric emission lines are detected in fewer of the ZAMS stars, or blended with nearby chromospheric emission lines or OH airgrow. We thus concentrate the following discussion on the Mg I at λ8807 Å and Hα lines.

4 Discussion

4.1 Mg I emission line

The line width of the Mg I emission line as a function of those of the Ca II IRT emission lines is plotted in figure 4. We used the measured line widths of six T Tauri stars from Hamann and Persson (1992). These T Tauri stars show several prominent emission lines of Mg I and Mg II, which are considered to be formed in the chromosphere or the transition region.

The Mg I line width shows a positive correlation with each Ca II IRT line width. The Mg I emission lines in most ZAMS spectra are narrower than the Ca II IRT lines. This is consistent with Hamann and Persson (1992), who claimed that these differences in the widths might be attributed to the different depths of the line formations, where the velocity fields are different. Based on the non-local thermodynamic equilibrium (non-LTE) solar model derived by Vernazza, Avrett, and Loeser (1981), the emission components of the Ca II IRT lines are formed 700–1200 km above the photosphere. Fleck et al. (1994) suggested that the Mg I emission line is formed in the chromosphere, 500 km above the photosphere.

Subsequently, we investigated the intensity of the Mg I emission line. To eliminate the dependence of the surface flux on the $T_{\rm eff}$ of the objects, we converted the EQW of the Mg I emission line into the ratio of the surface flux of the emission line to the stellar bolometric luminosity, $R'_{\rm Mg\,I}$. This $R'_{\rm Mg\,I}$ is similar to the parameter, $R'_{\rm HK}$, derived from the Ca II H and K lines, as described by Noyes et al. (1984). In addition to Ca II H and K emission lines, $R'_{\lambda 8542}$, the ratio of the surface flux of the Ca II λ8542 Å line to the stellar bolometric luminosity, was previously used by Soderblom et al. (1993) and James and Jeffries (1997). $R'_{\lambda 8498}$, $R'_{\lambda 8542}$, and $R'_{\lambda 8662}$ were used for the Ca II IRT emission lines by Marsden, Carter, and Donati (2009) and Yamashita, Itoh, and Takagi (2020). R' was used as a measure of the strengths of chromospheric emission lines, and its dependence on $N_{\rm R}$ has been examined. We first calculated the continuum flux per unit area at a stellar surface, F, as

$$\log \frac{f}{f_0} = -\frac{2}{5} \cdot m_{i*}, \tag{1}$$

$$F = f \cdot \left(\frac{d}{R_*}\right)^2, \tag{2}$$

where f is the i-band continuum flux of the object per unit area as observed on the Earth. m_{i*} is the apparent magnitude of the object in the i band. The i-band continuum flux per unit area under $m_i = 0$ mag (the AB system) condition, f_0, is 1.852×10^{-12} W m^{-2} Å^{-1} (Fukugita et al. 1996). d denotes the distance of an object from the Earth. R_* is the stellar radius estimated using the Stefan–Boltzmann law with the photospheric luminosity and $T_{\rm eff}$ of the objects. Subsequently, F was multiplied by the EQW of the Mg I emission line and converted into the surface flux, F',

$$F' = F \cdot {\rm EQW}. \tag{3}$$

Using $T_{\rm eff}$ of the target star, $R'_{\rm Mg\,I}$ is calculated as

$$R'_{\rm Mg\,I} = \frac{F'}{\sigma T_{\rm eff}^4}, \tag{4}$$

where σ is the Stefan–Boltzmann constant. The $R'_{\rm Mg\,I}$ values for the ZAMS stars are listed in table 2. We also took the EQW of an Ca II IRT emission line (λ8542 Å) from Marsden, Carter, and Donati (2009) and converted it into the ratio of the surface flux of the emission line to the stellar bolometric luminosity, $R'_{\lambda 8542}$, using equations (3) and (4).

Noyes et al. (1984) and many authors used $N_{\rm R}$ as an indicator of stellar dynamo activity:

$$N_{\rm R} \equiv \frac{P}{\tau_{\rm c}} = \frac{2\pi R_*}{\tau_{\rm c} v \sin i} \langle \sin i \rangle. \tag{5}$$

We used P for 42 ZAMS stars and $v \sin i$ for five ZAMS stars from Marsden, Carter, and Donati (2009). Following the method of Marsden, Carter, and Donati (2009), we

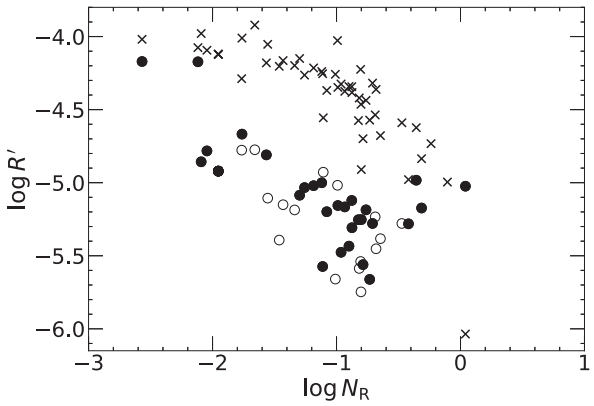

Fig. 5. Relationship between ratio of surface flux of Mg I emission line (λ8807 Å) to stellar bolometric luminosity $R'_{\mathrm{Mg\,I}}$ and Rossby number N_{R} of ZAMS stars (circles). Filled circles represent objects having $\sigma_{\mathrm{Ni\,I}}/\sigma_{\mathrm{cont}} < 1.2$. Open circles denote objects having $\sigma_{\mathrm{Ni\,I}}/\sigma_{\mathrm{cont}} \geq 1.2$. Crosses represent $R'_{\lambda 8542}$, which is the ratio of the surface flux of Ca II λ8542 Å line to the stellar bolometric luminosity, of ZAMS stars.

assumed the random inclinations and multiplied the average value, $\langle \sin i \rangle = 0.785$, in equation (5). We estimated the τ_{c} values of the ZAMS stars using the τ_{c} models for the stars with ages of 50 Myr (IC 2391) and 30 Myr (IC 2602) presented in Landin, Mendes, and Vaz (2010). We fitted $\log \tau_{\mathrm{c}}$ as a third-order polynomial function of $\log T_{\mathrm{eff}}$. The τ_{c} model is valid for objects with $T_{\mathrm{eff}} < 6810$ K. For six ZAMS stars with $T_{\mathrm{eff}} > 6180$ K (Cl* IC2391 L32, VXR PSPC 07, VXR PSPC 44, VXR PSPC 66, RSP95 7, and RSP95 79), we applied the approximation of τ_{c} of Noyes et al. (1984), where $(B-V)_0$ is taken from Marsden, Carter, and Donati (2009).

The relationship between the ratio of the surface flux of the Mg I emission line to the stellar bolometric luminosity, $R'_{\mathrm{Mg\,I}}$, and N_{R} of the ZAMS stars is shown in figure 5. The $R'_{\lambda 8542}$ values of the same ZAMS stars are also shown in the figure. When $N_{\mathrm{R}} > 10^{-1.1}$, $R'_{\lambda 8542}$ increases with decreasing N_{R} until it saturates. When $N_{\mathrm{R}} < 10^{-1.1}$, $R'_{\lambda 8542}$ reaches a constant level. Based on the discussion by Marsden, Carter, and Donati (2009), chromospheric saturation is suggested for the objects with $N_{\mathrm{R}} < 10^{-1.1}$.

In contrast, $R'_{\mathrm{Mg\,I}}$ increases with decreasing N_{R} even for the ZAMS stars with $N_{\mathrm{R}} < 10^{-1.1}$. The Mg I line is still unsaturated in the saturated regime for the Ca II IRT emission lines. The correlation coefficient between $R'_{\mathrm{Mg\,I}}$ and N_{R} for the ZAMS stars showing $\sigma_{\mathrm{Ni\,I}}/\sigma_{\mathrm{cont}} < 1.2$ is −0.70. The derived linear fit is

$$\log R'_{\mathrm{Mg\,I}} = -0.3918 \log N_{\mathrm{R}} - 5.532. \quad (6)$$

The correlation is valid even if other τ_{c} models (Noyes et al. 1984; Kim & Demarque 1996; Gunn et al. 1998) are used. The Mg I emission line is considered to be a good indicator of chromospheric activity, particularly of active objects.

VXR 45A and [RSP95] 88A show the largest $R'_{\mathrm{Mg\,I}}$. Both are fast rotators; $v \sin i$ values for VXR 45A and [RSP95] 88A are 235 km s^{-1} and 255 km s^{-1}, respectively. FWHMs of the Mg I emission component correspond to 222 km s^{-1} and 159 km s^{-1}. Both are comparable to the rotational velocity. It is known that the emission line is significantly broad if the line is formed by accretion (Yamashita et al. 2020). Thus, we consider that the Mg I emission line is broad for these two stars because of their fast rotation. The two ZAMS stars also show broad emission components of Si I (λ8728 Å), but they are blended with other chromospheric emission lines.

Four objects located at a Rossby number greater than −0.5 seem to be outliers, namely Cl* IC2391 L32, VXR PSPC 07, VXR PSPC 44, and VXR PSPC 66. This misalignment may be attributed to the difference of the applied τ_{c} models. For the objects with $T_{\mathrm{eff}} \leq 6180$ K, we applied the τ_{c} model of Landin, Mendes, and Vaz (2010). However, the four outliers have $T_{\mathrm{eff}} > 6180$ K. T_{eff} higher than 6180 K is out of range of the model. Instead, we applied the approximation of τ_{c} of Noyes et al. (1984) for such high-temperature objects. We constructed a relationship between τ_{c} of Landin's model and τ_{c} of Noyes' approximation for the ZAMS stars with $T_{\mathrm{eff}} \leq 6180$ K. The relationship is fitted by a linear function. We estimated the modified τ_{c} for the four objects by extrapolating the linear function. The modified τ_{c} is about 10^5 s smaller than τ_{c} estimated with Noyes' approximation, decreasing by 0.4 in $\log N_{\mathrm{R}}$. As a result, the misalignment seems insignificant.

Marsden, Carter, and Donati (2009) argued that chromospheric saturation is caused by a similar mechanism to coronal saturation. Stępień, Schmitt, and Voges (2001) suggested that coronal saturation is a result of the coronal-emitting regions of a star being filled. Marsden, Carter, and Donati (2009) claimed that the emitting regions of Ca II of the ZAMS stars in $N_{\mathrm{R}} < 10^{-1.1}$ completely cover the chromosphere. The unsaturation of the Mg I emission line suggests that the area of its emitting region may be smaller than the Ca II emitting region area.

The theoretical arguments on saturation are still being debated. The linear mean-field dynamo theory suggests that a small N_{R} allows exciting dynamo activity and leads to a strong magnetic strength. Therefore, the strengths of the Ca II emission lines should increase with decreasing N_{R}. However, numerous observations provide evidence that the Ca II emission lines saturate with small N_{R}. Schrinner (2013) explained the mechanism of the saturation based on Ohmic dissipation. They suggested that the ratio of the Ohmic dissipation rate to the power generated by the buoyancy increases with decreasing N_{R} for $10^{-2} < N_{\mathrm{R}} < 10^{-1}$. The ratio reaches maximum 0.8 for $10^{-3} < N_{\mathrm{R}} < 10^{-2}$, and it is independent of the rotation. This

implies that the dynamo activity is constant for a small-N_R object.

Many other absorption lines have also been shown to exhibit some filling-in with chromospheric activity. Thompson et al. (2017) investigated the difference between high- and low-activity spectra of α Cen B. For 48 nights, they generated "relative" spectra by dividing each of the spectra by their lowest-activity spectra and obtained a large number of narrow emission lines such as Fe I λ4375, 4427, 4462 Å, Ti II λ4443.81 Å, and V I λ4444.21 Å. These features most likely originate from plage, spots, or a combination of both.

It is probable that the intensity of the Mg I emission line has a positive correlation with the magnetic field strength. Folsom et al. (2016) observed the Zeeman broadening of rapidly rotating G and K dwarfs, the N_R of which was between 10^{-2} and 10^{0}. It was shown that the large-scale magnetic field strength increases with decreasing N_R. The magnetic field strength did not saturate with any Rossby number. Chang et al. (1991) confirmed that the Mg I emission lines at 7 μm and 12 μm provide sensitive measures of the magnetic and electric field strengths of the solar atmosphere. The relation between the magnetic field strength and the Mg I emission line at λ8807 Å needs to be investigated.

4.2 Hα emission line

We converted the EQW of the Hα emission line into the ratio of the surface flux of the Hα emission line to the stellar bolometric luminosity, $R'_{H\alpha}$. We first calculated F using equation (2) and equation (7):

$$\log \frac{f}{f_0} = -\frac{2}{5} \cdot m_{r*}, \tag{7}$$

where m_{r*} is the apparent magnitude of the object in the r-band. The r-band continuum flux per unit area for a 0 mag star (the AB system), f_0, was 2.780×10^{-12} W m^{-2} Å^{-1} (Fukugita et al. 1996). Subsequently, F was multiplied by the EQW of the Hα emission line and converted into F' using equation (3). By substituting T_{eff} and F' of the target star into equation (4), $R'_{H\alpha}$ were calculated. The $R'_{H\alpha}$ values for the ZAMS stars are listed in table 2.

The relationship between $R'_{H\alpha}$ and N_R of the ZAMS stars is shown in figure 6. We also plot R' of the Ca II IRT emission line at λ8542 Å taken from Marsden, Carter, and Donati (2009). The ZAMS stars tend to show larger $R'_{H\alpha}$ as N_R becomes smaller. In contrast, the ZAMS stars with $N_R < 10^{-1.1}$ have $R'_{H\alpha} \sim 10^{-3.9\pm0.5}$. This is the same as the results for the Ca II IRT emission lines. However, the scatter of $R'_{H\alpha}$ seems larger than that of $R'_{\lambda8542}$. It is likely that the extra scatter is due to the more strongly non-LTE nature of the Hα source function (Cram & Mullan 1979) and its strange optical depth behavior in cooler stars (Houdebine et al. 1995).

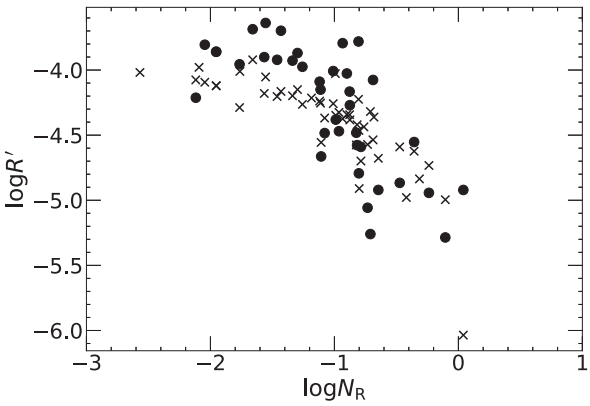

Fig. 6. Relationship between ratio of surface flux of Hα emission line (λ6563 Å) to stellar bolometric luminosity $R'_{H\alpha}$ and Rossby number N_R of ZAMS stars (filled circles). Crosses represent $R'_{\lambda8542}$, which is the ratio of the surface flux of Ca II λ8542 Å line to the stellar bolometric luminosity, of ZAMS stars.

Newton et al. (2017) investigated the relationship between N_R and $L_{H\alpha}/L_{bol}$, the Hα emission line to stellar bolometric luminosity ratio for M dwarfs. The M dwarfs with small N_R showed larger $L_{H\alpha}/L_{bol}$ in $N_R \geq 10^{-0.67}$. When $N_R \leq 10^{-0.67}$, $L_{H\alpha}/L_{bol}$ reached a constant level at 1.85×10^{-4}.

Frasca et al. (2017) observed the Hα, He I, Na I, and Ca II IRT lines of young stellar objects (YSOs) in the Lupus star-forming region. One object did not show the Hα emission line; however, it was proved that the photospheric absorption component was filled with the chromospheric emission. Most of the young stellar objects show chromospheric emission lines with $R'_{H\alpha} \leq 10^{-3.7}$. The ZAMS stars in our targets also show $R'_{H\alpha} \leq 10^{-3.7}$. Before subtracting the absorption component, a portion of the objects showing featureless spectra at Hα may indeed be chromospherically active stars.

5 Conclusion

We investigated the infrared Mg I emission lines (λ8807 Å) of 47 ZAMS stars belonging to IC 2391 and IC 2602. Archived data obtained using the AAT and the UCLES were used. After subtracting the spectra of the inactive stars from the ZAMS spectra, Hα, Ca II, and Mg I were detected as the emission lines.

(1) The infrared Mg I emission line width shows a positive correlation with each Ca II IRT line width. Most of the ZAMS stars show the narrower Mg I emission lines,

instead of the Ca II IRT emission lines. The Mg I emission lines are detected from most of the ZAMS stars. After subtracting the photospheric absorption components, the ZAMS stars with smaller Rossby numbers show stronger Mg I emission lines. The Mg I line is unsaturated even in "the saturated regime for the Ca II emission lines," i.e., $N_R < 10^{-1.1}$. The Mg I emission line is considered to be a good indicator of chromospheric activity, particularly for active objects.

(2) The strength of the Hα emission line is as strong as those of young stellar objects showing chromospheric emission lines.

Acknowledments

This study is based on the data acquired using the Anglo-Australian Telescope. We acknowledge the traditional custodians of the land on which the AAT stands, the Gamilaraay people, and pay our respects to the elders past and present. This research is also based on the observations made with the ESO Telescopes at the La Silla Paranal Observatory under programs ID 71.B-0529(A), 073.B-0607(A), 076.B-0055(A), 084.D-0965(A), 086.D-0062(A), 087.D-0010(A), 099.D-0410(A), and 266.D-5655(A). M. Y. was supported by a scholarship from the Japan Association of University Women, and would like to thank them. Y. I. is supported by JSPS KAKENHI grant number 17K05390.

References

Bailer-Jones, C. A. L., Rybizki, J., Fouesneau, M., Mantelet, G., & Andrae, R. 2018, AJ, 156, 58
Baliunas, S., Sokoloff, D., & Soon, W. 1996, ApJ, 457, L99
Barnes, S. A., Sofia, S., Prosser, C. F., & Stauffer, J. R. 1999, ApJ, 516, 263
Barrado y Navascués, D., Stauffer, J. R., & Jayawardhana, R. 2004, ApJ, 614, 386
Chang, E. S., Avrett, E. H., Mauas, P. J., Noyes, R. W., & Loeser, R. 1991, ApJ, 379, L79
Cram, L. E., & Mullan, D. J. 1979, ApJ, 234, 579
D'Antona, F., & Mazzitelli, I. 1994, ApJS, 90, 467
D'Orazi, V., & Randich, S. 2009, A&A, 501, 553
Dunn, R. B., Evans, J. W., Jefferies, J. T., Orrall, F. Q., White, O. R., & Zirker, J. B. 1968, ApJS, 15, 275
Feinstein, A. D., et al. 2019, PASP, 131, 094502
Fleck, B., Deubner, F.-L., Maier, D., & Schmidt, W. 1994, in IAU Symp. 154, Infrared solar physics, ed. D. M. Rabin et al. (Dordrecht: Kluwer Academic Publishers), 65
Folsom, C. P., et al. 2016, MNRAS, 457, 580
Frasca, A., Biazzo, K., Alcalá, J. M., Manara, C. F., Stelzer, B., Covino, E., & Antoniucci, S. 2017, A&A, 602, A33
Fukugita, M., Ichikawa, T., Gunn, J. E., Doi, M., Shimasaku, K., & Schneider, D. P. 1996, AJ, 111, 1748
Gaia Collaboration 2018, A&A, 616, A1
Gunn, A. G., Mitrou, C. K., & Doyle, J. G. 1998, MNRAS, 296, 150
Gutiérrez Albarrán, M. L., et al. 2020, A&A, 643, A71
Hamann, F., & Persson, S. E. 1992, ApJS, 82, 247
Houdebine, E. R., Doyle, J. G., & Koscielecki, M. 1995, A&A, 294, 773
James, D. J., & Jeffries, R. D. 1997, MNRAS, 292, 252
Kim, Y.-C., & Demarque, P. 1996, ApJ, 457, 340
Landin, N. R., Mendes, L. T. S., & Vaz, L. P. R. 2010, A&A, 510, A46
Linsky, J. L., Hunten, D. M., Sowell, R., Glackin, D. L., & Kelch, W. L. 1979, ApJS, 41, 481
Marsden, S. C., Carter, B. D., & Donati, J.-F. 2009, MNRAS, 399, 888
Newton, E. R., Irwin, J., Charbonneau, D., Berlind, P., Calkins, M. L., & Mink, J. 2017, ApJ, 834, 85
Nordström, B., Andersen, J., Holmberg, J., Jørgensen, B. R., Mayor, M., & Pont, F. 2004, PASA, 21, 129
Noyes, R. W., Hartmann, L. W., Baliunas, S. L., Duncan, D. K., & Vaughan, A. H. 1984, ApJ, 279, 763
Patten, B. M., & Simon, T. 1996, ApJS, 106, 489
Randich, S., Pallavicini, R., Meola, G., Stauffer, J. R., & Balachandran, S. C. 2001, A&A, 372, 862
Scargle, J. D. 1982, ApJ, 263, 835
Schrinner, M. 2013, MNRAS, 431, L78
Skumanich, A. 1972, ApJ, 171, 565
Soderblom, D. R., Stauffer, J. R., Hudon, J. D., & Jones, B. F. 1993, ApJS, 85, 315
Soubiran, C., et al. 2018, A&A, 619, A155
Stępień, K., Schmitt, J. H. M. M., & Voges, W. 2001, A&A, 370, 157
Stauffer, J. R., Hartmann, L. W., Prosser, C. F., Randich, S., Balachandran, S., Patten, B. M., Simon, T., & Giampapa, M. 1997, ApJ, 479, 776
Thompson, A. P. G., Watson, C. A., de Mooij, E. J. W., & Jess, D. B. 2017, MNRAS, 468, L16
Tonry, J. L., et al. 2018, ApJ, 867, 105
van Leeuwen, F. 2007, A&A, 474, 653
Vernazza, J. E., Avrett, E. H., & Loeser, R. 1981, ApJS, 45, 635
Yamashita, M., Itoh, Y., & Takagi, Y. 2020, PASJ, 72, 80
Yee, S. W., Petigura, E. A., & von Braun, K. 2017, ApJ, 836, 77
Zacharias, N., Finch, C. T., Girard, T. M., Henden, A., Bartlett, J. L., Monet, D. G., & Zacharias, M. I. 2013, AJ, 145, 44

Publ. Astron. Soc. Japan (2022) 74 (6), 1295–1308
https://doi.org/10.1093/pasj/psac069
Advance Access Publication Date: 2022 September 8

Starspots, chromospheric emission lines, and flares of zero-age main-sequence stars

Mai Yamashita,[1,*] Yoichi Itoh,[1] and Yumiko Oasa[2]

[1]Nishi-Harima Astronomical Observatory, Center for Astronomy, University of Hyogo, 407-2 Nishigaichi, Sayo, Sayo, Hyogo 679-5313, Japan
[2]Faculty of Education, Saitama University, 255 Shimo-Okubo, Sakura, Saitama, Saitama 338-8570, Japan

*E-mail: yamashita@nhao.jp

Received 2022 May 26; Accepted 2022 August 9

Abstract

Zero-age main-sequence (ZAMS) stars are considered to have enormous starspots and show strong chromospheric emission lines because of their strong surface magnetic field. We discuss the dynamo activities of ZAMS stars with respect to their periodic light variation caused by a starspot and with respect to the strength of the chromospheric emission lines. The light curves of 33 ZAMS stars in IC 2391 and IC 2602 were obtained from TESS (Transiting Exoplanet Survey Satellite) photometric data. The light curves can be grouped into the following four categories: single frequency, possible shape changer, beater, and complex variability. The amplitudes of the light curves are 0.001–0.145 mag, similar to those of ZAMS stars in Pleiades. The starspot coverages are 0.1%–21%. We found that the light variations and Ca II emission line strength of ZAMS stars in IC 2391, IC 2602, and the Pleiades cluster are as large as those of the most active superflare stars and two orders larger than those of the Sun, and are located on the extensions of the superflare stars. These results suggest that superflare stars link the properties of the Sun to those of the ZAMS stars of ages between 30 and 120 Myr. ZAMS stars with a single frequency or possible shape change in the light curve tend to have both large light variation, indicating large spot coverage, and saturated Ca II emission line strength. ZAMS stars with beat or complex variability have small spot coverage and a faint Ca II emission line. We also detected 21 flares in the TESS light curves of 12 ZAMS stars in IC 2391 and IC 2602, where most of these stars have saturated chromospheric Ca II emission lines. The energies of the flares are estimated to be $\sim 10^{33}$–10^{35} erg, which is comparable with the energy of a superflare.

Key words: stars: activity — stars: chromospheres — stars: flare — starspots — techniques: photometric

1 Introduction

The chromosphere is the active atmosphere in which atoms emit some permitted lines, such as Hα and Ca II. It is claimed that chromospheric activity is driven by the magnetic fields induced by the dynamo process. In the dynamo process, the Coriolis force (= rotational moment × convection velocity) balances the Lorentz force (= current × magnetic strength/density of plasma) (Baliunas et al. 1996). Stellar rotation and convection are considered to be the main processes that drive the evolution of magnetic

activities. Noyes et al. (1984) used the Rossby number, N_R, as an indicator of magnetic activity. It is defined as P/τ_c, where P is the stellar rotational period and τ_c is the convective turnover time. N_R can be approximated as the inverse square of the dynamo number, N_D, the wave solution of the dynamo equation. Magnetic fields develop when $|N_D| > 1$.

Chromospheric emission lines are observational evidence of a strong magnetic field. The relationship between chromospheric line strength and the Rossby number has been examined for zero-age main-sequence (ZAMS) stars. Marsden, Carter, and Donati (2009) detected Ca II infrared triplet (IRT; λ8498, 8542, 8662 Å) emission lines from low-mass stars in the young open clusters IC 2391 and IC 2602. The cluster members are considered to be on ZAMS or in the last evolution phase prior to ZAMS. They calculated R'_{IRT} from the equivalent widths (EQWs). R'_{IRT} describes the ratio of the surface flux of the Ca II IRT emission lines to the stellar bolometric luminosity. They found that R'_{IRT} decreases with increasing N_R for stars with $N_R \geq 10^{-1.1}$. This region is called the unsaturated regime. In contrast, R'_{IRT} is constant at levels of approximately $10^{-4.2}$ for stars with $N_R \leq 10^{-1.1}$. This region is called the saturated regime. Marsden, Carter, and Donati (2009) suggested that the chromosphere is completely filled by the emitting regions for the stars in the saturated regime. Recently, Fritzewski et al. (2021) found that some of the FGKM-type stars in the young open cluster NGC 3532 (300 Myr) also show saturation at $R'_{IRT} \sim 10^{-3.7}$. Yamashita, Itoh, and Takagi (2020) investigated the relationship between N_R and the Ca II IRT emission lines of 60 pre-main sequence (PMS) stars. Only three PMS stars showed broad and strong emissions, indicative of large mass accretion. Most of the PMS stars presented narrow and weak emissions, suggesting that their emission lines are formed in the chromosphere. All their Ca II IRT emission lines have $R'_{IRT} \sim 10^{-4.2}$, which is as large as the maximum R'_{IRT} of ZAMS stars. The PMS stars show $N_R < 10^{-0.8}$ and constant R'_{IRT} against N_R, i.e., their Ca II IRT emission lines are saturated. Yamashita and Itoh (2022) (hereafter Paper I) investigated the infrared Mg I emission lines at 8807 Å of 47 ZAMS stars in IC 2391 and IC 2602 using the archive data of the Anglo-Australian Telescope at the University College London Echelle Spectrograph. They found that ZAMS stars with smaller Rossby numbers show stronger Mg I emission lines, even for stars located in the Ca II saturated region.

Regarding the solar disk, it is known that spots are surrounded by emission regions, such as faculae in the photosphere and plages in the chromosphere. Other observational evidence for the strong magnetic field of a star includes the periodic light variation caused by a starspot. The amplitude of the solar brightness variation caused by sunspots on the rotating solar surface is 0.01%–0.1% (Lanza et al. 2003). In recent years, Kepler and Transiting Exoplanet Survey Satellite (TESS; Ricker et al. 2015) satellites have been utilized to investigate stellar magnetic activities. The typical photometric precision of Kepler is 0.01% for a star of 12 mag (Koch et al. 2010). The time resolution of Kepler is approximately 30 min and 1 min. Rebull et al. (2016a) presented K2 light curves for F-, G-, K-, and M-type ZAMS stars in the Pleiades cluster. The rotational periods ranged from 0.082 to 22.14 d. The amplitude of the brightness ranged from 0.001 to 0.556 mag. Rebull et al. (2016a) and Stauffer et al. (2016) investigated the relationship between the rotational periods and shapes of the light curves for ZAMS stars in the Pleiades cluster and found that approximately half of the F-, G-, and K-type ZAMS stars rotating rapidly have sinusoidal light curves.

Flares are also observational evidence for a strong magnetic field. Maehara et al. (2012) detected 365 flares with Kepler data regarding 148 solar-type stars. The releasing energy of the flare is 100 times larger than those of solar flares. Such objects are called superflare stars. Notsu et al. (2015b) found that the Sun and superflare stars show a positive correlation between the amplitude of the light curve and the $r_0(8542)$ index, the residual core flux of the Ca II IRT normalized by the continuum level at the line core. This correlation means that superflare stars have large starspots and high magnetic activity compared to the Sun. Ilin et al. (2021) detected 3844 flares from K2 data from 2111 objects associated with open clusters. The cluster ages range from 0.1 to 3.6 Gyr. They found that flaring rates decline with age and decline faster for stars with higher mass.

We discuss the relationship between the periodic light variation caused by a starspot, the strength of the chromospheric emission lines, and flare events. We measured the light variations of 33 ZAMS stars in IC 2391 and IC 2602 with TESS photometric data. In the next section, we describe the photometric data reduction procedure. In section 3, we present the results, and in section 4, we discuss the dynamo activities in terms of the light variation, the Rossby number, the chromospheric emission strength, and the flares.

2 Data sets and data reduction

2.1 Stellar parameters

Our targets are F-, K-, and G-type ZAMS stars in IC 2391 (50 ± 5 Myr; Barrado y Navascues et al. 2004) and IC 2602 (30 ± 5 Myr; Stauffer et al. 1997). The metallicity of both clusters has been determined to be similar to that of the Sun, which is [Fe/H] = −0.01 ± 0.02 for IC 2391 (D'Orazi & Randich 2009) and [Fe/H] = 0.00 ± 0.01 for IC 2602 (Randich et al. 2001). A total of 44 ZAMS stars have been

Table 1. Physical parameters of ZAMS stars in IC 2391 and IC 2602.*

Object name	RA	Dec	V	K	Period	log N_R	log $R'_{\lambda 8542}$	Amp	Spot	LC type
	[°]	[°]	[mag]	[mag]	[d]			[mag]	coverage	
(1)	(2)	(3)	(4)	(5)	(6)	(7)	(8)	(9)	(10)	(11)
IC 2391										
Cl* IC2391 L32	130.57590	−53.90227	9.38	8.325	—	−0.31	−4.84	0.002	0.002	III
VXR PSPC 07	129.74920	−53.02395	9.63	8.272	—	0.04	−6.04	0.002	0.002	III
VXR PSPC 12	129.97104	−52.96579	11.86	9.793	3.69	−0.90	−4.34	0.030	0.039	I
VXR PSPC 22A	130.20459	−53.62927	11.08	9.272	2.31	−0.88	−4.34	0.025	0.030	I
VXR PSPC 44	130.55122	−53.10105	9.69	8.364	0.57	−0.36	−4.62	0.009	0.010	II
VXR PSPC 45A	130.56148	−52.93398	10.70	8.648	0.22	−2.12	−4.08	0.020	0.026	I
VXR PSPC 52	130.69420	−53.01704	10.34	8.991	2.15	−0.79	−4.70	0.013	0.016	I’
VXR PSPC 66	130.96793	−53.23327	9.73	8.594	0.92	−0.42	−4.98	0.004	0.005	I’
VXR PSPC 67A	130.98671	−52.68489	11.71	9.424	3.41	−0.93	−4.37	0.014	0.018	I
VXR PSPC 69A	130.99590	−53.56213	11.67	9.675	2.22	−1.12	−4.24	0.098	0.131	I
VXR PSPC 77A	131.41306	−52.43321	9.91	8.635	0.65	−1.11	−4.56	0.019	0.022	I
IC 2602										
Cl* IC2602 W79	160.52952	−64.76884	11.57	—	6.55	−0.73	−4.57	0.011	0.014	III
RSP95 1	157.13011	−63.73767	11.57	9.537	3.85	−0.96	−4.33	0.026	0.033	I’
RSP95 7	157.93717	−63.48943	9.21	8.212	–	−0.11	−5.00	0.001	0.001	III
RSP95 10	158.11917	−65.10722	12.77	—	3.16	−1.18	−4.21	0.068	0.099	I’
RSP95 14	158.41530	−64.78116	11.57	9.572	2.73	−1.11	−4.25	0.020	0.025	I’
RSP95 29	159.15815	−64.79828	12.73	9.976	2.22	−1.34	−4.20	0.054	0.074	I
RSP95 35	159.57360	−64.13512	10.59	9.078	2.46	−0.71	−4.32	0.018	0.021	I’
RSP95 43	159.98321	−63.99169	12.14	9.622	0.78	−1.66	−3.92	0.103	0.141	I
RSP95 52	160.21399	−64.71329	12.19	9.555	0.39	−1.95	−4.12	0.145	0.206	I
RSP95 58	160.67298	−64.35120	10.52	8.840	0.57	−1.57	−4.18	0.038	0.046	I
RSP95 59	160.73377	−63.93087	11.86	9.537	1.31	−1.43	−4.16	0.066	0.089	I
RSP95 66	161.02838	−63.99307	11.07	9.311	3.28	−0.80	−4.46	0.028	0.035	I’
RSP95 68	161.05806	−64.77426	11.32	8.750	0.99	−1.55	−4.05	0.038	0.050	I’
RSP95 70	161.09396	−64.25837	10.92	9.322	4.25	−0.47	−4.59	0.018	0.021	I
RSP95 72	161.24842	−65.03863	10.89	9.157	1.05	−1.30	−4.15	0.048	0.060	I
RSP95 79	161.36767	−64.22918	9.08	7.989	0.75	−0.24	−4.73	0.003	0.003	I’
RSP95 80	161.37445	−64.42227	10.66	8.278	7.25	−0.69	−4.54	0.013	0.018	III
RSP95 83	161.56180	−64.04946	10.7	9.102	1.74	−1.08	−4.37	0.008	0.010	I’
RSP95 85	161.61995	−64.13266	9.87	8.680	1.33	−0.80	−4.91	0.003	0.004	I’
RSP95 89	161.71584	−63.57105	12.97	9.942	4.73	−1.01	−4.26	0.081	0.119	I
RSP95 92	162.07663	−64.16482	10.26	8.505	1.93	−0.82	−4.42	0.024	0.028	I
RSP95 95A	162.45167	−64.77457	11.73	9.480	1.22	−1.46	−4.20	0.007	0.009	I

*References for parameters. (4) V-mag: Marsden, Carter, and Donati (2009). (5) K_s-mag: 2MASS survey (Cutri et al. 2003). (6) Period: Yamashita and Itoh (2022). (7)–(9) The Rossby number N_R, the ratio of the surface flux of the Ca II IRT emission line at λ8542 to the stellar bolometric luminosity $R'_{\lambda 8542}$, and the amplitudes of the light curve: Yamashita and Itoh (2022).

confirmed as single stars in the IC 2391 and IC 2602 members based on the strength of the lithium 6708 Å absorption line (Marsden et al. 2009). In Paper I, we examined the proper motion and radial velocity of those stars, and five ZAMS stars were removed from our target list. The 39 targets investigated in this study are presented in table 1.

2.2 Data reduction

The members of IC 2391 and IC 2602 were observed in the long-cadence (1800 s exposure) mode of TESS Sectors 8 and 10, which extended from 2019 February 2 to 27, and from 2019 March 26 to April 21, respectively. These data were retrieved from the Multimission Archive at the Space Telescope Science Institute. We conducted principal component analysis using ELEANOR, an open-source tool for extracting light curves from TESS full-frame images (Feinstein et al. 2019). ELEANOR enables us to model a 2D background, and remove the extended point-spread function of bright stars across the TESS images. However, TESS pixels are substantially larger than those of Kepler. We excluded six ZAMS stars from the targets because another star whose magnitude is brighter than $<3 + V$ mag of the ZAMS star was located in the aperture of the ZAMS star.

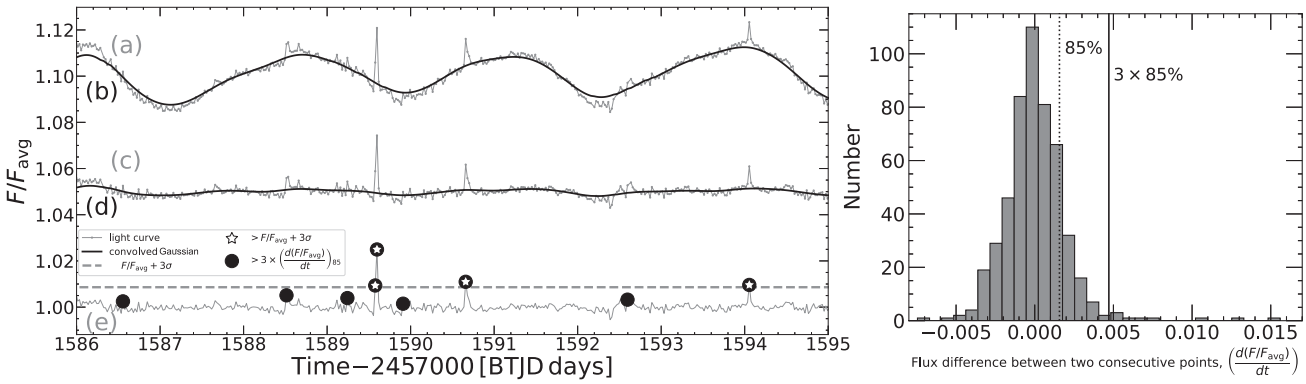

Fig. 1. Light curve of the ZAMS star, [RSP 95] 14. Horizontal and vertical axes correspond to days and normalized flux. Top: The original light curve is shown with the gray solid line (a). This is divided by the median of the counts and normalized to 1. The thick black line is the Gaussian convolved light curve (b). The standard deviation of the Gaussian function is set to 300 min. These lines are shifted by +0.10 for display purposes. Middle: The ratio between the original light curve and the Gaussian convolved light curve shown in the top panel is presented with the gray solid line (c). The thick black line is the Gaussian convolved light curve of the gray solid line (d). The standard deviation of the Gaussian function is set to 300 min. These lines are shifted by +0.05 for display purposes. Bottom: The ratio between the light curve shown in the middle and the second Gaussian convolved light curve is shown with the gray solid line (e). The dashed line denotes $1 + 3\sigma$ of the gray line. The open symbols represent data points greater than the dashed line. The filled circles represent data points whose brightness change is greater than the threshold of the change of the brightness. The three sudden brightenings (four points) are detected as flares. The histogram in the right-hand panel shows the number distribution of the flux differences between all pairs of two consecutive data points. The dotted line shows the top 15% of the distribution. The solid line shows the threshold of the change of the brightness, three times in the top 15% of the distribution.

First, we search for periodic signals and obtain the amplitudes of the light curves. We calculated the standard deviation of the flux, σ_1, and removed the flux data points greater than $3\sigma_1$ above the average. As described in Paper I, we searched for periodic signals by conducting Lomb–Scargle periodogram analysis (Scargle 1982). We note that VXR PSPC 44 showed beating signatures in its light curve; we adopted the period for the second maximum of the power as the period of the object. We calculated the amplitudes of the light curves by taking the 90th percentile flux and subtracting it from the 10th percentile flux. P was judged to be accurate if amplitude/meanfluxerror ≥ 10. The periods derived by us show good correlation with the periods measured by Patten and Simon (1996) and Barnes et al. (1999), with a correlation coefficient of 0.997.

Next, we detected sudden brightenings as flares. Starting from the original light curves (including $3\,\sigma_1$ outliers), first we removed the rotational light variations as described below (figure 1). TESS data was not obtained for several days in the middle of the observation period. We separated the light curve at the center time. Each light curve was divided by the median of the counts and normalized to 1 (figure 1a). Each light curve was convolved with a Gaussian function (figure 1b) and divided by the convolved light curve. The derived light curve (figure 1c) was again convolved with a Gaussian function (figure 1d). We set the standard deviation of the Gaussian function to between 15 min and 2.5 d for each light curve. With these processes, no rotational light variation remained in the light curve, and most of the data points were set around unity (figure 1e). We then measured the standard deviation of the counts in the light curve, σ_2, for each ZAMS star.

We defined two thresholds for flare detection. The first threshold is the height of sudden brightening. After removing the rotational light variations, we searched for sudden brightenings whose relative flux exceeded $1 + 3\sigma_2$ for at least one data point. The second threshold is the change of the brightness. We calculated the brightness changes between all pairs of consecutive data points. We searched for any brightness change that occurred more than three times in the top 15% of the distribution (the solid line in the right-hand panel of figure 1). We identified a sudden brightening that exceeded both thresholds as a flare. The time at which the flux first exceeded the first threshold, $1 + 3\sigma_2$ of the relative flux, was determined to be the flare start time. The flare end time was defined as the time at which the flux became smaller than $1 + 3\sigma_2$ of the relative flux.

3 Results

The rotational periods of the ZAMS stars in IC 2391 and IC 2602 range from 0.22–7.25 d. The amplitudes of the light curves range from 0.001–0.145 mag. The measured periods and amplitudes are similar to those of 88 ZAMS stars in Pleiades (Rebull et al. 2016a). Previous ground-based observation (Messina et al. 2011) also detected a variation of 0.2 mag in the brightness of eight ZAMS stars in IC 2391 (namely, VXR PSPC 12, VXR PSPC 14, VXR PSPC 22A, VXR PSPC 35A, VXR PSPC 69, VXR PSPC 70, VXR PSPC 72, VXR PSPC 76A).

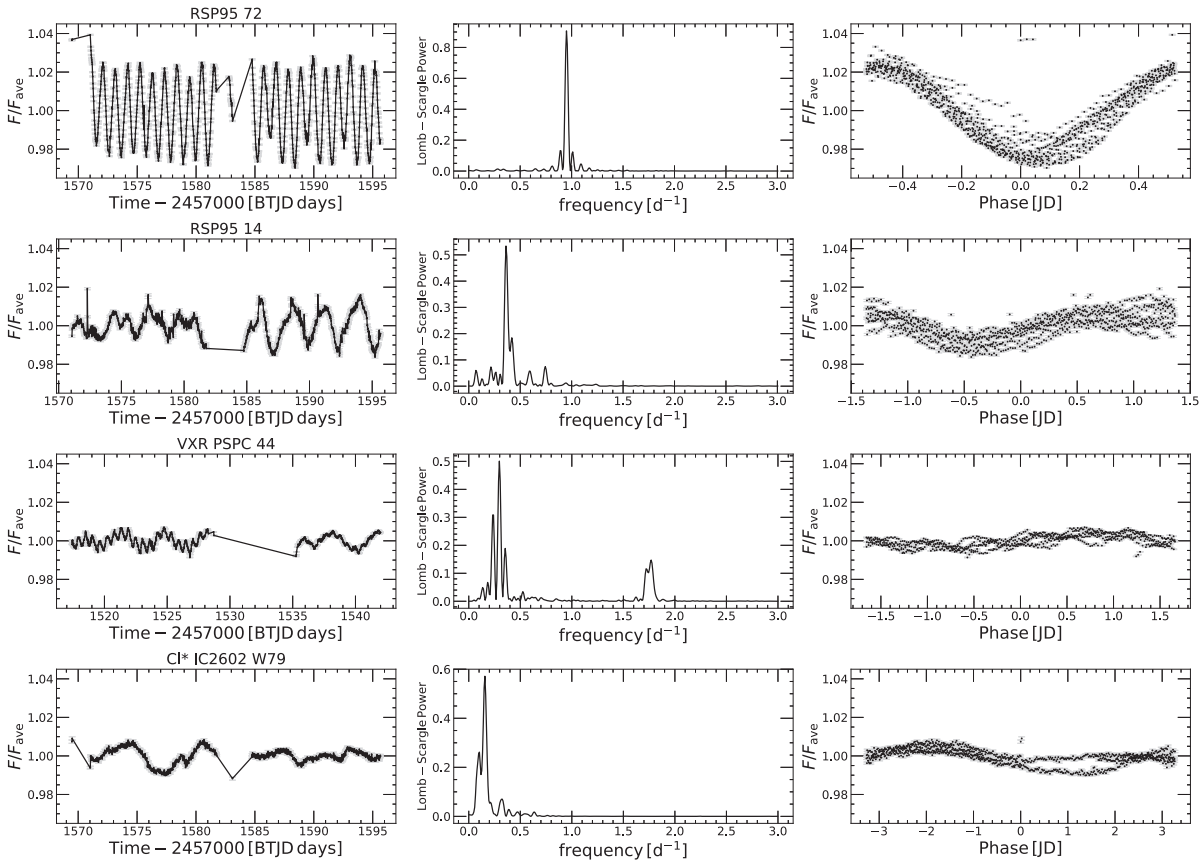

Fig. 2. Four examples of the light curves of ZAMS stars. The four features of the light curve, (I) single frequency, (I') possible shape changer, (II) beater, and (III) complex variability, are presented in order from the top to the bottom. Left-hand column: full light curve; middle column: Lomb–Scargle periodogram; right-hand column; phased light curve. Data points greater than $3\sigma_1$ above the average flux were removed from the phased light curve.

Figure 2 shows four examples of light curves. We categorized the light curves into the following groups:

(I) Single frequency: the star has a single period. A single spot or spot group is interpreted as rotating into and out of view.

(I') Possible shape changer: subcategory of type (I) single frequency. The star usually has a single period. Shape of the light curve changes over the campaign, but not enough that a separate period can be derived.

(II) Beater: the light curve appears to have a beating signature. The star has multi periods. Spot or spot group evolution and/or strong latitudinal differential rotation are suggested.

(III) Complex variability; the light curve has periodicity but seems complex. It is considered that the star has multiple sunspot groups.

Single frequency and beater are all classes found in Rebull et al. (2016b). For the 33 ZAMS stars in IC 2391 and IC 2602, we categorized 16 ZAMS stars as type (I) single frequency, 11 ZAMS stars as type (I') possible shape changer, one ZAMS star as type (II) beater, and five ZAMS stars as type (III) complex variability (table 2).

The apparent area of the spot, $A_{\rm spot}$, was estimated from the amplitude of light variation ($\Delta F/F$) using the following equation (Notsu et al. 2013; Shibata et al. 2013):

$$A_{\rm spot} = \frac{\Delta F}{F} A_{\frac{1}{2}\,\rm star} \left[1 - \left(\frac{T_{\rm spot}}{T_{\rm eff}} \right)^4 \right]^{-1}, \quad (1)$$

where $A_{\frac{1}{2}\,\rm star}$ is the effective area of the stellar hemisphere. $T_{\rm spot}$ and $T_{\rm eff}$ are the temperature of the starspot and photosphere of the star. We applied equation (4) of Notsu et al. (2019). It is an empirical equation for the temperature difference between photosphere and spot, $T_{\rm eff} - T_{\rm spot}$, deduced from Berdyugina et al. (2005).

The starspot coverages, $A_{\rm spot}/A_{\frac{1}{2}\,\rm star}$, are estimated to be 0.1%–21% for the ZAMS stars in IC 2391 and IC 2602. The mean coverage of each group is listed in table 2. ZAMS stars with single frequency have the largest mean spot area, and possible shape-changer ZAMS stars have the second largest values. The mean spot area of the beater and complex variability ZAMS stars are the same as the solar value: $\lesssim$1%.

Table 2. Light curve groups and mean spot coverage of the 33 ZAMS stars.

Features of the light curve		Number		Mean spot coverage [%]	
		IC 2391	IC 2602	IC 2391	IC 2602
(I)	Single frequency	6	10	4.43 ± 4.33	7.93 ± 6.15
(I')	Possible shape changer	2	9	1.01 ± 0.79	3.12 ± 2.97
(II)	Beater	1	0	1.00	—
(III)	Complex variability	2	3	0.19 ± 0.03	1.09 ± 0.86

Table 3. List of detected flares.

Object name	$N_{\rm flare}$	Flare rate [d^{-1}]	Start	End	Duration time [s]	$E_{\rm flare}$ [erg]
			−2457000 [BTJD days]			
(1)	(2)	(3)	(4)	(5)	(6)	(7)
IC 2309						
VXR PSPC 7	1	0.061	1527.732	1527.911	15500	2.79×10^{34}
VXR PSPC 22A	2	0.119	1521.507	1521.691	15900	1.10×10^{34}
			1538.712	1538.893	15600	3.57×10^{34}
VXR PSPC 67A	1	0.066	1522.810	1523.031	19100	4.99×10^{33}
IC 2602						
RSP95 14	4	0.211	1572.245	1572.394	12900	9.19×10^{33}
			1589.550	1589.651	8700	9.09×10^{33}
			1590.634	1590.788	13300	4.49×10^{33}
			1594.010	1594.113	8900	2.39×10^{33}
RSP95 43	1	0.049	1576.154	1576.233	6800	1.09×10^{33}
RSP95 59	1	0.049	1595.024	1595.061	3200	3.59×10^{33}
RSP95 66	1	0.049	1571.844	1571.953	9400	6.49×10^{33}
RSP95 68	5	0.241	1578.423	1578.485	5400	6.00×10^{33}
			1579.994	1580.064	6000	9.59×10^{33}
			1580.417	1580.671	21900	3.79×10^{33}
			1585.552	1585.652	8600	1.55×10^{34}
			1586.795	1586.872	6700	1.69×10^{33}
RSP95 72	1	0.050	1575.538	1575.639	8700	1.66×10^{34}
RSP95 83	1	0.048	1586.471	1586.517	4000	3.19×10^{33}
RSP95 89	1	0.050	1578.693	1579.124	37200	1.32×10^{34}
RSP95 95A	2	0.096	1571.429	1571.710	24300	2.10×10^{34}
			1588.191	1588.419	19700	2.13×10^{34}

The middle column of figure 2 shows examples of Lomb–Scargle periodograms. The false alarm probability for the strongest peaks was calculated to be $3 \times 10^{-290} - 0.007$. TESS data was not obtained for several days in the middle of the observation period. This leads to aliasing on the side of the strongest peak in the periodogram. When we split the light curve at the center time and applied Lomb–Scargle periodogram analysis, the aliasing disappeared.

We also detected 21 flares in the light curves of 12 ZAMS stars in IC 2391 and IC 2602. The properties of each flare are listed in table 3. Their peak amplitude and duration time range from 0.3% to 5.2% and from 3200 to 37200 s, respectively. For the case of the first flare shown in figure 1, the relative flux and the duration are 2.0% and 2.4 hr, respectively. As we will discuss in subsection 4.4, the total bolometric energy of the flare is estimated to be $\sim 10^{33}$–10^{35} erg. It is comparable to that of superflares detected in Maehara et al. (2012), in which the energy of the superflare is calculated to be 100 times larger than those of solar flares, i.e., 10^{33} to 10^{36} erg. The occurrence frequency of flares can be estimated from the number of observed flares, the number of observed stars, and the length of the observation period. In this study, 21 flares were detected from the 33 ZAMS stars in the observational period, so that the occurrence frequency of flares is calculated to be 10.9 flares per year per star. Maehara et al. (2012) detected 14 superflares from data collected from approximately 14000 slowly rotating G-type main-sequence stars over 120 d. The occurrence frequency of superflares was 2.9×10^{-3} flares per year per star. Therefore, superflares occur more frequently on ZAMS stars than on main-sequence stars.

Table 4. Rossby numbers and R' of solar-type superflare stars listed in Notsu et al. (2015b).

Object name (1)	log N_R (2)	log $R'_{\lambda 8542}$ (3)
KIC 4742436	−0.48	−5.60
KIC 6865484	0.23	−4.85
KIC 7354508	0.34	−5.16
KIC 7420545	0.31	−5.14
KIC 8802340	−0.13	−5.02
KIC 9583493	−0.25	−4.81
KIC 9652680	−0.78	−4.45
KIC 10471412	0.44	−5.18
KIC 10528093	−0.10	−4.47
KIC 11140181	0.00	−4.74
KIC 11303472	−0.11	−4.83
KIC 11390058	0.35	−5.43
KIC 11455711	0.24	−5.29
KIC 11494048	0.53	−5.39
KIC 11764567	0.22	−4.97
KIC 12266582	−0.18	−4.81

4 Discussion

4.1 Stellar chromospheric activity and starspots of ZAMS stars

Notsu et al. (2015b) indicated that the Sun and superflare stars show a rough positive correlation between the amplitude of the light curve and the $r_0(8542)$ index, the residual core flux normalized by the continuum level at the line core of the Ca II IRT. They claimed that the magnetic field strengths of superflare stars are higher than that of the Sun.

We investigated the relationship between the strength of the Ca II IRT emission line (λ8542 Å) and the amplitude of the light curve for the ZAMS stars in IC 2391, IC 2602, and the Pleiades cluster. We obtained the amplitude of the light curve of the ZAMS stars in the Pleiades cluster from Rebull et al. (2016a). $R'_{\lambda 8542}$ for the ZAMS stars in IC 2391 and IC 2602 was already calculated in Paper I and is listed in table 1. We also obtained $R'_{\lambda 8542}$ for the ZAMS stars in the Pleiades cluster from Stauffer et al. (1997). We also compare the relationship with the superflare stars studied in Notsu et al. (2015b). With $F_{\lambda 8542}$ and $T_{\rm eff}$ as listed in Notsu et al. (2015a, 2015b), we calculated $R'_{\lambda 8542}$ for the superflare stars (table 4) as

$$R'_{\lambda 8542} = \frac{F_{\lambda 8542}}{\sigma T_{\rm eff}^4}, \tag{2}$$

where σ is Stefan–Boltzmann's constant.

Figure 3 shows that the ZAMS stars with a large light curve amplitude have large $R'_{\lambda 8542}$. The $R'_{\lambda 8542}$ and light curve amplitudes of ZAMS stars are approximately two orders of magnitude larger than those of the Sun. We also found that the ZAMS stars are located on the extensions of the superflare stars (Notsu et al. 2015b). This result suggests that superflare stars link the properties of the Sun to those of the ZAMS stars of ages between 30 and 120 Myr. The ZAMS stars belonging in each open cluster are almost evenly distributed. For the ZAMS stars in IC 2391, IC 2602, and the Pleiades cluster, the mean amplitudes are calculated to 0.025 ± 0.023 mag, 0.081 ± 0.060 mag, and 0.036 ± 0.030 mag, respectively. Their mean $R'_{\lambda 8542}$ are $10^{-4.79 \pm 0.22}$, $10^{-4.54 \pm 0.29}$, and $10^{-4.57 \pm 0.22}$. The difference of their average values differ less than 1σ.

Objects with different types of light curves seem to be unevenly distributed in figure 3, as represented by the colors of the symbols. The ZAMS stars with single frequency have larger light curve amplitudes and larger $R'_{\lambda 8542}$ compared with other types, whereas the ZAMS stars with complex variability have smaller light curve amplitudes and smaller $R'_{\lambda 8542}$ compared with other types. The possible shape-changer ZAMS stars tend to be located between the ZAMS stars with single frequency and the ZAMS stars with complex variability. The relationship between the type of light curve and the magnetic activity will be discussed in the next sub-section.

Figure 4 shows $A_{\rm spot}/A_{\frac{1}{2}{\rm star}}$ as a function of the convective turnover time, τ_c, of the ZAMS stars in IC 2391, IC 2602, and the Pleiades cluster, and the superflare stars listed in Notsu et al. (2015b). In Paper I, we estimated the τ_c values of the ZAMS stars using the τ_c models for stars with the age of 50 Myr (IC 2391) and 30 Myr (IC 2602) presented in Landin et al. (2010). We also estimated τ_c for 130 Myr (the Pleiades) using the same method. For the ZAMS stars with $T_{\rm eff} > 6180$ K, we applied the approximation of τ_c of Noyes et al. (1984). We also estimated τ_c for the solar-type superflare stars (Notsu et al. 2015b) by applying the approximation of τ_c of Noyes et al. (1984), where $(B-V)_0$ is referenced from Reinhold and Gizon (2015). We have estimated $A_{\rm spot}/A_{\frac{1}{2}{\rm star}}$ with equation (1), as mentioned above. $T_{\rm eff}$ values of the Pleiades members and the solar-type superflare stars are taken from Gaia Data Release 2 (DR2; Gaia Collaboration 2018) and Notsu et al. (2015b), respectively.

Figure 4 indicates that $A_{\rm spot}/A_{\frac{1}{2}{\rm star}}$ shows a positive correlation with τ_c. The linear fit, $A_{\rm spot}/A_{\frac{1}{2}{\rm star}} = 10^{-8.7}\tau_c^{1.2}$, was derived . τ_c used in this study is the local convective turnover time. According to the result of Jung and Kim (2007), there is an approximately linear relationship between τ_c and the global convective turnover time, τ_g. For a $1\,M_\odot$ star at ZAMS, we obtain $\tau_g = 1.7\tau_c$. Argiroffi et al. (2016) investigated the relationship between the ratio of the thickness of the convective zone to the stellar radius, H_c/R_* and τ_g. We derived a linear fit as $\tau_g\,[{\rm d}] = 10^{3.1}(H_c/R_*)^{2.2}$.

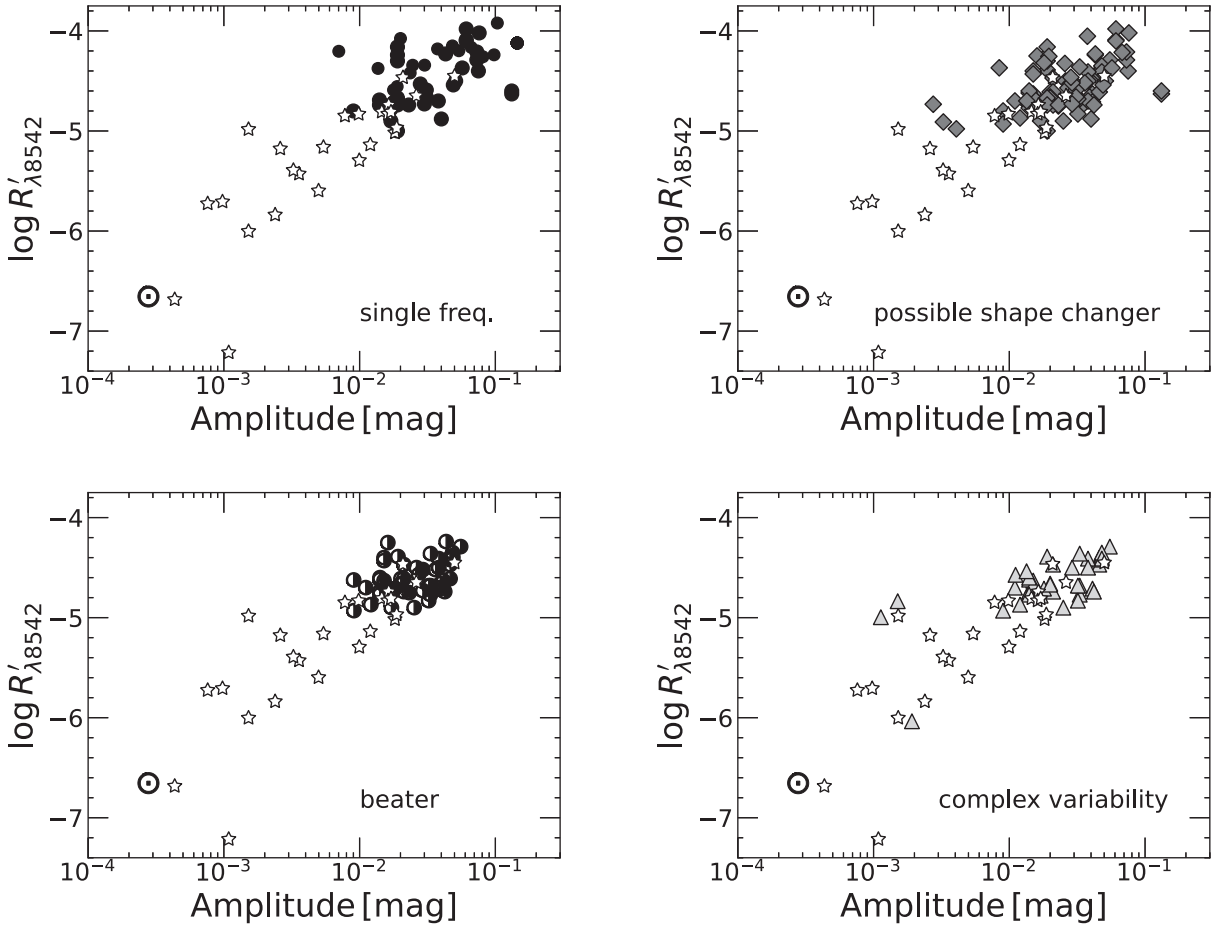

Fig. 3. Relationship between the amplitude of the light curve and the ratio of the surface flux of the Ca II IRT emission line (λ8542 Å) to the stellar bolometric luminosity, $R'_{\lambda 8542}$ of the ZAMS stars in IC 2391, IC 2602, and the Pleiades cluster. The filled circles denote the ZAMS stars with single frequency. The gray diamonds represent the possible shape-changer ZAMS stars. The half-filled circles denote the beater ZAMS stars. The light gray triangles show the ZAMS stars with complex variability. Star marks represent superflare stars (Notsu et al. 2015b). The light variations and $R'_{\lambda 8542}$ of the ZAMS stars are as large as those of the most active superflare stars and two orders larger than those of the Sun. The ZAMS stars are located on the extensions of the superflare stars. This suggests that superflare stars link the properties of the Sun to those of the ZAMS stars of ages between 30 and 120 Myr.

$$\begin{cases} A_{\rm spot}/A_{\frac{1}{2}\,\rm star} = 10^{-8.7}\tau_{\rm c}^{1.2} \\ \tau_{\rm g} = 1.7\tau_{\rm c} \\ \tau_{\rm g}\,[\rm d] = 10^{3.1}(H_{\rm c}/R_*)^{2.2}. \end{cases} \tag{3}$$

Therefore

$$\frac{A_{\rm spot}}{A_{\frac{1}{2}\,\rm star}} = 4.6\left(\frac{H_{\rm c}}{R_*}\right)^{2.6}. \tag{4}$$

When we assume that the geometry of a starspot is single circle whose diameter is $D_{\rm spot}$, we can obtain

$$\left(\frac{D_{\rm spot}}{2R_*}\right)^2 = 4.6\left(\frac{H_{\rm c}}{R_*}\right)^{2.6}. \tag{5}$$

Therefore,

$$D_{\rm spot} = 2\sqrt{4.6{H_{\rm c}}^{2.6}} \sim 4.3{H_{\rm c}}^{1.3}. \tag{6}$$

Numerical simulation indicates that for a large sunspot, the ratio of the horizontal size at the photosphere to $H_{\rm c}$ ranges from 2.04 to 6.75 (Vickers 1971). Mullan (1973) discussed the relationship between the thickness of the convection zone and the size of a starspot. They considered that the depth of the spot, $H_{\rm s}$, is equal to the depth of the convection zone, $H_{\rm c}$, which yields $2.04 < D_{\rm spot}/H_{\rm c} < 6.75$. We derived $D_{\rm spot}/H_{\rm c} \sim 4.3$, which is well within the values presented in Mullan (1973).

4.2 Starspots and rotation–activity relationship

In this section, we examine the relationship between the spot area and the rotation–activity relationship. In Paper I, we calculated $N_{\rm R}$ for the ZAMS stars in IC 2391 and IC 2602. We also calculated $N_{\rm R}$ for the Pleiades members and the superflare stars listed in Notsu et al. (2015b). Their

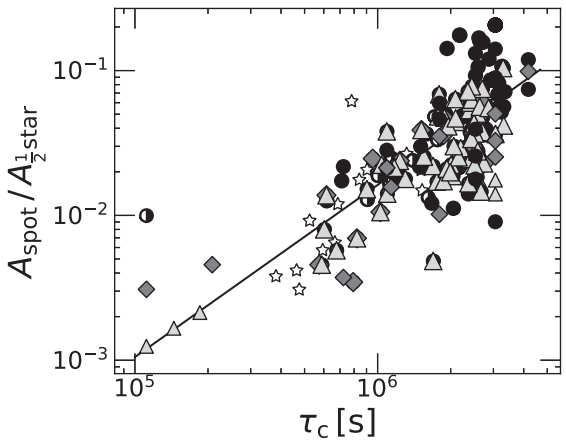

Fig. 4. Coverage of the starspot, $A_{\rm spot}/A_{\frac{1}{2}{\rm star}}$, as a function of the convection turnover time, $\tau_{\rm c}$, of the ZAMS stars in IC 2391, IC 2602, and the Pleiades cluster. The filled circles denote the ZAMS stars with single frequency. The gray diamonds show the possible shape-changer ZAMS stars. The half-filled circle denotes the beater ZAMS star. The open triangles represent the ZAMS stars with complex variability. The star marks represent superflare stars (Notsu et al. 2015b). The solid line indicates the least-squares linear fit line of all the objects shown here. $A_{\rm spot}/A_{\frac{1}{2}{\rm star}}$ shows a positive correlation with $\tau_{\rm c}$.

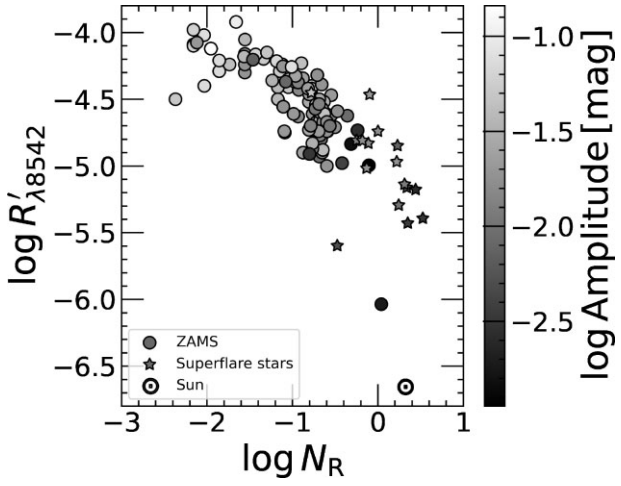

Fig. 5. Relationship between the ratio of the surface flux of the Ca II emission line (λ8542 Å) to the stellar bolometric luminosity, $R'_{\lambda 8542}$, and the Rossby number, $N_{\rm R}$, of the ZAMS stars in IC 2391, IC 2602, and the Pleiades cluster (circles). Star marks represent superflare stars (Notsu et al. 2015b). The gray scale of all the symbols represents the amplitude of the light curve. Objects with a smaller $N_{\rm R}$ have both a saturated $R'_{\lambda 8542}$ and a larger light curve amplitude.

P values were taken from Rebull et al. (2016b) and Notsu et al. (2015b), respectively. $N_{\rm R}$ for the superflare stars is shown in table 4. The relationship between $N_{\rm R}$ and the ratio of the surface flux of the Ca II IRT emission line to the stellar bolometric luminosity, $R'_{\lambda 8542}$, is shown in figure 5. For the ZAMS stars in IC 2391, IC 2602, and the Pleiades cluster with $N_{\rm R} > 10^{-1.1}$, $R'_{\lambda 8542}$ increases with decreasing $N_{\rm R}$ until it saturates. For the ZAMS stars with $N_{\rm R} < 10^{-1.1}$, $R'_{\lambda 8542}$ reaches a constant level. All the superflare stars and the Sun belong to the unsaturated regime. The ZAMS stars belonging in each open cluster are almost evenly distributed.

Objects with a smaller $N_{\rm R}$ have both a saturated $R'_{\lambda 8542}$ and a larger light curve amplitude (figure 5). It is known that small $N_{\rm R}$ objects are strongly activated by their dynamo process. The dynamo process is thought to induce a strong magnetic field, resulting in large starspots and saturated strong emission lines. The Ca II saturation is consistent with the existence of a large-scale starspot or starspot group.

Figure 6 shows the relationship between $R'_{\lambda 8542}$ and $N_{\rm R}$ of the ZAMS stars in IC 2391, IC 2602, and the Pleiades cluster. We noticed that the ZAMS stars with single frequency or possible shape change have small $N_{\rm R}$ and large $R'_{\lambda 8542}$. By combining with figure 5, it is suggested that those objects show larger light curve amplitude, indicating huge spot/spot groups. The ZAMS stars with beat or complex variability have large $N_{\rm R}$, small $R'_{\lambda 8542}$, and smaller light curve amplitude. This result suggests that those ZAMS stars do not have huge spot/spot groups.

We consider that the strong magnetic field generates a limited number of large starspots. With Kepler observations, Reinhold et al. (2020) revealed that 369 stars with near-solar rotational periods have much stronger and more regular light variation than the Sun. Isik et al. (2020) constructed the light curve model of such stars by injecting active regions on stellar surfaces with highly inhomogeneous distribution compared with the Sun. The injected active region consists of spot groups and faculae. They used wavelength-dependent contrast models of faculae and spots on the Sun calculated by Unruh, Solanki, and Fligge (1999). Different activity levels lead to different types of light curves, i.e., periodic, strong variation, and complex variation. They qualified the activity level in terms of the chromospheric S-index. By extrapolating the relationship between the disk coverage by spots and the S-index of the Sun (Shapiro et al. 2014), they obtained the S-index for a more active star with a given light curve. Isik et al. (2020) found that the light curve amplitude increases with larger S-index because of the increasing occurrence of active regions. Active longitude nesting, in which active regions appear on the opposite side, leads to highly regular variability. The regularity and light curve amplitude decrease for small S-index objects. As mentioned above, $R'_{\lambda 8542}$ of the ZAMS stars in IC 2391, IC 2602, and the Pleiades cluster with single frequency tend to be saturated, and that of the ZAMS stars with complex variability is relatively small. This result supports the assumption in Isik et al. (2020) that the active regions are inhomogeneously distributed on the surface of an active star.

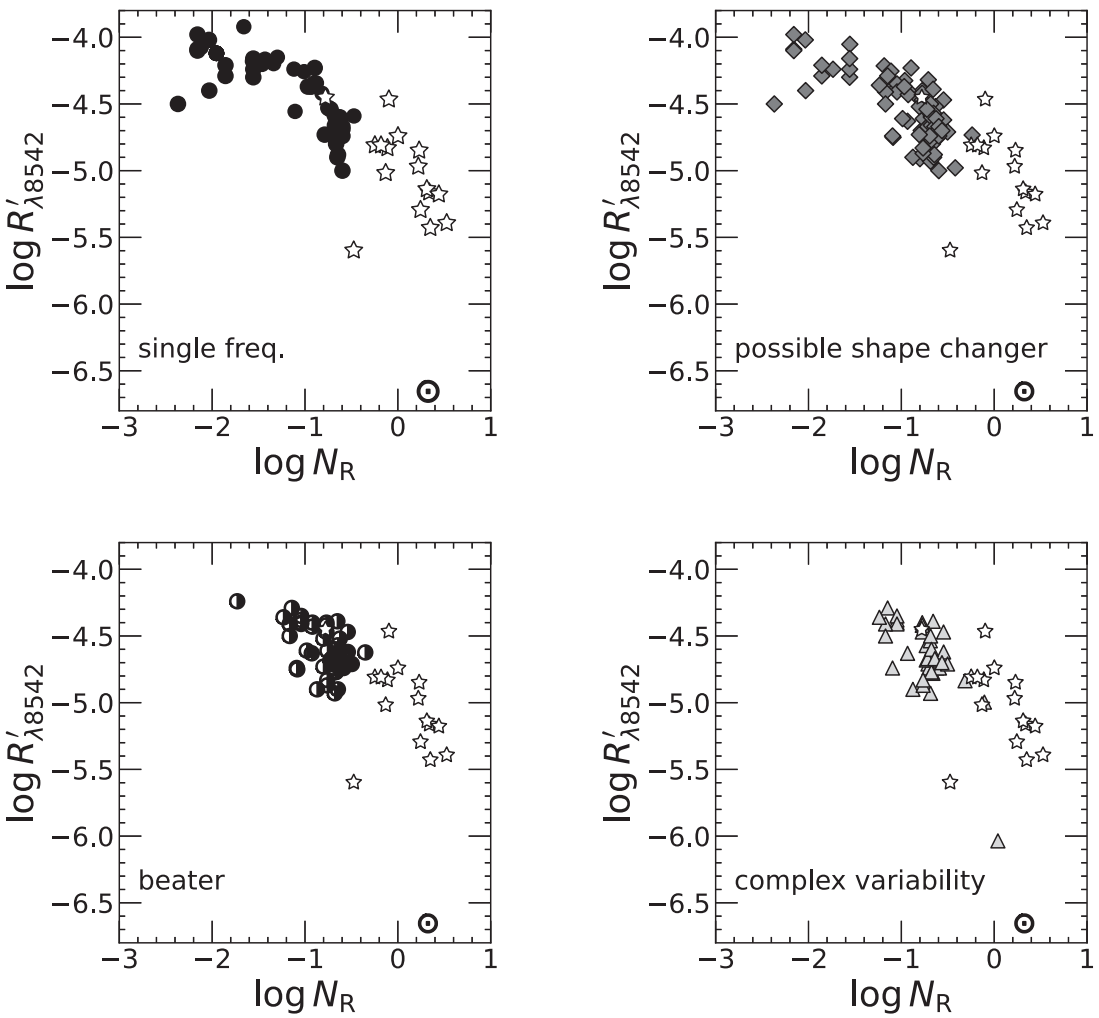

Fig. 6. Relationship between the ratio of the surface flux of the Ca II emission line (λ8542 Å) to the stellar bolometric luminosity, $R'_{\lambda 8542}$, and the Rossby number, N_R, of the ZAMS stars in IC 2391, IC 2602, and the Pleiades cluster. The filled circles denote ZAMS stars with single frequency. The gray diamonds denote the possible shape-changer ZAMS stars. The half-filled circles denote the beater ZAMS stars. The open triangles denote ZAMS stars with complex variability. Star marks represent superflare stars (Notsu et al. 2015b). The ZAMS stars with single frequency or possible shape change have small N_R, large $R'_{\lambda 8542}$, and larger light curve amplitude, while the ZAMS stars with beat or complex variability have large N_R, small $R'_{\lambda 8542}$, and smaller light curve amplitude.

4.3 Period–color distribution

Rebull et al. (2020) investigated the relationship between $(V - K_s)_0$ and P with K2 data for six clusters: Rho Oph, Taurus, Upper Sco, Taurus foreground, Pleiades, and Prasepe (1–790 Myr) and discussed spin-down evolution to the main-sequence.

We investigated the P of the members of IC 2391 and IC 2602 as a function of $(V - K_s)_0$ (figures 7 and 8). We took the V magnitudes from Marsden, Carter, and Donati (2009) and the K_s magnitudes from the 2MASS survey (Cutri et al. 2003). These values are listed in table 1. The $(V - K_s)$ values were converted to unreddened values, $(V - K_s)_0$, using the reddening parameters for the clusters; $E(B - V) = 0.006$ for IC 2391 from Patten and Simon (1996) and $E(B - V) = 0.04$ for IC 2602 from Braes (1961) were converted to $E(V - K_s) = 0.016$ and $E(V - K_s) = 0.110$ for IC 2391 and IC 2602 by multiplying the $E(V - K_s)/E(B - V)$ value given in Rieke and Lebofsky (1985).

We found that the ZAMS stars in IC 2391, IC 2602, and the Pleiades cluster whose Ca II emission lines are saturated tend to be distributed in the lower part of the figure 7, while the ZAMS stars whose Ca II emission lines are unsaturated are located close to the majority of the Pleiades members. It is possible that the ZAMS stars whose Ca II emission lines are saturated have not reached the spin down stage yet. In figure 8, we also found that most of the ZAMS stars rotating rapidly have a single frequency period. These results obtained from figures 7 and 8 show that the ZAMS stars that have not reached the spin down stage have saturated Ca II emission lines and single frequency periods. As

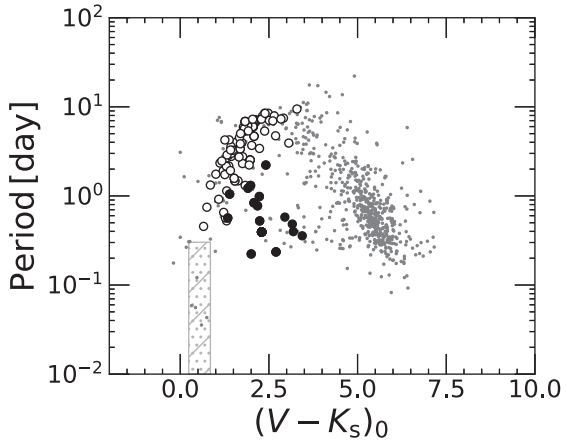

Fig. 7. Relationship between the $(V-K_s)_0$ color and the rotational period of ZAMS stars in IC 2391, IC 2602, and the Pleiades cluster. The filled circles show the ZAMS stars whose Ca II IRT emission lines are saturated ($R'_{\lambda 8542} \sim 10^{-4.2}$). The open circles show the ZAMS stars with $R'_{\lambda 8542} < 10^{-4.2}$ whose Ca II IRT emission lines are unsaturated. The tiny circles denote the Pleiades members examined by Rebull et al. (2016a) but whose Ca II IRT emission lines had not been observed in Stauffer et al. (1997). The hatched area represents $0.24 < (V-K_s)_0 < 0.85$ and $P \leq 0.3$ d. The ZAMS stars whose Ca II emission lines are saturated tend to be distributed in the lower part of the figure, while the ZAMS stars whose Ca II emission lines are unsaturated are located close to the majority of the Pleiades members.

mentioned in the discussion on figure 6, the ZAMS stars with single frequency tend to have strong Ca II IRT emission lines. These results are consistent with Rebull et al. (2016b) and Stauffer et al. (2016), in which approximately half of the ZAMS stars rotating rapidly have sinusoidal light curves. Here, we do not think that stellar pulsation is the cause of the light variation. Rebull et al. (2016a) considered that only 1% of the Pleiades members are pulsators, including the δ Sct-type, which have very small light curve amplitudes, $0.24 < (V-K_s)_0 < 0.85$, and short rotational periods. No ZAMS stars in IC 2391 and IC 2602 have both a short period and an early spectral type.

4.4 Superflare

After removing the rotational light variations in the TESS light curves, we detected 21 flares from 12 ZAMS stars in IC 2391 and IC 2602. These flares show characteristics similar to those of solar-type main-sequence stars. figure 9 shows the relationship between the light curve amplitude and the number of the flares on the ZAMS stars in IC 2391 and IC 2602. More frequent flares are observed on the ZAMS stars with larger light curve amplitudes. We found

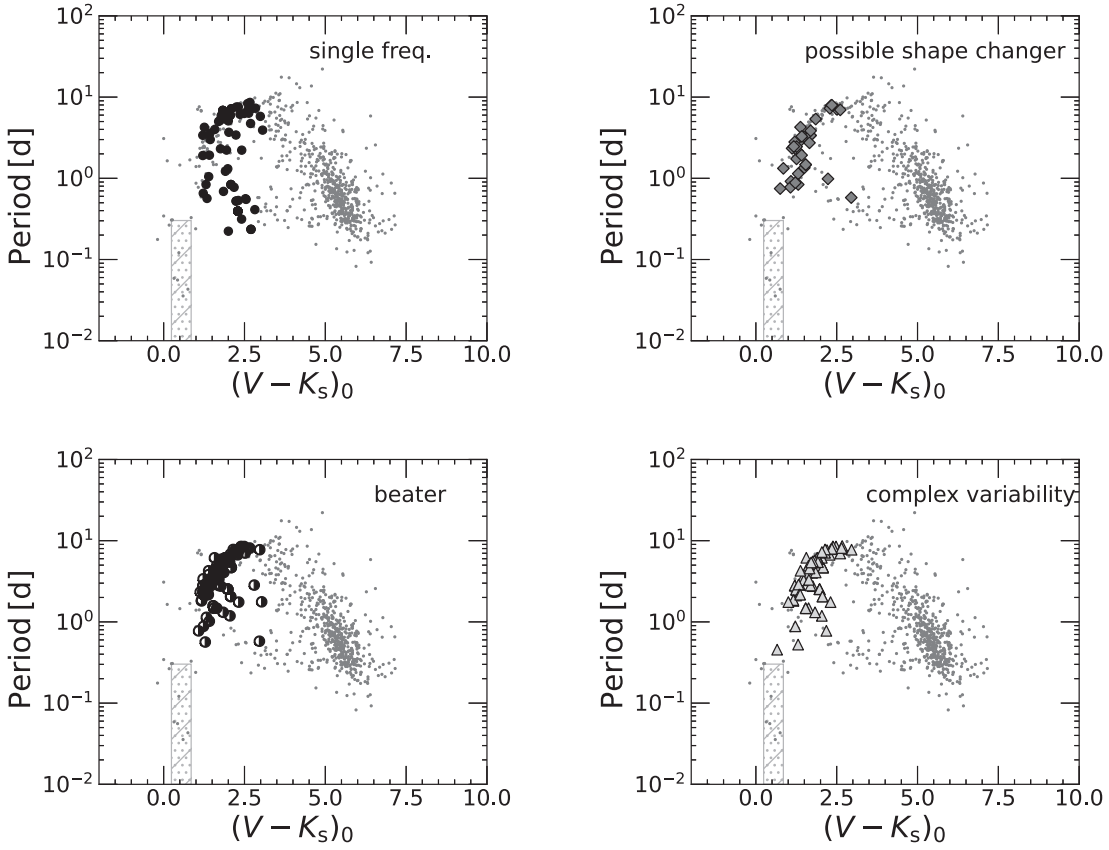

Fig. 8. Relationship between the $(V-K_s)_0$ color and the rotational period of ZAMS stars in IC 2391, IC 2602, and the Pleiades cluster. The filled circles denote the ZAMS stars with single frequency. The gray diamonds denote the possible shape-changer ZAMS stars. The half-filled circles denote the beater ZAMS stars. The open triangles denote the ZAMS stars with complex variability. The tiny circles denote the Pleiades members examined by Rebull et al. (2016a) but whose Ca II IRT emission lines had not been observed in Stauffer et al. (1997). The hatched area represents $0.24 < (V-K_s)_0 < 0.85$ and $P \leq 0.3$ d. Most of the ZAMS stars rotating rapidly have light curves with a single frequency period.

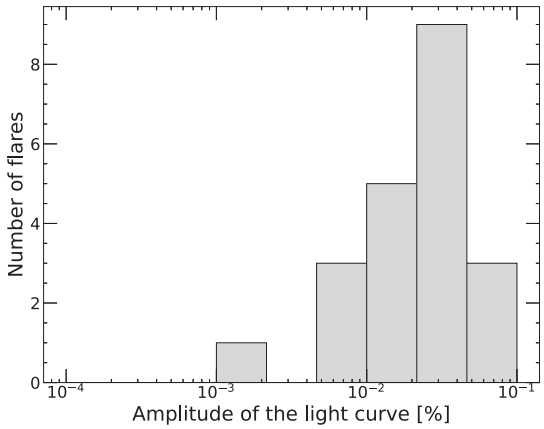

Fig. 9. Relationship between the light curve amplitude and the number of flares on the ZAMS stars in IC 2391 and IC 2602. More frequent flares are observed on the ZAMS stars with larger light curve amplitudes.

no correlation between the rotational phase and the number of flares, which is also claimed in a study on M dwarfs (Doyle et al. 2018).

The energy of a flare can be estimated from the amplitude of a flare ($\Delta F_{\rm flare}/F$) and the duration time. A detailed description is presented in Shibayama et al. (2013) and their related studies. $\Delta F_{\rm flare}/F$ can be written as

$$\frac{\Delta F_{\rm flare}}{F} = \frac{A_{\rm flare}}{A_{\frac{1}{2}\,\rm star}} \frac{\int B(T_{\rm flare}, \lambda) S(\lambda) d\lambda}{\int B(T_{\rm eff}, \lambda) S(\lambda) d\lambda}, \tag{7}$$

where $A_{\rm flare}/A_{\frac{1}{2}\,\rm star}$ is the fraction of the flare-emitting area normalized by the effective area of the stellar hemisphere. With the Stefan–Boltzman law regarding the photospheric luminosity and $T_{\rm eff}$ of the ZAMS stars in Gaia DR2, we estimated the stellar radius and converted it to $A_{\frac{1}{2}\,\rm star}$. $T_{\rm flare}$ is the effective temperature of a flare component. We assumed that the spectral energy distribution of the flare component is similar to blackbody radiation, with an effective temperature of 10000 K (e.g., Hawley & Pettersen 1991; Hawley & Fisher 1992). $B(T_{\rm flare}, \lambda)$ is the Plank function, and $S(\lambda)$ is the spectral response function of the TESS detector (λ6000–10000 Å; Ricker et al. 2015). We estimated $A_{\rm flare}$ with equation (7) and substitute it into equation (8), by which we obtain the bolometric luminosity of the flare, $L_{\rm flare}$:

$$L_{\rm flare} = \sigma T_{\rm flare}^4 A_{\rm flare}. \tag{8}$$

The total bolometric energy of a superflare, $E_{\rm flare}$, is an integral of $L_{\rm flare}$ over the flare duration,

$$E_{\rm flare} = \int L_{\rm flare}(t) dt. \tag{9}$$

Figure 10 is a scatter plot of the flare energy, $E_{\rm flare}$, as a function of spot coverage, $A_{\rm spot}/A_{\frac{1}{2}\,\rm star}$. In the figure,

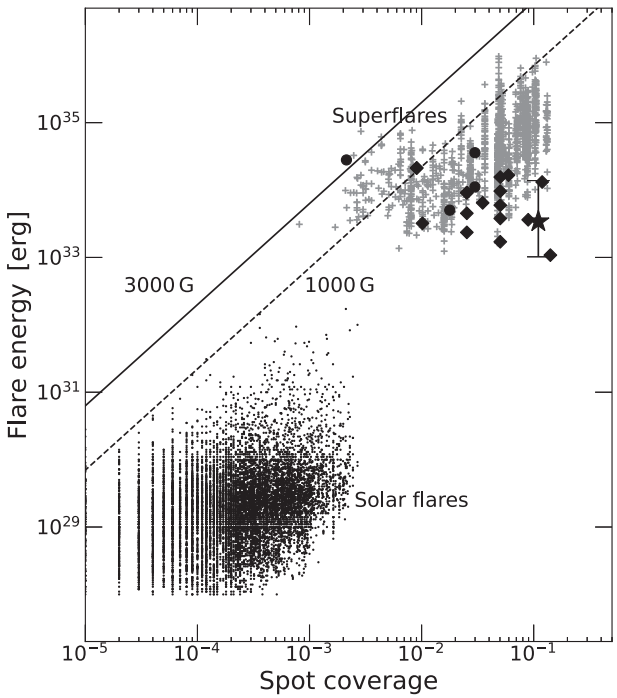

Fig. 10. Relationship between spot coverage, $A_{\rm spot}/A_{\frac{1}{2}\,\rm star}$, and flare energy, $E_{\rm flare}$. Circles and diamonds denote flares on the ZAMS stars in IC 2391 and IC 2602, respectively. The star symbol represents the flare distribution of EK Dra detected by TESS (Namekata et al. 2022). The tiny circles show solar flares (Shibayama et al. 2013), and the cross symbols show superflares on Sun-like stars with $T_{\rm eff}$ = 5100–5600 K. The black solid and dashed lines correspond to the analytical relationship between $E_{\rm flare}$ and $A_{\rm spot}$ for B = 3000 G and 1000 G, respectively. For the flares on the ZAMS stars in IC 2391 and IC 2602, the energy is estimated to be ~10^{33}–10^{35} erg, which is comparable with the energy of a superflare.

solar flares and superflares, including those of EK Draconis (EK Dra), are also shown. EK Dra is known as an active G-type ZAMS star that exhibits frequent flares. For EK Dra, we referenced the spot coverage from Strassmeier and Rice (1998), and the flare energy from Namekata et al. (2022). We found that the spot coverage of the ZAMS stars in IC 2391 and IC 2602 is similar to that of superflare stars. The energy of the flares is estimated to be ~10^{33}–10^{35} erg, which is comparable with the energy of a superflare. One flare is above the analytical relationship for B = 3000 G.

We compare the occurrence rate of flares on ZAMS stars in IC 2391 and IC 2602 with those of solar flares (figure 11). Flares with larger energy have a lower occurrence rate, the same as solar flares. For the 12 ZAMS stars from which flares were detected, we obtained the distribution $dN/dE \propto E^{-\alpha}$ with index $\alpha \sim 0.7$. We found that the flare frequency on EK Dra is similar to that of our ZAMS stars.

Figure 12 shows the relationship between the flares and the rotation–activity. Most of the ZAMS stars in IC 2391 and IC 2602 on which the flares are detected are located in the saturated regime. Flares occur more frequently on

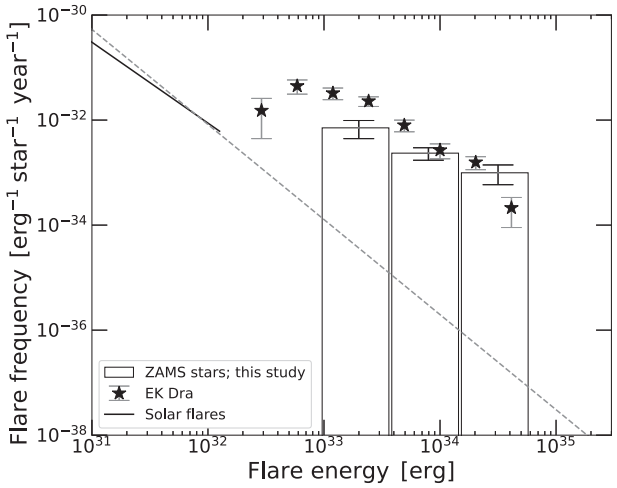

Fig. 11. Occurrence rate of flares on ZAMS stars and of solar flares. The histogram shows the frequency distribution of flares on the 12 ZAMS stars in IC 2391 and IC 2602 on which flares were detected. The star symbols represent the flare distribution of EK Dra detected by TESS (Namekata et al. 2022). The solid line indicates the power-law distribution of solar flares observed in hard X-rays (Crosby et al. 1993), with the distribution $dN/dE \propto E^{-\alpha}$ with index $\alpha \sim 1.8$. The dashed line corresponds to the power-law distribution estimated from superflares in Sun-like stars and solar flares (Shibayama et al. 2013). The flare frequency on the 12 ZAMS stars is similar to that of EK Dra.

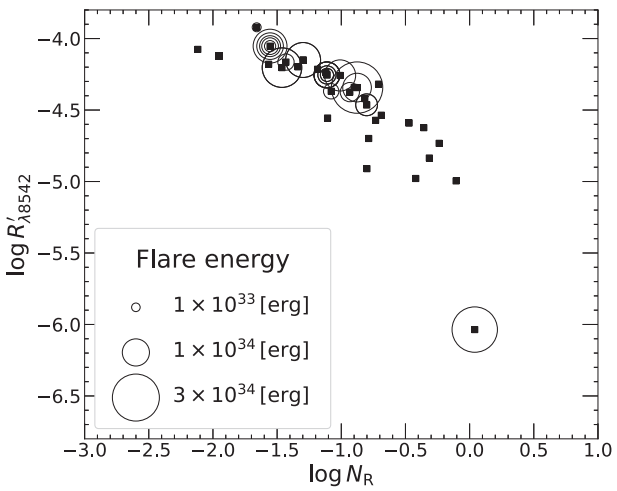

Fig. 12. The 21 flares are shown for the relationship between the ratio of the surface flux of the Ca II emission line (λ8542 Å) to the stellar bolometric luminosity, $R'_{\lambda 8542}$, and the Rossby number, N_R, of the ZAMS stars in IC 2391 and IC 2602 (squares). The flares and their energies are represented by open circles and their size, respectively. Most of the ZAMS stars on which the flares are detected are located in the saturated regime. Flares occur more frequently on the ZAMS stars that have small N_R.

the ZAMS stars that have small N_R. Davenport (2016) show that GKM stars with small N_R show luminous flares. Medina et al. (2020) examined the relationship between N_R and the flare rate for mid- to late-M dwarfs. They found a high flare rate for small N_R stars. Our results indicate that small N_R objects experience superflares, even for ZAMS stars.

5 Conclusion

We analyzed the TESS light curves for the 33 ZAMS stars belonging to IC 2391 and IC 2602. Light variation was detected in all the ZAMS stars. This was considered to be caused by starspots. The amplitudes of the light curves range from 0.001–0.145 mag. The starspot coverages range from 0.1%–21%.

(1) The $R'_{\lambda 8542}$ and light curve amplitudes of ZAMS stars in IC 2391, IC 2602, and the Pleiades cluster are approximately two orders of magnitude larger than those of the Sun. These ZAMS stars are located on the extensions of the superflare stars and the Sun. This result suggests that superflare stars link the properties of the Sun to those of the ZAMS stars of ages between 30 and 120 Myr.

(2) The ZAMS stars in IC 2391, IC 2602, and the Pleiades cluster with small N_R show a light curve with a single frequency or possible shape change. The light curves have large amplitude, indicating inhomogeneous longitudinal distribution of large starspots. They also show saturated chromospheric Ca II emission lines, and have not reached the spin-down period. Most of the flare events were detected on such objects in IC 2391 and IC 2602. Those enegies are more than 10^{33} erg, so that these flare events correspond to superflares.

(3) The ZAMS stars in IC 2391, IC 2602, and the Pleiades cluster with large N_R show beat or a complex light curve with a small amplitude. They have weak Ca II emission lines. The superflare events are rare on such objects in IC 2391 and IC 2602.

Acknowledgment

We wish to thank Dr. Notsu Y. and Dr. Namekata K. for comments. This paper includes data collected with the TESS mission, obtained from the MAST data archive at the Space Telescope Science Institute (STScI). M. Yamashita was supported by a scholarship from the Japan Association of University Women and would like to acknowledge them. This research was supported by a grant from the Hayakawa Satio Fund awarded by the Astronomical Society of Japan. Y. I. is supported by JSPS KAKENHI grant number 17K05390.

References

Argiroffi, C., Caramazza, M., Micela, G., Scienceortino, S., Moraux, E., Bouvier, J., & Flaccomio, E. 2016, A&A, 589, A113
Baliunas, S., Sokoloff, D., & Soon, W. 1996, ApJ, 457, L99
Barnes, S. A., Sofia, S., Prosser, C. F., & Stauffer, J. R. 1999, ApJ, 516, 263

Barrado y Navascues, D., Stauffer, J. R., & Jayawardhana, R. 2004, ApJ, 614, 386
Berdyugina, S. V. 2005, Living Rev. Sol. Phys., 2, 8
Braes, L. L. E. 1961, Mon. Notes Astron. Soc. S. Afr., 20, 7
Crosby, N. B., Aschwanden, M. J., & Dennis, B. R. 1993, Sol. Phys., 143, 275
Cutri, R. M., et al. 2003, VizieR Online Data Catalog, II/246
Davenport, J. R. A. 2016, ApJ, 829, 23
D'Orazi, V., & Randich, S. 2009, A&A, 501, 553
Doyle, L., Ramsay, G., Doyle, J. G., Wu, K., & Scullion, E. 2018, MNRAS, 480, 2153
Feinstein, A. D., et al. 2019, PASP, 131, 094502
Fritzewski, D. J., Barnes, S. A., James, D. J., Järvinen, S. P., & Strassmeier, K. G. 2021, A&A, 656, A103
Gaia Collaboration 2018, A&A, 616, A1
Hawley, S. L., & Fisher, G. H. 1992, ApJS, 78, 565
Hawley, S. L., & Pettersen, B. R. 1991, ApJ, 378, 725
Ilin, E., Schmidt, S. J., Poppenhäger, K., Davenport, J. R. A., Kristiansen, M. H., & Omohundro, M. 2021, A&A, 645, A42
Işık, E., Shapiro, A. I., Solanki, S. K., & Krivova, N. A. 2020, ApJ, 901, L12
Jung, Y. K., & Kim, Y.-C. 2007, J. Astron. Space Sci., 24, 1
Koch, D. G., et al. 2010, ApJ, 713, L79
Landin, N. R., Mendes, L. T. S., & Vaz, L. P. R. 2010, A&A, 510, A46
Lanza, A. F., Rodonò, M., Pagano, I., Barge, P., & Llebaria, A. 2003, A&A, 403, 1135
Maehara, H., et al. 2012, Nature, 485, 478
Marsden, S. C., Carter, B. D., & Donati, J.-F. 2009, MNRAS, 399, 888
Medina, A. A., Winters, J. G., Irwin, J. M., & Charbonneau, D. 2020, ApJ, 905, 107
Messina, S., Desidera, S., Lanzafame, A. C., Turatto, M., & Guinan, E. F. 2011, A&A, 532, A10
Mullan, D. J. 1973, ApJ, 186, 1059
Namekata, K., et al. 2022, ApJ, 926, L5
Notsu, Y., et al. 2013, ApJ, 771, 127
Notsu, Y., et al. 2019, ApJ, 876, 58
Notsu, Y., Honda, S., Maehara, H., Notsu, S., Shibayama, T., Nogami, D., & Shibata, K. 2015a, PASJ, 67, 32
Notsu, Y., Honda, S., Maehara, H., Notsu, S., Shibayama, T., Nogami, D., & Shibata, K. 2015b, PASJ, 67, 33
Noyes, R. W., Hartmann, L. W., Baliunas, S. L., Duncan, D. K., & Vaughan, A. H. 1984, ApJ, 279, 763
Patten, B. M., & Simon, T. 1996, ApJS, 106, 489
Randich, S., Pallavicini, R., Meola, G., Stauffer, J. R., & Balachandran, S. C. 2001, A&A, 372, 862
Rebull, L. M., et al. 2016a, AJ, 152, 113
Rebull, L. M., et al. 2016b, AJ, 152, 114
Rebull, L. M., Stauffer, J. R., Cody, A. M., Hillenbrand, L. A., Bouvier, J., Roggero, N., & David, T. J. 2020, AJ, 159, 273
Reinhold, T., & Gizon, L. 2015, A&A, 583, A65
Reinhold, T., Shapiro, A. I., Solanki, S. K., Montet, B. T., Krivova, N. A., Cameron, R. H., & Amazo-Gómez, E. M. 2020, Science, 368, 518
Ricker, G. R., et al. 2015, J. Astron. Telesc., Instrum. Syst., 1, 014003
Rieke, G. H., & Lebofsky, M. J. 1985, ApJ, 288, 618
Scargle, J. D. 1982, ApJ, 263, 835
Shapiro, A. I., Solanki, S. K., Krivova, N. A., Schmutz, W. K., Ball, W. T., Knaack, R., Rozanov, E. V., & Unruh, Y. C. 2014, A&A, 569, A38
Shibata, K., et al. 2013, PASJ, 65, 49
Shibayama, T., et al. 2013, ApJS, 209, 5
Stauffer, J., et al. 2016, AJ, 152, 115
Stauffer, J. R., Hartmann, L. W., Prosser, C. F., Randich, S., Balachandran, S., Patten, B. M., Simon, T., & Giampapa, M. 1997, ApJ, 479, 776
Strassmeier, K. G., & Rice, J. B. 1998, A&A, 330, 685
Unruh, Y. C., Solanki, S. K., & Fligge, M. 1999, A&A, 345, 635
Vickers, G. T. 1971, ApJ, 163, 363
Yamashita, M., & Itoh, Y. 2022, PASJ, 74, 557 (Paper I)
Yamashita, M., Itoh, Y., & Takagi, Y. 2020, PASJ, 72, 80